X-ray studies of radio-loud AGN

Beatriz Mingo Fernandez

Centre for Astrophysics Research

University of Hertfordshire

A thesis submitted to the University of Hertfordshire in partial fulfilment of the requirements for the degree of

Doctor of Philosophy

April 2013

Sapere Aude!

Horatio, Epistularum liber primus

The Beautiful in nature is connected with the form of the object, which consists in having boundaries. The Sublime, on the other hand, is to be found in a formless object, so far as in it or by occasion of it boundlessness is represented, and yet its totality is also present to thought. [. . .] Natural beauty (which is self-subsisting) brings with it a purposiveness in its form by which the object seems to be, as it were, pre-adapted to our Judgement, and thus constitutes in itself an object of satisfaction. On the other hand, that which excites in us, without any reasoning about it, but in the mere apprehension of it, the feeling of the sublime, may appear as regards its form to violate purpose in respect of the Judgement, to be unsuited to our presentative faculty, and, as it were, to do violence to the Imagination; and yet it is judged to be only the more sublime.

Immanuel Kant, Kritik der Urteilskraft (Critique of Judgement), transl. J. Bernard

Abstract

In this thesis I use X-ray observations to study the cores and extended structures of radio-loud AGN, to determine their structure, accretion properties and the impact they have on their surroundings.

I use new *Chandra* data and archival *XMM-Newton* observations of Markarian 6 to look for evidence of emission from shocked gas around the external radio bubbles, using spatially resolved regions in *Chandra* and spectral analysis of the *XMM* data. The results show that the bubbles in Mrk 6 are indeed driving a shock into the halo of the host galaxy, with a Mach number of ∼3.9. I also find that the spectrum of the AGN has a variable absorbing column, which changes from $\sim 8 \times 10^{21}$ atoms cm^{-2} to $\sim 3 \times 10^{23}$ atoms cm^{-2} on short timescales (2-6 years). This is probably caused by a clump of gas close to the central AGN, passing in front of us at the moment of the observation.

Using new and archival *Chandra* observations of the Circinus galaxy, I match them to pre-existing radio, infrared and optical data to study the kpc-scale emission. As for Mrk 6, I find that the radio bubbles in Circinus are driving a shock into the interstellar medium of the host galaxy, with Mach numbers $\mathcal{M} \sim 2.7$–3.6 and $\mathcal{M} \sim 2.8$–5.3 for the W and E shells respectively. Comparing the results with those we previously obtained for Centaurus A, NGC 3801 and Mrk 6, I show that the total energy in the lobes (thermal+kinetic) scales approximately with the radio power of the parent AGN. The spatial coincidence between the X-ray and edge-brightened radio emission in Circinus resembles the morphology of some SNR shocks, a parallel that has been expected for AGN, but has never been observed before. I investigate what underlying mechanisms both types of systems may have in common, arguing that, in Circinus,

the edge-brightening in the shells may be accounted for by a B field enhancement caused by shock compression, but do not preclude some local particle acceleration.

I also carry out a systematic study of the X-ray emission from the cores in the $0.02 < z < 0.7$ 2Jy sample, using *Chandra* and *XMM-Newton* observations. I combine the results with the mid-IR, optical emission line and radio luminosities, and compare them with those of the 3CRR sources, to show that the low-excitation objects in our sample show all the signs of radiatively inefficient accretion. I study the effect of the jet-related emission on the various luminosities, confirming that it is the main source of soft X-ray emission for our sources. I also find strong correlations between the accretion-related luminosities, and identify several sources whose optical classification is incompatible with their accretion properties. I derive the bolometric and jet kinetic luminosities for the sample and find a difference in the total Eddington rate between the low and high-excitation populations, with the former peaking at $\sim$ 1 per cent and the latter at $\sim$ 20 per cent Eddington. There is, however, an overlap between the two, indicating that a simple Eddington switch may not be possible. The apparent independence of jet kinetic power and radiative luminosity in the high-excitation population in our plots allows us to test the hypothesis in which jet production and radiatively efficient accretion are in fact independent processes that can coexist in high-excitation objects.

Contents

List of Figures

List of Tables

Declaration

I declare that the work described in this dissertation was carried out in accordance with the Regulations of the University of Hertfordshire. This work is original, except where specified otherwise, and has not been previously submitted for any degree or diploma at this or any other university.

The results presented in Chapters 3 and 4 have been published in The Astrophysical Journal (respectively, Mingo et al. 2011, 2012), and are presented in their publication form. The results in Chapters 5 and 6 are part of two papers to be submitted to the Monthly Notices of the Royal Astronomical Society for publication. Contributions to these chapters by my collaborators are indicated in the text.

Beatriz Mingo

April 2013

Acknowledgements

I would need another dissertation to properly thank all the people that have made this possible! I will try to keep this brief, in the hope that those that are not explicitly mentioned know that they are still remembered and acknowledged.

First and foremost, thanks to Martin Hardcastle for his infinite patience, ready encouragement and boundless insight. I believe he has an endless supply of all three, by the way I have been putting them to the test over the last years. Thanks to Judith Croston for tirelessly answering my questions, providing advice and reading drafts at impossible hours. Thanks also to Andy Pollock, for setting me on this path and teaching me to ask even more questions (that one backfired, I'm afraid). I can only hope to, eventually, be worthy of their teachings.

Thanks to my grandfather Pedro, the first victim of my questioning and the one who set me on my quest for knowledge at the tender age of two. I miss him every day. Thanks to my grandmother Josefina, my inspiration. If I can ever be half as resolute and strong as her nothing will stand in my path (tremble!). Thanks to my mother, Nora, and my father, Pedro. They are my example, my guide and the best parents anyone could ask for, which is why I do the opposite of whatever they say. Thanks to my sisters Elisa and Sara, my rocks, without whom I would be incomplete. They are extraordinary, and the world is a better place with them.

To my 'extra sister' Maria, for being an incredible person, and the best study partner I could have asked for. For giving me balance, and for her unconditional friendship. To my 'adoptive brother' Pablo, he is a better version of me in many ways, and my sounding board. They have stood by me through thick and thin (or rather, they have not managed to get rid of me yet - I am rather bad at taking hints). To them I owe any vestigial social skills I have.

Thanks to the people at the University of Hertfordshire, for making me feel like

I belonged from the very first day, despite the massive dent I've made on their tea supplies. Thanks to Jo, Gulay and Jeremy for all the help, and for sharing my moments of scientific frustration. Special thanks to those that put up with AGN accretion physics in the pub and my quotes from wikipedia during tea, over the last year (longer, in some cases). In random order (truly, I cast a die for this!): Geert, Neil, Roberto, Nicky, Carla, Silvia, Hywel, Lientjie, Federico, Nick, Liz, James, Andy, Joana and Niall. If I have any sanity left at this point, and if I have made it this far, it is thanks to them.

To *Chandra* and *XMM* for giving me endless hours of fun!

Last, but not least, thanks to Beethoven and Be'lakor for providing most of the soundtrack to this thesis. Data crunching felt meaningful while listening to them. And to Gene Roddenberry, Douglas Adams, Ray Bradbury and Stanislaw Lem, for planting the seeds of this dream.

I am so deeply indebted to all of the above that I hope my bank doesn't ever read this.

Chapter 1

Introduction

In the most general sense, the term Active Galactic Nucleus (AGN) refers to energetic phenomena, in the central part of a galaxy, that are not related to stellar activity. The optical light emitted in this manner is comparable to the total stellar light of the galaxy ($\sim 10^{11}\ L_{\odot}$) for the average Seyfert galaxy (Peterson 1997), much brighter in the case of quasars, but rather faint for some objects, in which the vast majority of the energy is output in the form of jets.

Although the first spectrum of an active galaxy (NGC 1068) was obtained in 1908 (Fath 1909), it was only in the 1940s that Carl Seyfert noticed that there is a category of galaxies with very bright nuclei and high-excitation emission lines (Seyfert 1943). In 1959 Woltjer tried to infer some of the physics of these objects, and deduced that, in order for the material in the nucleus to be gravitationally bound, its mass must be very high, thus tying AGN activity and black holes for the first time (Woltjer 1959).

In parallel, radio-loud quasars were discovered and catalogued during the 1950s and 1960s, as part of the first radio surveys of the sky. The 3C (Edge et al. 1959) and 3CR (Bennett 1962) catalogues contained a number of radio sources that were associated with resolved galaxies, but also compact objects whose nature seemed more akin to that of a star, which is why they were denominated quasi-stellar objects. In 1969 Schmidt summarised some of the properties of quasars, but was not able to relate them to Seyfert galaxies, since their spectral properties are very different (Schmidt 1969).

X-ray observations of the sky started in the 1960s, using instruments carried in hot air balloons. The first active galaxy to be observed in X-rays was M 87, in 1967 (Friedman & Byram 1967). 3C 273 and Centaurus A were identified shortly afterwards

(Bowyer et al. 1970). It was not until 1978, however, that a correlation between X-ray and optical emission in Seyfert galaxies was established by Martin Elvis (Elvis et al. 1978). By the end of that decade the relation between AGN activity and X-ray emission was established, and Marshall et. al. established the importance of X-ray variability shortly afterwards (Marshall et al. 1981).

Our knowledge of AGN, their observational properties and underlying mechanisms has vastly increased over the last few decades. We now know that these objects are powered through gas accretion onto some of the supermassive black holes that sit in the centres of most galaxies (e.g. Magorrian et al. 1998). Radio-loud objects are particularly important to our understanding of AGN, since, despite the fact that they constitute only a small fraction of the overall population, it is during this phase that AGN have the most direct impact on their surrounding environment through the production of jets and large-scale outflows and shocks (e.g. Kraft et al. 2003; Croston et al. 2011; Cattaneo et al. 2009; McNamara & Nulsen 2007).

In this thesis I use X-ray observations, as well as auxiliary radio, infrared and optical data, to investigate the role of low-power and low-luminosity, radio-loud AGN, in our current understanding of AGN activity and its effects on galaxy evolution. In this Chapter I describe the general properties of AGN, with particular focus on the structures that conform them, and how they reflect on what we observe.

Throughout this thesis I use a concordance cosmology, with H_0=70 km s^{-1} Mpc^{-1}, Ω_m=0.3 and Ω_Λ=0.7.

1.1 Active Galaxy structures and their properties

Given that the observational properties of AGN depend both on intrinsic (gas availability, accretion mode and rate) and external (orientation, observation wavelength) factors, their characterisation and classification has been subject of long debate. It is difficult to conceive, a priori, how objects that produce such different observational signatures can be unified under a single scheme (see e.g. Fig. 1.1).

The most successful model so far is based on that originally proposed by Antonucci (see Antonucci 1993, and references therein), and is presented in Fig. 1.2. According to this model AGN consist of a central black hole, an accretion structure which can itself be broken into individual features (broad line clouds and a thin disk in the inner-

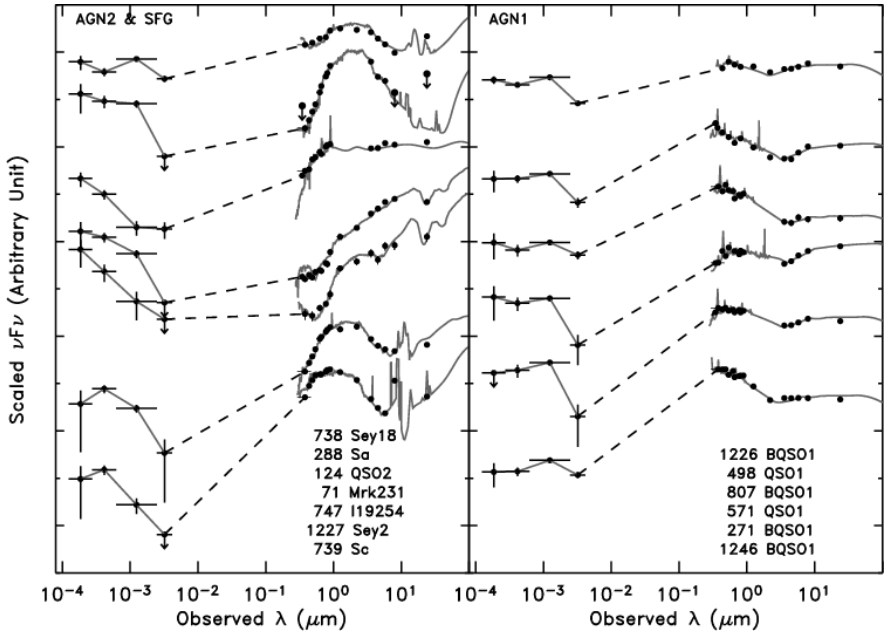

Figure 1.1: Example of IR-optical spectral energy distributions (SEDs) for a variety of radio-quiet objects, from Tajer et al. (2007). This Figure illustrates the difference between obscured/unobscured Seyfert galaxies and quasars.

most regions, and a torus of cold gas further out, which is itself surrounded by clouds that produce narrow optical lines), and a hot corona which produces X-ray photons via inverse-Compton scattering. This model also considers the presence of jets, which originate at or near the accretion disk and carry relativistic electrons and positrons (and possibly protons), and can thus be observed in radio frequencies via their synchrotron emission. The inclination angle of the object determines which of these structures we can observe, directly or indirectly, and the amount of obscuration we can expect.

In the following Sections I will describe the role of each of the structures listed in this model, and their observational properties. The work presented in this thesis focuses only on radio-loud AGN. An AGN is traditionally considered radio-loud if

$$R = \frac{S_{5GHz}}{S_B} \geq 10 \tag{1.1}$$

where S_{5GHz} is the flux at 5 GHz, and S_B is the flux in the optical B band (4400 Å) (Kellermann et al. 1989). The objects described in Chapters 3 and 4 have low R ratios, so that their core spectra show mostly characteristics typical of radio-quiet objects,

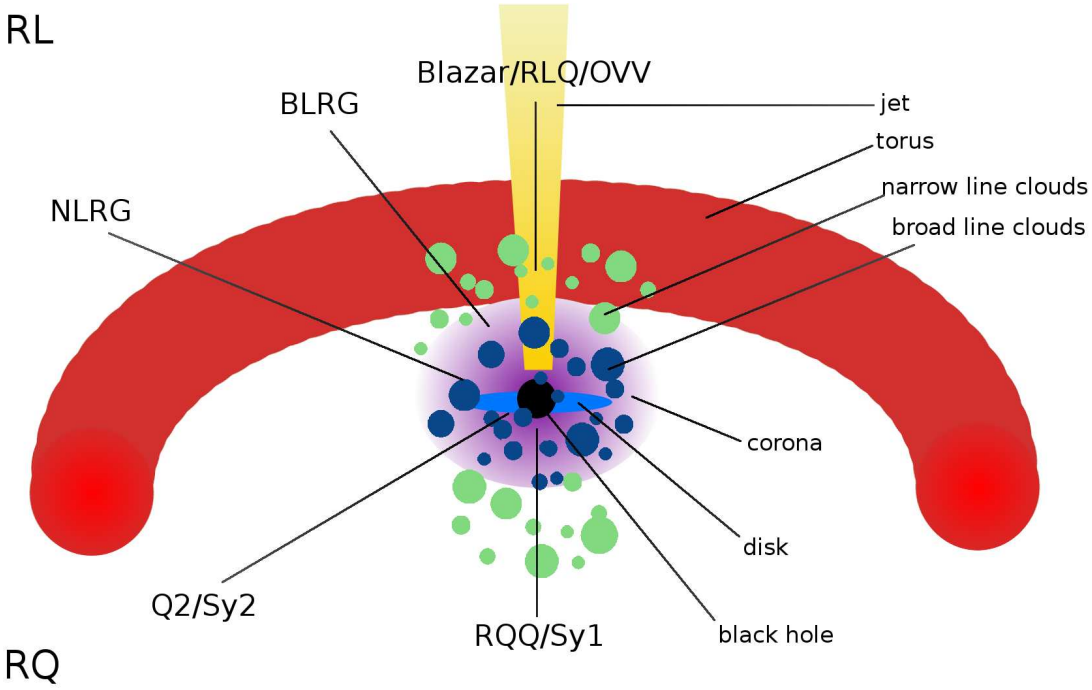

Figure 1.2: Diagram displaying the structures of high-excitation ('traditional') AGN according to unification models. The nomenclatures given according to the different viewing angles are given on the left side of the image (top half for the radio-loud objects, bottom half for radio-quiet ones), while the different structures are labelled on the right side of the image. The structures are not to scale.

yet they possess the extended structures characteristic of radio-loud AGN, albeit on a smaller scale than other, more powerful objects. The objects studied in Chapters 5 and 6 are all, by definition, radio galaxies, and hence have large R ratios.

An important caveat, and one of the main focuses of this thesis, is that there is a category of radio-loud AGN, originally identified by Hine & Longair (1979), that cannot be explained under the scheme presented in Fig. 1.2. The properties of these 'low-excitation' AGN will be described in Section 1.1.3.

Although only a small fraction of AGN are radio-loud ($\sim$ 10 – 20 per cent, see e.g. Sramek & Weedman 1980; Kellermann et al. 1989), it is possible that all massive galaxies have undergone a radio-loud phase, since evidence seems to indicate that this activity is likely to be cyclical (e.g Saikia & Jamrozy 2009; Best et al. 2005). It is during this phase, when the jet interacts with the interstellar gas of the host galaxy (ISM), reaching into the intracluster medium (ICM) in the most powerful systems, that

the AGN really affects its environment on large scales (see Section 1.2). While the relationship between mergers, starbursts, AGN activity and feedback is still a subject of intense debate, it is quite clear that the significant amounts of energy transferred to the ISM by this nuclear activity in the radio-loud phase must affect the environment dramatically (e.g. Kraft et al. 2003; Croston et al. 2011; Cattaneo et al. 2009).

1.1.1 The central black hole

It is now commonly accepted that most, if not all galaxies host a black hole. These objects are believed to reach masses of $10^6 - 10^{10}\ M_\odot$. The initial black hole is thought to form in the bulge before star formation occurs (Silk & Rees 1998), and its growth is regulated through galaxy mergers, although the exact process is still quite uncertain, due to the elusive nature of intermediate-mass black holes, which are expected to have masses of $10^4 - 10^6\ M_\odot$ (Gebhardt et al. 2005).

The relation between the growth of the black hole and the merger history of its host galaxy is supported by the correlations that exist between the mass of the galaxy's bulge and the black hole mass (Magorrian et al. 1998), as well as apparent correlations of the latter with the number of globular clusters in some objects (Harris & Harris 2011). There are also a few examples of post-merger galaxies where the individual black holes have not yet merged (e.g. NGC 6240, Komossa et al. 2003). However, parameters such as the total mass of the galaxy and the dark matter halo do not correlate well with black hole mass (Kormendy & Bender 2011), suggesting that the relationship between the host galaxy and its supermassive black hole is far from simple.

Although the black hole has a dynamical effect on stars of the galaxy's bulge even when it is quiescent (its mass can be derived even in these cases through the M-σ relation of Ferrarese & Merritt 2000), it is only when the black hole is accreting matter that its effect can be directly observed, and the galaxy is denominated active.

For AGN the mass of the central black hole can be determined in several ways. The most well known correlations are those relating the luminosity of the AGN in different bands to the mass of the black hole (see e.g. Graham 2007). These correlations, however, do not work very well for sources with low luminosities or low accretion rates (e.g. Capetti et al. 2009, see also Chapter 6).

For objects with a low orientation angle, where broad optical emission lines can be

detected (see Section 1.1.5), these lines can be used as a probe for the black hole mass. For objects with bright spectra and long-term monitoring, it is possible to measure the time delay between luminosity variations in the continuum and in the Hβ (4861 Å) emission line. This yields an estimate of the extension of the broad-line region ($R_{BLR} = c\tau$, where τ is the time elapsed between the continuum and line variations). Examples of this technique can be found in Wandel et al. (1999) and Kaspi et al. (2000). Assuming that the gas in the emission-line region is gravitationally bound and virialized, the width of the line can be used to estimate the black hole mass according to the following equation:

$$M_{BH} = G^{-1} R_{BLR} V_{BLR}^2 \tag{1.2}$$

Where R_{BLR} is the radius of the broad-line region, V_{BLR} is the Keplerian velocity of the gas (derived from the line width), and G is a constant (McLure & Jarvis 2002).

1.1.2 Accretion in high-excitation objects

The definition of high-excitation AGN stems from the fact that all these objects possess strong optical lines (see Section 1.1.5). All radio-quiet, and most radio-loud AGN belong to this category, whose underlying structure is summarised by unification models such as the scheme presented in Fig. 1.2. These 'traditional' AGN are believed to be powered through cold gas accretion (see e.g. Hardcastle et al. 2007a), which is distributed around the central black hole in the following structures:

The disk

The structure closest to the black hole is a geometrically thin, optically thick accretion disk, originally described by Shakura & Sunyaev (1973). This disk forms because the angular momentum of the gas is too high for it to directly fall into the black hole. The loss of angular momentum is presumed to happen through viscosity, perhaps driven by magnetorotational instabilities (Balbus & Hawley 1991), although some models predict mass loss through winds (e.g. Ostriker et al. 2010). The mechanism is still poorly understood (Frank et al. 2002).

Following the derivations of King (2008), it can be shown that such a disk is radia-

tively efficient, that is, the gas has time to dissipate some of its energy through radiation before falling into the black hole, and thus cool down. The height of the disk is given by

$$H \approx \frac{C_s}{v_K} R << R \tag{1.3}$$

where C_s is the local sound speed, R is the radius of the disk, and v_K is the Keplerian velocity.

The total accretion luminosity is given by integrating the dissipation per unit area over both sides of the disk, applying relativistic corrections for the inner regions:

$$L_{acc} = \epsilon \dot{M} c^2 \tag{1.4}$$

Where ϵ is the efficiency of rest-mass conversion. The value of ϵ varies from model to model, and depends on the boundary conditions and the black hole spin. It is generally assumed to range between 0.05 and 0.42 (see e.g. Kovács et al. 2011).

The timescales in which changes happen in the disk are of three types: viscous (given by the kinematic viscosity), dynamical (which gives the characteristic time for changes in the dynamical equilibrium) and thermal, with the dynamical timescale being the smallest and the viscous timescale being the largest of the three. For a typical AGN ($M \sim 10^8 M_\odot$, $\dot{M} \sim 1 M_\odot$ yr^{-1}), the radius of the disk is $\sim 10^{13}$ cm, and the dynamical and thermal timescales are short ($\sim 10^3$ and $\sim 10^4$ s respectively). The viscous timescale, however, is very long, and gives a powerful constraint on the angular momentum of the infalling gas: it must be very low even before forming the disk.

The expected average temperature for the bulk of the disk is $\sim 10^5$ K. The thermal emission from the disk, therefore, follows a blackbody distribution that peaks in the UV to X-ray energies. This emission constitutes part of the UV continuum in unobscured objects (Seyfert 1 and narrow-line galaxies, respectively for radio-quiet and radio loud objects).

The intensity of blackbody radiation is given by Planck's law (Rybicki & Lightman 1986):

$$I_\nu(T) = B_\nu(T) = \frac{2h\nu^3}{c^2} \frac{1}{e^{\frac{h\nu}{kT}} - 1} \tag{1.5}$$

Where k is the Boltzmann constant, h is the Planck constant, T is the temperature and

ν is the frequency.

The peak frequency of the emission, which also depends on the temperature, is given by the Wien displacement law:

$$h\nu_{max} = 2.82kT \tag{1.6}$$

The equations 1.3 to 1.4 assume that the accretion rate of the black hole is relatively small, which is the case for all the objects covered in this thesis, and therefore the accretion luminosity is smaller than the Eddington luminosity (defined as the maximum luminosity the object can reach when radiation pressure is in balance with the gravitational force):

$$L_{acc} < L_{Edd} = \frac{4\pi Mc}{\kappa} \tag{1.7}$$

where κ is the electron scattering opacity. For super-Eddington objects the luminosity is so high that it has an effect on the accretion rate, effectively driving outflows through radiation pressure.

The X-ray corona

The majority of the continuum X-ray emission in unobscured, radio-quiet AGN is thermal and produced in the hot corona that surrounds the disk. For radio-loud objects the jet must also be taken into account (see Section 1.1.6). The corona is created when the UV photons from the disk are upscattered to higher energies through inverse-Compton collisions with the electrons in the hot gas; this process is often called thermal Comptonization (see e.g. Haardt & Maraschi 1991).

The energy change of a moving photon when it is Compton-scattered by an electron, is given by (Rybicki & Lightman 1986):

$$E' = \frac{E}{1 + \frac{E}{m_e c^2}(1 - \cos\theta)} \sim E\left[1 - \frac{E}{m_e c^2}(1 - \cos\theta)\right] \tag{1.8}$$

where θ is the scattering angle, m_e the electron rest mass, and c the speed of light. The change in wavelength is given by:

$$\lambda' = \lambda + \frac{h}{m_e c}(1 - \cos\theta) \tag{1.9}$$

where h is the Planck constant, and $\frac{h}{m_e c}$ is the Compton wavelength of the electron (2.43×10^{-12} m).

If the moving electron has sufficient kinetic energy compared to the photon, the energy transfer is from the electron to the photon, and the process is called inverse-Compton scattering. When the electron is relativistic ($\gamma^2 >> h\nu/mc^2$, where γ is the Lorentz factor) the energy transfer is very efficient, and the final energy of the photon is increased by a factor of γ^2.

For an isotropic distribution of photons scattering off an isotropic distribution of electrons, average formulas must be derived. Following Rybicki & Lightman (1986), and for the electron rest frame, the net power lost by the electron and converted into radiation is given by:

$$P_C = \frac{4}{3}\sigma_T c \gamma^2 \beta^2 U_{ph} \tag{1.10}$$

where σ_T is the Thompson cross-section, $\beta = v/c$, and U_{ph} is the initial energy density of the photon. However, electron radiative losses from synchrotron radiation must be taken into account.

For repeated scatterings by non-relativistic electrons the exact equation was derived by A. Kompaneets in 1957, and is known as the Kompaneets equation. Although the detailed derivation is beyond the scope of this thesis, the equation is given here for reference:

$$\frac{\partial n}{\partial y} = \frac{1}{x^2}\frac{\partial}{\partial x}\left[x^4\left(n + n^2 + \frac{\partial n}{\partial x}\right)\right] \tag{1.11}$$

where n is the photon occupation number:

$$n = I(E)\frac{(hc)^2}{8\pi E^3} \tag{1.12}$$

x is the photon energy:

$$x = \frac{E}{kT_e} \tag{1.13}$$

and y is the Kompaneets parameter:

$$y = \frac{4kT_e}{m_e c^2}\sigma_T c t \tag{1.14}$$

which is sometimes expressed as a function of t_c, the mean time between scatterings

($t_c = n_e \sigma_T / c$).

The three parameters in n in eq. 1.11 account for, respectively, the recoil effect, the induced/stimulated emission, and the Doppler motion.

The photon spectra can be obtained by analytically solving eq. 1.11; some examples are given by Sunyaev & Titarchuk (1980). For the most common case found in AGN, unsaturated Comptonization, the spectrum is given by:

$$I(x) \propto \begin{cases} x^3 e^{-x}, & x >> 1. \\ x^{3-\Gamma}, & x << 1 \end{cases} \tag{1.15}$$

where

$$\Gamma = -\frac{3}{2} \pm \sqrt{\frac{9}{4} + \frac{4}{y}} \tag{1.16}$$

where the negative root is taken for $y >> 1$, the positive one for $y << 1$, and the average for $y \sim 1$, which is the typical case for most AGN, giving a spectral index ~ 1.5 (and an exponential cutoff at higher energies). This value is consistent with the observations of the 2-10 keV emission in both radio-loud and radio-quiet sources. Throughout this thesis this component is labelled as the 'hard' or 'accretion-related' component (given that the emission from the corona is a direct consequence of the accretion process in the disk).

In radio-quiet sources this accretion-related component is reflected onto the accretion disk, which results in the soft excess observed in most sources (see e.g. Haardt & Maraschi 1991). For radio-loud sources, however, the soft emission is directly related to the jet (see Hardcastle & Worrall 1999, and Section 1.1.6). Some radio-loud sources, where the radiative energy output is much larger than the jet-related one, are best modelled with reflection models, as is the case for Markarian 6 (Chapter 3).

The luminosity of the corona is proportional to that of the disk (Sazonov et al. 2012), which is further evidence for the fact that these two structures are closely tied: the corona almost immediately reflects any changes in the accretion rate and the properties of the disk, which is one of the reasons behind the observed rapid X-ray variability McHardy et al. (see e.g. 2004), though the correlations between optical, UV and X-ray variability can be rather complex (Dewangan et al. 2007).

The Torus

Observations of Seyfert galaxies in the 1970s (e.g. Harper & Low 1973) showed that these objects are very bright in the IR. This emission is associated with the dusty torus of cold gas that is found at distances of a few pc from the central black hole. Unlike what happens for the inner regions of the AGN, where the structures are too small to be spatially resolved, there is observational evidence for tori in a few systems through interferometric work (e.g. NGC 1068, see Jaffe et al. 2004).

These structures would be expected to collapse on timescales shorter than the active phase of an AGN, and can only survive if there is a continuous input of energy. This energy is provided by the high-energy photons from the disk and corona, which are absorbed by the cold gas in the torus, and re-radiated at lower energies. The properties of tori have been constrained through the need to account for unification among the Seyfert galaxies (see e.g. Ramos Almeida et al. 2011b, and references therein). They are optically and geometrically thick, and dense enough to obscure the broad-line region, but not the narrow-line region, which is seen in all Seyferts (and their radio-loud equivalents, the NLRGs or narrow-line radio-galaxies). The temperature of the gas in the torus is expected to be below 300 K, so that its (modified) blackbody emission peaks in the IR range (see eqs. 1.5 to 1.6).

Although models initially predicted tori to be uniform and smooth, it is clear that a temperature gradient must be expected. The hypothesis that the torus may be clumpy was originally suggested over two decades ago (see e.g Krolik & Begelman 1988), and has gained strength in recent years, through long-term observations of obscured sources (typically intermediate Seyferts) where the absorption column changes with time (e.g. Maiolino et al. 1998; Risaliti et al. 2002, and Chapter 3). The different variability timescales suggest, in some cases, the presence of clouds between the torus and the disk. These clouds would be of the same nature as those associated with the broad-line region (Section 1.1.5).

A detailed analysis of the structure of clumpy tori is given by e.g. Nenkova et al. (2008b), and the details for radiative transfer processes by e.g. Nenkova et al. (2008a).

Hardcastle et al. (2009) have shown that the IR and accretion-related X-ray emission are correlated in radio-loud AGN. This correlation has also been found in Seyfert galaxies (Gandhi et al. 2009). This is to be expected, since the mechanism that pro-

duces the thermal radiation in the torus is directly linked to the production of high-energy photons in the disk and corona, which are detected in X-rays. This can also be used as a probe to determine the luminosity of heavily obscured AGN. Chapter 6 uses this correlation to investigate the accretion properties of the 2Jy sample.

1.1.3 Accretion in low-excitation objects

There is a category of radio-loud AGN, first identified by Hine & Longair (1979), which lack the high-excitation optical lines characteristic of 'traditional' AGN, which were thus denominated low-excitation (radio)galaxies (LEG or LERG). These objects emit most of their light in the radio band, they lack the IR excess and 'big blue bump' characteristic of most AGN, and are generally very faint in X-rays, with their emission being dominated by the soft, jet-related component (see e.g. Mason et al. 2012; van der Wolk et al. 2010; Fernández-Ontiveros et al. 2012). It seems clear that the accretion model applied to 'traditional' AGN does not apply to LERGs. Due to their faintness LERGs tend to escape detection in any surveys that are not based on radio selection, overlapping with the population of star-forming galaxies, and thus have been difficult to characterise until recently.

Until a model was developed to explain their intrinsic differences, these objects puzzled the astronomical community (e.g. Fabian & Canizares 1988). Obscuration as a cause behind the low luminosity at all bands can be discarded through the absence of IR emission, since any obscuring structure would re-radiate the emission from the central core in the same manner the torus does. It is also not possible to 'starve' the central black hole to make it almost quiescent, since LERGs are generally found in systems that have enough gas to fuel an AGN (see e.g. the review by Ho 2008), and something must be creating the powerful jets seen in these systems. Shakura-Sunyaev disks are remarkably efficient at turning gravitational energy into radiation; thus it is clear that the structure fuelling the AGN must be different for LERGs. Spherically symmetric accretion, as proposed by Bondi (1952) had been proved to work for LERG (Allen et al. 2006; Balmaverde et al. 2008), but it has some issues with reducing the angular momentum of the gas before it falls into the central black hole (Proga & Begelman 2003) and the effective accretion rate.

The Bondi accretion rate is used as a basis for accretion rates in most models. It is

given by:

$$\dot{M}_B = 4\pi\lambda\rho G^2 M_{BH}^2 c_S^{-3} \tag{1.17}$$

where λ=0.25, ρ is the density of the gas at the Bondi radius, and c_S is the speed of sound in the medium ($c_S = \sqrt{\Gamma kT/\mu m_p}$, with Γ being the polytropic index for the gas).

The most successful models so far predict radiatively inefficient accretion, which occurs when the gas is so tenuous that its cooling timescale is longer than the accretion timescale. The most popular model to describe accretion in LERGs is that of advection dominated accretion flows (ADAF, see e.g. Narayan & Yi 1995; Yuan 2007, for reviews), which has been successfully applied to some sources (Di Matteo et al. 2003; Pellegrini et al. 2003; Fabbiano et al. 2003). Variants of this model contemplate convection (CDAF) (e.g. Abramowicz et al. 2002) or inflow-outflow solutions (ADIOS, see Blandford & Begelman 1999). Radiatively inefficient accretion flows (RIAF), based on ADAF, are also successful in describing the properties of accretion in our own galaxy (Sagittarius A*, Yuan et al. 2002), but this may also be described with jet models (e.g. Maitra et al. 2009).

ADAF models predict an accretion structure that is optically thin but geometrically thick, with the hot ions ($kT \sim 10^{12}$ K) and slightly cooler electron plasma ($kT \sim 10^9 - 10^{11}$ K) forming a nearly spherical shell in the regions near the black hole. The accretion rate also plays an important role; it is expected to be much lower for these systems than it is for high-excitation sources (HEG). Narayan & Yi (1995) predict that the thin disk transforms into an ADAF structure when the accretion rate falls below ten per cent of the Bondi rate ($\dot{M} \leq 0.1\dot{M}_B$). The low accretion rate is also achieved through the rotation of the disk, in the regions farther away from the black hole. Recent surveys seem to back up this assumption, showing that the accretion rate in LERGs is indeed very low (see e.g. Best & Heckman 2012; Russell et al. 2012; Lin et al. 2010; Ho 2008; Mason et al. 2012; Evans et al. 2011; Plotkin et al. 2012, and Chapter 6).

The efficiency predicted by Narayan & Yi (1995) for ADAF is a function of the accretion rate:

$$\eta_{ADAF} \sim 0.1\left(\frac{\dot{M}}{\dot{M}_B}\right) \tag{1.18}$$

and so is the luminosity:

$$L_{ADAF} \propto \left(\frac{\dot{M}}{\dot{M}_B}\right)^2 \tag{1.19}$$

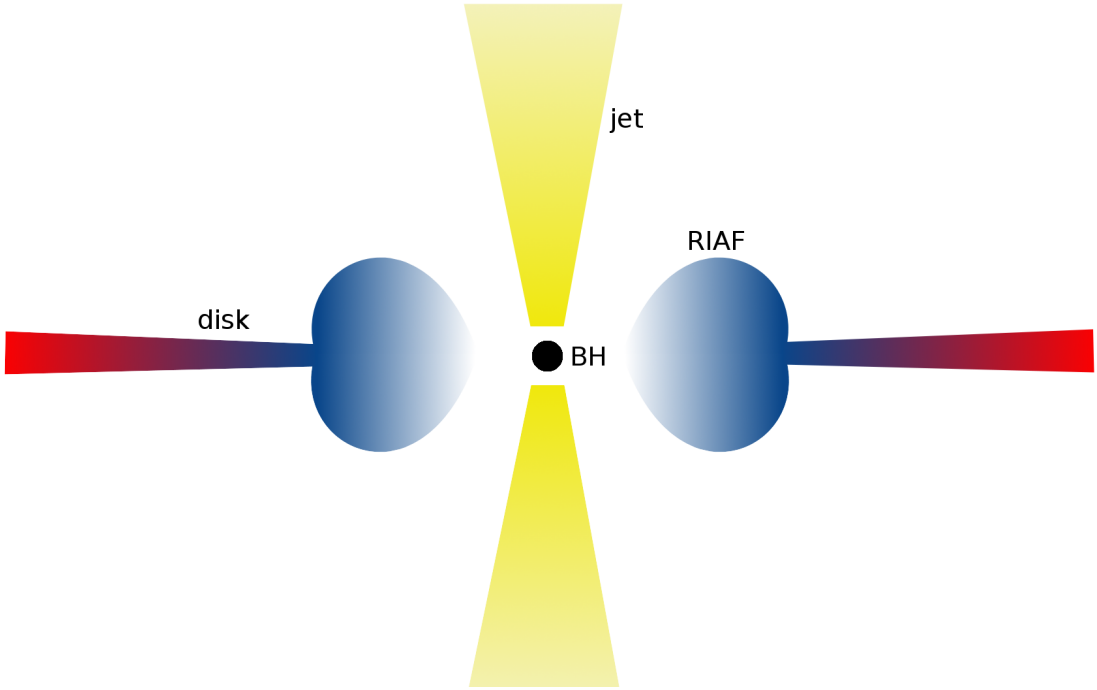

Figure 1.3: Example of model proposed for low-excitation AGN, based on the illustration by Ho (2008). The region represented corresponds roughly to the inner disk shown in Fig. 1.2, with accretion occurring through radiatively inefficient flows (RIAF).

to impose a continuity with the thin disks of the low-luminosity end of the HEG population. It is not yet clear that this may be possible, however, as there is a possibility that the switch in accretion rate may not be continuous (see e.g. Hardcastle et al. 2007a; Russell et al. 2012; Mason et al. 2012, and Chapter 6).

RIAF models (e.g. Fig. 1.3) predict an even lower accretion rate. The outflows in ADIOS are introduced to couple with the jet, predicted in simulations e.g. McKinney & Gammie (2004); it is, however, unknown exactly how jets are generated. According to Narayan & Yi (1995) jets and outflows are needed to reduce the accretion rate.

The emission predicted for ADAF/RIAF models is thermal synchrotron (i.e. synchrotron emission from a hot electron plasma, as proposed in the case of Sagittarius A*) and/or comptonization.

1.1.4 Other sources of continuum emission

Aside from blackbody radiation and inverse-Compton scattering, there is an additional contribution to what we observe as the continuum in AGN spectra at different frequencies.

Thermal bremsstrahlung, or 'braking radiation', is produced through the acceleration of a charged particle. It is also known as free-free emission, and although it has a contribution at all frequencies, it is potentially most important in the X-ray and γ-ray regimes. In AGN the main process through which thermal bremsstrahlung occurs is the interaction of an electron with an ion. The derivation of the full expression is quite lengthy, as it consists of summing the radiation emitted for each electron-ion interaction for a Maxwell-Boltzmann distribution of electrons. The result for the energy emitted per unit volume of the gas, per unit time, is given by (Rybicki & Lightman 1986):

$$\epsilon_\nu^{ff} = \frac{dW}{dVdtd\nu} = \frac{32\pi e^6}{3m_e c^2}\left(\frac{2\pi}{3km_e}\right)^{\frac{1}{2}} T^{-\frac{1}{2}} Z^2 n_e n_i e^{-\frac{h\nu}{kT}} \overline{g_{ff}} \tag{1.20}$$

where n_e and n_i are, respectively, the electron and ion density, Z is the electronic charge and $\overline{g_{ff}}$ is the velocity averaged Gaunt factor, which is $\overline{g_{ff}} \sim 1$ when $h\nu/kT \sim 1$ and $1 < \overline{g_{ff}} < 5$ when $10^{-4} < h\nu/kT < 1$.

The 'big blue bump' observed in the optical and UV frequencies for unobscured sources is a combination of optically thin and optically thick thermal bremsstrahlung, and inverse-Compton scattered photons. There is also some contribution to the spectrum from the creation and annihilation of particle pairs (e.g. Zhou et al. 1997), and, most important in radio-loud sources, non-thermal synchrotron radiation from the jet, which is described in detail in Section 1.1.6.

In addition to the continuum, emission lines are produced through bound-bound and bound-free transitions in the emission-line regions (ELR), contributing mainly to the optical and near-IR spectrum. The ELR are described in detail in Section 1.1.5.

1.1.5 Emission lines

Optical and near-infrared emission lines from AGN have been studied since the times of Seyfert's classification, and have been one of the most useful tools to characterise the properties of AGN (extensive reviews and books have been written on the topic, see

e.g. Osterbrock 1989). Based on line strength ratios, Woltjer (1959) constrained some of the properties of the gas, like its temperature, density and physical extent. Broad lines were identified for the first time in NGC 1068 (Burbidge et al. 1959).

In the X-rays, emission lines are produced via two mechanisms: photoionization (which dominates for the soft, thermal emission up to 2 keV) and fluorescence in the inner part of the accretion disk (which is behind the Fe K-α line observed at 6.4 keV).

Broad line clouds (BLR) are closest to the central engine. The emission in these regions is caused by photoionization and collisional de-excitation processes, which suppress the forbidden transitions (Rees et al. 1989). These lines are present only in high-excitation objects (although there is an ongoing debate on whether ADAF can also produce broad lines, see e.g. Eracleous & Halpern 1994; Sulentic et al. 2000; Plotkin et al. 2012), and can only be seen in objects with a low inclination angle (Seyfert 1, BLRG and some QSOs), since at larger angles they are obscured by the torus. The geometry of the broad-line region is not well understood, since some of the line emission may be produced within the disk itself, even though we know there is clumpy material very close to the central core (e.g. Risaliti et al. 2002, 2007, and Chapter 3). The shape of the lines is produced by the high kinetic temperature of the gas ($\sim 10^4$ K), which causes Doppler broadening. For gas very close to the central black hole relativistic broadening is also observed (see e.g. Brenneman & Reynolds 2009), which is why the Fe K-α line is so often used for disk diagnostics.

Narrow line regions (NLR) can be resolved for nearby objects, since they extend up to a few tens of pc around the central engine (see e.g. Peterson 1997, for an overview). NLR represent the extent to which the AGN can effectively photoionize the material around it, and are colder and less dense than BLRs, allowing for forbidden transitions to occur. Ratios between certain pairs of forbidden lines allow the estimation of the temperature and electron densities in the gas. Ratios of [OIII] to [OII] lines are also the main technique used to classify AGN as high or low excitation (see e.g. Heckman 1980, for radio-quiet sources; the same technique applies to radio-loud objects), but this diagnostic is not always reliable, since in some cases the lines might be present but not detected, or might be caused by stellar processes rather than the AGN (see Fig. 1.4, the case of 3C 338 and M 87, as discussed by Hardcastle et al. 2009, and Chapter 6).

Where large gas outflows are involved, these may clear a path for the radiation

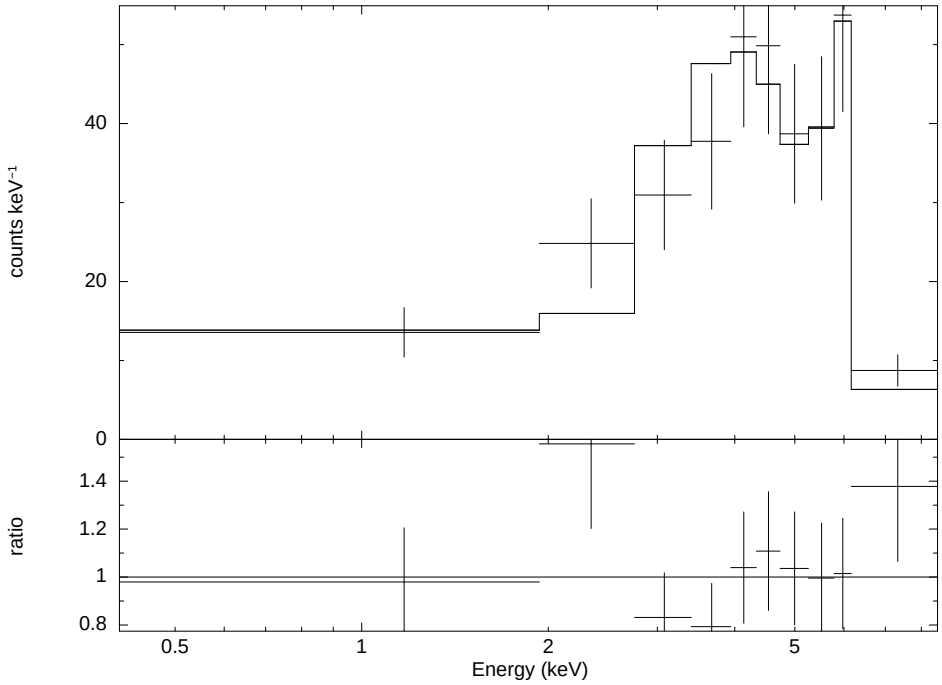

Figure 1.4: X-ray spectrum of the atypical LERG PKS 0043-42. The presence of the Fe K-α emission line suggests that there is indeed a 'traditional' accretion structure in this object, although no strong optical emission lines are detected (see also Ramos Almeida et al. 2011a).

from the AGN to reach much larger distances than it would in a quiescent medium. This is observed in the inner regions of Circinus, for example (Chapter 4). Shocks can also compress and heat the gas to temperatures where collisional ionization can be observed (e.g. Hardcastle et al. 2010a). The models used in this thesis to research the properties of the hot gas in Markarian 6 and Circinus (Chapters 3 and 4) predict a number of emission lines caused in this manner. There is some evidence suggesting that radio jets can cause an enhancement in [OIII] emission, although it is not clear whether this is caused by shocks or direct photoionization (Labiano 2008).

1.1.6 Large-scale emission

Although jets and lobes are characteristic of powerful radio galaxies, these structures, on a smaller scale, can also be found in objects that are not strictly considered radio-loud (according to the definition in eq. 1.1). Examples of these structures in elliptical

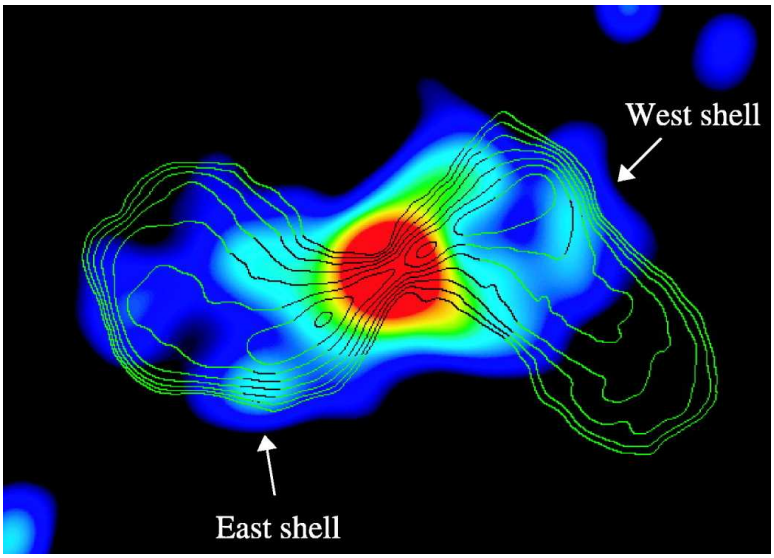

Figure 1.5: Example of radio emission in a low power source. Image from Croston et al. (2007), illustrating the match between X-ray and radio emission in NGC 3801. The lobes in this source are believed to be driving a shock into the ISM.

galaxies can be found in e.g. NGC 3801 (Croston et al. 2007, and Fig. 1.5), NGC 1062 (Kadler et al. 2004) and Markarian 6 (Chapter 3). The effect of jets and lobes on the host galaxy is even more interesting in the case of Seyferts, which are typically hosted by spirals (see e.g. Croston et al. 2008b; Hota & Saikia 2006; Gallimore et al. 2006, and Chapter 4), where the effects on dynamics and star formation are potentially much larger (see Section 1.2).

The classification of Fanaroff & Riley (1974) divides radio galaxies into two subgroups. FR I objects are core-brightened, and exhibit lobes, while FR II objects are edge-brightened. Although this is a purely morphological classification, Fanaroff & Riley showed that the luminosity of the source is related to its morphology, so that FR I galaxies (typically) have $L_{178MHZ} \leq 2 \times 10^{25}$ W Hz^{-1} sr^{-1}. Ledlow & Owen (1996) showed that the division between both classes depends on the optical luminosity density of the host galaxy, so that the break rises with luminosity as $L_{opt}^{1.7}$. The boundary can also be defined in terms of the long-term average jet power, $\bar{Q} \sim 5 \times 10^{43}$ erg s^{-1} (Rawlings & Saunders 1991).

Both classes of radio galaxy have common structures: jets (which may or may not be visible, the latter case being more common for FR II sources) and lobes. Some

examples of the different morphologies can be seen in Fig. 1.6. It is important to note that the FR I / FR II division does not correspond to the high/low-excitation one (Hardcastle et al. 2009). While most low-excitation objects seem to be FRI, there is a population of bona-fide FRII LERGs, as well as numerous examples of FRI HERGs (e.g Laing et al. 1994). This is most likely caused by the complex underlying relation between fuelling, jet generation and environmental interaction.

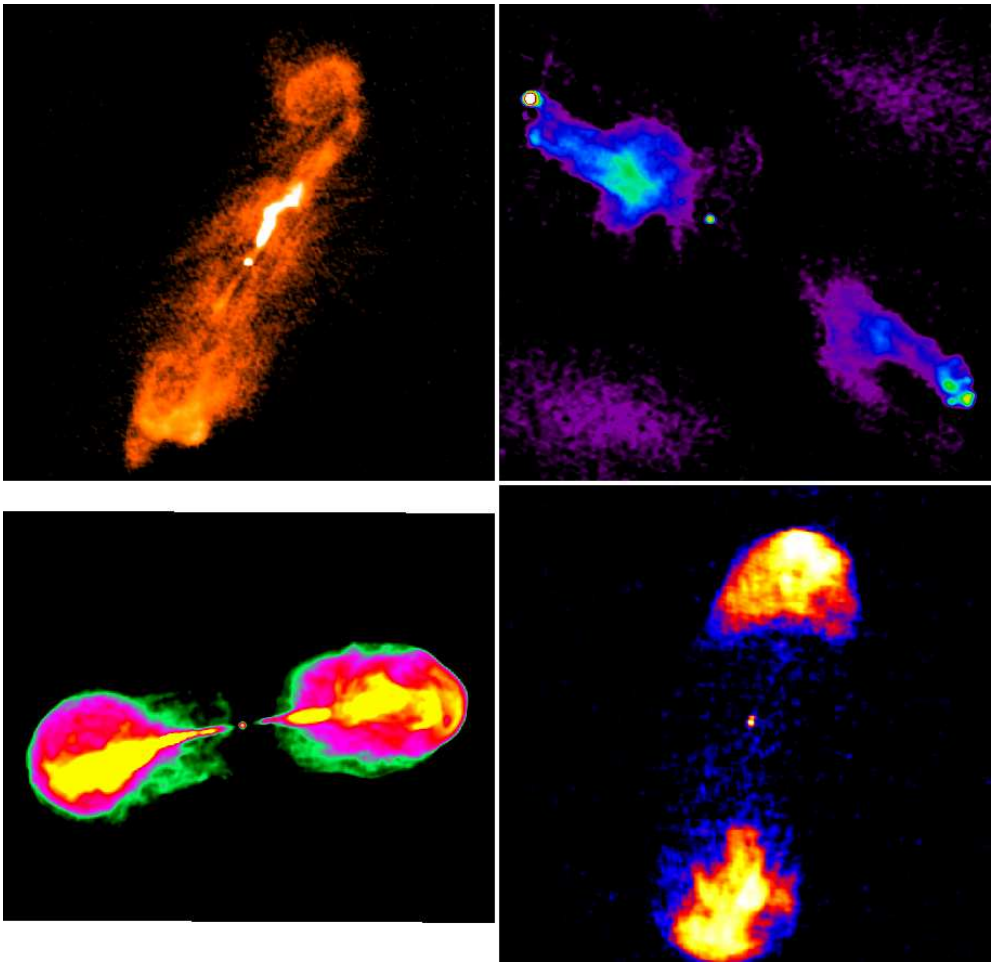

Figure 1.6: Mosaic displaying radio maps (Morganti et al. 1993, 1999) for a variety of sources in the 2Jy sample. **Top left**: PKS 0034-01 (3C 15), an FR I LERG with a classic radio morphology and a jet. **Top right**: PKS 0349-27, an FR II NLRG. **Bottom left**: PKS 1648+05 (Hercules A) an FR I LERG in a very dense cluster environment, that is collimating the jet near the central AGN. **Bottom right**: PKS 2211-17 (3C 444), a somewhat atypical FR II LERG in a dense cluster environment, into which the lobes are driving a shock (Croston et al. 2011).

Jets and hotspots

Jets are defined as collimated, relativistic outflows that are produced near the central black hole and extend to scales ranging from kpc to Mpc. The base of the jet is thought to be very similar for FR I and FR II galaxies, and highly relativistic, which sometimes produces an apparent superluminal motion (see e.g. Pearson 1996; Zensus 1997). The jets of FR I are generally shorter, and decelerate to sub-relativistic speeds, presumably due to entrainment of the environment (see e.g. Bicknell 1984; Laing & Bridle 2002). The large opening angle, and the presence of knots (e.g. Hardcastle et al. 2007b; Jorstad et al. 2005), suggest that the energy transport to large scales is not very efficient in these objects. By contrast, the jets of FR II remain collimated and relativistic for much larger distances (typically of the order of 10^2 kpc, see e.g. Hardcastle 2009), and are more efficient at transporting the energy. FR II jets typically terminate in hotspots, bright compact regions where particle acceleration occurs, which results in a flat radio spectral index ($0.5 < \alpha < 0.7$).

The composition of the jets is not well understood. We know that they contain electrons, possibly positrons (e.g. Reynolds et al. 1996; Dunn et al. 2006), and that magnetic fields are involved (see e.g. Pudritz et al. 2012, for a review). Observations seem to indicate that B fields are initially parallel to the jet axis, and that interaction with the environment and shocks alters this, introducing a perpendicular component (Attridge et al. 1999). This may be the reason why perpendicular fields are more often detected in FR I galaxies in polarization measurements (Reichstein & Gabuzda 2012).

The emission mechanism that allows us to see these jets is synchrotron radiation, which is emitted when a charged particle travelling at relativistic speeds interacts with a magnetic field (in the non-relativistic regime the emission is called cyclotron). The particle moves in a helicoidal trajectory, with a characteristic orbital frequency given by (Rybicki & Lightman 1986):

$$\omega_B = \frac{qB}{\gamma mc} \tag{1.21}$$

where q is the charge and γ is the Lorentz factor (related to the total energy of the particle by $E = \gamma mc^2$). For an isotropic distribution of velocities, the particle loses energy at a rate given by eq. 1.23. The spectrum of synchrotron radiation spans a broad range of frequencies for a given particle energy, but it is narrowly peaked around

a critical frequency, given by (in the case of an electron, see e.g. Longair 1992):

$$\nu_c = \gamma^2 \frac{eB}{2\pi m_e} \tag{1.22}$$

Since the energy loss time scale is proportional to γ^{-1} and E^{-1}, an X-ray emitting electron loses energy $\sim 10^5$ times faster than a radio-emitting electron, and protons of a given energy lose their energy $\sim 10^6$ times more slowly than electrons.

The synchrotron power emitted by each electron is given by:

$$P_S = \frac{4}{3}\sigma_T c \gamma^2 \beta^2 U_B \tag{1.23}$$

where U_B is the magnetic energy density, $U_B = B^2/2\mu_0$ (μ_0 is the vacuum permeability). This has the consequence that the ratio between P_C (the inverse-Comptom power) and P_S is the same as the ratio between that of the magnetic and photon energy densities. Another consequence of this is that the cooling of the electrons via inverse-Compton processes is very efficient, which limits the brightness temperature of radio sources to $\sim 10^{12}$ K (this effect is often called the Compton catastrophe).

In radio galaxies the electron population emitting synchrotron radiation has a broad range of Lorentz factors. To obtain the power law spectrum that we see at radio frequencies, the electrons must also have a power law distribution in energy, given by $N(E) = N_0 E^{-p}$ over a given energy range. The total emissivity for the electron population is then given by:

$$J(\nu) = \int_{E_{min}}^{E_{max}} j(\nu) N(E) dE = \int_{E_{min}}^{E_{max}} j(\nu) N_0 E^{-p} dE \tag{1.24}$$

where $j(\nu)$ is the emissivity of a single electron, which is a function of the critical frequency.

If we assume that $j(\nu)$ is a narrow function, and deriving E from eq. 1.22, the total emissivity is:

$$J(\nu) \propto N_0 \nu^{-\frac{p-1}{2}} B^{\frac{p+1}{2}} \tag{1.25}$$

The shape of the synchrotron spectrum is often described as a function of the radio spectral index α, given in terms of the flux density as $S(\nu) = S_0 \nu^{-\alpha}$. From above, $\alpha = \frac{p-1}{2}$ for a power law electron energy spectrum.

The relativistic nature of the jet emission causes a boost in the luminosity of the core in radio-loud sources with low orientation angles (BL-Lacs, BLRGs and QSOs), due to relativistic Doppler beaming. This is studied in Chapter 6 for a range of sources.

Given the rapid energy losses at higher frequencies, synchrotron emission from jets and hotspots can only be observed in X-rays if there is a source of particle acceleration (Hardcastle et al. 2007c). See e.g. Worrall (2009) for a review of X-ray jets.

Lobes

Although some of the dynamics and energetics of FR I and FR II radio lobes are very different, many assumptions can be applied to both categories.

Lobes are created when the jet interacts with the surrounding environment (ISM, IGM at larger scales), creating bubbles that expand through this medium and are filled with the particles that travel up the jet. The early models of Scheuer (1974) proposed a variety of scenarios for the propagation of the lobes through the interstellar medium of the host galaxy. If the lobes are always overpressured with respect to their surroundings, they expand supersonically, driving a bow shock, and are not influenced by the external medium (other than for their expansion speed). Most of the analytical models describing the dynamics of radio lobes are based on this assumption (e.g. Begelman & Cioffi 1989; Kaiser & Alexander 1997), and this is the case for the sources studied in Chapters 3 and 4. However, this is not always so, in many cases, and particularly as the lobes evolve, the pressure inside and outside the lobes becomes roughly equal, and the situation becomes more complicated (e.g. Alexander 2002; Hardcastle & Krause 2013).

The particle content of FR I and FR II lobes is thought to be quite different: the former are dominated by non-radiating particles (Croston et al. 2008a), while the opposite applies for FR II (Croston et al. 2005). This has implications for the overall energy budget of the lobes, and means that, a priori, the same correlations between jet kinetic energy and radio luminosity cannot be applied across both populations (although the dependence of radio luminosity with environment compensates for this fact to some extent, see Hardcastle & Krause 2013; Godfrey & Shabala 2013, and Chapter 6).

As such, the emission inside the lobes of FR I sources is synchrotron in the radio regime, but thermal emission from the shocked shells dominates at X-ray frequencies,

while in FR II the higher electron content (and larger scale) makes inverse-Compton the dominant mechanism for X-ray emission.

The minimum energy stored in the lobes can be calculated if the magnetic field strength and particle distribution are known, as Burbidge (1956) showed that the minimum energy condition is very close to equipartition. If we assume equal filling factors in the radiating particles and magnetic fields, equipartition is given by:

$$U_B = (1 + \kappa) \int_{E_{min}}^{E_{max}} EN(E)dE \tag{1.26}$$

where κ is the proton to electron energy ratio, and U_B is the magnetic energy density, $U_B = B^2/2\mu_0$.

The main issue with this assumption, however, is that the magnetic field cannot be directly determined from synchrotron emission alone. Inverse-Compton emission in X-rays can be used to constrain the electron density, and used in conjunction with the radio observations to determine the magnetic field strength (see e.g. Croston et al. 2005). X-ray emission can also be used to test how far from equipartition the lobes are. We now know that in FR I sources the thermal contribution to the energy budget cannot be neglected, since the equipartition pressure is much lower than the pressure of the gas outside the lobes (Morganti et al. 1988). In FR II systems deviations from equipartition are not so drastic (Croston et al. 2005), though they are difficult to measure in some cases, due to the limitations of geometrical assumptions for sources with low projection angles.

The main sources of photons for inverse-Compton scattering in radio lobes are the cosmic microwave background, the AGN and stellar light. Of these, AGN photons are slightly more problematic, since their distribution is not isotropic, but they are relevant mostly at small scales, close to the central engine. There is also synchrotron-self-Compton emission from the radio-synchrotron photons themselves. For the first (CMB) and last (SSC) cases we can assume an isotropic distribution of photons (Hardcastle et al. 1998b). The emissivity equations are not derived in detail here, and can be found in Rybicki & Lightman (1986).

While in FR II lobes inverse-Compton is the main contribution to the total energy budget, thermal processes contribute to the total energy as well. Shocks around FR II lobes have proved quite elusive, but there are some examples (see e.g. 3C 444 Croston

et al. 2011). The thermal energy contribution for low power sources is much larger, and is studied in detail for two objects in this thesis (Chapters 3 and 4). This energy can be derived from assumptions on the thermal spectrum and the shock conditions. Details on the interactions of the lobes with the environment, and shock physics, are given in Section 1.2.

1.2 Environments of radio-loud AGN

Powerful radio galaxies inhabit, almost universally, elliptical galaxies (though there are exceptions, see Ledlow et al. 1998; Keel et al. 2006). Seyferts are often found in spiral galaxies, some of which have small jets and lobes (like Circinus, see Chapter 4, and NGC 6764, see Hota & Saikia 2006; Croston et al. 2008b), but they are not generally classified as radio-loud due to their small R factors (see eq. 1.1). The reasons behind the correlation between the presence of radio jets and lobes and the host galaxy morphology are not entirely clear. It has been suggested that the richer environments in which ellipticals are generally found are needed to confine the jet and lobes, but some radio galaxies (Best 2004), even some LERGs, are found in sparse environments (e.g. 3C 15, see Chapters 5 and 6). It has also been suggested that the correlation has its origin in the larger black hole masses found in elliptical galaxies (e.g. Sabater et al. 2013; Alexander & Hickox 2012), or in the higher cold gas content in spirals, which may interfere with the formation or propagation of the jet (e.g Ledlow et al. 2001).

Evidence supporting the hypothesis that mergers trigger AGN activity (Heckman et al. 1986) can be found in the presence of disks, dust lanes (e.g. Cen A Kraft et al. 2003; Croston et al. 2009) and bluer colours than expected for quiescent ellipticals (Govoni et al. 2000). However, it is possible that heavy merger activity, such as that found in superclusters, can suppress radio source formation (Venturi et al. 2000), perhaps due to ram pressure stripping. This is perhaps the reason why powerful radio galaxies are generally found in groups and sparse clusters (Hill & Lilly 1991; Belsole et al. 2007). There is also an environmental dependence of morphology, with FR I sources (especially those with bent or distorted features) being found in clusters more often than FR II (e.g. Wing & Blanton 2011), but this may be caused by the fact that most LERG are FR I, and they are found in richer environments (Hardcastle 2004), and it may not be universal (see e.g. Ineson et al. 2012).

Environments are also potentially important in the fuelling process for the AGN. In the models of Hardcastle et al. (2007a), low-excitation sources, in particular, need a reservoir of hot gas, which could originate in a rich ICM or in winds caused by star formation. The former seems to be supported by the fact that LERG are more predominantly found in red galaxies compared to HERG (Janssen et al. 2012).

Dense environments are characterised by very hot ICM gas, with temperatures of $\sim 10^7 - 10^8$ K, and are very bright in X-rays (thermal bremsstrahlung emission being the primary contribution to their luminosity, as well as line emission from collisional excitation and de-excitation of the hot gas). Where no ICM is detected in X-rays, it is still possible to have a sparser group where some of the galaxies are interacting (see e.g. the 2Jy hosts in Ramos Almeida et al. 2010, and Chapters 5 and 6). Optical observations are helpful in these cases to determine the presence of bridges and tidal features.

The most efficient way in which radio-loud AGN release energy into their surrounding environment is through shocks driven by the lobes. A shock happens when a medium, gas in this case, moves at a bulk velocity that is greater than the local sound speed. This creates a sharp discontinuity in the medium, which reflects in an abrupt change in temperature, density and pressure (and magnetic field density, if one is present and favourably aligned with the shock front). For the cases studied in this thesis shocks can be approximated with the simplest conditions, since there are no relativistic effects involved (and we assume no magnetic fields either). To do this, the Rankine-Hugoniot jump conditions are applied (Landau & Lifshitz 1987), imposing mass, momentum and energy conservation at the front, and assuming a perfect monatomic gas (with polytropic index $\Gamma = 5/3$). This yields an expression for the temperature ratio between the gas in the shocked shells and the external medium:

$$\frac{T_{shell}}{T_{out}} = \frac{[2\Gamma\mathcal{M} + (1-\Gamma)]\,[\Gamma - 1 + (2/\mathcal{M})]}{(\Gamma+1)^2} \tag{1.27}$$

where $\mathcal{M}$ is the Mach number. This equation can be rewritten for density (or the pressure), using the ideal gas law:

$$\frac{p_{out}}{\rho_{out} T_{out}} = \frac{p_{shell}}{\rho_{shell} T_{shell}} \tag{1.28}$$

so that the density ratio is

$$\frac{\rho_{shell}}{\rho_{out}} = \frac{\Gamma + 1}{\Gamma - 1 + (2/\mathcal{M})} \tag{1.29}$$

We can immediately see that for strong shocks, where the Mach number is large, the last term in the denominator of eq. 1.29 becomes negligible. For a perfect monatomic gas this implies that the density ratio for a strong shock cannot be greater than 4. This condition is used in Chapters 3 and 4 to constrain the temperature of the external medium, given that the statistics are too low to obtain a fit to a thermal model. Once the parameters of the gas and the shock velocity are known, the relative contributions from thermal energy ($\frac{3}{2}NkT$), mechanical work (PV) and kinetic energy ($\frac{1}{2}m_{gas}\left(\frac{1}{4}v_{shell}\right)^2$, assuming the velocity ratios for a strong shock) can be determined, as well as which is the dominant emission process (thermal or non-thermal).

While radio-quiet AGN, even the most luminous ones, restrict their effect to their immediate surroundings, radio-loud objects transport the energy from the central source to much larger scales, affecting the host galaxy in the less powerful cases, and the entire cluster in the most powerful ones. The amount of energy released into the external gas in this manner is not negligible: even for small sources it is comparable to that of $10^4 - 10^6$ supernova explosions (Croston et al. 2007, 2008b; Kraft et al. 2003, and Chapters 3 and 4), enough to have an effect on the host galaxy's star formation processes, and even on its dynamical properties.

The relationship between AGN activity and star formation is not entirely clear, in part because most of the studies focus on radio-quiet AGN, but it is clear that there must be a co-dependence (see e.g. Best & Heckman 2012; Hardcastle et al. 2010b). The key may lie in the timescales involved in both processes (e.g. Wild et al. 2010) and how they relate to merger events. It is also possible that for radio-loud sources the effect may be delayed even longer, since the gas from the lobes needs time to mix with the ISM, making it impossible to estimate its effect directly (by then the radio structures would no longer be detectable).

For very powerful sources the energetic impact is even more dramatic (e.g. 3C 444 Croston et al. 2011). The inner regions of dense clusters are expected to cool very rapidly through X-ray emission, but the observations show that this is not happening as fast as expected (e.g Peterson & Fabian 2006). The energy input from radio-loud AGN is very likely to be one of the main causes behind this 'quenched cooling', by

driving shocks into the ICM. Giant lobes must also physically disrupt the ICM, causing compression, and heat dissipation even if no strong shocks are involved (see also the review by McNamara & Nulsen 2007).

1.3 Summary: observational properties of AGN

This Section provides a concise scheme of the main observational properties of the different AGN classes, as a summary of the structures, emission mechanisms and signatures discussed throughout this Chapter.

1.3.1 Core

- **Radio**: synchrotron emission (jet) in RL AGN, perhaps free-free emission in RQ HEGs. Main emission in LEGs.
- **FIR-MIR**: (modified) blackbody (torus) in both RQ and RL AGN, synchrotron (jet) in RL AGN. No accretion-related emission expected in LEGs, only synchrotron contamination.
- **NIR**: continuum (some blackbody from the torus?, tail of blackbody from the disk, some IC-scattered photons from the corona?) for both RL and RQ HEGs. Emission lines (broad and/or narrow, depending on orientation) for both RL and RQ HEGs. Some synchrotron contamination in RL HEGs. No accretion-related emission or lines expected in LEGs, only synchrotron contamination.
- **Optical**: continuum (blackbody from the disk, some IC-scattered photons from the corona) for both RL and RQ HEGs. Absorption expected for obscured sources. Emission lines (broad and/or narrow, depending on orientation) for both RL and RQ HEGs. Some synchrotron contamination in RL HEGs. No accretion-related emission or lines expected in LEGs, only synchrotron contamination.
- **UV**: 'big blue bump' continuum (blackbody from the disk, IC-scattered photons from the corona) for both RL and RQ HEGs. Absorption expected for obscured sources. Emission lines (broad and/or narrow, depending on orientation) for both

RL and RQ HEGs? No accretion-related emission or lines expected in LEGs, only synchrotron contamination.

- **X-rays**: continuum mostly from the corona, both in RL and RQ HEGs. Soft X-rays produced by reflection in RQ LEGs, by the jet in RL HEGs and LEGs. Absorption expected for obscured sources. Emission lines (broad and/or narrow, depending on orientation, Fe K-α line) for both RL and RQ HEGs. Synchrotron emission from the jet in RL sources with low orientation angle.

- **γ-rays**: continuum mostly from the corona, both in RL and RQ HEGs. Synchrotron emission from the jet in RL sources with low orientation angle. Inverse-Compton.

1.3.2 Intermediate scale

- **Radio**: jets, lobes, hotspots in RL HEGs and LEGs. No AGN-related emission in RQ objects.

- **IR to UV**: jets in RL HEGs and LEGs. Line + bremsstrahlung emission from photoionized/hot outflows in powerful RQ HEGs.

- **X-rays**: jets, shocked gas around the lobes of some HEGs and LEGs. IC inside the lobes of radio-powerful objects. Some emission expected from strongly photoionized regions near RQ cores.

1.3.3 Large scale

- **Radio**: jets, lobes, hotspots in very powerful RL HEGs and LEGs.

- **IR to UV**: some blackbody and line emission from hot gas in dense environments.

- **X-rays**: bremsstrahlung emission from very hot gas in cluster environments.

1.3.4 Caveats

Contamination from the old stellar population is relevant for the mid-IR band in fainter sources. This is particularly important for low-excitation objects, where there is no torus and therefore no accretion-related emission in the IR, although IR emission is detected in most sources.

1.4 The role of AGN in galaxy evolution

The previous Sections have introduced some of the effects AGN activity has on the host galaxies and their environments.

It is clear that galaxy evolution cannot be understood without considering the role of AGN in the energetic and dynamical properties of their hosts (see e.g. the review by Benson 2010). Models such as that of Croton et al. (2006) and Bower et al. (2006) simulate the growth and evolution of galaxies and their central black holes (see also Merloni & Heinz 2008), and prove the importance of the AGN, 'radio mode' (i.e. jet- and lobe-driven) feedback in the star-formation timescales and the creation of hot haloes. They also show the impact of AGN activity on the ICM, and its effect on the cooling timescales for the hot ICM (see also McNamara & Nulsen 2007). The energy input from AGN to the ICM is not just limited to the emission properties of the gas: it also has consequences on merger activity and the growth of the most massive cluster galaxies (De Lucia & Blaizot 2007).

It is thus clear that achieving a better understanding of how radio-loud AGN work and their effects on their surroundings is essential at all scales, if we aim to acquire a better knowledge of how the Universe works, from star formation to the dynamics of dark matter haloes.

1.5 Aims of this thesis

In this Chapter I have introduced the general properties of radio-loud AGN and their classifications. I have introduced some of the open questions that are addressed throughout this thesis.

The main aims of this work are:

- To study the impact of radio activity (jets and lobes) in low-power systems; to characterise the dynamics and energetics of these structures and how they influence their hosts (Chapters 3 and 4).
- To analyse the correlation between jet-related X-ray and radio emission, and test the threshold where 'radio-quiet', reflection models start to apply (Chapters 3 and 6).
- To investigate the mechanisms ruling accretion in radio-loud objects, and the signatures they produce, and use them as probes for source classification (Chapters 3, 4, 5, and 6).
- To understand the relationship between jet activity (time-averaged) and radiative, 'quasar mode' activity (immediately measured) (Chapter 6).
- To test the reliability of bolometric corrections, source classification diagnostics and black hole mass calculations (Chapters 3, 4, and 6).

Chapter 2

Data Analysis

In this thesis I use X-ray data to study the properties of radio-loud AGN cores and the extended structures that form as a consequence of the interaction between the jet and the interstellar medium in the host galaxy. Chapters 3, 5 and 6 are based on new and archival data from the *Chandra* and *XMM-Newton* telescopes, while Chapter 4 is based on *Chandra* data alone.

X-ray data from these instruments are stored in events files which contain information on the energy, detection time and position of each photon, as well as the orientation of the telescope as a function of time. The number of photons can be combined with each of these parameters to produce, respectively, spectra, lightcurves and images for the X-ray emission of any given source. The data reduction and the extraction of these final products is specific to each instrument, and requires a series of techniques which are described in this Chapter.

Although no data reduction has been performed for other instruments, images and maps from radio, optical and infrared telescopes are used for this thesis. Details on the origin of the data and the authorship of the images and maps are given in each Chapter.

2.1 *Chandra*

The *Chandra* X-ray satellite was launched on July 1999. It consists of a series of imaging and spectroscopic instruments, set behind 4 pairs of concentric Wolter Type-I mirrors called the High Resolution Mirror Assembly (HRMA). To the imaging cate-

gory belong the Advanced CCD Imaging Spectrometer (ACIS) and the High Resolution Camera (HRC), and the spectroscopic category covers the High and Low Energy Transmission Gratings (HETG and LETG). For this thesis I have only used data from the ACIS instrument.

The telescope also has a particle detector, the Electron, Proton, Helium Instrument (EPHIN), which monitors the presence of charged particles which could damage the other instruments.

2.1.1 Data reduction

The ACIS instrument consists of two subsets of CCD cameras, the ACIS-I and the ACIS-S. The first instrument is formed by a square array of four 1024 by 1024 pixel, front-illuminated CCDs. The ACIS-S is a longitudinal set of 6 1024 by 1024 pixel chips, of which two are back-illuminated (S1 and S3). The observer can specify a subset of chips from both instruments; the most popular combinations use the central chips of the ACIS-S (S1 to S4), with two of the ACIS-I chips (I2 and I3), or the entire ACIS-I array with two ACIS-S chips (S2 and S3). For targets that are not very spatially extended the main chip is usually the S3, since back-illuminated chips are less sensitive to background contamination, and yield a better signal to noise ratio in the final images and spectra.

For very bright sources telemetry saturation can be an issue, and thus smaller subarrays of chips are selected, and the Graded telemetry format is selected, which stores less information than the Faint and Very Faint modes, which are best suited for fainter targets where background contamination is a more pressing issue.

The pixel size of the ACIS CCDs is 0.492 arcsec.

The initial processing of the data is carried out by the *Chandra* X-ray Center (CXC) through a pipeline that performs different conversions and corrections. The first level, L0, converts the raw *Chandra* telemetry into FITS files. The L1 stage applies a series of instrumental corrections to the data, and produces the events files that can be used for analysis.

Although it is possible to obtain files with a higher level of standard processing, most users choose to use the level 1 files and apply their own corrections in the subsequent reduction phases. This reprocessing is carried out using the CXC software

CIAO. For the work presented in this thesis I used different versions of CIAO: 4.2 was used for Chapters 3 and 4, and 4.4 for Chapters 5 and 6.

During the L2 phase several filters are applied. The grade value of each event is assessed, and used to discard events produced by cosmic rays (which form specific patterns in the CCDs). Good Time Interval (GTI) files are then created, to discard the time intervals during the observation in which the instruments may not have been performing correctly. The calibration files can then be applied to detect and exclude the observation-specific bad pixels.

To achieve the maximum possible spatial precision in my images, and the best possible signal to noise ratio, I also specified conditions that removed the pixel randomization (automatically applied in older versions of the pipeline to reduce aliasing effects), minimised the streaking (described in detail in Section 2.1.4), and removed the afterglow effect from cosmic ray events. These corrections are automatically applied in the latest version of the basic pipeline and the CIAO reprocessing tool, but had to be specified manually at the time my data reduction was carried out.

2.1.2 Imaging

Once a 'clean' events file is obtained, it can be used to produce images and spectra. Images are created by extracting the spatial information out of the events file, and generally applying an energy filter to minimise issues with instrument calibration and contamination from background events. The typical energy range is $0.4 \leq E \leq 7$ keV.

For the work presented in Chapter 4 I carried out additional filtering. I used the CIAO tool *wavdetect* to identify any point sources, which were then removed using the task *dmfilth*. This filtering was done to guarantee that the extended emission in the X-ray image corresponded only to the radio lobes of the source.

For the work described in Chapter 4 it was also necessary to combine images from three different exposures. This was done with the CIAO tool *merge_all*, after careful weighting of the individual images. This tool automatically aligns the individual images and co-adds them according to the weights specified by the user. It does not, however, re-normalise the areas covered by only one or two of the individual images (due to the differences in orientation and pointing), so the user must be aware of where the chip edges and gaps are for each observation. Fig. 2.1 shows the individual and

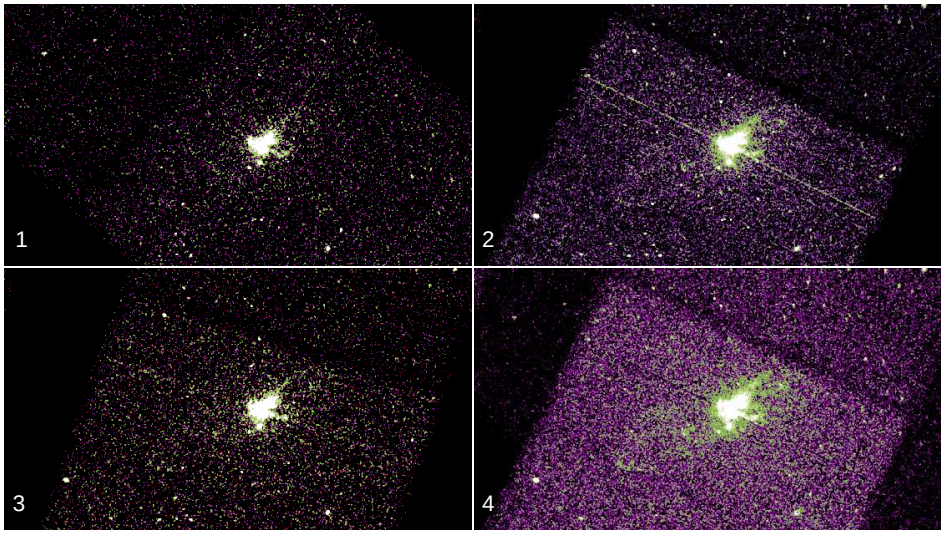

Figure 2.1: Individual 0.3-7 keV and merged 0.4-5 keV images for the Circinus galaxy. The first three panels illustrate the different orientations of the individual observations, detailed in Table 4.1. The last panel shows the final reduction stage, after the individual observations were combined, and the point sources and readout streak excluded. The last image has also been cut to exclude the regions that are not relevant to the analysis of the source. The images are smoothed with a $\sigma = 3$ pixel Gaussian profile for clarity.

co-added observations for the Circinus galaxy, the object studied in Chapter 4.

The qualitative analysis of the X-ray images was carried out using the program ds9 and some tools from the FUNTOOLS C libraries, in particular those used to generate histograms and radial profiles. Some of the images in Chapters 3 and 4 have been smoothed with a Gaussian kernel to better show the details of the extended structures. The smoothing process transforms each individual photon event to an extended Gaussian distribution, so that the overall effect fills in the gaps between pixels and better represents what the image would look like for a longer exposure. This technique is well suited to analyse faint, extended structures, but it must be used carefully with brighter regions, since it dilutes the effects of smaller-scale structure.

2.1.3 Spectroscopy

Spectra are extracted from the L2 events files using the CIAO tool *specextract*, using a series of constraints. Spatial constraints are usually derived from a qualitative analysis

of the X-ray image, in which regions are determined for the source and background spectra to be extracted from. Time constraints can also be specified as a GTI file, for example when there are periods of higher background contamination during an observation that need to be excluded from the final spectra.

In order to use χ^2 statistics I rebinned my spectra using the tool FUNGROUP, written by M. Hardcastle using the FUNTOOLS C libraries. I binned my spectra to 20 counts per bin (after background subtraction) in most cases, but allowed for a lower grouping (15 counts/bin) for spectra with very few counts, for example in some of the sources analysed in Chapter 6.

Spectra alone are not suitable for model fitting. The tool *specextract* also creates an auxiliary response file (ARF) and a redistribution matrix file (RMF). The ARF contains combined information on the effective area of the detector and its quantum efficiency, so that when it is multiplied by the spectrum the result is the count distribution that would be seen with an instrument with perfect energy resolution. The RMF describes the instrumental response as a function of energy and detector channel, effectively mapping what energy range corresponds to each channel. Since the detector is not perfect, the counts need to be spread over the energy resolution of the instrument, which is why this file takes a matrix form.

Older versions of CIAO, which I used for data processing in Chapters 3 and 4, required separate tasks to generate spectra, ARFs and RMFs, but they have been unified under *specextract* in the latest versions.

For the work described in Chapter 4 I had to co-add spectra taken from three individual observations. This was done with the CIAO tool *combine_spectra*, which also combines the individual ARF and RMF files. This tool automatically weights the individual spectra, ARFs and RMFs according to their exposures. While this tool is very powerful for the analysis of faint structures, it must be used carefully. Some sources, like active galactic nuclei, have spectra that vary not only in intensity, but also in shape, and should not, therefore, be blindly added together. When the background rates are very different between the observations being added it is also not advisable to use this tool.

2.1.4 Instrumental issues

The two main issues I encountered during the data analysis and reduction process were the degradation of the energy resolution of the CCDs, and pileup.

The first issue is caused by the eventual degradation of the CCDs, due to a loss of charged transfer efficiency caused by low energy protons. This issue affects mainly the sensitivity at soft energies, and the CCDs that are front-illuminated, rather than back-illuminated chips, which are better protected by the telescope gates. The data reduction pipeline and calibration files take into account this loss of sensitivity for individual observations; however, it becomes relevant when trying to combine observations from very different epochs, and can only be tackled by carefully adding up the images and spectra.

Pileup occurs when two or more photons of similar energies hit the same CCD pixel between two readouts, so that the instrument detects them as a single photon with a total energy that is the sum of the individual ones. This is very problematic for bright sources, in which the regions with higher emissivity can even appear as completely dark, the pileup being so severe that the energy of the combined photons falls outside the detection range of the CCD.

Pileup can be minimised by choosing a smaller area of the chip for imaging, so that the time between readouts is shortened. Some models (e.g. *pileup* for XSPEC) try to take into account the effect pileup has on the resulting spectra, but they are not effective in all cases.

Several of the sources described in this thesis are piled-up to different degrees, the worst case being the spectrum of the AGN in Circinus (chapter 4), which I did not have to analyse in detail, since it was beyond the scope of that particular project.

To correct the effect of pileup on my data I carried out simulations of the affected sources with the tools ChaRT and MARX. ChaRT generates a PSF from a given model, which is then fed to MARX, which produces an image of the simulated PSF. A ratio is made between this image and the original one, in which the central pixels are excluded. A code fits a 5th-degree polynomial to this ratio as a function of energy, to create a new ARF that compensates for the missing pixels using the ratio of the simulated and real images. The process is described in more detail in Sections 3.3.1 and 6.2.1.

2.2 *XMM-Newton*

XMM-Newton was launched in December 1999. It consists of an optical/UV telescope with an instrument called the Optical Monitor (OM), and three Wolter type-1 X-ray telescopes with two different types of instruments: the European Photon Imaging Camera (EPIC) and the Reflection Grating Spectrometer (RGS). I used data taken with the EPIC cameras for Chapters 3, 5 and 6 of this thesis.

2.2.1 Data reduction

The EPIC camera consists of three instruments, situated in each of the three telescopes. The MOS1 and MOS2 (Metal Oxide Semiconductor) instruments are made of two sets of 7 front-illuminated, CCDs, which are rotated 90° between MOS1 and MOS2. The PN is an array of 12 rectangular CCDs, and it is slightly offset with respect to the optical axis of the telescope, so the pointing does not make the source fall onto the CCD gaps. The pixel size is 1.1 arcsec for the MOS CCDs, 4.1 arcsec for the PN.

The spatial resolution of the EPIC cameras is worse than that of *Chandra*'s ACIS: the PSF FWHM is 6 arcsec, compared to 0.4 arcsec in *Chandra*. The EPIC, however, is more sensitive, and thus better for fainter or more distant sources. The EPIC cameras can work in timing mode and with a reduced area to minimise pileup in very bright sources. Since the large PSF means that pileup is negligible in all the sources considered in this thesis, no observations required timing mode.

As in the case of *Chandra*, the *XMM-Newton* Science Archive (XSA) provides the users with end-level data that can be used directly for analysis, although it is usually best to manually perform the data reduction to optimise it for the specific scientific objectives of each project.

The XSA provides the users with a series of Observation Data Files (ODF), which include the instrument science, housekeeping, spacecraft details, radiation monitor and summary files. These files are used in conjunction with the Science Analysis System software to create the final images and spectra.

The standard reduction process consists of the tasks *cifbuild*, which applies the calibration conditions to each observation, *odfingest*, which loads the observation files, and *emchain* (MOS) or *epchain* (PN), which generate the events files that will be used

to produce images, spectra and lightcurves.

2.2.2 Imaging

Once the 'clean' events file is obtained, the procedure to create an image is very similar to the one described for *Chandra* in Section 2.1.2. The conditions for the image are selected by filtering out the events with a pattern that corresponds to cosmic-ray processes, rather than photons from the source, and choosing an energy filter (which usually covers the 0.2 – 12 keV range, since further filtering can be applied when generating spectra to exclude the ranges in which the instruments are not well calibrated).

It is also at this stage that user-specified GTI files can be created and applied, to exclude parts of the observation (e.g. to avoid periods of high particle background, see Section 2.2.4).

2.2.3 Spectroscopy

The spectra for the source and background are generated from the images using the same task, *evselect*, by specifying the spatial coordinates. The tasks *arfgen* and *rmfgen* generate the ARF and RMF files, respectively.

2.2.4 Instrumental issues

Despite the high sensitivity of the EPIC cameras, since the PSF of the sources is spread over a larger area, they are less affected by pileup than the *Chandra* cameras. Pileup is still an issue for very bright sources such as Cygnus X-1 and the Crab, but none of the *XMM* data presented in this thesis are affected by it.

The CCDs of *XMM* are also affected by degradation due to damage from low-energy protons. As for the case of the ACIS in *Chandra*, it is necessary to bear this in mind when coadding EPIC images or spectra taken at very different epochs.

The main issue with the EPIC cameras is the high X-ray background present in some observations. Due to its orbit *XMM* is very sensitive to solar flares, which release charged particles that interfere with the instruments. While a higher background noise may not be an issue for bright sources, it is problematic for fainter targets or extended structures.

The only way to address this issue is careful filtering of the observations to exclude periods of flaring particle background. This is done by creating a lightcurve for energies greater than 10 keV for the MOS and between 10 and 12 keV for the PN. It is at these energies that the background noise is most easily identified. The user then specifies a threshold count rate and feeds it to the SAS task *tabgtigen*, which creates a GTI file that excludes the time intervals in which the count rate is higher than the specified limit.

2.3 Spectral fitting

Spectral fitting was carried out using XSPEC, apiece of software developed by NASA's HEASARC (High Energy Astrophysics Science Archive Research Center).

The detectors in *Chandra* and *XMM* do not measure the actual spectra of the sources, but rather the photon counts in instrument channels. The observed counts are related to the original spectrum $f(E)$ (in units of photons cm^{-12} s^{-1}) by:

$$C(I) = \int_0^\infty f(E)R(I,E)dE \tag{2.1}$$

where $R(I,E)$ is the instrumental response (it is proportional to the probability that a photon with energy E will be detected by the instrument channel I). It is not possible, in general, to obtain the original spectrum from the measured one. What is usually done is to fit a model to the observed spectrum, and establish the goodness of fit based on a series of parameters.

XSPEC allows the user to choose from different statistical methods for fitting. For the work presented in this thesis the method of choice is χ^2 statistics. The manner in which fitting is done is as follows: XSPEC loads the observed source and background spectra, normalises them by the exposure time and the effective areas, and subtracts the background. It then loads the response files, to apply the instrumental response to the observed, background-subtracted spectrum. This response, parametrized in terms of a single response $R(I,E)$ in equation 2.1, is split into two components within XSPEC: the response matrix (RMF) and the auxiliary response file (ARF), described in Section 2.1.3. XSPEC uses the ARF to assign a response to each instrumental channel, and the RMF to assign and an energy interval to each channel.

The model is expressed as a vector of energies and a set of functions that assign detector channels to energies. For each model $F(E)$ a count rate is predicted (through eq. 2.1) and is then compared to the observed count rate, using a modified Levenberg-Marquardt fitting algorithm. The final output is a series of values and confidence ranges (by default 90 per cent confidence) for each model parameter, and a χ^2 value and number of degrees of freedom, to establish the goodness of fit.

The XSPEC model components fall into several categories: additive, multiplicative, convolution, pileup and mixing. For my analysis I have used additive models, which include *apec* (emission from collisionally-ionised diffuse gas), *powerlaw* (to model the AGN continuum) and *gaussian* (for emission and absorption lines), and multiplicative models, such as *wabs* (which models the effects of foreground and intrinsic absorption). The components can be combined to produce an overall model that accurately represents the spectra.

The user can specify several options, such as the cosmological parameters, statistics and confidence ranges to be used.

XSPEC can also be used to do simulations of spectra with longer exposures from existing data, which is essential when planning future observations.

Chapter 3

Markarian 6

Markarian 6 is a nearby (D∼78 Mpc) Seyfert 1.5, early-type galaxy, with a double set of radio bubbles. The outer set spans ∼7.5 kpc and is expanding into the halo regions of the host galaxy. We present an analysis of our new *Chandra* observation, together with archival *XMM-Newton* data, to look for evidence of emission from shocked gas around the external radio bubbles, both from spatially resolved regions in *Chandra* and from spectral analysis of the *XMM* data. We also look for evidence of a variable absorbing column along our line of sight to Mrk 6, to explain the evident differences seen in the AGN spectra from the various, non-contemporaneous, observations. We find that the variable absorption hypothesis explains the differences between the *Chandra* and *XMM* spectra, with the *Chandra* spectrum being heavily absorbed. The intrinsic N_H varies from $\sim 8 \times 10^{21}$ atoms cm^{-2} to $\sim 3 \times 10^{23}$ atoms cm^{-2} on short timescales (2-6 years). The past evolution of the source suggests this is probably caused by a clump of gas close to the central AGN, passing in front of us at the moment of the observation. Shells of thermal X-ray emission are detected around the radio bubbles, with a temperature of ∼0.9 keV. We estimate a temperature of ∼0.2 keV for the external medium using luminosity constraints from our *Chandra* image. We analyse these results using the Rankine-Hugoniot shock jump conditions, and obtain a Mach number of ∼3.9, compatible with a scenario in which the gas in the shells is inducing a strong shock in the surrounding ISM. This could be the third clear detection of strong shocks produced by a radio-powerful Seyfert galaxy. These results are compatible with previous findings on Centaurus A and NGC 3801, supporting a picture in which these AGN-driven outflows play an important role in the environment and evolution of the host galaxy.

3.1 Introduction

Recent *Chandra* observations of the environments of several powerful radio galaxies (e.g. Hydra A, McNamara et al. 2000; M87, Young et al. 2002; Hercules A, Nulsen et al. 2005a; see also the review by McNamara & Nulsen 2007) have led to significant progress in understanding the AGN-driven gas outflows in these systems and the role they play in galaxy formation and evolution (Croton et al. 2006; Bower et al. 2006).

We now know that, although the most powerful radio outflows, spanning hundreds of kpc, are associated with massive elliptical systems, smaller structures also connected to an active nucleus can be found in a variety of systems and environments, including spiral and disk galaxies (see e.g. Gallimore et al. 2006, Kharb et al. 2006, Hota & Saikia 2006, Saikia & Jamrozy 2009). The mechanism by which these structures are produced is likely to be related to the one we see in the most powerful sources, but on a smaller scale. Most of the observed AGN-driven bubbles have been found to be overpressured with respect to their surroundings, and may be thus inducing shocks into their surrounding medium. The wide range of morphologies of the galaxies where radio bubbles have been found, and the fact that this AGN-driven phenomenon is most likely episodic (Saikia & Jamrozy 2009) make understanding the energetics involved in this process fundamental to estimate its impact on AGN feedback and galaxy evolution, and extrapolate how common this mechanism can be in low-power systems.

In our search for evidence of galaxy feedback associated with kpc-scale radio bubbles, we have carried out observations of a variety of systems, the most notable perhaps being the nearby Fanaroff-Riley type I (FR I, Fanaroff & Riley 1974) galaxy Centaurus A (Kraft et al. 2003, Croston et al. 2009), finding evidence for shocks also in smaller, more distant systems such as NGC 3801 (Croston et al. 2007) and a rather more complex scenario in the spiral galaxy NGC 6764 (Croston et al. 2008b). We recently carried out a *Chandra* observation of Markarian 6 (Mrk 6, IC 450, $z = 0.018676$), an early-type S0 Seyfert 1.5 galaxy (Osterbrock & Koski 1976) whose characteristics have been studied in the radio ($L_{1.4GHz} = 1.7 \times 10^{23}$ W Hz^{-1} sr^{-1}), infrared, optical and X-ray wavelengths over the last 30 years. Recent radio studies have unveiled a complex structure surrounding the AGN, with a double set of bubbles and a radio jet (Kukula et al. 1996), suggesting a jet precession scenario (Kharb et al. 2006). In this paper we describe the results of our analysis of the *Chandra* observation.

We have also analysed three previous datasets from *XMM-Newton* to study the evolution of the AGN and its immediate environment over time. These data were analysed in detail previously (Schurch et al. 2006; Immler et al. 2003), using different models to address the complex scenario surrounding the AGN. We have approached this analysis by searching for consistency between the *Chandra* and *XMM-Newton* datasets in the context of variable absorption, following both the methods used by Hardcastle et al. (2009) when modelling a sample of 3CRR radio sources, and a double partial covering model that has previously been successful in describing the properties of the nuclear spectrum of Mrk 6.

3.2 Observations and data reduction

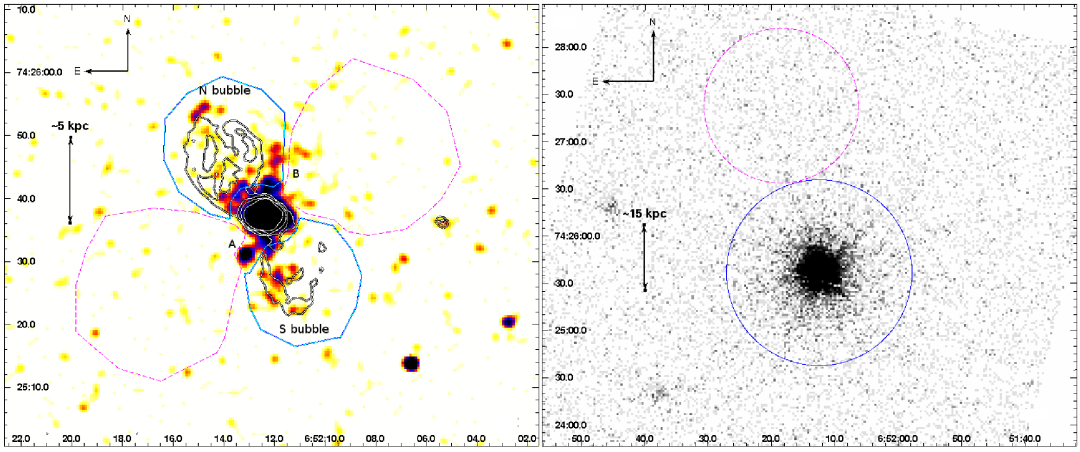

Figure 3.1: **Left:** *Chandra* ACIS-S 0.4-3 keV image of Mrk 6, with σ=3 pixels Gaussian smoothing and overlaid VLA radio contours (Kharb et al. 2006), showing the match between the radio and X-ray emission. In this frame are also displayed the source (blue, continuous) and background (magenta, dashed) extraction regions for the bubble spectra. The label A shows a possible background quasar, while B indicates the emission coincident with the extended [OIII] emission-line regions, see Figure 3.2. The energy range has been selected to highlight the shell-like structure surrounding the bubbles and the overlap between the X-ray emission and the radio structure. **Right:** (non-smoothed) *XMM-Newton*'s MOS 1 image (obsid 0305600501) of Mrk 6, with the source (blue, continuous) and background (magenta, dashed) extraction regions for all the AGN spectra (*Chandra* and *XMM*).

We observed Mrk 6 with *Chandra*'s ACIS-S CCD on July 12 2009, with a total

exposure of 75 ksec. The observation was carried out in faint mode, to minimise issues with the background and at the same time avoid telemetry saturation. There were no intervals of high background during this observation, hence we analyse the full exposure. We reprocessed the data from level 1 events in the standard manner, using CIAO 4.2 and CALDB 4.2.0. To improve the quality of the data for the purposes of a study of the extended radio bubbles, we removed the pixel randomization and ran the destreaking routines on the data. We produced two filtered images (0.3-7 keV and 0.5-5 keV) to assess the extent and structure of the radio bubbles, and chose our regions accordingly, but extracted all the spectra from the original events file. We performed our spectral fits with XSPEC, constraining the energy range to be coincident with that covered by the instrument calibration (0.3-7 keV). We estimated the pileup fraction for these data from the *Chandra* documentation and calculated a numerical value using the PIMMS tools. The pileup fraction is about 12% throughout the observation (there are no substantial differences in the count rate during the observation).

The *XMM-Newton* observations were taken in March 2001 (obsids 0061540101 and 0061540201), April 2003 (obsid 0144230101) and October 2005 (obsid 0305600501). We reduced the data using the standard routines from SAS version 9.0 and the latest calibration files. Table 3.1 gives details on the exposure times. The 2001 and 2003 observations were taken with the medium filter, while 0305600501 was taken with the thin filter. We decided not to use the observation 0061540201 because it was taken in calibration closed mode. We discarded the first 10 ksec from the observation 0144230101 due to high background. Despite the background contribution being uneven during this observation, after examining the relative count rates of the source and the background, we decided not to discard any other time intervals, since the background in these periods was always below 10% of the intensity of the source across the whole energy range, which is accurate enough for our purposes. We extracted spectra for the PN, MOS1 and MOS2 cameras, except in the case of the observation 0144230101, where a PN spectrum could not be obtained. We limited our spectral fits to the 0.3-8.0 keV energy range, to analyse an energy range comparable to that covered by *Chandra*.

For the study of the properties of the AGN we used the same extraction region for the *Chandra* and *XMM* data, a ~60 arcsec radius circle centred in the source, which contains most of the MOS and PN PSF. Although we know from the *Chandra* image

that there are a few point sources other than the AGN within this extraction region (see Figure 3.1), they are not resolved by the *XMM* instruments, and their intensities are so low compared to the AGN that we can consider their effects negligible. We also use the same background region for all the data, a ~50 arcsec radius circle, North of the source region to avoid contamination from the host galaxy, as seen on Figure 3.1.

To simulate the AGN on the *Chandra* detector we used the ChaRT 1.0 web interface and MARX version 4.5.

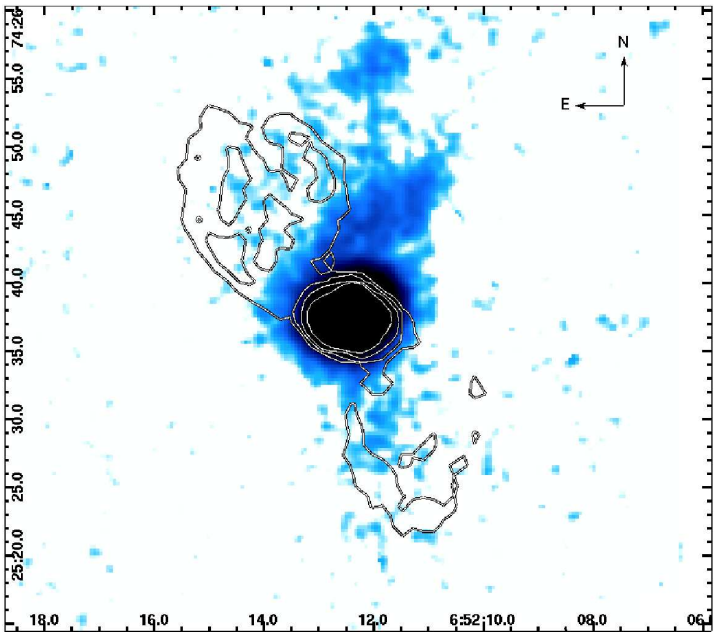

Figure 3.2: [OIII] image of Mrk 6 from Kukula et al. (1996), with overlaid radio contours, showing the structure of the extended emission-line region (ENLR). **Scale:** 1″=366 pc.

For the study of the extended bubble area, we used as a reference the radio data from Kharb et al. (2006), defined contours around the largest-scale bubbles and drew source regions outside these contours, keeping well away from the central AGN to avoid contamination from its PSF, as well as from the inner radio bubbles and jet. Figure 3.1 shows details on the extraction regions and the structure of the extended emission from the bubbles. In this case, we took care to exclude the only likely background source (South of the source, see discussion in Section 3.3.2) in order to avoid contamination in our spectra.

All the spectra were grouped to 20 counts per bin after background subtraction, before spectral fitting, to be consistent with χ^2 statistics. We used a fixed Galactic absorption of $N_H = 6.39 \times 10^{20}$atoms cm^{-2} (Dickey & Lockman 1990a) for all our spectral fits, and a redshift $z = 0.018676$ (*SIMBAD*).

Table 3.1: Summary of Mrk 6 X-ray observations.

Telescope	Instruments	Date	Obsid	ksec
XMM-Newton	PN, MOS1,2	2001/04/26	0061540101	31
XMM-Newton	MOS1,2	2003/04/26	0144230101	41
XMM-Newton	PN, MOS1,2	2005/10/27	0305600501	20
Chandra	ACIS	2009/06/12	10324	75

All the parameters estimated with XSPEC are quoted with 90% confidence uncertainties. The errors on the upper limit of counts for the extended regions are 1σ.

3.3 Results

3.3.1 The Seyfert core

Instrumental corrections

When we first approached the analysis of our data, we extracted a spectrum using the regions illustrated in the right panel of Figure 3.1 and fitted a model consisting of a double power law with Galactic and heavy intrinsic absorption. We were surprised to find that the *Chandra* and *XMM-Newton* spectra looked radically different. After checking the observation details of the *Chandra* data, using the on-line tool *PIMMS*, we found that the AGN spectrum had a noticeable pileup fraction ($\sim$ 12 per cent), compatible with the frame time of the observation (3.1 s) and the background-subtracted count rate of the AGN ($\sim$ 0.11 counts/s). This resulted in a "ghost" peak around 2 keV in our spectra, caused by piled up 1 keV photons. We could not obtain satisfactory results from the XSPEC *pileup* model, perhaps due to the complexity of our underlying model, so we decided to attempt a different approach, previously applied with success by Getman et al. (2005), Evans et al. (2005), and Hardcastle et al. (2006).

In most sources only the central pixels of the PSF are affected by pileup. These innermost pixels also contain a large fraction of the total photon counts; so eliminating them effectively removes any issues with pileup, but it also results in a lower signal to

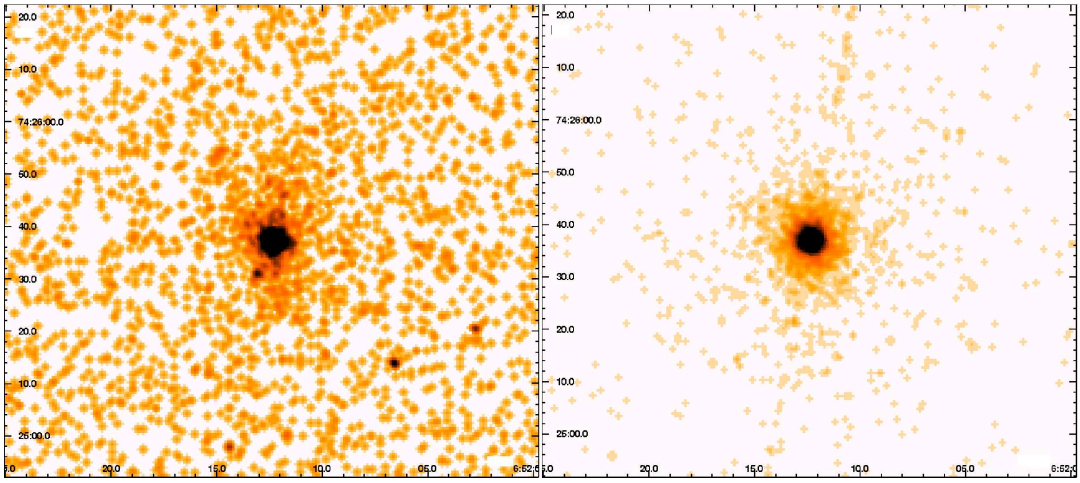

Figure 3.3: **Left:** real *Chandra* ACIS-S (75 ks) 0.3-7 keV image of Mrk 6, with σ=2 pixels Gaussian smoothing. **Right**: ChaRT/MARX simulated data (150 ks) 0.3-7 keV, with σ=2 pixels Gaussian smoothing. The scales and colour bars in both pictures are the same. The simulated image contains only AGN photons, with no background, and helps us correct the pileup effects in our AGN spectra (we did not simulate pileup) and establish a statistical contribution of photons from the AGN to the bubbles and external regions of the galaxy. Since the exposure time of the simulation is twice as long as the one of the original data, we have corrected for any exposure-dependent effects when using it for our analysis. The equivalent of the faint streak in the simulated image is below the background level in the real data. **Scale:** 1″=366 pc.

noise ratio. If pileup is significant enough to cause a bias in the spectral fits, however, removing its effects often results in improved fits. In our case, excluding the central four pixels of the PSF effectively eradicates any pileup issues in our spectra; we extracted a spectrum from such a region, centered on the core, and generated an RMF and ARF in the standard way. However, since the PSF is energy-dependent, excluding these pixels and extracting a spectrum from the resulting annular region alone does not solve the problem; it is necessary to correct the ARF to account for this energy dependence.

To correct the ARF we followed the procedure described by Hardcastle et al. (2006). We generated an energy (keV) versus flux (photons/cm^2/s) table from our model fit and fed it to ChaRT, the Chandra Ray Tracer (Carter et al. 2003), a code that simulates a PSF from a specified model. We selected an exposure time of 150 ks, twice as long as our real exposure, to get the best possible photon statistics in the simulated

data while trying not to exceed the limit on the ray density. We did not simulate the pileup with ChaRT. The output from ChaRT is a set of rays that cannot be directly used for analysis: they need to be projected on the detector plane and converted into an events file using MARX[1].

We then generated a new events file from our original data and an annular extraction region, identical to the one we used to generate our spectra, but excluding the central four pixels. We used a code to fit a 5-th degree polynomial to the ratio of this events file and the whole simulated events file as a function of energy. This code reads in the ARF generated by CIAO and scales the effective area at each energy, using the polynomial fit, to effectively correct for the missing effective area due to the exclusion of the central pixels. The code then writes a new ARF which can be used to correct for the effects of excluding the central pixels.

We were then able to carry out fits to our extracted spectrum. As expected, the loss of counts from the central pixels slightly decreased the signal to noise ratio, but eliminating the bias caused by pileup resulted in a noticeably improved fit (see Section 3.3.1 for details) and we obtained a better statistical result. The simulated image is displayed on the right panel of Figure 3.3, next to the original data. Although the simulation predicts some streaking in the image, in our real exposure it is so weak it is not detectable over the background noise, so that we cannot use it to constrain the AGN spectrum.

Models

Early *ASCA* data on Mrk 6 have already made clear the difficulties underlying the study of intermediate type Seyferts (Feldmeier et al. 1999), particularly when disentangling the absorption component from the intrinsic continuum shape, and several attempts have been made since then to successfully model both the underlying, complex physical scenario, and the properties of the X-ray emission we see. The partial covering model used for the *ASCA* data was also employed in the analysis of an early *XMM-Newton* dataset by Immler et al. (2003), while analysis of a later observation (Schurch et al. 2006) favoured the inclusion of a reflection component.

After correcting for pileup in our *Chandra* spectrum, it still looked very different

[1] See http://space.mit.edu/CXC/MARX/docs.html

to the *XMM-Newton* spectra. Moreover, we encountered some problems when fitting the *Chandra* spectrum alone, using a double power law model with local and intrinsic absorption (see below for a detailed description of the model). XSPEC is unable to disentangle the contribution to the model from the power law from that of the absorbing column, which results in extremely low or even negative values of the photon index for the second power law. Seeing that the *Chandra* spectrum has fewer relative counts and a different shape in the 2-5 keV range, we decided to test the hypothesis of a variable absorption column along our line of sight to Mrk 6, which may be caused by the movement of clumpy gas from the regions within a few pc of the black hole, happening on timescales of months to years. This hypothesis has been successfully used over a variety of Seyfert 1 and 2 X-ray spectra (see e.g. Risaliti et al. 2002) and has already been suggested before for Mrk 6 by Immler et al. (2003) after they observed a substantial change in the absorption column between their *XMM* and *BeppoSAX* observations. However, the absorption variations between the *XMM* spectra from 2001, 2003 and 2005 are much smaller (Schurch et al. 2006). Disentangling intrinsic AGN variability from the variable obscuration is a difficult task, both in the X-rays and at other wavelengths. We know from the optical wavelengths that changes in intensity of the Hα and Hβ optical emission lines are a good probe of the variability of the central AGN itself, but there is also evidence that suggests that the gas where these lines are produced can undergo substantial variations over time (Rosenblatt et al. 1992).

We decided to approach the modeling of the AGN both from the perspective used in Hardcastle et al. (2009) and Croston et al. (2007), which has proved successful in describing the properties of many powerful radio sources at low to intermediate redshifts, and under the partial covering models that have been successful at describing not only the properties of the spectrum of Mrk 6 (Feldmeier et al. 1999; Immler et al. 2003; Schurch et al. 2006), but also several other classical Seyferts. The radio galaxy model assumes that the soft X-ray emission arises from the jet, while the hard X-ray powerlaw is associated to accretion, through emission from the disk. The partial covering models assume that the soft component originates in the reflecion of the hard component on the disk (see Section 1.1.2), and the partial covering is caused by either structures within the clumpy torus (cold absorbers) or in the broad-line region, closer to the AGN (hot absorbers).

The first model provides an accurate description of the nuclear spectrum of Cen A

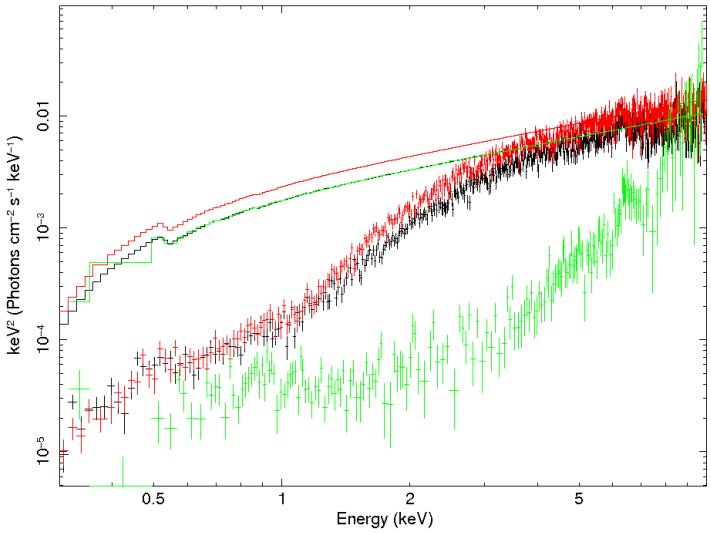

Figure 3.4: Energy-unfolded *XMM-Newton* PN (black: 0061540101; red: 0305600501) and *Chandra* ACIS-S (green) spectra of Mrk 6 to illustrate the changing spectral shape caused by the variation in N_H. The model (lines) is a power law with local absorption, with the photon index and normalization fixed to the values obtained in the fit of the second model (see Table 3.2).

(Evans et al. 2004) and is often used to fit spectra of narrow-lined radio galaxies. We fitted a single power law with a fixed Galactic absorption to the data (*wabs* XSPEC model). We added to this model a second absorption column (*zwabs* XSPEC model) at the source's redshift, which was allowed to vary, and a second power law. We added a redshifted Gaussian to account for the Fe Kα emission line. See Figure 3.5 for an overview of the *Chandra* spectrum.

Table 3.2: Best fitting parameters for the *Chandra* and *XMM-Newton* AGN fit. **Model 1:** wabs(apec+po+zwabs(po+zgauss)); **Model 2:** wabs(apec+zpcfabs$_1$*zpcfabs$_2$(po+zgauss)). Both models include the contribution from the thermal emission from the radio bubbles (see Section 3.3.2 for details).

				apec		Model 1			Model 2						
Obsid	Line E	Eq. Width	Local N_H	kT	abundance	Γ_1	N_H	Γ_2	f^1_{cov}	N^1_H	f^2_{cov}	N^2_H	Γ	Norm	$L_{2-10keV}$
	keV	eV	$\times10^{20}$at. cm^{-2}	keV	$\odot$		$\times10^{22}$at. cm^{-2}			$\times10^{22}$at. cm^{-2}		$\times10^{22}$at. cm^{-2}		$\times10^{-3}$ ph. keV^{-1} cm^{-2} s^{-1}	$\times10^{43}$erg s^{-1}
10324	$6.46^{+0.06}_{-0.07}$	309^{+331}_{-207}	6.39	$0.87^{+0.25}_{-0.23}$	0.35	1.5	$30.78^{+3.28}_{-4.57}$	$1.16^{+0.03}_{-0.03}$	$0.68^{+0.01}_{-0.01}$	$17.93^{+3.04}_{-2.54}$	$0.83^{+0.01}_{-0.01}$	$55.89^{+5.46}_{-4.70}$	$1.28^{+0.01}_{-0.01}$	$1.94^{+0.12}_{-0.08}$	1.23
0061540101	$6.43^{+0.02}_{-0.03}$	94^{+36}_{-32}	6.39	$0.87^{+0.25}_{-0.23}$	0.35	1.5	$2.70^{+0.08}_{-0.08}$	$1.16^{+0.03}_{-0.03}$	$0.68^{+0.01}_{-0.01}$	$0.87^{+0.05}_{-0.05}$	$0.83^{+0.01}_{-0.01}$	$3.32^{+0.09}_{-0.08}$	$1.28^{+0.01}_{-0.01}$	$1.99^{+0.03}_{-0.02}$	1.25
0144230101	$6.40^{+0.05}_{-0.05}$	62^{+60}_{-58}	6.39	$0.87^{+0.25}_{-0.23}$	0.35	1.5	$0.80^{+0.05}_{-0.05}$	$1.16^{+0.03}_{-0.03}$	$0.68^{+0.01}_{-0.01}$	0.0	$0.83^{+0.01}_{-0.01}$	$0.90^{+0.03}_{-0.03}$	$1.28^{+0.01}_{-0.01}$	$2.05^{+0.02}_{-0.02}$	1.29
0305600501	$6.42^{+0.03}_{-0.04}$	53^{+31}_{-29}	6.39	$0.87^{+0.25}_{-0.23}$	0.35	1.5	$2.38^{+0.07}_{-0.07}$	$1.16^{+0.03}_{-0.03}$	$0.68^{+0.01}_{-0.01}$	$1.05^{+0.05}_{-0.05}$	$0.83^{+0.01}_{-0.01}$	$2.38^{+0.06}_{-0.06}$	$1.28^{+0.01}_{-0.01}$	$2.64^{+0.03}_{-0.03}$	1.66
						χ^2=3116 / 2980 DOF						χ^2=3046 / 2978 DOF			

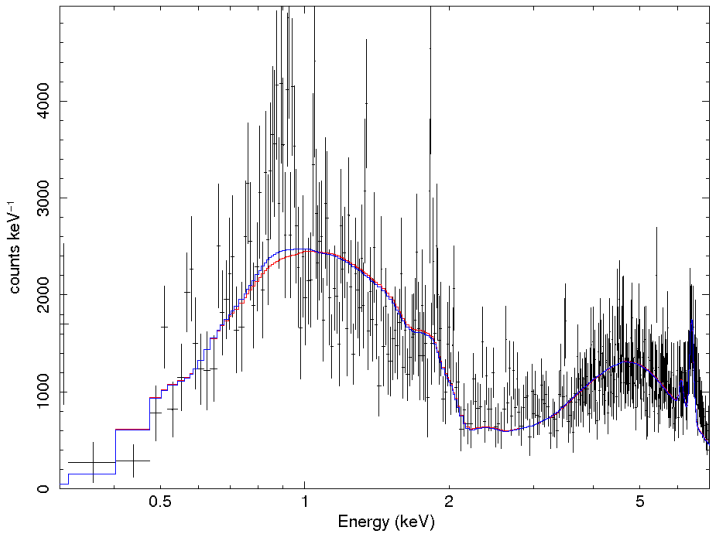

Figure 3.5: *Chandra* AGN spectrum with the best fitting parameters for Model 1 (see Table 3.2 for details). The model in red does not take into account the thermal emission from the radio bubbles; the model in blue does, and fits the data better around 1 keV. The addition of the thermal component increases the model predicted flux by 12% in the 0.7-1.1 keV range.

Although the *Chandra* data have the spatial resolution required to differentiate the AGN contribution from the extended thermal emission of the radio bubbles, we used the same extraction regions on all our spectra (see Figure 3.1), so as to be able to make a direct comparison between them. We decided to take into account the contribution of the thermal emission from the bubbles in our spectra by adding the *apec* XSPEC component to our model. We will discuss the details and implications of this extended emission in Section 3.3.2; an overview of its effect on our AGN spectrum can be seen in Figure 3.5.

We individually fitted all the spectra, for each instrument of the *XMM* and *Chandra*, and then tied together the parameters for the *XMM* spectra belonging to the same observation, to assess the number of variable parameters: we assumed that the normalizations do not vary within the same observation between the MOS and PN instruments, and tied together the values for the three instruments, with no significant impact on the final statistical result. We finally attempted a full joint fit with four groups of data, one for *Chandra* and one for each *XMM* observation. When setting the variable parameters for the joint fit, we also decided that the photon indices for the second power law

should be tied across the datasets, to break possible degeneracies with the local absorption columns, and froze the first photon index to a reasonable value (1.5) to minimise the overlap degeneracy between both power laws. This allowed us to make the joint (*Chandra* + *XMM*) fitting considerably faster. See Figures 3.5 and 3.6 for an overview of the *Chandra* and *XMM* spectra and Table 3.2 for details on the fit parameters for this model (Model 1).

The initial fit to the data resulted in χ^2=3331 for 3149 degrees of freedom (reduced χ^2=1.058). After correcting for the pileup effects, with the methods described in Section 3.3.1, we obtained χ^2=3125 for 2980 degrees of freedom (reduced χ^2=1.049). After adding the contribution from the radio bubbles, with the parameters frozen to their best fit values, we obtained χ^2=3116 for 2980 degrees of freedom (reduced χ^2=1.046). Since the corrections mainly affect the *Chandra* spectrum their contribution to the global result is quite small, but not negligible.

As shown in Table 3.2, we obtained a combined value for the index of the second power law of $1.16^{+0.03}_{-0.03}$, which is quite flat. This is partly caused by the difficulty of disentangling the index of the power law from the heavy absorption in the *Chandra* spectrum, as mentioned above. We found and fitted the Fe Kα emission line, setting σ=0 to simplify the fit. The best fitting energies and equivalent widths for the emission line are shown in Table 3.2. The line energy is consistent for all the datasets, although the intensity of the line does change with the AGN state and the local absorption column, as expected. The errors on the equivalent widths are quite big, which may be a sign of the line having some breadth, as suggested by Feldmeier et al. (1999), or be a side effect of the complicated model.

To compare our results with the previous *ASCA* and *XMM* results, and verify our hypothesis of variable absorption, we tested a few other models. We found that a single power law, with local absorption, or local + intrinsic absorption, results in values similar to those obtained by Immler et al. (2003), although it gives a very poor fit to the 2003 *XMM* spectra and does not fit at all the *Chandra* data (reduced χ^2 ~6). This is most likely caused by the varying absorption column, which cannot be properly accounted for with such a simple model.

We found that the only model that could allow a direct comparison with all of the previous results was one consisting of local absorption, a double partial covering (*zpcfabs*), a power law and a Gaussian to account for the Fe emission line. We tied together

the covering fractions across the different spectra, allowing only the N_H to vary. We did not add any reflection components to this model, since they are not considered in the *ASCA* analysis by Feldmeier et al. (1999), but we did add the contribution due to the thermal emission from the radio bubbles. The results of this fit are shown in Table 3.2 under the label "Model 2". We find that this model gives χ^2=3046 for 2978 degrees of freedom, reduced χ^2=1.023. We found that the photon index of the power law in our fit is lower than the one obtained in previous analysis of Mrk 6, only similar to the value obtained by Schurch et al. (2006) with their third model. This is partly due to the addition of the thermal emission component, which we deem necessary since it has been spatially resolved and fitted to the *Chandra* data and results in a statistical improvement in our other model. It is also partly caused by the effect of the variable absorption. We find the values of the Fe Kα emission line energy and equivalent width to be consistent with the ones we obtained for the previous model. We found that it is necessary for the two partial covering components to overlap ($f^1_{cov} + f^2_{cov} > 1$) for the fit to be statistically acceptable. We tried to fix the values to the ones employed by Schurch et al. (2006) in their analysis, but this results in a reduced χ^2 ~1.7.

While Immler et al. (2003) cite a value for this photon index of 1.81 from their analysis of the *Beppo-SAX* data, which is less affected by variable absorption, they mention in their analysis that the source was in a higher state when those data were obtained. Another *Beppo-SAX* observation analysed by Malizia et al. (2003) gives a photon index ~1.5. Schurch et al. (2006); Feldmeier et al. (1999) also favour a higher value for the photon index (1.6-2.2), but setting the photon index to 1.6 results in a reduced χ^2 ~1.13 in our joint fit, and the fit requires a heavier absorbing column for the second partial covering ($N_H = 66.61^{+4.92}_{-4.74} \times 10^{22}$ cm^{-2} for the *Chandra* spectrum).

As shown in Table 3.2, the absorption column is over an order of magnitude larger in the *Chandra* data than in the *XMM*, for both models. This high value is more similar to the ones obtained by Feldmeier et al. (1999) in their analysis of the *ASCA* data. The hypothesis of "obscuring" clouds near the AGN was proposed by Immler et al. (2003), and Schurch et al. (2006) supported it after obtaining a relatively smaller absorption column in their analysis of the *XMM* data from 2003. This detection by *Chandra* rules out instrumental bias. Although more data are needed to make a statistical test, current evidence seems to point towards denser material having been observed in 1997 (*ASCA*) and 2009 (*Chandra*), with the passing clouds being least dense in 2003 and interme-

diate obscuration values in 2001 and 2005 *XMM-Newton*. This allows us to establish a variability timescale of 2-6 years, which translates to a distance to the central black hole of just a few pc. Since grating data would be very useful to get an additional insight on the structure and composition of this variable absorption, we briefly investigated the *XMM-Newton* RGS spectra from the three observations. Unfortunately, the signal to noise is rather bad, and no evident emission or absorption lines can be inferred from them, as already noted by Schurch et al. (2006) and Immler et al. (2003).

Although the statistical result is better for the second model, we must consider the physical implications of both models. This AGN seems to fall between the behaviour expected from a classical Seyfert and that of a radio galaxy, it is therefore interesting to explore the consequences of these results in the light of what we know about these classifications. As explained by Hardcastle et al. (2009), the soft excess characteristic of most Narrow-Line Radio Galaxies (NLRGs) can be explained by three classes of model:

- It is thermal or line emission, from the photoionized material close to the AGN or from the IGM of the host galaxy.
- It is non-thermal, power law emission from the central AGN, visible through the partial covering material.
- It is non-thermal, power law emission related to the jet.

The first model can most likely be discarded in this case, since neither the *Chandra* nor the *XMM* spectra show evidence for strong emission lines. The RGS spectra do show some residuals over a pure continuum model in the 0.5-1 keV region that could be a hint of oxygen emission lines (Schurch et al. 2006), but they are quite faint, and since the area is not spatially resolved, they could be due to the thermal emission from the radio lobes.

To test which of the two other models is most likely to apply in this case we calculated the X-ray luminosity of the unabsorbed power law from our first model, $L_{X,u} = 9.6 \times 10^{41}$ erg s^{-1}, and the νF_ν 5GHz luminosity at the base of the jet from our radio maps, $L_{5GHz} = 1.41 \times 10^{38}$ erg s^{-1}. On the plots by Hardcastle et al. (2009) this falls quite far from the behaviour expected for radio galaxies. We must therefore conclude that the jet-related soft emission must be quite low, and the dominant

contribution to the soft excess is most likely the emission from the central AGN.

Following the results of Evans et al. (2010) we also applied their model to our data, to check if it would fit a photon index for the power law more consistent with the values expected from other intermediate Seyferts. This model tests a different absorption component for the soft and hard power laws: *wabs(apec+zwabs*po+zwabs*zpcfabs(zgauss+po))*. We obtained a fit to the data similar to that of our previous partial covering model, χ^2=3037.22 for 2971 DOF, reduced χ^2=1.022, and a similar photon index for the second power law, 1.25.

We also tested a model with a multiphase medium. We found that a single warm absorber does not provide a good fit to the data, and hence split the intrinsic partial covering absorptions of our second model into a cold (*zpcfabs*) and a warm (*zxipcf*) component. This model seems to provide a better fit for the soft end of the spectra, and yields a χ^2=3000.98 for 2977 DOF, reduced χ^2=1.007. The absorbing columns are similar to those we found for the double cold partial covering, and the photon index of the power law is $1.41^{+0.04}_{-0.03}$, higher than with any other model we have tested. However, the ionization parameter (defined as $log(\Xi)$, where $\Xi = L/nr^2$) is not very well constrained, $log\Xi = -0.09^{+0.38}_{-0.47}$, since the model is limited by the resolution of our spectra. Warm absorbers have been observed in other Seyferts, albeit at higher ionization values (see e.g. Longinotti et al. 2009), but in our case the situation is less clear. The soft excess this model successfully accounts for can have several origins: the jet, warm-hot gas from other regions of the galaxy, or a higher normalization of the thermal emission from the lobes, since we decided to freeze the latter to the maximum value provided by the spatially resolved fit. Unfortunately the grating spectra are not sensitive enough to test either hypothesis, but future, longer exposures may hold the key to the complexity we are observing in Mrk 6.

3.3.2 Radio bubble-related emission

To extract the spectra of the extended radio bubbles we only used the *Chandra* data, since in the *XMM* images this area is completely dominated by the PSF of the central AGN. We used the contours from the radio images obtained by Kharb et al. (2006) to define our extraction regions around the 7-kpc radio bubbles, which can be seen in Figure 3.1. The photon statistics for the bubbles are not very good; we do not have

enough counts to fit to both bubbles separately and determine their temperatures independently, and even for the joint extraction the photon count is quite low (~200 counts after background subtraction, see Figure 3.7). Even though we were careful to keep these regions well away from the central AGN, there is still some contamination from its PSF in our spectra. The data we simulated with ChaRT and MARX to correct the effects of pileup in the AGN spectrum (see Section 3.3.1) show the number and energy distribution of photons from the AGN PSF across all the CCD, see Figure 3.3, and can thus be used to estimate the AGN photon contribution to our spectra from these external regions. Our calculations show that this contamination amounts to up to 60% of the counts in the spectra prior to background subtraction. However, the background regions that we have chosen contain a similar number and energy distribution of photons from the AGN, its PSF being quite homogeneous on these scales, and their effect is hence mostly eliminated. We carried out a study of the AGN contamination in our regions by studying the energy distribution of the AGN counts in our simulated data, within the same extraction regions. We found most of the counts to be contributing at energies above 4 keV. There is a minor contribution at energies slightly above 1 keV. The residuals we get from our fit at these energy ranges are likely to have an origin in this contamination (see Figure 3.7).

We have found a source of contamination from high energy photons in the form of a small bright region ($L_X \sim 1.5 \times 10^{39}$ erg s^{-1}) that can be seen on the left panels of both Figure 3.1 and Figure 3.3 just South of the source (labeled as "A" in the left panel of figure 3.1). We plotted a histogram of the counts from this region, and by their distribution, and the fact that it has no radio or optical counterpart, we infer this is clearly a point source, most likely a background, more distant quasar. It is quite unlikely that this object may be an X-ray binary (XRB), but it could be an ultra-luminous X/ray source (ULX), since its magnitude should be above our detectability threshold for this distance ($L_{ULX} \sim 10^{39} - 10^{41}$ erg s^{-1}) although the morphology of the host galaxy indicates that this is not very likely (Swartz et al. 2004).

The other bright structure North of Mrk 6, labeled as "B" in the left panel of Figure 3.1, does seem to have a thermal origin, and a similar energy histogram to the photons we find in the bubbles; part of it is clearly surrounding the radio structure, and we therefore assume that it is part of the hot shell outside the radio bubbles and include it in our extraction regions. It must be noted, however, that Mrk 6 has an inner set

of ~1.5 kpc radio bubbles, almost perpendicular to the outer ~7.5 kpc structure (see Kharb et al. 2006), and this is likely to cause some turmoil in the gas surrounding the AGN. These inner bubbles are not resolved by *Chandra*. The jet of Mrk 6 was detected by *MERLIN* (Kukula et al. 1996) and is aligned in the North-South direction, so that this is the presumed photoionizing axis of the AGN.

This direction also corresponds to the Extended Narrow-Line Region (ENLR) of Mrk 6, see Figure 3.2 and Capetti et al. (1995); Kukula et al. (1996); Kharb et al. (2006) for details. An overlap between [OIII] and X-ray emission has been observed in many Seyfert 2 AGNs before, and it is believed to happen when the X-ray photons heat up and ionize the cold gas around the AGN. The [OIII] emission in this system seems to correspond to different structures: the emission closer to the active nucleus is clearly caused by direct photoionization from the AGN, while the two bulges that extend in the N-S direction, showing both enhanced [OIII] and X-ray emission, are most likely caused by the interaction of the current jet with the surrounding material, which heats it up both through shocks and photoionization (see Capetti et al. 1995 and Kukula et al. 1996 for details on these inner structures). Since the overlap between the [OIII] and X-ray emission can also be observed at kpc distances, extending to the North of the AGN, we calculated whether the nucleus could be photoionizing these regions to X-ray and [OIII] emitting temperatures, following the steps of Wang et al. (2009) and the models from Kallman & McCray (1982). For the X-ray emission that can be seen ~3 kpc North of the AGN, around the edge of the radio structure, we used the parameters derived from our fits of the nuclear spectrum and the radio lobes. We found that such X-ray emission cannot be caused by photoionization from the AGN, since the unabsorbed luminosity of Mrk 6 ($\sim 1.3 \times 10^{43}$ erg s^{-1}) can only account for photoionized X-ray emission at distances within 300 pc of the central source. The [OIII], however, could be photoionized by the AGN at much larger distances, as long as the electron density stays low ($< 10^{-1}$ cm^{-3} for distances over 3 kpc). It is likely that some of the [OIII] emission to the North of the source may have been caused by the shock itself, both via direct heating and photoionization. The fact that the [OIII] emission follows the outline of the radio structure, but is mostly detached from it, also supports this scenario.

With our photon statistics we cannot rule out a model in which this emission is produced in some way by a precessing jet, which would also explain some of the

emission in the ENLR. Both assumptions could explain the structures that surround the real, but not the simulated AGN, on Figure 3.3. For details on the radio structure of Mrk 6 and the discussion of a possible jet precession scenario see Kharb et al. (2006).

We fitted to our data an emission spectrum from collisionally-ionized diffuse gas (*apec* model in XSPEC) with the abundance fixed at 0.35$\odot$ and Galactic absorption, using again the averaged column density result $N_H = 6.39 \times 10^{20}$atoms cm^{-2} from Dickey & Lockman (1990a). We estimated a temperature for the bubbles of $0.94^{+0.12}_{-0.19}$ keV. This model yields a χ^2 value of 9.39 for 8 PHA bins and 6 degrees of freedom. Different extraction regions yield slightly lower values of kT, but still well within the errors, and different values of χ^2, due to the reduced number of bins. We also tested a larger abundance of 0.6$\odot$ consistent with our estimations on the thermal emission of Cen A (Kraft et al. 2003), but this requires a lower normalization and yields a poorer fit to the data (χ^2 of 11.42 for 8 PHA bins and 6 DOF).

The normalization of this component is $8.5^{+1.8}_{-1.8} \times 10^{-6}$cm^{-5}, just high enough to be noticeable on the spectra we extracted for the AGN (~2% of the flux between 0.8-1.1 keV). We added an *apec* component to our AGN model and performed a statistical test on the temperature, finding it to agree with the results from the spatially constrained spectrum ($kT = 0.87^{+0.25}_{-0.23}$ keV). This addition also improves the statistics of the joint fit, if only slightly (reduced χ^2 reduced from 1.051 to 1.049). The effects of adding this component to the *Chandra* spectrum can be seen on Figure 3.5.

To discard the possibility of the emission being non-thermal synchrotron or inverse Compton, we attempted to fit a model consisting of a power law and local absorption to the data, and obtained very poor results (reduced χ^2 of 3.79). Therefore we can quite safely assume the emission to be thermal.

Although the abundance that best describes the thermal emission from the bubbles is 0.35$\odot$, more consistent with NGC 3801 (0.3-0.4$\odot$) than with Cen A (0.6$\odot$), the statistical difference alone is not enough to rule out a higher value for the abundance, due to the low number of photon counts. We could argue that we are studying a quite small early-type S0 galaxy which probably has, as our results show, a very low gas density outside the central regions. The dust lane that is hinted at in the optical images may be a result of a past merger; there is an equivalent structure in NGC 3801. Furthermore, we must consider the influence of the active nucleus on the star formation history of Mrk 6. While it has been argued for more powerful systems that the AGN activity

may indeed be suppressing star formation in the host galaxy (see e.g. McNamara & Nulsen 2007, Schawinski et al. 2009, Nesvadba et al. 2010) the situation may be more complex for lower power systems, and early type galaxies in particular, as suggested by Schawinski (2010). While these arguments might be enough to support the low abundance we are observing, our tightest constraint comes from imposing the shock conditions for the bubbles. The details of these constraints and their consequences will be discussed in Section 3.3.4.

Even though the data show a significant correspondence between the radio contours and the X-ray emission inside the North bubble (see Figure 3.1), which could be associated with jet/ISM interactions leading to the heating of gas in these regions, as in NGC 6764 (Croston et al. 2008a, Kharb et al. 2010), most of the X-ray photons seem to correspond to the edges of the bubbles or even the regions just outside them, which is more compatible with the presence of shells of strongly shocked gas outside the bubbles, just as in NGC 3801 (Croston et al. 2007). While some structure can be seen both in the radio maps and in the X-ray image, we will assume in a first approach that the shells are spherical and uniformly filled with gas, and will later discuss the implications of a non uniform density.

The fact that the radio emission is apparently fainter in the South bubble (see Figure 3.1), and the small difference in the apparent sizes of the bubbles, the North one being slightly bigger (see the discussion of the size of the shocked shells in Section 3.3.4), is probably due to a different past history for both bubbles, due to the gas expanding in each direction having encountered a surrounding medium with a different density, or to an asymmetric energy output from the AGN. The radio images show there is also a similar asymmetry in the inner E-W bubbles (Kharb et al. 2006) and the N-S current jet (Kukula et al. 1996). The [OIII] emission is also asymmetric (see Figure 3.2). These asymmetries are not visible in the optical (*HST*) images of the host galaxy, the apparent dust lane being roughly perpendicular to the outer radio bubbles, but if the jet is indeed precessing, it could have created a somewhat cluttered environment around the AGN. A precessing jet is not likely to explain an asymmetry in the energy fed by the AGN to each bubble, but we cannot rule this out. Doppler boosting has been suggested for some Seyfert jets such as the one in Mrk 231 (Reynolds et al. 2009), but it is unlikely to be the cause of the asymmetry of the lobes in Mrk 6, since it would require relativistic speeds for the gas in the shells, which is inconsistent with our results

(see Section 3.3.4). This asymmetry only underlines how challenging it is to make a self-consistent model for this kind of object. We will assume that these effects are minor for our purposes.

3.3.3 Luminosity constraints on the external environment

To establish whether the gas from the bubbles is driving a shock into its surroundings we need to estimate the temperature of the external medium, derive the relative pressures and impose the Rankine-Hugoniot conditions for pressure balance (Landau & Lifshitz 1987). However, we have found that due to the galaxy's morphology and size, the halo regions where the gas is expanding are not bright enough in the X-rays to allow us to obtain a spectrum. While the *Chandra* spectrum appears to admit an additional thermal component with kT ~0.35 keV, there is no statistical improvement on the *XMM* spectra from adding it; we therefore cannot state that the component is real.

To obtain an upper limit on the luminosity and normalization of the gas component in these halo regions, we calculated the background-subtracted counts from a wide annular shell centred in the AGN (R_{int}=21 arcsec, R_{ext}=59 arcsec, excluding a few point sources resolved by *Chandra*). We calculated the relative contribution of counts from the AGN using the simulated dataset, applying a scaling factor obtained from the ratio of counts within the innermost regions of the PSF (excluding the pixels we used for pileup correction) in the real and simulated data, which takes into account possible energy-dependent variations. We then subtracted the AGN contribution from the total number of counts in the halo, and added the 3σ error, obtaining an upper limit of 270 counts, equivalent to a rate of 3.65×10^{-3} counts s^{-1}.

Using these statistical constraints on the number of photons from the halo, we can derive upper limits on the luminosity of this region. These upper limits also constrain the possible temperature, electron density and pressure for the gas, allowing us to test the shock conditions. To achieve this, we chose a range of possible temperatures for the medium outside the radio bubbles (0.1-0.6 keV) and used XSPEC with a toy *apec* model to determine the limit on the normalization corresponding to our count rate for each of our chosen temperatures. We maintained the N_H and redshift parameters fixed to the appropriate values for the system (see previous sections), and the abun-

dance fixed at 0.35⊙; we will discuss the implications of larger abundances in the next Section. We then derived from the flux in these models the range of possible X-ray bolometric luminosities (see Table 3.3).

We then estimated the B band luminosity of Mrk 6 from the data in the catalogue by de Vaucouleurs et al. (1995), obtaining a value of $1.15\times10^{10}L_{B}\odot$. Since Mrk 6 contains an AGN, it is likely that we are observing a blue excess, therefore this value is to be considered an upper limit. We used as a reference the work of O'Sullivan et al. (2001) to estimate the feasibility of our results on the X-ray luminosity. Their work catalogues the X-ray extended emission detected by *ROSAT* on several hundred early-type galaxies, and attempts to establish a relationship between the X-ray and B band bolometric luminosities for these systems. We overplotted our results on their diagram[1] (see Figure 3.8) to see whether Mrk 6 falls near or above their correlation. They excluded AGNs on their fit, and are thus only measuring the extended emission from the galaxy, which is what we are looking for in the outer regions of Mrk 6. Our results cover a wide range of possible X-ray luminosities, but especially for the lower temperatures, and considering that our estimate for the B luminosity is an upper limit, the data do fall in the right region of the plot. We can therefore assume that, although we are not directly resolving it in our *Chandra* image, our upper limit of counts is consistent with the luminosity expected for the galaxy, excluding the AGN. This means these photons indeed come from the extended X-ray emission of the galaxy, not from the background or the AGN.

We also tested the K-band luminosity of Mrk 6 ($1.17\times10^{11}L_{\odot}$) against its X-ray luminosity using the relations proposed by Mulchaey & Jeltema (2010), to avoid the effects of blue excess from the AGN. We found the results to agree with our estimations from the B band. Our results also agree with Mulchaey & Jeltema (2010) on the hot gas content of a sample of early-type galaxies in different environments. Their work shows that although some of these objects seem to retain their hot gas halos when living in clusters, others lose it, while for isolated galaxies the hot gas content is mostly related to the mass of the galaxy. Mrk 6 is quite small and seems to be living in a poor environment; it is therefore likely to have lost most of its halo gas.

Finally, it must be noted that in the ChaRT/MARX simulations the wings of the PSF are known to be underestimated at large distances from the point source, espe-

[1] We obtained the data from http://www.sr.bham.ac.uk/~ejos/catalogue.html

cially at low energies. We contacted the *Chandra* Calibration team via the HelpDesk[1] and consulted the available bibliography[2], and estimated that, for the regions we are considering in the halo of Mrk 6, the simulated PSF wings could be underestimated by up to a factor of 2. If this were the case, our upper limit of counts would be more conservative (~30% lower) and we would be near the limit of non detection, implying an external gas temperature below 0.1 keV (see discussion in the next Section). If the gas were much colder than 0.1 keV we would not be able to constrain any limits on the density or assume a shock scenario. This would not be very consistent with what we know about the virial temperatures of the halo gas in early type galaxies (see e.g. Naab et al., 2007), but since we do not have the instruments to measure the extreme UV emission a gas of these characteristics would produce, it cannot be ruled out. We must also note that the X-ray emission cannot be accounted for by photoionization mechanisms (see discussion on the [OIII] emission in the previous Section). We conclude that the shock scenario provides the most plausible explanation for the emission we are observing.

3.3.4 Physical properties of the gas shells and ISM

Table 3.3: Estimated *apec* normalization, upper luminosity limits, electron densities and gas pressure outside the bubbles for a sample of possible gas temperatures.

kT keV	*apec* norm $\times 10^{-5}$cm^{-5}	L_X $\times 10^{40}$erg s^{-1}	$n_{e,out}$ $\times 10^{-4} cm^{-3}$	P_{out} $\times 10^{-13}$Pa
0.1	49.00	3.07	40.60	1.20
0.2	6.10	1.87	14.30	0.85
0.3	3.50	1.27	10.90	0.96
0.4	2.50	1.16	9.18	1.09
0.5	2.00	1.12	8.21	1.22
0.6	1.75	1.11	7.68	1.36

[1] http://cxc.harvard.edu/helpdesk/
[2] See http://cxc.harvard.edu/cal/Hrma/hrma/psf/index.html

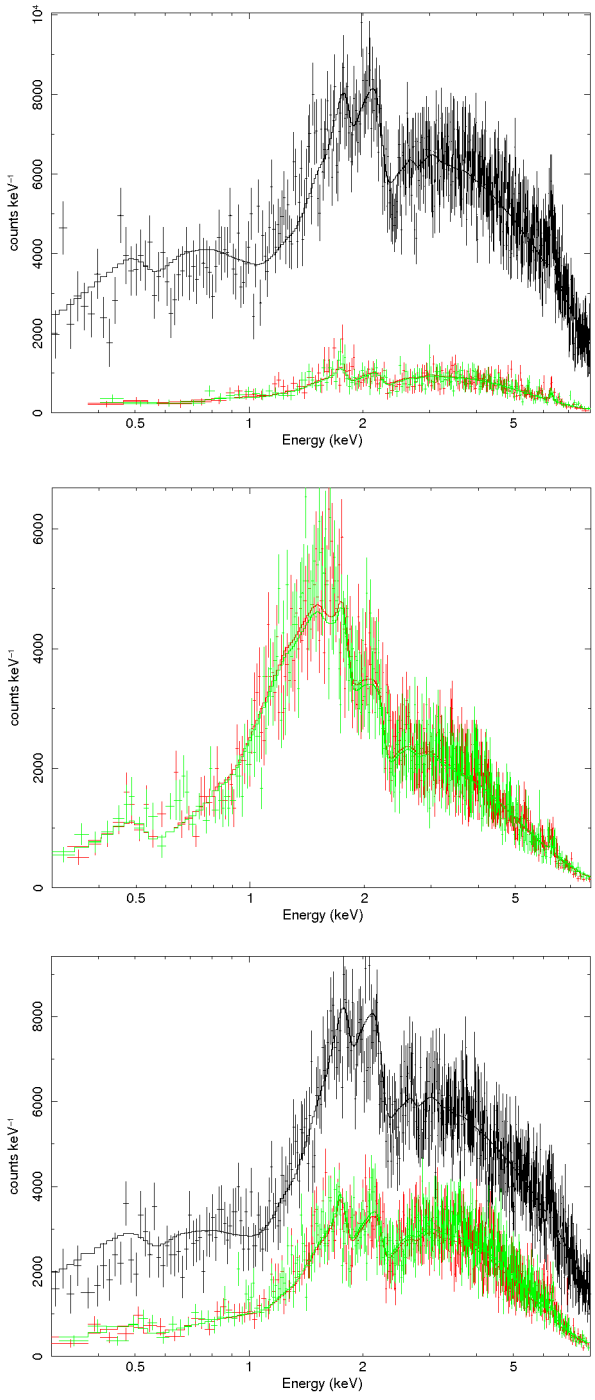

Figure 3.6: *XMM* AGN spectra with the best fitting parameters for Model 1 (two power laws + intrinsic absorption + thermal emission from the bubbles, see Table 3.2 for details). From top to bottom, obsids 0061540101, 0144230101, 0305600501, with the PN spectrum in black, MOS1 in red and MOS2 in green.

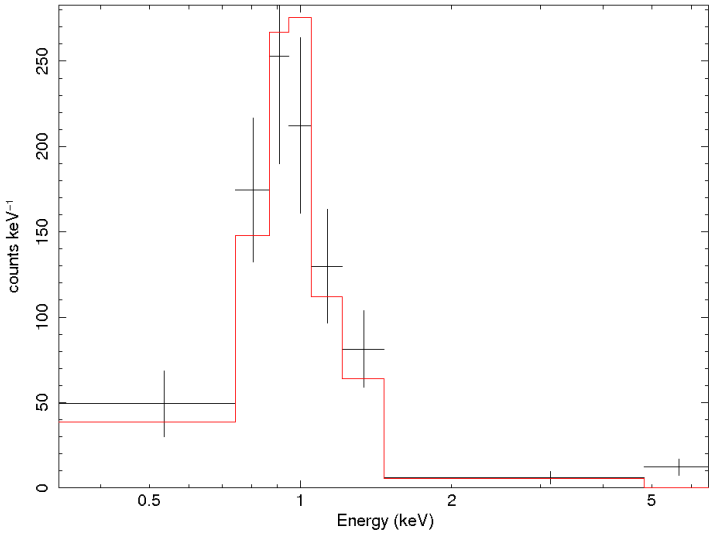

Figure 3.7: Spectral fit to the spatially constrained radio bubble regions, with the best fitting *apec* (T=$0.94^{+0.12}_{-0.19}$ keV, abundance=0.35$\odot$, χ^2=9.39 for 8 PHA bins and 6 DOF).

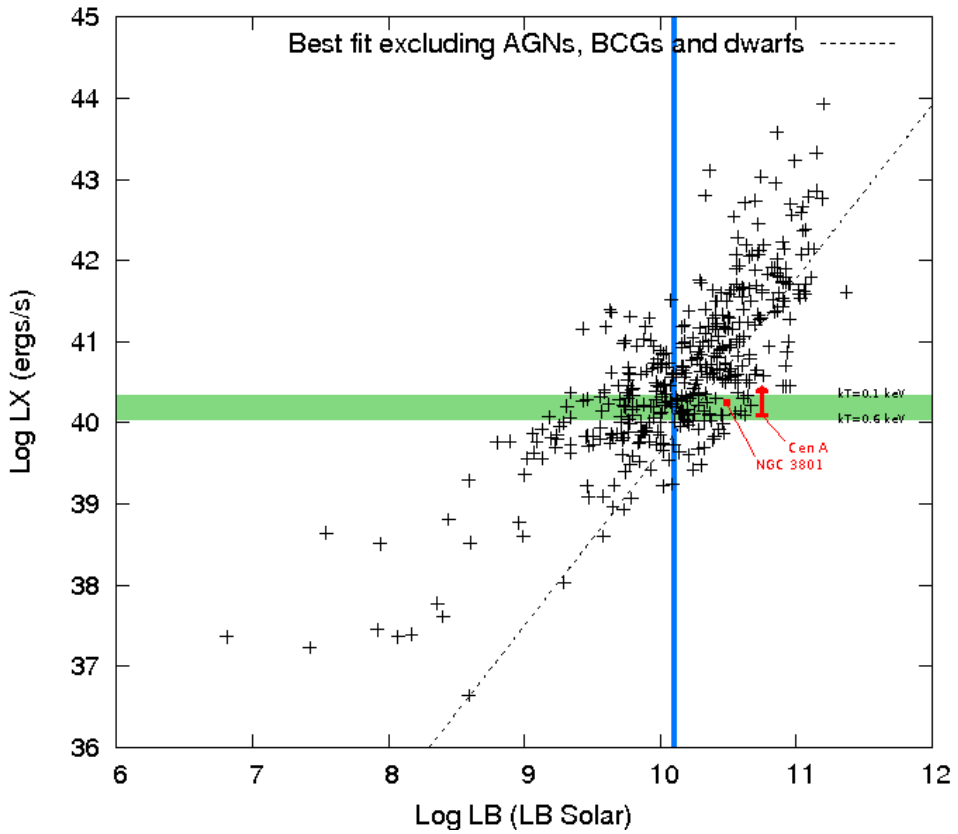

Figure 3.8: L_X vs. L_B plot from O'Sullivan et al. (2001) with superimposed Mrk 6 B band bolometric luminosity (vertical blue line) and the expected (upper limit) X-ray luminosity range we calculated for the extended thermal emission outside the shells (horizontal green strip). The diagonal dashed line is the best fit to the data excluding AGNs, BCGs and dwarf galaxies (i.e. quiescent early-type systems). The AGN is most likely causing a blue excess in the optical, so the B-band luminosity is an upper limit. Given that the temperature of the external medium is most consistent with 0.1-0.2 keV, an X-ray excess caused by this emission is likely to be happening.

Table 3.4: **Top:** Model normalization, estimated n_e upper and lower limits for the shells, derived limits for $n_{e,out}$ required to comply with the Rankine-Hugoniot conditions for a strong shock, and inferred limits on the mass, pressure, total thermal energy, work available from the gas filling the shells and total kinetic energy. **Bottom:** Same estimations for a set of Cen A-like 200 pc-wide shells (Croston et al. 2009). The errors on the pressures and energies are derived from the errors in the temperatures of the shells in the XSPEC fit ($kT = 0.94^{+0.12}_{-0.19}$ keV)

Model norm	$n_{e,N\,shell}$	$n_{e,S\,shell}$	N/S Limit to $n_{e,out}$	$M_{N\,shell}$	$M_{S\,shell}$	$P_{N\,shell}$	$P_{S\,shell}$	$E_{N\,shell}$	$E_{S\,shell}$	$W_{N\,shell}$	$W_{S\,shell}$	$K_{N\,shell}$	$K_{S\,shell}$
$\times10^{-6}$cm^{-5}	$\times10^{-2}$cm^{-3}	$\times10^{-2}$cm^{-3}	$\times10^{-3}$cm^{-3}	$\times10^{7}M\odot$	$\times10^{7}M\odot$	$\times10^{-12}$Pa	$\times10^{-12}$Pa	$\times10^{56}$erg	$\times10^{56}$erg	$\times10^{55}$erg	$\times10^{55}$erg	$\times10^{55}$erg	$\times10^{55}$erg
6.71	1.44	1.76	3.59/4.40	2.79	2.28	$4.01^{+0.48}_{-0.82}$	$4.91^{+0.59}_{-1.01}$	$1.64^{+0.19}_{-0.34}$	$1.34^{+0.16}_{-0.28}$	$10.90^{+1.30}_{-2.23}$	$8.92^{+1.06}_{-1.84}$	$1.84^{+0.26}_{-0.37}$	$1.50^{+0.21}_{-0.30}$
10.33	1.78	2.18	4.46/5.46	3.46	2.82	$4.98^{+0.59}_{-1.02}$	$6.10^{+0.72}_{-1.26}$	$2.03^{+0.24}_{-0.42}$	$1.66^{+0.20}_{-0.34}$	$13.50^{+1.70}_{-2.70}$	$11.10^{+1.30}_{-2.31}$	$2.28^{+0.32}_{-0.46}$	$1.86^{+0.26}_{-0.37}$
6.71	2.80	3.43	6.99/8.56	1.43	1.17	$7.81^{+0.93}_{-1.60}$	$9.57^{+1.14}_{-1.97}$	$0.84^{+0.10}_{-0.17}$	$0.69^{+0.08}_{-0.14}$	$5.61^{+0.67}_{-1.15}$	$4.58^{+0.54}_{-0.94}$	$0.94^{+0.14}_{-0.19}$	$0.77^{+0.11}_{-0.15}$
10.33	3.47	4.25	8.67/10.63	1.78	1.45	$9.69^{+1.16}_{-1.99}$	$11.87^{+1.42}_{-2.44}$	$1.04^{+0.13}_{-0.21}$	$0.85^{+0.10}_{-0.18}$	$6.96^{+0.83}_{-1.43}$	$5.68^{+0.68}_{-1.17}$	$1.17^{+0.17}_{-0.24}$	$0.96^{+0.13}_{-0.20}$

Using the results from the previous section we can now calculate the upper limits on the electron densities, n_e, for each temperature, from the definition of the model's normalization:

$$\frac{10^{-14}}{4\pi[D_A(1+z)]^2}\int n_e N_H dV \tag{3.1}$$

where D_A is the angular diameter distance to the source. We assumed the volume to be the one mentioned in the previous subsection, a wide spherical shell centred on the AGN and beginning just outside the edge-brightened emission around the radio bubbles. The results are displayed in Table 3.3. Notice how the derived $n_{e,out}$ increases sharply below temperatures of 0.3 keV. This is caused by the loss of sensitivity of the instrument at low energies, and a change in the behaviour and type of emission lines found at these temperatures. We can derive from these values the pressure of the gas, also displayed in Table 3.3. The pressures are consistent with the environment of Mrk 6 being quite cold and rarefied. Notice the increase of the pressure for very low temperatures: this is a consequence of the steep increase in the electron density estimations. Our choice of the ~60 arcsec region is based on the most likely dimensions of the halo; in order to test these constraints we selected a larger region (R_{ext}=75 arcsec) and found that the densities and pressures change by 15% at most.

We also estimated the limits on the electron densities for the shells, to compare them with these upper limits we obtained for the surrounding gas. This is necessary to verify that the proposed shock scenario holds, and see whether any limits on the external temperature can be derived. To do this we assumed that the dominant thermal contribution to the spectral fit we obtained for the radio bubbles (Section 3.3.2) originates in the edge-brightened, shell-like emission around them. Our extraction region covers the whole surface of the bubbles to include any photons from the nearest and farthest areas of the spherical shells, which have a lower surface brightness due to projection effects. The gas inside the bubbles is radio emitting plasma, and therefore does not contribute to our spectrum, and any emission from gas immediately outside the shells is accounted for by the background.

Using the constraints on the temperature and model normalization from our bubble fit, we then estimated the North and South shell thickness from the apparent thickness of the edge-brightened emission around the radio bubbles, which in Mrk 6 is quite evident, see Figure 3.1. Since the spectral resolution is not enough to allow us to

discern the detailed structure of the shells, we assumed a simple spherical geometry for each structure. From the extent of the emission we estimated for the North shell a width of ~980 pc ($R_{int,N}$ = 2.24 kpc, $R_{ext,N}$ = 3.22 kpc), and for the South shell ~1100 pc ($R_{int,S}$ = 1.55 kpc, $R_{ext,S}$ = 2.65 kpc). Estimating the thickness of the shells is difficult due to the poor photon statistics, hence these values were taken as a conservative upper limit. They are larger than what we expected a priori, but this may partly be due to the apparent lower density of the external environment in Mrk 6, as well as to the limited resolution we can achieve with our photon statistics. The results we obtained are shown in Table 3.4. This table also shows what the limits on the n_e would be, both for the shells and the external environment, assuming a thickness of ~200 pc, similar to the one estimated for Cen A.

From these values we can derive the total mass of the gas contained in each structure and the resulting pressure. These results are also displayed in Table 3.4. When comparing these results with NGC 3801 (Croston et al. 2007), we find that even though the electron density is lower in Mrk 6, the apparent thickness of the shells is much bigger, hence the total mass of the gas is higher by slightly less than one order of magnitude. The inferred pressures for the gas are roughly the same as the ones found on NGC 3801, due to the temperature of the gas being higher in Mrk 6. The errors on the pressure are calculated from the uncertainty in the gas temperature, $0.94^{+0.12}_{-0.19}$ keV. We can see that choosing thinner shells, like the ones found on Cen A, would imply a much smaller (~0.5) fraction of gas, while the pressure would almost double (see lower section of Table 3.4). The pressure jump P_{shell}/P_{out} for a 1 kpc shell is ~7-63, higher than in NGC 3801, but again this is to be expected, due to the bigger temperature contrast and more rarefied external environment in Mrk 6. The contrast would be much higher for thinner ~200 pc shells, ~14-122.

We calculated the minimum internal pressure of the Northern bubble under equipartition conditions from the radio data, fitting a broken power-law electron energy spectrum with $p = 2$ at low energies, steepening to $p = 3$ at the electron energy that gives the best fit to the data. We assume no protons and γ_{min}=10. We obtained a value of P~4×10^{-13} Pa, consistent with the results obtained by Kharb et al. (2006), and roughly an order of magnitude lower than the pressures we derive from our X-ray data. This departure from minimum energy is often found in FR I radio galaxies (e.g. Morganti et al. 1988), and although there are very few examples where the minimum internal

pressure is higher than the external pressure in the ISM, we also found this effect in NGC 3801 and Cen A. These results imply that there is some additional contribution to the internal pressure, caused by a large deviation from equipartition conditions, a high fraction of non-radiating particles, such as thermal or relativistic protons originated from the interaction of the galaxy's gas with the jet, or a low filling factor. Of these, the second explanation is the most plausible (see Hardcastle et al. 2007c; Croston et al. 2008a), even more so if the jet is indeed precessing, as suggested by Kharb et al. (2006), or if it is just episodic.

In the limit where there is no shock the pressures of the external medium, P_{out}, and the shells, P_{shell} should be equal (Landau & Lifshitz 1987). The difference in the apparent luminosities of both regions already rules out this situation if both temperatures are equal. We can also rule it out by noticing that these values of $n_{e,out}$ and P_{out} would imply external temperatures far below 0.1 keV (see the results from Tables 3.3 and 3.4) which is unlikely, as discussed in the previous Section. The density ratio ρ_{out}/ρ_{shell} tends to 4 in the case of a strong shock. For values of ρ_{out}/ρ_{shell} smaller than 4 the required values of the external temperature are below or just above 0.1 keV; the most plausible scenario is therefore that of a strong shock.

Assuming a density contrast of 4, and using again the limits on $n_{e,out}$ from Table 3.3, we can constrain the possible temperature for the external gas to be around 0.2 keV. This result is consistent for both the North and South shell values and for both the 1 kpc and 200 pc shell thicknesses (the 200 pc hypothesis would imply a higher gas density within the shells, thus to maintain the density contrast of 4 the upper cap on the external temperature would be lowered, but the results still imply $kT > 0.1$ keV). We were able to directly measure the temperature of the external medium in Cen A (Kraft et al. 2003), and found the temperature of the ISM to be ~0.29 keV. For NGC 3801 (Croston et al. 2007) we obtained a value of $0.23^{+0.21}_{-0.09}$ keV. These values directly applied to Mrk 6 would cause an inconsistency, since the density ratio cannot exceed a value of 4, but given the uncertainties they are still in very good agreement with the current results.

As an additional test we repeated our calculations for Z=0.6$\odot$ and Z=1.0$\odot$. The model normalizations, and consequently the electron densities, inversely depend on the abundance, so we found lower values as we approached the solar values. However, the impact of this effect is bigger on the results from the external gas than to that

contained in the shells. This causes an inconsistency when applying the conditions for a strong shock, since the external gas would be required to have temperatures far below 0.1 keV, which are implausible, as we discussed above. Higher abundances also have an impact on the energy yield. The pressure and total energy for Z=0.6⊙ would be ∼ 20% lower than the ones we calculated with Z=0.35⊙, and ∼ 40% lower for Z=1.0⊙.

To further test these results, we used the B-band luminosity of Mrk 6 to relate it to other galaxies following the relations from O'Sullivan et al. (2001, 2003). We found that both the temperature of the external gas (0.2 keV) and the abundance we fit to the data (0.35⊙) are consistent with their relations. Their sample includes two galaxies with gas X-ray and B-band luminosities slightly larger ($L_X \sim 10^{40}$ erg s^{-1}, $L_B \sim 10^{11} L_\odot$) than what we found for Mrk 6 where these parameters can be directly related. For NGC 1549 they find an outer gas temperature ∼0.25 keV and an abundance ∼0.14⊙. For NGC 4697 their results show T ∼0.24 keV and Z ∼0.4⊙. We therefore consider our best estimates of the properties of the large-scale hot gas in Mrk 6 to be plausible ones.

We can calculate the Mach number for the shock, as follows (Landau & Lifshitz 1987):

$$\mathcal{M} = \sqrt{\frac{4(\Gamma+1)(T_{shell}/T_{out}) + (\Gamma-1)}{2\Gamma}} \tag{3.2}$$

where Γ is the polytropic index of the gas, assumed to be 5/3. The results for our chosen temperature range are displayed in Table 3.5.

Table 3.5: Possible values of the Mach number given by our temperature constraints. The values of T_{shell} are the best fit value and the 1σlimits allowed by the errors. The most likely value is shown in bold.

	kT_{shell} (keV)		
kT_{out} (keV)	0.75	0.94	1.06
0.10	4.92	5.50	5.84
0.20	3.49	**3.90**	4.14
0.30	2.86	3.20	3.39
0.40	2.49	2.78	2.95
0.50	2.24	2.49	2.64
0.60	2.05	2.28	2.42

From the previous constraints we can assume the most likely value for the temperature to be $0.2^{+0.1}_{-0.1}$ keV. This yields a value for the Mach number of $3.90^{+1.94}_{-1.04}$, of the same order of magnitude as the one we obtained for NGC 3801 (Croston et al. 2007), although smaller than the one found for Cen A (Kraft et al. 2003). This is to be expected, since the morphology of Mrk 6 is more similar to the one of NGC 3801 than to that of Cen A, where only one shell is detected.

The speed of sound in the ISM ranges from ~190 km s^{-1} in the case where the external temperature is 0.1 keV to ~460 km s^{-1} when $kT = 0.6$ keV. Since the Mach number also varies with the temperature (see Table 3.5), we derived a consistent value of 1030^{+75}_{-110} km s^{-1} for the speed of the gas. This allows us to derive the kinetic energy of the gas, which is displayed in Table 3.4. The total thermal energy and total work available for each radio bubble are also displayed in Table 3.4.

The total energy (thermal + kinetic) from both radio bubbles, under the 1 kpc width assumption, is $\sim 2.6 - 4.6 \times 10^{56}$ erg. This corresponds to ~3.6×10^5 supernova explosions with individual explosive energy of 10^{51} erg. This result also agrees with the value derived by Kharb et al. (2006) from the radio data of Mrk 6, $\sim 1 \times 10^{55}$ erg, since it was a lower limit. They estimate a kinetic luminosity for the jet of $\sim 10^{42}$ erg s^{-1}, derived from an inferred radio luminosity of $\sim 10^{40}$ erg s^{-1} and an efficiency of 1%. With our results, the jet would require $\sim 1.1 \times 10^7$ years to deposit all its energy into the nuclear ISM and produce this pair of radio bubbles. This result is almost two orders of magnitude larger than the one they obtained, but not incongruent, since their estimation was a lower limit derived from the equipartition pressure. These results also agree with the timescales they propose in the context of a precessing jet. Another timescale can be inferred from the supersonic expansion speed of the bubbles, which would require a time of $\sim 2.5 - 3.1 \times 10^6$ years to inflate to their current size, assuming $M \sim 4$ throughout their lifetime. If we adopt this timescale, the required jet power is $\sim 7 \times 10^{42}$ erg s^{-1}.

The thermal energy stored in the shells is an order of magnitude larger than the kinetic energy required to inflate the cavities (see Table 3.4), meaning shock heating must be the dominant energy transfer mechanism during this stage of the evolution of the radio source. Although the emission from the surrounding gas is too weak for us to fit a model to its brightness profile, which would be ideal to determine the direct impact of this thermal energy into the surrounding ISM, our results, and comparison

with those obtained for Cen A and NGC 3801, show that this energy is enough to significantly alter the surrounding ISM, sweeping out the remaining halo gas.

With our current photon statistics we have no direct evidence of changes in the brightness (and therefore gas density) across the shells, therefore we cannot state whether these structures are brighter in the inner edge, closer to the nucleus, in Mrk 6. However, this would be expected if the bubble expansion is supersonic everywhere: even though the shock is weakest close to the nucleus, the ISM is much denser in this direction, hence the associated X-ray emission is higher.

If we assumed the density of the gas not to be constant across the shell, with a higher density in the area closer to the radio source, the derived constraints on the temperature of the external medium would be relaxed, allowing higher values. Consequently, the pressure and density of the external gas could also be higher. This situation would bring our results closer to the values we obtained for Cen A and NGC 3801. While this would be desirable for consistency, we must note the scenario in Mrk 6 is quite different, both due to its morphology and to its lower radio power, thus we could indeed be seeing a case of the AGN driving a strong shock into a very cold environment. It could also be the case that the shells are not continuous all around the radio bubbles, which would change the constraints on the density of the gas. This hypothesis could be tested with a longer exposure.

To conclude our analysis and study the fueling mechanism of the AGN, we used our estimates on the external gas temperature and density to calculate the Bondi accretion rate from the central hot gas. We used the relations from Marconi & Hunt (2003) and the K-band luminosity of Mrk 6 and obtained a mass for the black hole of $3.7{\times}10^8 M_\odot$. The Bondi rate is given by

$$\dot{M} = 4\pi\lambda\rho G^2 M_{BH}^2 c_S^{-3} \tag{3.3}$$

where λ=0.25, ρ is the density of the gas at the Bondi radius, and c_S is the speed of sound in the medium ($c_S = \sqrt{\Gamma kT/\mu m_p}$). Since the density and temperature at the Bondi radius cannot be lower than the ones we estimated for the gas outside the shells, we used those values to obtain a lower limit of $\dot{M} = 2.04 \times 10^{-5} \mathrm{M}_\odot\ \mathrm{yr}^{-1}$. Assuming μ=0.1 this translates to a Bondi power $P_B = 1.1 \times 10^{41}$ erg s^{-1}. The energy output we measured from the AGN bolometric luminosity ($\sim 2.4 \times 10^{44}$ erg s^{-1}, using a bolometric correction factor of 19) and the shocked gas shells ($\sim 7 \times 10^{42}$ erg s^{-1})

imply an accretion rate of $\dot{M} \sim 5.7 \times 10^{-2}$ $M_{\odot}$ yr^{-1}. This suggests that Bondi accretion is unlikely to provide all the energy we observed to be transferred to the ISM, even with an efficiency of 100 per cent. Assuming μ=0.1, the density would have to be over three orders of magnitude higher than our estimates of the density of the unshocked gas in order for Bondi accretion to be viable. If Bondi accretion cannot account for the energy we are observing, the main fuel source for this system is likely to be cold gas. Cold accretion does not depend on the black hole mass and can happen in poor environments as long as there is a fuel reservoir, which may be the case in Mrk 6 if the central obscuring material seen in the optical is indeed cold gas from a past merger.

3.4 Conclusions

We conclude that there is a high probability that we are observing shells of strongly shocked gas around both radio bubbles of Mrk 6, with Mach numbers 3.2-5.5 consistent with the Rankine-Hugoniot conditions for a strong shock. This is the third clear detection of such a process in a low-power radio source, and therefore reinforces the hypothesis that this mechanism may be very common and may play a fundamental role in the process by which these young radio sources form their stellar populations.

It is very likely that much of the gas in the shells will escape the gravitational potential of the host galaxy. Our results show shock heating is the dominant process, thermal energy being an order of magnitude larger than the work required to inflate the radio cavities, implying the outburst impact on the host galaxy's ISM is likely to be dramatic. Moreover, the inner set of bubbles is expanding perpendicularly to the external ones, and into denser regions of the host galaxy. Although the shock will probably be weaker, due to the increased density, the expansion of the inner bubbles is likely to cause a more direct disruption on the ISM and are likely to have a bigger impact on star formation. Unfortunately the resolution of the current generation of X-ray telescopes does not allow us to determine the details of this ejection of gas.

We also conclude that the hypothesis of a variable absorption gas column, with timescales of 2-6 years, caused by clumpiness of the accreting gas close to the black hole, is a likely explanation for the variations we see between the *Chandra* and *XMM* spectra. If this is indeed the case, and as already pointed out by Risaliti et al. (2002), this scenario could be more common than previously thought, and applicable also to

intermediate Seyfert systems, such as Mrk 6. Observations of more such sources may lead to better constraints on the geometry and composition of the gas distribution surrounding the AGN. Further observations at soft and hard energies, and detailed X-ray spectroscopy of this source would be of extremely useful for this purpose.

The variable obscuration also poses some questions about the mechanism fueling the AGN. Our analysis of the AGN core shows that the dominant contribution to the soft excess in this system comes from the AGN non-thermal emission, although there is some contribution from the jet, which could explain the flat power law spectra we are observing. Our results on the energetics of the source show that Bondi accretion might not be enough to power it, so that it is possible that cold gas accretion is the dominant mechanism in this system, unlike what is seen in many more powerful radio sources (Hardcastle et al. 2007a; Balmaverde et al. 2008). Cold gas has also been suggested as the primary source of fuel for Cen A and NGC 3801 (Croston et al. 2007). It is also possible that the active nucleus of Mrk 6 is accreting both the hot phase of the ISM and cold gas from a past merger. This is consistent with recent results on early-type galaxies by Pellegrini (2010).

While the precessing jet scenario is challenging, due to the high torque required to rotate the axis of the black hole nearly 180° within a time of $\sim 10^6$ years, required to create both perpendicular sets of bubbles, it cannot be ruled out. The dust lane hinted in the optical images could be a sign of a merger, which could have provided the necessary torque, and the evidence for obscuration variability near the black hole could be further evidence. It would be interesting to follow this hypothesis and find any correlations with other systems where a similar variation in absorption has been studied. However, this evidence can also be interpreted in terms of a cluttered and uneven environment, which can be inferred on bigger scales from the [OIII] emission distribution, causing the radio bubbles to expand asymmetrically and in different directions. Again, more evidence, both from future observations of Mrk 6 and from other sources, will be useful to achieve an accurate interpretation of the underlying physics behind the variable absorption and the asymmetries we have observed.

Chapter 4

The Circinus Galaxy

After the promising results found on Markarian 6 (Chapter 3), the Circinus Galaxy was an obvious choice to carry out a similar study, and see the impact of small-scale radio bubbles in an actively star forming system. For this purpose, I wrote and submitted a *Chandra* proposal in March 2010, requesting 120 kiloseconds of exposure time, to be added to the existing observation of this galaxy. The proposal was successful, and the following Sections describe the work carried out on the data thus obtained.

We analyse new *Chandra* observations of the nearest (D = 4 Mpc) Seyfert 2 active galaxy, Circinus, and match them to pre-existing radio, infrared and optical data to study the kpc-scale emission. The proximity of Circinus allows us to observe in striking detail the structure of the radio lobes, revealing for the first time edge-brightened emission both in X-rays and radio. After considering various other possible scenarios, we show that this extended emission in Circinus is most likely caused by a jet-driven outflow, which is driving shells of strongly shocked gas into the halo of the host galaxy. In this context, we estimate Mach numbers $\mathcal{M} \sim 2.7$–3.6 and $\mathcal{M} \sim 2.8$–5.3 for the W and E shells respectively. We derive temperatures of $0.74^{+0.06}_{-0.05}$ keV and $0.8 - 1.8$ keV for the W and E shells, and an expansion velocity of $\sim$ 900–950 km s^{-1}. We estimate that the total energy (thermal and kinetic) involved in creating both shells is $\sim 2 \times 10^{55}$ erg, and their age is $\sim 10^6$ years. Comparing these results with those we previously obtained for Centaurus A, NGC 3801 and Mrk 6, we show that these parameters scale approximately with the radio power of the parent AGN. The spatial coincidence between the X-ray and edge-brightened radio emission in Circinus resembles the morphology of some SNR shocks. This parallel has been expected for AGN, but has never been

observed before. We investigate what underlying mechanisms both types of systems may have in common, arguing that, in Circinus, the edge-brightening in the shells may be accounted for by a *B* field enhancement caused by shock compression, but do not preclude some local particle acceleration. These results can be extrapolated to other low-power systems, particularly those with late type hosts.

4.1 Introduction

Recent *Chandra* observations of the environments of several radio galaxies (e.g., NGC4636, Jones et al. 2002; Hydra A, McNamara et al. 2000; Centaurus A, Kraft et al. 2003) have led to significant progress in understanding the AGN-driven gas outflows in these systems and the role they play in galaxy formation and evolution (as required by models such as those of Croton et al. 2006; Bower et al. 2006). We now know that, although the most powerful radio outflows, spanning hundreds of kpc, are associated with massive elliptical systems, smaller structures also connected to an active nucleus can be found in a variety of systems and environments, including spiral and disky galaxies (e.g. Gallimore et al. 2006; Kharb et al. 2006; Saikia & Jamrozy 2009).

The mechanism by which these structures are produced appears to be similar to the one we see in the most powerful sources, but on a smaller scale: the relativistic plasma ejected by the AGN interacts with the surrounding medium, pushing it out in kpc-scale radio-bright lobes, and inducing shocks that heat the medium to X-ray emitting temperatures (see e.g. Heinz et al. 1998; McNamara & Nulsen 2007; Shabala & Alexander 2009). The temperature structure of these bubbles has been analysed in a variety of systems, the most famous being Centaurus A, where the bow shock has been studied in detail after highly detailed images of the South-West lobe were obtained with *Chandra* (see e.g. Kraft et al. 2003; Croston et al. 2009).

The varied morphologies of the galaxies where this mechanism is found, and the fact that it is most likely episodic (Saikia & Jamrozy 2009; Kharb et al. 2006) make understanding the energetics involved in this process fundamental to estimating its impact on galaxy evolution. The thermodynamics of the expanding gas provide details on the energy output from the AGN, the radiative timescales involved in this energy being transferred to the ISM, and the way in which the energy input scales with the mass of the host galaxy, its morphology and the power output of the AGN, which also

yields estimates of its lifetime. The injection rate, temperature and pressure of the gas determine star formation triggering and quenching in the central regions of the host galaxy.

Our previous results on systems such as Cen A (Croston et al. 2009), NGC 6764 (Croston et al. 2008b), NGC 3801 (Croston et al. 2007) and Markarian 6 (Mingo et al. 2011), show that gas outflows in these systems leave distinct signatures (thermal emission inside and in the rim of the lobes, synchrotron emission in very powerful shocks) whose physical properties indicate that the radio bubbles are overpressured with respect to their surroundings (as predicted by e.g. Capetti et al. 1999) and are, in several cases, driving shocks into them. For some of these galaxies (e.g. NGC 3801, Mrk 6) we have been able to calculate the (substantial) fraction of the AGN power that is being transferred to the ISM by this mechanism, setting the conditions for episodic AGN activity and star formation rates. Although the number of suitable sources for X-ray studies is limited, due to their small angular sizes, for nearby galaxies this technique is particularly fruitful, since with long exposures we can even resolve different regions in the shocks driven by the lobes, allowing us to distinguish between thermal and non-thermal (synchrotron) emission.

In this paper we investigate the low-power AGN in the Circinus galaxy. Circinus is a nearby ($D = 4$ Mpc) spiral galaxy, which exhibits a complex extended radio structure (Elmouttie et al. 1998a). While its nucleus and X-ray binary populations have been studied in some depth in the past (Smith et al. 2000; Smith & Wilson 2001; Sambruna et al. 2000, 2001a,b), the only preexisting X-ray observation where the extended emission was spatially resolved was too short to permit the study of the fainter emission. Our new, deep *Chandra* data allow us for the first time to study the X-ray counterparts of the larger-scale radio structures. Our main aim in the present paper is to test our new X-ray data, in conjunction with the existing radio observations, to test the different scenarios that might have created the extended emission we observe, and to derive the physical mechanisms and energetics involved.

Although Circinus is very close to us, the fact that it lies so close to our own Galaxy's plane has kept it from being observed in more detail in the past ($n_H = 5.56 \times 10^{21}$ cm^{-2}, Dickey & Lockman 1990b). Even the distance to the galaxy is not very well constrained, with most authors relying on the estimation by Freeman et al. (1977) of $4.2^{+0.8}_{-0.8}$ Mpc, with slight variations. We have settled for what seems to be the

Table 4.1: *Chandra* observations of the Circinus galaxy.

Obsid	Date	Exposure (ks)
00356	2000-03-14	25
12823	2010-12-17	160
12824	2010-12-24	40

most commonly accepted value, 4 Mpc, since this degree of uncertainty ($\sim$ 5 per cent variation in distance, $\sim$ 10 per cent in luminosity) should not have an impact on our conclusions, as we estimate it to be below the systematics.

4.2 Data

We observed Circinus with *Chandra* in December 2010, for a total of 200 ks. We also used a pre-existing observation from 2000, originally analysed by Smith & Wilson (2001) (see Table 4.1), adding up to a total of 225 ks. We reduced our data using the standard CIAO 4.2 pipeline, applying the latest calibration files. The observations show no trace of background flares, so that we could use the full exposures for all of them.

We generated event files for each *Chandra* observation, and merged them into a single image with the CIAO tool *merge_all*. We identified the point sources with *wavdetect* and cross-checked them manually for false or omitted identifications. We then removed the point sources and the readout streak (which is very prominent in the longest observation, running roughly in the same orientation as the galaxy's disk) from the merged image, to keep them from interfering in the analysis and to achieve the best possible characterization of the extended emission. Finally, we filled in the resulting gaps with the CIAO tool *dmfilth*. The resulting image can be seen in Fig. 4.1.

We used radio maps from archival *ATCA* (Australia Telescope Compact Array) observations at 21, 13, and 6 cm. The analysis of the original data is described by Elmouttie et al. (1998a), who also discuss the radio properties of the source in detail.

In addition to the data of Elmouttie et al. (1998a), we also obtained wide-band (2 GHz) *ATCA* data collected during CABB (Compact Array Broadband Backend, Wilson et al. 2011) commissioning and as part of an ATNF Summer Student observation

of Circinus. The CABB commissioning data were taken on 02 April 2009 (~8 hr, 6 cm only) using a compact 352 m configuration and 13 April 2009 (~6 hr, 3 cm and 6 cm) using a compact 168 m configuration. The ATNF Summer Student observations were made on 16 January 2010 (~9 hr, 3 cm and 6 cm) using a 6 km configuration.

The *ATCA* CABB data were calibrated in the MIRIAD package (Sault et al. 1995) and flagged using the new MIRIAD task mirflag. Model fitting of the source was performed using uv-components in DIFMAP (Shepherd et al. 1994) with an additional parameter used to model the spectral index of each component (thus accounting for spectral variation of the source across the 2 GHz wide band). Both phase and amplitude self-calibration were performed iteratively to improve the calibration and subsequent models. The final model achieves a 1 sigma sensitivity of 50 μJy/beam.

We also compared our data to the results on the ionized gas of the galaxy (Elmouttie et al. 1998b), the HI emission (Jones et al. 1999; Curran et al. 2008) and the optical images of the centre of the galaxy obtained with the *HST* (Wilson et al. 2000).

We used XSPEC 12.5 to fit models to the X-ray spectra. All the model parameters thus estimated are quoted with 90 per cent confidence uncertainties.

4.3 Analysis

4.3.1 Imaging

The reduced and merged X-ray image we obtained is presented in Fig. 4.1. Overlaid over the X-ray image are the 13 cm radio contours and the regions we used to extract the surface brightness profiles shown in Figs. 4.3 and 4.4. This image shows several extended structures, with different orientations (see also Curran et al. 2008). Our proposed geometry is detailed in Fig. 4.2, which was drawn over the combined X-ray/radio/optical image, to reflect the scale, reach and orientation of each component as accurately as possible. Our Figure is similar to the picture proposed by Elmouttie et al. (1998a), but there are some differences, particularly in the interpretation of the different structures. The AGN and circumnuclear star-forming ring are at the centre of the galaxy, the ring facing towards us. The galaxy's disk extends in the NE-SW direction, with an orientation of $\sim 60^{\circ}$ relative to the plane of the sky (Jones et al. 1999; Curran et al. 2008) and shows some X-ray emission, though it is fainter than the other

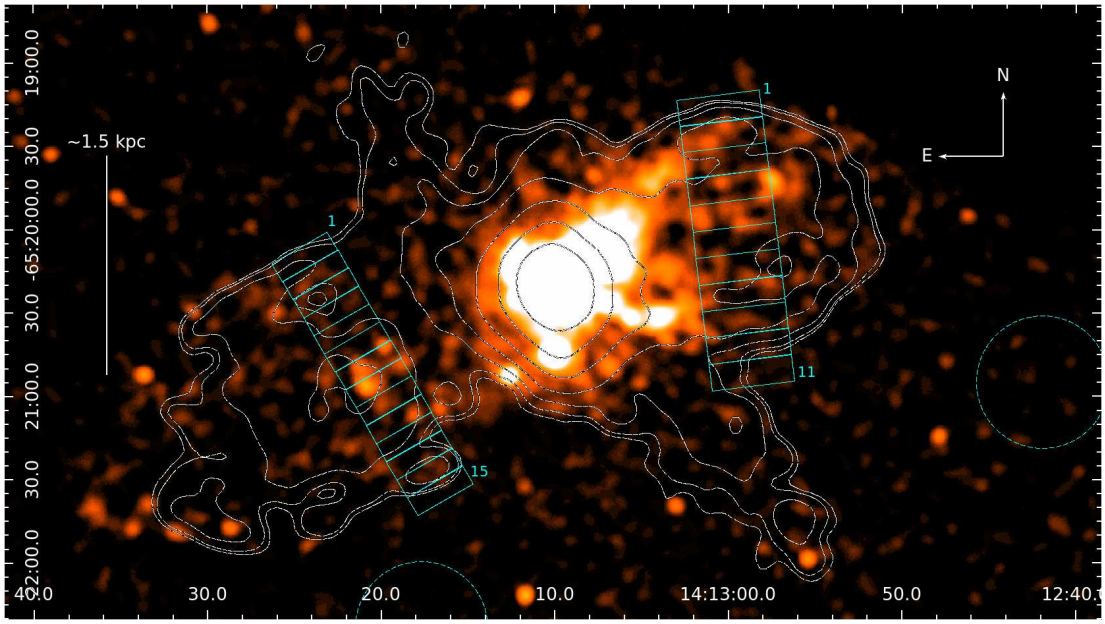

Figure 4.1: Merged (new+archival ACIS-S observations) 0.4-5 keV *Chandra* emission with overlaid *ATCA* 13 cm contours and $\sigma = 8$ *Chandra* pixels (4 arcsec) Gaussian smoothing, displaying the extent and morphology of the extended emission. All point sources except the nucleus and the SNR have been masked out. The X-ray emission coincides with the edges of the radio lobes (NW and SE structures), although there is some diffuse X-ray emission coinciding with the galaxy's disk (extending NE-SW). This image also shows the regions we used to extract surface brightness profiles for both radio lobes (the background was chosen from the circular, dashed regions). The numbers indicate the first and last regions in each strip. Scale: 19.4 pc arcsec^{-1}. The resolution of the 13 cm radio map is 11.8×11.0 arcsec.

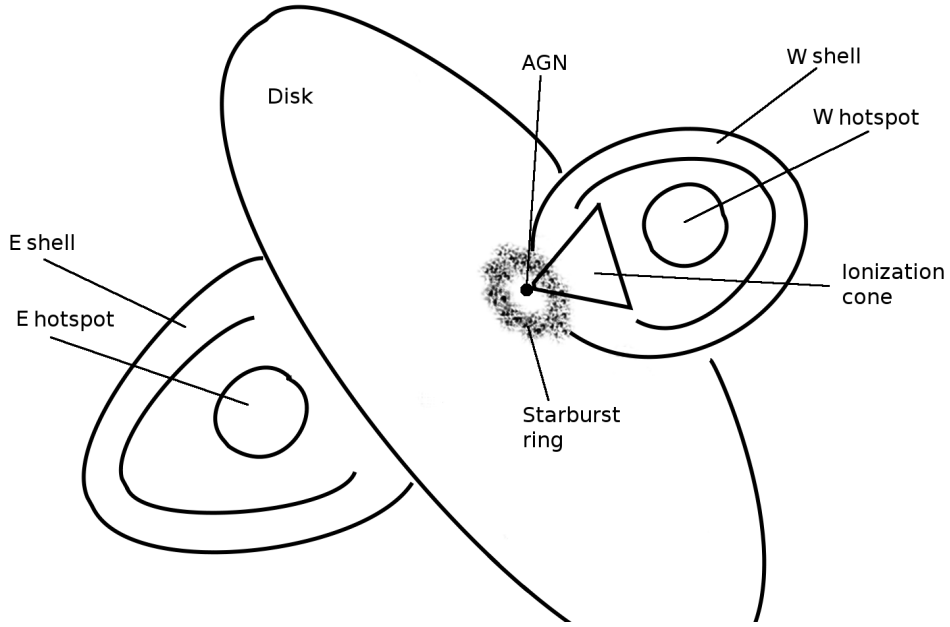

Figure 4.2: Scheme of the different components we identify in the X-ray and radio images.

structures. The NW lobe is unobscured, on the near side of the disk, and the SE lobe is partly obscured, showing a clear dip in X-ray emission in the areas covered by the disk. Both lobes appear to be edge-brightened, though the NW lobe is much brighter and somewhat smaller. The orientation of the lobes is roughly perpendicular to that of the disk. There is a dip in X-ray luminosity on both lobes behind the bright edges, and a rise towards the centre of both, suggesting that there is further structure within the lobes. We extracted surface brightness profiles for both lobes, to quantitatively verify the correspondence between the X-ray and radio structures, as well as to confirm the edge-brightening in both cases. The results are illustrated in Figs. 4.3 and 4.4. Near the AGN, coinciding with the base of the NW lobe, quite strong X-ray emission coincides with a region of highly ionized gas that is believed to be an ionization cone (Marconi et al. 1994; Elmouttie et al. 1998b; Wilson et al. 2000; Smith & Wilson 2001). The X-ray emission from the galaxy's halo is very faint and not directly discernible from the images shown.

The radio contours show the overlap between radio and X-ray emission (for a detailed analysis of the radio maps see Elmouttie et al. 1998a). There is faint radio

emission in the NE-SW direction, coincident with the disk of the galaxy, while the radio lobes extend perpendicularly to it. The pattern of radio emission in the lobes matches the X-ray structures perfectly: the edge-brightened emission in the lobes, the dip in luminosity behind the edges and the rise towards the centre of the lobes are spatially coincident across both wavelengths, except in a few points. We tested different orientations and distances when extracting the radial profiles in Figs. 3 and 4. The coincidence between the radio and X-ray edge peaks persists across most of both lobes, though it is clearer in some areas. We chose regions that covered all the appropriate structures: shells, lobe interior and hotspots, while trying to avoid the main emission from the ionization cone, which has no radio counterpart, and the edges of the CCD.

The differences in the morphology of the emission between the two lobes can only be partly explained by orientation effects. The E lobe is larger, and does show X-ray emission outside the confines of the radio lobe edges in the regions farthest from the AGN. The W lobe is smaller, more spherical, and its emission seems to be confined within what is seen in the radio maps. However, the edge of the CCD is just outside the edge of the W lobe in our long observations, and it is possible that we may be missing some of the outermost edge in this direction, in which case both lobes could exhibit a tip of X-ray emission outside the radio lobe. It is possible that the outflow may have encountered very different environments on its way to its current position, which could explain the asymmetry between the W and E lobes.

The W structure also shows the base of the ionization cone detected by Marconi et al. (1994), while no counterpart is visible in the E, most likely due to its being obscured by the galaxy's disk (see Figs. 4.5 and 4.2). The *Chandra* images show three distinct tails, propagating from the AGN in the W direction. The two brighter tails to the North have [OIII] and Hα counterparts (see the right panel of Fig. 4.5 and Smith & Wilson 2001; Wilson et al. 2000; Elmouttie et al. 1998b) while the southernmost edge only shows up in Hα + [NII]. This southernmost edge could be obscured, as suggested by Elmouttie et al., or could be produced by a different mechanism. While the top tail is clearly one of the edges of the ionization cone, it is unclear whether the other edge is given by the central or the southernmost tail (Elmouttie et al. 1998b).

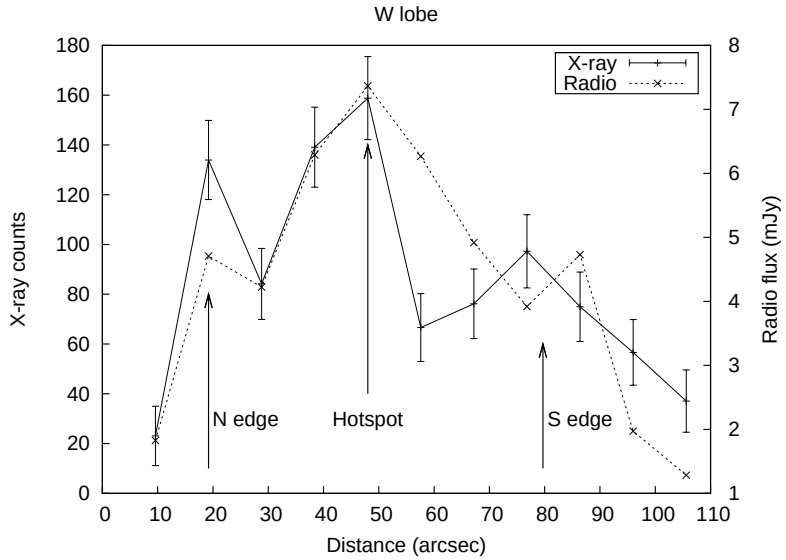

Figure 4.3: Surface brightness profiles for the W lobe of Circinus, as extracted from the regions in Fig. 4.1. The regions are 30×9.6 arcsec in size, and have an inclination angle of 6.9°. The distance is measured along the regions in the N-S direction, starting on the northernmost edge of the first region. The arrows indicate the N and S edges of the shell, and the hotspot, as illustrated in Fig. 4.2. Scale: 19.4 pc arcsec^{-1}

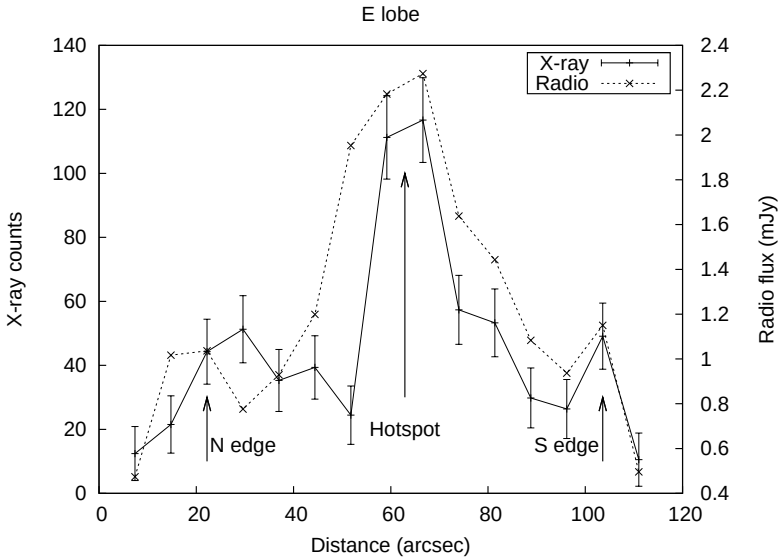

Figure 4.4: Surface brightness profiles for the E lobe of Circinus, as extracted from the regions in Fig. 4.1. The regions are 23 × 7.4 arcsec in size, and have an inclination angle of 30°. The distance is measured along the regions in the N-S direction, starting on the northernmost edge of the first region. The arrows indicate the N and S edges of the shell, and the hotspot, as illustrated in Fig. 4.2. Scale: 19.4 pc arcsec^{-1}

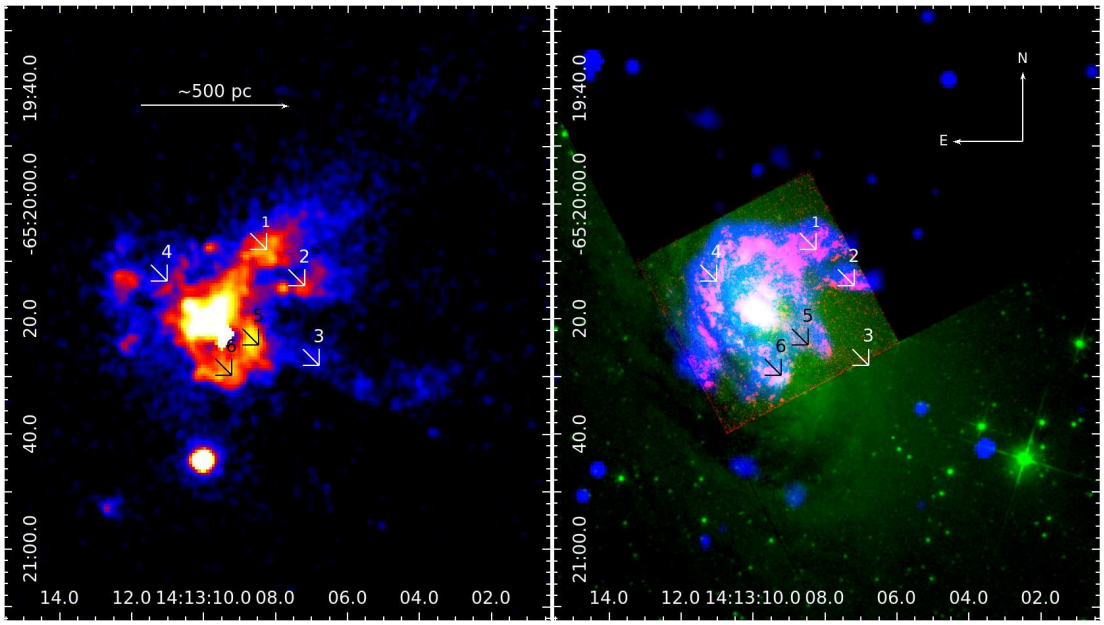

Figure 4.5: Left: The central regions of Circinus as seen in our merged, masked Chandra image, with $\sigma = 2$ pixel (1 arcsec) Gaussian smoothing. The image shows the AGN, the circumnuclear star-forming ring and the ionization cone at the base of the W radio lobe. Right: composite image showing the *HST* data on [OIII] emission (red), and F814W filter (broad I) continuum (green) from Wilson et al. (2000), and the H_α emission (blue) from Elmouttie et al. (1998b), kindly provided by Bi-Qing For, illustrating the correspondence between the structures we observe in X-rays and those visible in the optical. The arrows point to matching structures: the N tail of the ionization cone (1,2), the S tail (3), which is obscured in the optical images, and parts of the circumnuclear ring (4, 5, 6). See Fig. 4.2 for more details on the geometry around these structures. Scale: 19.4 pc arcsec^{-1}

4.3.2 Spectroscopy

As we discussed in Section 4.1, the nucleus of Circinus and its immediate surroundings have been studied in detail in the past. The objective of our analysis is to study the larger scale X-ray emission associated with the radio lobes of Circinus.

We extracted X-ray spectra of the radio lobes from regions excluding the AGN and circumnuclear emission, as well as the (presumably) photoionized plume in the W lobe, to avoid contamination. Our W region also avoids most of the area covered by the part of the disk that lies behind the lobe, thus minimising any possible contamination from it in the resulting spectrum. The spectra were binned to 15 counts per bin to allow Gaussian statistics to be used. We also binned the spectra to 20 counts per bin to check the robustness of the fits.

We used regions that cover most of the radio lobes, excluding the circumnuclear emission and any point sources, after verifying that the spectrum of the gas inside the lobes does not differ from those of the gas in the shells, presumably due to the low surface brightness emission from the shells contributing in these regions. We worked with a number of different source and background regions to minimize contamination. The spectra of the W lobe are fairly consistent regardless of our choice of source and background, but the E lobe was problematic in this respect: we found that the overall shape of the spectrum was independent of our choice of regions, but not entirely consistent with any simple single or double component model. As discussed below, this anomalous shape may be caused by a higher contribution of star-related emission from the galaxy's disk. The statistics on the E lobe are also poorer than those of the W counterpart, most likely due to the higher obscuration, making it difficult to mask out bright regions and still obtain a good fit.

We fitted to our spectra a model consisting of local Galactic absorption (wabs) and emission from a collisionally ionized gas (apec) (see Figs.4.6 and 4.7). We approached the analysis by fitting the model both to the individual spectra together and to the coadded spectrum (generated with the CIAO tool *combine_spectra*). Only the former approach is shown in the Figures, but the results are consistent for both methods. Given that the abundance is not well constrained (especially for the E lobe, where we have problems with both multiphase gas and covering absorbers), and if left free during the fitting the values tend to become implausibly low, we assumed a fixed abundance

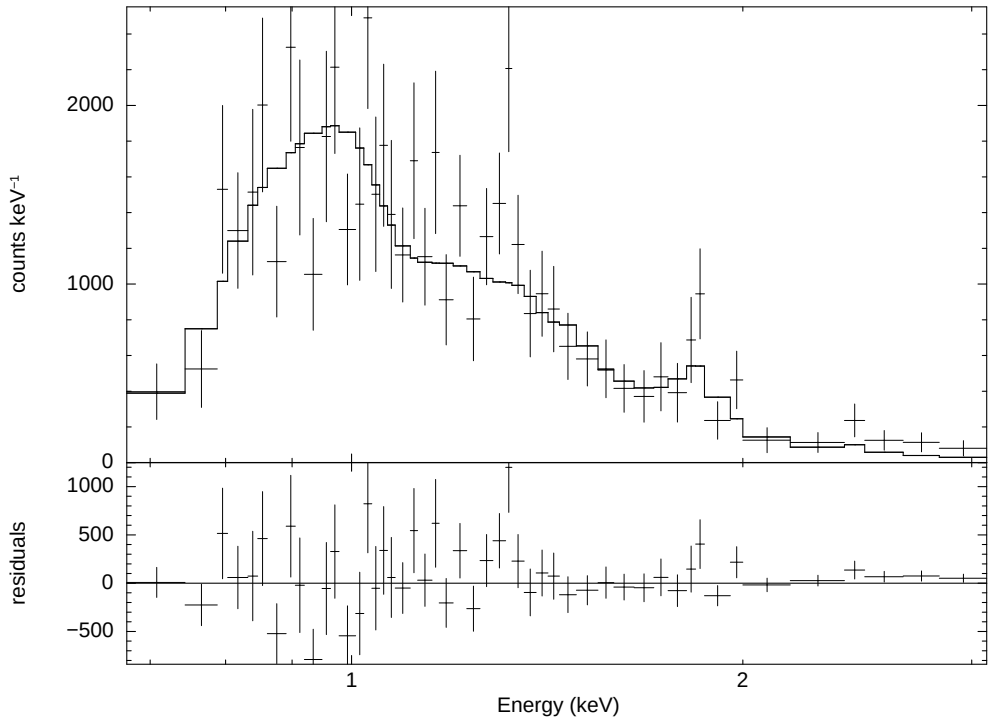

Figure 4.6: Spectral fit to the combined spectrum of the W lobe of Circinus. Model: wabs*apec, $kT = 0.74^{+0.06}_{-0.05}$ keV.

of 0.15, compatible with the lower limit set by the abundances in the IGM (see e.g. Danforth et al. 2006). Abundances higher than 0.2 do not affect the estimated values for the temperature, but the fit statistics are much worse. See the last paragraph of Section 4.4.2 for a discussion on the implications of a different value of Z.

We found that the emission in the W lobe is very well fitted with this single temperature model, although there are some residuals, especially at high energies, most likely caused by contamination from the AGN PSF. We obtained a best-fitting temperature of $0.74^{+0.06}_{-0.05}$ keV, and a reduced χ^2 of 1.09. See Fig. 4.6 and Table 4.2 for details.

The E lobe, however, proved to be more problematic. This area is partially covered by the galaxy's disk, and the spectrum (see Fig. 4.7) is not successfully modelled by a single temperature model (reduced $\chi^2 \sim 1.5$). Adding a powerlaw or a second thermal component does improve the fit, albeit slightly (reduced $\chi^2 \sim 1.2$) and most of the residuals persist. Adding an extra absorbing column does not improve the fit. The poor fit could be caused by emission from an unresolved X-ray binary population and massive stars in the disk, or unavoidable contamination from the nearby, strong AGN.

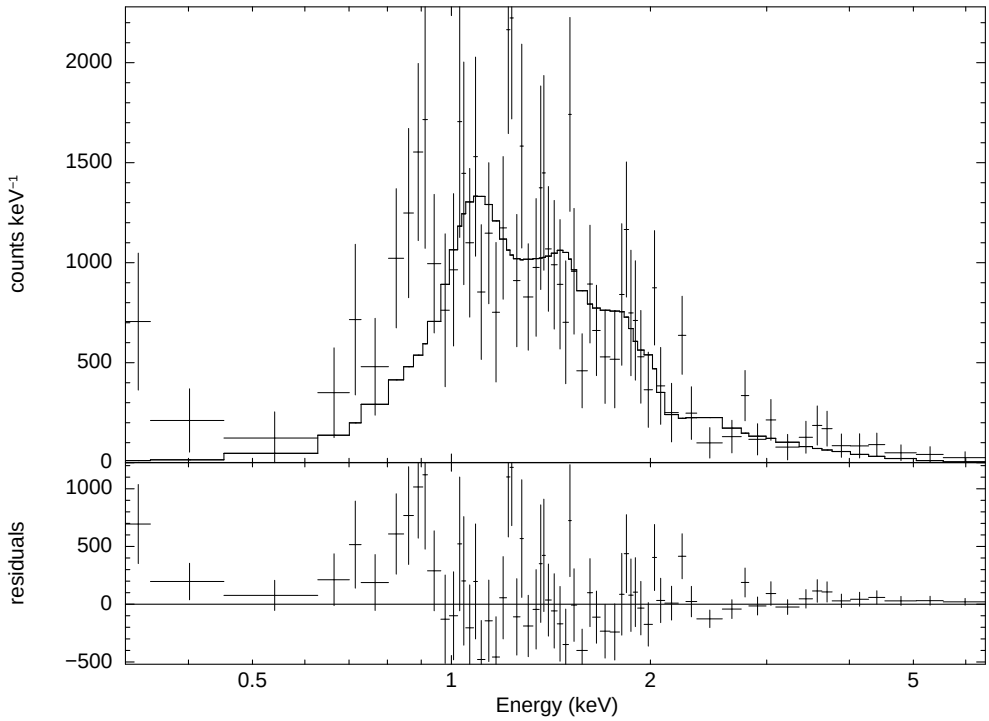

Figure 4.7: Spectral fit to the combined spectrum of the E lobe of Circinus. Model: wabs*apec, $kT = 1.6^{+0.6}_{-0.2}$ keV.

XSPEC determined a best fitting temperature for the E lobe of $kT = 1.6^{+0.6}_{-0.2}$ keV, but it is not well constrained. A detailed analysis shows local minima when the model assumes $kT = 0.8$ and $kT = 1.8$ keV. Thus we used these values as a lower and upper limit, respectively, for the shell calculations displayed in Table 4.2.

The disk over the E lobe is problematic not only because it may be introducing some contamination, it might also be masking an E counterpart to the W ionization cone, which could also be contributing to our spectra. Given the different morphologies of the two lobes, it is also possible that the temperature structure may be different for the E structure. We will discuss the nature of the emission in the lobes and its structure in the following Sections.

We also carried out a fit over the regions corresponding to the disk (NE-SW), and found that a single temperature model works remarkably well, with $kT = 0.69^{+0.19}_{-0.17}$ keV. This temperature is very similar to the one we found for the W shell, but not so well constrained (mainly due to a higher fraction of contamination from the AGN).

To test whether there are any changes in the nature of the emission in the brighter

areas within the lobes, we extracted spectra from these regions. A fit to a single powerlaw model gave very poor results, since the thermal emission from the shells is still present. We then fitted to the spectra a model equal to the one we used for each shell plus either a powerlaw or a second thermal component. The addition of a second component improves the fit; however, the poor statistics (the brightest individual spectrum has just ~100 counts) do not allow us to distinguish between a thermal and a non-thermal model in this case. Although the fit is slightly better with the non-thermal model, the difference is not statistically significant. We will discuss the nature of this emission in Section 4.4.3.

4.4 Discussion

In this Section we discuss the possible scenarios that may be causing the emission we observe. In Section 4.4.1 we discuss the possibility that the large-scale emission is caused by photoionization from the AGN. In Section 4.4.2 we argue that what we are observing is, instead, a shock. As possible causes behind this shock, we contemplate the possibility of a starburst-driven superbubble (Section 4.4.3) or a radio jet-ISM interaction (Section 4.4.4).

4.4.1 Photoionization

Given that the edges of the ionization cone coincide with the base of the W shell almost exactly (see Fig. 4.5 and the discussion at the end of Section 4.3.1), it is possible that some of the line emission studied by Marconi et al. (1994) may be caused by collisional ionization rather than photoionization. However, without [OIII], [NII] and Hα maps with a large field of view and good resolution to measure the intensities and ratios, it is hard to tell. Given the intensity of the AGN and the light from the starburst ring, photoionization must indeed play a role in the emission we see in this region. However, it is extremely unlikely that photoionization from the central AGN could explain the edge-brightened, large-scale emission we are observing further out. We calculated the extent of photoionization caused by the AGN following the methods of Wang et al.

(2009) and the models from Kallman & McCray (1982). Given that:

$$\xi = \frac{L}{nR^2} \tag{4.1}$$

where ξ is the ionizing parameter, which we assume to be between 10 and 100 (reasonable values for AGN outflows, as demonstrated by Ogle et al. 2003, see also Wang et al. 2009). $n \sim n_e$ is the particle density (which we assume to be between 10^{-2} and 10^{-1} cm^{-3}), R is the distance (in cm) and L is the unabsorbed X-ray luminosity of the AGN required to produce the observed ionization factor (we assumed $L = 1.6 \times 10^{42}$ erg s^{-1}, after de Rosa et al. 2012). In the case of Circinus, this implies that the AGN would be able to weakly ionize ($\xi \sim 10$) gas up to $\sim$ 700 pc away, but strong ionization ($\xi \sim 100$) would only be produced within the inner $\sim$ 200 pc. Given the relative low luminosity of the AGN (Yang et al. 2009) and the dense environment surrounding it, this is consistent with what is observed for the ionization cone, but shows that the edge-brightened emission in the shells cannot be accounted for by photoionization. Given that the X-ray emission at the edges of the radio lobes extends up to 2-3 kpc in projection (for the W and E shell respectively), even the possibility that the AGN was more powerful 10^3–10^4 years ago makes photoionization unrealistic to explain the level of emission we are detecting at these distances, requiring densities an order of magnitude smaller than those we measure in these regions to achieve weak photoionization.

While there are no high resolution, large scale [OIII] or Hα maps that cover all of the ionization cone, the existing images (Elmouttie et al. 1998b; Wilson et al. 2000) do show other regions of the galaxy that coincide with part of the lobes, and there seems to be no enhancement in emission in these regions, matching the radio and X-ray data, while this enhancement is observed in the ionization cone. From a morphological perspective, since the base of the W shell coincides with the ionization cone (Marconi et al. 1994), and given the results above, we can infer that there is a transition between predominantly photoionized and shock-ionized gas at these distances, which could be further investigated with large scale [OIII] and Hα maps and more X-ray observations.

For consistency, we extracted a spectrum of the two northernmost tails of the ionization cone (see left panel of Fig. 4.5) in our longer exposure, covering distances of 150–500 pc from the AGN. We fitted the resulting spectrum to a *photemis* model (part of WARMABS, an analytical XSPEC model implemented from XSTAR) and fore-

ground Galactic absorption. We assumed a gas density of 10^4 cm^{-3} and an ionizing powerlaw with $\Gamma \sim 1.6$ (de Rosa et al. 2012). We found that photoionized emission alone does not fully account for the spectral shape, yielding a reduced $\chi^2 \sim 2.5$. This may be due to the less than ideal background subtraction (a local background region that can compensate for the AGN contamination, without including the readout streak or emission from the star-forming ring will still include thermal emission from the galaxy's disk) or to a more complex spectral structure derived from the large volume covered by our region (a requirement to obtain the necessary statistics for the fit). By testing the addition of different continua to improve the fit, we observed that the ionization parameter remained stable, at values of $\log(\xi) \sim 1.7$–2.0, which supports our assumptions in the previous paragraph. We also found very low abundance constraints ($\sim 10^{-2}$) on O, Mg and Si, and higher values ($\sim$ 0.1–0.3) for Fe and Ne. We were unable to constrain the abundances for the other elements, but increasing them over our initial assumption ($0.15\odot$) increases the χ^2.

We also studied the likelihood of detecting an identical structure in the E lobe, behind the disk of the galaxy. We estimated the countrate we would expect in our image from this structure with the PIMMS tool, assuming it to have the same unabsorbed flux as our W ionization cone spectrum ($F_{0.3-10keV,unabs} = 1.5 \times 10^{-12}$ erg cm^{-2} s^{-1}) and a foreground absorbing column from the disk comparable to that of the Cen A dust lane ($N_H \sim 1.5 \times 10^{22}$ cm^{-2}). We found that we would only obtain ~300 counts from this structure in our image, below the emission level from the disk of the galaxy itself, and thus we would not be able to detect it. Although the obscuration from the disk might be lower, it is also possible that the E ionization cone, if present, may be fainter than its W counterpart, if the environment through which the radiation must pass is denser. The possibility of an ionization cone in the E lobe, therefore, cannot be discarded.

4.4.2 A shock model

The match between the X-ray and radio emission is striking in Circinus (see Figs. 4.3 and 4.4). Unlike in other, more distant systems, where we lack the spatial resolution to resolve these structures in such detail, the proximity of Circinus allows us to observe that the emission from the shells coincides extremely well in radio and X-rays. In all the radio frequencies there is a dip in luminosity behind the shell, and a rise in

Table 4.2: Results for the shells of Circinus. These results are for the temperatures discussed in the text and $Z = 0.15\odot$. The columns, from left to right, show the shell, temperature, model normalization, electron density, mass, pressure, total thermal energy, work available from the gas filling the shells and total kinetic energy.

Shell	kT	Norm	N_e	M	P	E	PV	K
	keV	$\times10^{-4}$cm^{-5}	$\times10^{-2}$cm^{-3}	$\times10^{36}$Kg	$\times10^{-12}$Pa	$\times10^{54}$erg	$\times10^{54}$erg	$\times10^{53}$erg
W	$0.74^{+0.07}_{-0.05}$	$1.39^{+0.24}_{-0.13}$	$2.27^{+0.11}_{-0.11}$	$1.97^{+0.09}_{-0.10}$	$4.98^{+0.14}_{-0.25}$	$4.56^{+0.22}_{-0.23}$	$3.04^{+0.14}_{-0.15}$	$5.15^{+0.25}_{-0.26}$
E	0.8	$1.30^{+0.12}_{-0.12}$	$2.20^{+0.10}_{-0.11}$	$1.90^{+0.09}_{-0.09}$	$5.21^{+0.23}_{-0.25}$	$6.10^{+0.28}_{-0.29}$	$4.07^{+0.18}_{-0.20}$	$5.38^{+0.24}_{-0.26}$
E	1.8	$1.08^{+0.12}_{-0.12}$	$2.00^{+0.11}_{-0.11}$	$1.73^{+0.10}_{-0.11}$	$10.1^{+0.5}_{-0.6}$	$5.55^{+0.30}_{-0.30}$	$8.32^{+0.43}_{-0.45}$	$4.89^{+0.27}_{-0.26}$

emission towards the centre of the radio lobes. Given the edge-brightened nature of the emission, the abrupt jump in luminosity and the spectral properties we derived for the gas, we consider that the most likely scenario is that we are observing shells of shocked gas around the radio lobes of Circinus. We will discuss below whether this shock may be starburst or jet-driven. The dip and rise in luminosity behind the shells suggests further complexity in their structure, since we would expect the lobes to be uniformly filled with gas. We will discuss the nature of this emission for both the starburst and jet scenarios.

The fact that the X-ray emission does not appear to be outside the radio lobes (except at the tip of the E lobe, as discussed in Section 4.3.1) suggests that the same shock that is causing the X-ray emission in the shells (which, as detailed in Section 4.3.2, is thermal in origin) is also giving rise to enhanced synchrotron emission at radio frequencies. The apparent thickness of the shells, measured from the X-ray images, is $\sim$ 300 pc, and appears constant across the entire structure.

To test the shock hypothesis we assumed two ellipsoidal shells (the geometry that most closely follows the shells as depicted in Fig. 4.2, with the smallest departure from spherical symmetry) with the two minor axes equal. The two-dimensional regions we used in our images have eccentricities of 0.74 and 0.52 for the E and W shells respectively. The E structure is larger, with $R_{int,maj} = 1.0$ kpc, $R_{ext,maj} = 1.4$ kpc, $R_{int,min} = 0.7$ kpc, $R_{ext,min} = 0.9$ kpc. The W shell has $R_{int,maj} = 0.8$ kpc, $R_{ext,maj} = 1.1$ kpc, $R_{int,min} = 0.7$ kpc, $R_{ext,min} = 0.9$ kpc. These dimensions correspond to volumes of 7.8×10^{64} cm^3 and 6.1×10^{64} cm^3 for the E and W shells respectively.

We derived the electron densities for both shells from the normalization of the

thermal model (see Table 4.2), assuming a uniform filling factor. From these densities it is also possible to calculate the total mass of gas in the shells, the pressure, the total thermal energy, and the work available from the gas. We found the densities to be slightly higher than those we found for Mrk 6, but the total energy involved is lower by roughly two orders of magnitude, which is to be expected given the much lower radio power observed in Circinus.

In order to test our hypothesis of a shock scenario we attempted to extract spectra of the gas immediately outside the lobes, but were unable to fit a model to the data, due to the poor statistics. We then generated radial profiles for the longest observation from concentric annuli (r_{min} = 132 arcsec, r_{max} = 305 arcsec, δr = 8.7 arcsec), excluding the emission from the AGN, the lobes and the galactic disk, and a suitable background. The surface brightness of the gas in the halo is extremely low, and it barely shows up in radial profiles (see Fig. 4.8). The drop in luminosity at R$\sim$ 440 pixels ($\sim$ 4.2 kpc) indicates the possible extent of the halo, but the errors are too large to consider this anything more than a qualitative indication.

To better constrain the surface brightness we estimated the count statistics for a circular region centered in the AGN in the longest observation, excluding the regions coincident with the lobes, the disk of the galaxy, any point sources, the readout streak and any CCD gaps or adjacent chips in the process. We used two different radii for this circular region, r = 246 and r = 305 arcsec, to better assess the effect of the background, which was extracted from all the remaining S3 chip. We detected the halo at a 3.8σ level in the 0.3–7 keV energy range (1439 ± 382 and 884 ± 239 counts for the larger and smaller source regions respectively, corresponding in both cases to a surface brightness of 0.011 ± 0.003 counts pixel^{-2}), and at a 5.5σ level in the 0.5-2 keV range (1259 ± 245 and 852 ± 154 counts for the larger and smaller source regions respectively, corresponding in both cases to a surface brightness of 0.010±0.002 counts pixel^{-2}). Since the orientation of the chips in the other two observations is different, it is not possible to apply the same regions to them, instead we extrapolated the statistics from the first observation to the total observed time. We thus obtained a 1σ range for the surface brightness of the halo, in the 0.3–7 keV energy band, of 0.01–0.02 counts pixel^{-2} (0.04–0.08 counts arcsec^{-2}).

The constraints on the surface brightness allowed us to test a thermal model with different temperatures, assuming a suitable extraction region outside the radio lobes (a

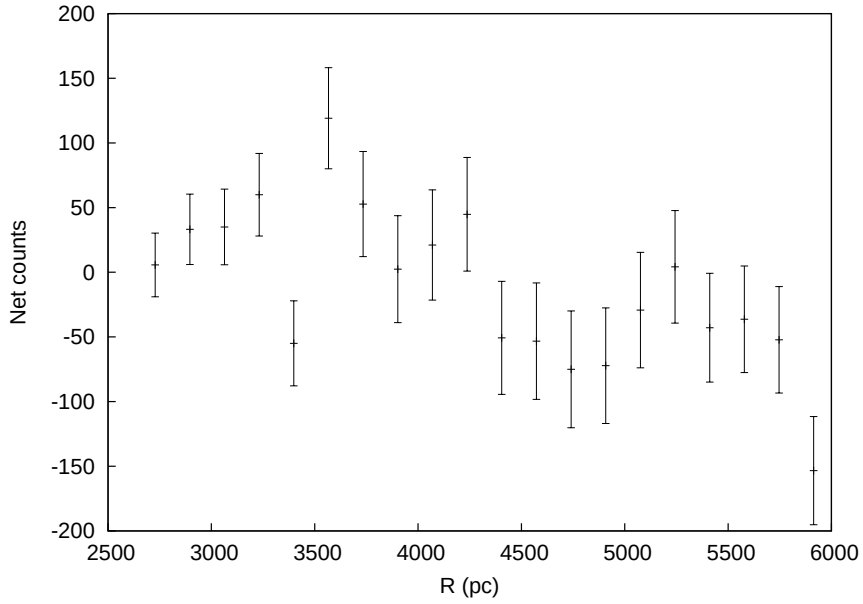

Figure 4.8: Radial profile of background-subtracted counts for the longest *Chandra* observation of Circinus. Scale: 1 pixel = 0.492 arcsec = 9.54 pc. The emission from the halo of Circinus is barely above the background level, but there seems to be a net count drop after $R \sim 4.2$ kpc (~ 440 pixels), indicating that this may be the extent of the halo. Combining the results for the three observations we obtained a surface brightness estimate of $4\text{–}8 \times 10^{-2}$ counts/arcsec^2.

spherical shell centred in the AGN, with R_{int} = 3.68 kpc, $R_{Circinus_ext}$ = 5.24 kpc). Given the range of temperatures found in the haloes of similar galaxies (see e.g. Tüllmann et al. 2006b; Yamasaki et al. 2009), we derived the electron densities for kT = 0.1 keV, 0.2 keV and 0.3 keV.

We used our low/high values for the surface brightness and the halo shell region to obtain estimated count rates for each temperature. We then derived the *apec* normalizations required to obtain these count rates, and derived the electron densities and pressures from those normalizations. The results are displayed in Table 4.3. We find that the electron densities we derive are compatible with those estimated by Elmouttie et al. (1998a), based on observations of other nearby spiral galaxies. We also estimated the cooling time for the gas, obtaining results of 0.3–3.6$\times 10^8$ yr for kT = 0.2–0.3 keV, and as low as 6.2 Myr for kT = 0.1 keV. These times are very short, since line cooling is very important at these low temperatures, suggesting that the hot gas into which the lobes are expanding must have a comparatively recent origin, possibly in a starburst and/or supernova wind.

To verify our assumptions on the properties of the gas in the halo we used the relations of Tüllmann et al. (2006a), which give the correlation between the X-ray luminosity of the halo and other parameters for a sample of star-forming spiral galaxies. Some of their correlations indicate a very strong dependence between the soft X-ray luminosity of the halo and parameters such as the FIR/Hα star formation rate, and between the overall galactic X-ray luminosity and the mass of dust or HI in the galaxy.

Given how obscured and nearby Circinus is, most previous studies have focused just on the central star-forming ring or the supernova remnant, so that some of the parameters we could use to derive the luminosity of the halo are not known, but we were able to use the values from Curran et al. (2008); Jones et al. (1999); Elmouttie et al. (1998b); For et al. (2012) ($L_{B,bol} \sim 2.9 \times 10^{43}$ erg s^{-1}, $L_{UV,bol} \sim 9.1 \times 10^{42}$ erg s^{-1}, $M_{dust} \sim 10^6$ $M_\odot$, $M_{stars} \sim 10^{11}$ $M_\odot$, $SFR_{FIR} \sim 3-8$ $M_\odot$ yr^{-1}) with Tüllmann et al.'s correlations. This allowed us to constrain the soft (0.3-2 keV) luminosity of the halo of Circinus to 1.6-6.3$\times 10^{39}$ erg s^{-1} from the correlations of Tüllmann et al. Given that the extraction region we used in our analysis does not cover the full halo of the galaxy, we find that our results are consistent with what is expected from these correlations and the observations (see Table 4.3). The luminosity we thus constrained is also compatible with the count rates we estimated from our images.

Table 4.3: Results for the external medium. The columns, from left to right, show the low/high values of the model normalization, electron density, luminosity and gas pressure for each assumed gas temperature.

kT	Norm	N_e	$L_{0.2-3keV}$	P
keV	$\times 10^{-2}$ cm^{-5}	$\times 10^{-2}$ cm^{-3}	$\times 10^{38}$ erg s^{-1}	$\times 10^{-12}$ Pa
0.1	2.80/5.70	2.35/3.35	0.71/1.45	0.70/0.99
0.2	1.00/2.10	1.40/2.03	5.30/10.70	0.83/1.20
0.3	0.33/0.66	0.80/1.14	5.04/10.07	0.72/1.01

Comparing the electron densities we derive for the shells and the external gas, we see that density ratios of $\sim$ 1.1–3 can be derived from $kT_{Circinus_{ext}} = 0.2$ or $kT_{Circinus_{ext}} = 0.3$ keV, and smaller values (0.6–0.9) for $kT_{Circinus_{ext}} = 0.1$ keV. The small density contrast makes the latter temperature less consistent with our shock interpretation, given that the density ratio ρ_{out}/ρ_{shell} tends to 4 in the case of a strong shock. Based on observational results (see e.g. Hummel et al. 1991; Beck et al. 1994), the electron densities we derived from $kT = 0.2$ and $kT = 0.3$ keV are compatible with those seen in the haloes of spiral galaxies.

Although the fact that we do not directly detect the external gas is still a limitation, since it would allow us to rule out a slow shock into a cold, dense medium, or pressure conditions where a shock is not possible, the morphology of the X-ray emission, the observed properties, and the agreement of the extrapolated values for the external gas with what we would expect in our assumed scenario indicate that we are indeed observing a strong shock being driven into the ISM of Circinus.

Using the observed parameters we can calculate the Mach number for the shock, as follows (Landau & Lifshitz 1987):

$$\mathcal{M} = \sqrt{\frac{4(\Gamma+1)(T_{shell}/T_{out}) + (\Gamma-1)}{2\Gamma}} \tag{4.2}$$

where Γ is the polytropic index of the gas, assumed to be 5/3. We find Mach numbers $\mathcal{M} \sim$ 2.7–3.6 for the W shell (up to $\mathcal{M} = 5.1$ if the external temperature is closer to $kT = 0.1$ keV) and $\mathcal{M} \sim$ 2.8–5.3 for the E shell (up to $\mathcal{M} = 7.6$ for $kT = 0.1$ keV). The sound speed is $\sim 264^{+59}_{-78}$ km s^{-1}, and the velocity of the shells is 915^{+45}_{-35} km s^{-1} for the W shell and 950^{+470}_{-130} km s^{-1} for the E shell. The errors on these values reflect the

temperature range of both the shell and the external gas; the uncertainty on the E shell is very large due to the range of possible shell gas temperatures, as indicated in Table 4.2. It is clear, in any case, that the velocity of the shells must be supersonic, and close to 1000 km s^{-1}, in agreement with what is observed in similar systems (e.g. Mrk 6, NGC 3801: Mingo et al. 2011; Croston et al. 2007)

If we assume that the shells have been expanding with a constant velocity, equal to the one we have derived for the W structure, we can constrain their age to $\sim 10^6$ years. The total energy (enthalpy of the cavity and kinetic energy from the shock) involved in creating both shells is $\sim 2 \times 10^{55}$ erg, the equivalent of 10^4 supernova explosions with individual energy 10^{51} erg, assuming a 100 per cent efficiency.

While the spectral fits of the ionization cone (see Section 4.4.1) seem to support our initial assumption of $Z = 0.15\odot$, this value is still poorly constrained. It is very likely that the areas of the galaxy covered by our regions contain a multi-phase gas, and a range of abundances, but these cannot be studied in detail without deeper observations. The gas density we derive from our models depends both on the abundance and the emission measure, so that, assuming that there are no abrupt variations in the abundance between the shells and the regions immediately outside them, for $Z = 0.30\odot$ the electron density in the shells would be $\sim$ 25% lower, while that of the external gas would go down by $\sim$ 20%. The ratio between both densities, however, only depends weakly on Z, so even if our assumptions on the abundance were wrong, and the densities were smaller, our conclusions would stand. The Mach number and the shock velocity would not change, but the total energy involved in the process would be slightly smaller.

4.4.3 Starburst-driven bubble

Given that Circinus is a spiral galaxy, with active star formation, it is possible that the bubbles that we are observing perpendicular to the plane of the galaxy may be caused by a starburst or supernova-driven wind. As pointed out by Elmouttie et al. (1998a), however, the particle component within starburst-driven "bubbles" is expected to be a mixture of thermal and non-thermal electrons, with the thermal material causing depolarization. The W "bubble" in Circinus does not show a high degree of depolarization. In the E "bubble" the higher depolarization is most likely caused by the gas in the disk,

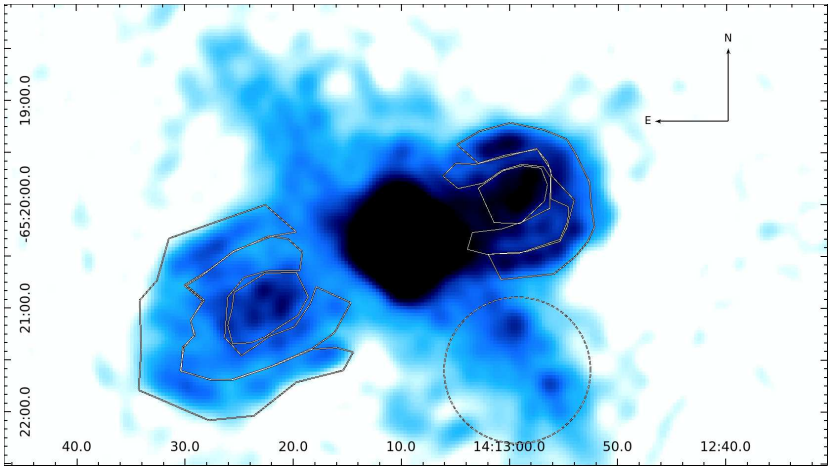

Figure 4.9: 13 cm *ATCA* radio map displaying the regions we used to calculate the spectral index for the different areas (hotspots, lobes and shells, the RMS error was estimated from the dashed circle South of the AGN). With this colour scale the full extent of the radio emission can be appreciated, showing the edge-brightening in the shocked shells, and the dip in luminosity immediately behind them. The resolution of the radio map is 11.8×11.0 arcsec.

which is obscuring part of the structure (for full details on the radio polarization of Circinus see Elmouttie et al. 1998a).

As we saw in Section 4.4.2, the total energy involved in the creation of both "bubbles" in Circinus is $\sim 2 \times 10^{55}$ erg. This value is similar to the one Matsushita et al. (2005) calculated for the superbubble observed in M82 ($0.5–2 \times 10^{55}$ erg), one of the most powerful examples of superbubbles. The efficiency with which supernova explosions transfer energy to the ISM is quite low (3–20 per cent, depending on the density of the ISM and time lapse between subsequent explosions). Elmouttie et al. (1998a) inferred a supernova rate of 0.02 sn yr^{-1} from their radio observations. To check this value we used the far-infrared data from Genzel et al. (1998) ($L_{FIR} = 7 \times 10^9 L_\odot$) and the correlations from Condon (1992) to estimate a massive star formation rate ($SFR_{M \geq 5M_\odot} \sim 0.64\ M_\odot$ yr^{-1}) and derived a supernova rate of ~ 0.026 sn yr^{-1}. With either of these values, the possibility of a supernova-driven wind is energetically viable in Circinus. However, the enhanced emission at the centre of the "bubbles" is not easy to explain, morphologically, with this model. Multiple generations of "bubbles", within the 10^6 yr age estimated for the larger structure, seem unlikely.

Some consideration must be given to how the radio "bubbles" are related to the structures closer to the AGN. Elmouttie et al. (1998b) suggest that there is an ongoing outflow of gas in the W ionization cone (with a total kinetic energy of 5×10^{53} erg), which could be powered by the AGN or a starburst wind. They suggest that the similar sizes of the $H\alpha$ central ring and the base of the central radio emission indicate that these structures are related, and that an ongoing starburst wind is the cause of both the inner outflow and the enhanced radio emission at the centre of the "bubbles". Emission line ratios in the cone, however, suggest that the emission in the cone may be caused by AGN-driven photoionization. For Circinus, Elmouttie et al. also point out that the morphologies of the ionization cone and the radio "plume" are quite different, indicating that these structures may not have the same origin. As suggested by Schulz (1988) for NGC4151, it is possible that, as the shock that created the larger structures in Circinus made its way through the halo gas, it created a low-density region through which ionizing radiation, from the AGN or a starburst-wind, could escape, giving rise to the cone. It is thus entirely possible that there is an ongoing starburst wind in the central regions of Circinus, feeding material into the ionization cone, but that this is not powerful enough to be the cause behind the large-scale emission in the shells and at the centre of the "bubbles".

The strongest argument against the starburst-driven scenario as an explanation for the large-scale emission, however, comes from the variations in the radio spectral index we observe across the "bubbles". Variations in the spectral index are a sign of a change in the electron population; a lower value of α may indicate a region where particle acceleration is occurring. An increasing value of α indicates radiative losses and an aging electron population. We calculated the fluxes for the shells, the areas immediately behind the "bubbles", and the regions with enhanced radio and X-ray emission inside them (which we labelled as hotspots), as illustrated in Figure 4.9. We convolved the 6 cm, 13 cm and 20 cm *ATCA* radio maps so that the spatial resolution was the same in all of them (20.5×20.5 arcsec), thus ensuring that we are measuring the emission from the same structures in all cases. To best estimate the extent of the RMS noise we chose a background region over the galaxy's disk, where there are flux variations, rather than a region off-source. We then derived spectral index values for each structure from the 6 cm/13 cm and from the 13 cm/20 cm flux measurements. The results are illustrated in Table 4.4.

Table 4.4: Spectral indices. The spectral indices for the different extended structures (hotspots, shells and lobes) of Circinus, have been derived from the *ATCA* 6 cm, 13 cm and 20 cm maps. The regions we used to calculate the relative fluxes are illustrated in Fig. 4.9.

Structure	λ	S		α
	cm	mJy		
W hotspot	20	29.0 ± 2.0	]	0.62 ± 0.09
	13	20.7 ± 1.4	]	0.59 ± 0.05
	6	13.6 ± 0.7		
E hotspot	20	20.9 ± 3.3	]	0.60 ± 0.13
	13	15.1 ± 1.7	]	0.96 ± 0.07
	6	7.7 ± 0.8		
W shell	20	36.9 ± 3.3	]	0.70 ± 0.13
	13	25.3 ± 2.3	]	0.94 ± 0.08
	6	13.0 ± 1.0		
E shell	20	37.6 ± 4.8	]	0.84 ± 0.20
	13	23.9 ± 3.4	]	1.12 ± 0.12
	6	10.8 ± 1.5		
W lobe	20	35.3 ± 2.6	]	0.71 ± 0.11
	13	24.1 ± 1.8	]	0.77 ± 0.06
	6	14.0 ± 0.8		
E lobe	20	37.2 ± 3.9	]	0.78 ± 0.16
	13	24.3 ± 2.7	]	0.97 ± 0.09
	6	12.2 ± 1.2		

Although our results are limited by the very low flux levels and by the fact that at 6 cm the structures we are observing are slightly different, it is clear that the spectral index does vary between these three regions, and consistently so for both the Western and Eastern structures, in the sense that there is flattening (α decreases) in both hotspots and steepening (α increases) in both shells, even if the individual values are slightly different (this may be attributed to low spatial resolution, disk obscuration of the E lobe, and/or different spectral indices in the pre-shock electrons for both shells). These results are also consistent with the spectral index map from Elmouttie et al. (1998a). As stated above, this symmetrical flattening of the spectral index at the centre of the "bubbles" is most easily explained if there is ongoing particle acceleration. The simplest scenario to explain this is that these regions are points where a radio jet interacts with the ISM, and thus the equivalents of the hotspots observed in more powerful systems (see Section 4.4.4 for more details). It is natural to assume that this same jet is the one that provided the energy injection that caused the shock we are observing. This is further supported by the morphology of the emission, which is coincident in X-rays and radio, and symmetrical for both lobes, roughly equidistant from the nucleus of the galaxy.

4.4.4 Jet-driven shocks

In light of these results we find that the scenario that best describes the data is that which is typically assumed for radio galaxies (see e.g. Scheuer 1974; Kaiser & Alexander 1997). In this scenario the jet emanating from the central AGN makes its way into the ISM of the host galaxy, transferring part of its energy to the surrounding gas at the termination points (or hotspots). This energy transfer heats up the ISM gas, creating a supersonic bow shock. The material that has flowed up the jet is observed in the form of radio lobes.

Hotspots in X-rays are characterised by a non-thermal powerlaw spectrum, though they are generally very faint, given that synchrotron losses are very high at these energies. As we stated in Section 4.3.2, the statistics of the spectra of the hotspot regions are quite poor, and they do not allow us to distinguish between thermal and non-thermal emission. If the emission were non-thermal, it would be unlikely to have its origin in widespread inverse Compton scattering, since the contribution of such a component for

low-power radio galaxies is negligible. We estimate the IC luminosity density at 1 keV to be $\sim 6\times10^{34}$ erg s^{-1} keV^{-1} for the case of Circinus (equivalent to 2–5$\times10^{-5}$ counts s^{-1} in *Chandra* ACIS-S, depending on the IC powerlaw photon index), using the assumptions on the B field detailed in Section 4.4.5. Moreover, if there was a detectable contribution from inverse Compton it would appear uniformly across both lobes. We calculated the spectral index between 6 cm and 1 keV for the W hotspot, and found it to be $\sim$ 1. This value is in the range of radio/X-ray ratios seen in FR I jets (see e.g. Harwood & Hardcastle 2012), suggesting that synchrotron emission could account for at least part of the X-ray emission we are observing.

Although our images do not show an active jet (at either radio, optical or X-ray frequencies), we know that this does not rule out the possibility that there is one, from what is observed in powerful FR II radio galaxies, where the jets are rarely seen, yet the presence of hotspots clearly indicates their presence (e.g. Kharb et al. 2008). The jet's rest-frame emissivity may be very low in Circinus. Moreover, the orientation of the lobes suggests that the jet should be at a large angle to the line of sight, so that relativistic beaming may be reducing the visibility of a jet that would intrinsically be visible. Doppler-dimmed jets and hotspots have been found in other Seyfert galaxies with low radio luminosities (see e.g. Kukula et al. 1999), illustrating how the interactions of the jet with different, complex environments can change the observed radio properties of these sources. This might also explain why the X-ray emission in the shells extends further than the radio along the (presumed) direction of propagation of the radio jet. This geometry is expected from some jet propagation simulations (see e.g. Sutherland & Bicknell 2007).

In this context, to further verify our shock scenario, we calculated the minimum internal pressure of the radio lobes under equipartition conditions from the radio data, fitting a broken power-law electron energy spectrum with $p = 2$ at low energies, steepening to $p = 3$ at the electron energy that gives the best fit to the data. We assumed ellipsoidal geometry, no protons and $\gamma_{min} = 10$. We obtained a value of $P \sim 6$–9×10^{-14} Pa, consistent with the results obtained by Elmouttie et al. (1998a), and roughly 2 orders of magnitude lower than the pressures we derive from our X-ray data. This departure from minimum energy is often found in FR I radio galaxies (e.g. Morganti et al. 1988); we also found this effect in NGC 3801, Mrk 6 and Cen A. These results imply that there is some additional contribution to the internal pressure, caused by a large de-

Table 4.5: Power scaling. The columns display the radio core luminosity, jet kinetic luminosity, and total energy (thermal+kinetic) inferred from the radio lobes for different galaxies, illustrating power scaling.

Source	$L_{1.4GHz}$	$L_{jet,kin}$	$E_{tot,lobes}$
	W Hz^{-1} sr^{-1}	erg s^{-1}	erg
Circinus	2.2×10^{20}	10^{41}	2×10^{55}
Cen A	1.2×10^{23}	10^{43}	
Mrk 6	1.7×10^{23}	10^{42}	$2.6-4.6\times10^{56}$
NGC 3801	1.2×10^{23}	3×10^{42}	1.7×10^{56}

viation from equipartition conditions, a high fraction of non-radiating particles, such as thermal or relativistic protons originating from the interaction of the galaxy's gas with the jet, or a low filling factor. Of these, the second explanation is the most plausible one (see Hardcastle et al. 2007c; Croston et al. 2008a).

From the age of the shells and the total energy we can infer the kinetic luminosity of the (invisible) jet, which is $\sim 10^{41}$ erg s^{-1}. Comparing these results to those we obtained for Mrk 6 (Mingo et al. 2011), NGC 3801 (Croston et al. 2007) or Cen A (Kraft et al. 2003) shows that these parameters scale down with the radio power of the parent AGN (see Table 4.5).

The fact that the X-ray emission in the shells is thermal is expected, if our shock scenario is correct. As pointed out by Croston et al. (2009), it is likely that fast shocks are required to produce in-situ particle acceleration and X-ray synchrotron emission in the shocked shells, as observed in Cen A. The velocities we derive, smaller than those found in Cen A, and the unequivocally thermal nature of the emission we observe, suggest that the case of Circinus is more similar to that of NGC 3801 or Mrk 6.

4.4.5 Implications for particle acceleration and parallels with SNR

The fact that the radio and X-ray emission are spatially coincident in the shells of Circinus resembles the morphology that is observed in some SNR, and poses the question of how similar the underlying physical processes are. Given that we do not observe non-thermal emission in the X-rays in the shells of Circinus, but we do see edge-brightening in radio, we investigate whether this enhancement of the radio synchrotron emission

in Circinus can be fully accounted for through a shock-driven enhancement of the B field strength, similar to what has been observed in ongoing cluster mergers (e.g. Markevitch et al. 2005; van Weeren et al. 2010). The configuration of the magnetic field in Circinus is not very clear. The argument of Elmouttie et al. (1998a), stating that the dominant component of the magnetic field in the shells of Circinus seems to be predominantly radial (perpendicular to the shock front, parallel to its direction of propagation) is based on polarization maps and is not very strong. Other systems such as NGC 1068 (Wilson & Ulvestad 1987; Simpson et al. 2002) and NGC 3079 (Duric & Seaquist 1988) indicate that fields tangential to the shock front (perpendicular to the direction of propagation of the shock) are more often found in radio galaxies. Both radial and tangential B field configurations can be found on SNR (see e.g. Milne 1987), but only the component that is tangential to the shock front is compressed by it. Compressed magnetic fields have been found around the leading edges of FR I radio galaxies (Guidetti et al. 2011, 2012) from rotation measure analysis, suggesting that, given the right conditions (a component to the magnetic field tangential to the front and a strong shock) this phenomenon may be common to many low-power systems.

To investigate whether this shock-driven B enhancement could be enough to account for the enhancement in radio emission, we must calculate whether the jump in emissivity (of a factor of at least 40) observed between the shells and the gas just outside them can be explained by this mechanism. The synchrotron emissivity of a powerlaw distribution of electrons is given by :

$$J(\nu) = CN_0\nu^{-\frac{(p-1)}{2}}B^{\frac{p+1}{2}} \tag{4.3}$$

where C can be assumed constant, N_0 is the normalization of the relativistic electron spectrum, and $(p-1)/2 = \alpha$. If we assume that B is tangential to the shock front, applying the Rankine-Hugoniot conditions for a strong shock results in $B_{shells}/B_{Circinus_{ext}} \propto \rho_{shells}/\rho_{Circinus_{ext}}$, which, substituting the values from Tables 4.2 and 4.3, results in $B_{shells} \sim 1.1\text{–}3B_{Circinus_{ext}}$. In Eq. 4.3 N_0 is proportional to the electron density, but given that the electron density depends on the energy density, which scales with the temperature in the shock, we have that $N_{0,shells}/N_{0,ext} \propto (\rho_{shells}/\rho_{Circinus_{ext}})(T_{shells}/T_{Circinus_{ext}})^{p-1}$. Substituting the values from Tables 4.2, 4.3 and 4.4 we can calculate the emissivity jump. Taking only the values for the W shell, which are better constrained, we

see that $\alpha \sim 0.70$–0.94 and $T_{shell} \sim 0.69 - 0.81$ keV. If $T_{Circinus_{ext}} = 0.2$ keV, using the densities from Tables 4.2 and 4.3, we have $(\rho_{shells}/\rho_{Circinus_{ext}}) \sim 1.1$–$1.7$, and $(T_{shells}/T_{Circinus_{ext}}) \sim 3.5$–$4.1$, thus $(J_{shells}/J_{Circinus_{ext}}) \sim 7$–$68$. If $T_{Circinus_{ext}} = 0.3$ keV we have $(\rho_{shells}/\rho_{Circinus_{ext}}) \sim 1.9$–$3.0$, and $(T_{shells}/T_{Circinus_{ext}}) \sim 2.3$–$2.7$, thus $(J_{shells}/J_{Circinus_{ext}}) \sim 18$–$164$.

These results show that shock-compression alone could be enough to fully account for the enhancement in radio synchrotron emission if the conditions are favourable (a strong shock and a magnetic field tangential to the shock front). It is likely that, even in the best conditions, there is a component of the magnetic field that is perpendicular to the shock front. Our results do not preclude local particle acceleration—it is in fact needed if the conditions at the shock are not ideal—but we know that any particle reacceleration is not efficient enough to power synchrotron emission in the X-rays.

When making the parallel between the shells of Circinus and what is observed in SNR, some caution must be exercised. In young SNR where B field amplification is observed, it is mediated by efficient particle acceleration (Völk et al. 2005). It seems to be clear that, in most cases, field compression alone cannot account for the acceleration of cosmic rays that is observed in SNR, which are in fact the main source of Galactic cosmic rays. The field amplification in SNR is much larger than the enhancement expected from shock compression alone, given that the values of B in SNR tend to be of the order of mG (Vink & Laming 2003), 2–3 orders of magnitude higher than the values found in spiral galaxies, where typical values for the ISM of the disk are ~ 10 μG, (see e.g. Beck et al. 1996; Vallée 2011; Hummel et al. 1991; Beck et al. 1994). Synchrotron losses also become substantial at the values of B found in most SNR. Rayleigh-Taylor instabilities at the shock front (Guo et al. 2012) seem to be present in most SNR. While Rayleigh-Taylor instabilities may be behind some of the B enhancement in shock shells around radio galaxy lobes, strong instabilities are not expected to develop until the jet has switched off and the radio lobes have become buoyant (see e.g. Brüggen & Kaiser 2001).

The fact that the spectral index in the hotspots of Circinus is flatter than that of the lobes suggests that there is spectral ageing of the synchrotron emission, evolving radially outwards from the hotspots. In the model we discuss here the electron population in the shells, however, must come from electrons from the external medium swept up in the shock. These electrons are already relativistic, as we know from synchrotron

observations of the haloes of spiral galaxies (see e.g. Beck et al. 1996). We cannot directly measure the spectral index of the emission outside the shells, since it is too faint. However, we studied the spectral index in the disk, and found a value $\alpha \sim 1$. This value is similar to that found in the shells, hinting that this is the spectral index of the electron population outside the shells as well. This provides additional support to the idea that the halo electrons swept up in the shock are not strongly reaccelerated, since that would flatten their spectral index, and that the main mechanism behind the enhanced synchrotron emission in the shells we observe in the radio maps is indeed a B field enhancement. The thermal nature of the X-ray emission in the shells also supports the hypothesis of shock compression as the dominant mechanism behind the radio emission enhancement.

We carried out equipartition calculations for the shells, and found that, under those conditions, the pressures we derive are over an order of magnitude below our measurements. This suggests that the shells are not in equipartition and that the contribution to the total energy density from the synchrotron-emitting electrons is not the dominant one. This is to be expected, since the spatial coincidence between the X-ray emitting hot gas and the synchrotron-emitting plasma implies that they coexist in this region, and the former component is expected to dominate the energy density.

As mentioned above, compressed magnetic fields may be common to low-power radio galaxies. Given that field enhancement through shock compression does not preempt particle acceleration, it is likely that in most systems a combination of both is responsible for the observed emission. An accurate measurement of the spectral index and emissivity of the electrons outside the lobes, and better X-ray statistics for both the shells and the external environment, would allow us to estimate the contributions from both processes in Circinus and in other systems. In the case of systems more similar to Cen A, where particle acceleration seems to be causing synchrotron emission in the shells, all the way to the X-rays, constraints on the magnetic field in the shock, e.g. via rotation measure analysis, as in Guidetti et al. (2011), could be used for estimations on the contribution to the emission caused by magnetic field compression.

Our results suggest that the parallel between the jet-driven shocks of low power FR I galaxies and those of SNR, where a similar morphology and some of the same physical processes can be expected, is more common than we previously thought. The fact that it has only been observed in Circinus is mainly due to the small distance between

this galaxy and our own, which allows us to spatially resolve these structures, and observe their characteristics with the level of sensitivity of our current instruments. This is particularly relevant for more distant low-power radio galaxies in general, and those with late-type hosts in particular. It is also significant for the edge-brightening in the radio lobes of Mrk 6 (Kharb et al. 2006; Mingo et al. 2011), which could be explained through this mechanism. As pointed out in Section 4.4.2, the shock results suggest that we are facing a scenario similar to the one we found in NGC 3801, suggesting that some of our conclusions may apply to this object, as well as, possibly, to NGC 6764.

4.5 Conclusions

We have presented a detailed analysis of the X-ray emission associated with the radio lobes of the Circinus galaxy. Our deep *Chandra* observation has allowed us to study both the morphological correspondence between radio and X-ray emission, and the X-ray spectral properties of the gas in these structures. We conclude that we are observing shells of shocked gas around the radio lobes of Circinus, expanding into the halo regions of the galaxy with Mach numbers $\mathcal{M} \sim 2.7$–3.6 for the W shell and $\mathcal{M} \sim 2.8$–5.3 for the E shell, consistent with the Rankine-Hugoniot conditions for a strong shock.

We rule out the possibility that this emission is caused by AGN photoionization, and discard the scenario in which the radio structures are the result of star formation or a supernova-driven wind; instead we argue that they are caused by the interaction of a radio jet with the surrounding gas. The total energy (thermal and kinetic) involved in the creation of these shells is $\sim 2 \times 10^{55}$ erg. We estimate their age to be $\sim 10^6$ years. From these parameters we infer the kinetic luminosity of the jet, which is $\sim 10^{41}$ erg s^{-1}. When comparing these results with those previously obtained for Cen A, Mrk 6 and NGC 3801, we observe that they scale with the radio power of the source.

The presence of two symmetrical structures resembling jet termination points or “hotspots”, together with the slightly different X-ray spectra and flattening of radio spectral index in these regions, suggests that the radio jet may still be active, even if it is not visible. This suggests that “invisible” jets may be a more common occurrence among Seyfert and late type galaxies than previously thought, given that it is difficult to separate the different radio structures in galaxies with active star formation, when

the radio bubbles are faint or their orientation is similar to that of the disk. This opens new questions on the role of low radio luminosity, star-forming, active galaxies, which are often ignored in survey studies.

In Circinus the X-ray and radio emission from the shocked shells are spatially coincident. This, added to the fact that the radio emission is edge-brightened, allows us to draw a parallel between these structures and what is observed in supernova remnants: the radio emission from the shells comes from shock-compressed or (re)accelerated cosmic ray electrons in the environment, but particle acceleration, if present at all, is not efficient enough to produce TeV electrons, so that only thermal emission is observed in X-rays. This correspondence has been long expected for AGN, given the similarity between the physical processes involved in SN and jet-driven shocks, but has not been unequivocally observed before. We believe this scenario may be common to other low-power radio galaxies, and potentially very relevant to those with late-type hosts, but can only be observed where we are able to spatially resolve the different structures, something that has been achieved for Circinus due to its proximity to us.

Chapter 5

The 2Jy sample of radio-loud AGN

5.1 Introduction: the 2Jy sample of Southern radio galaxies

The 2Jy sample of radio galaxies[1] was defined by Wall and Peacock in 1985 (Wall & Peacock 1985). It includes all the galaxies with flux greater than 2Jy at 2.7 GHz, with a maximum redshift z=0.7. Tadhunter et al. (1993) and Morganti et al. (1993) defined a subsample of Southern sources with $\delta < +10^{\circ}$ with a complete radio and optical study.

In this Chapter I describe the objects in a statistically complete subsample of the 2Jy steep-spectrum sources defined by Dicken et al. (2008), containing 47 objects with with $\delta < +10^{\circ}$ and redshifts $0.05 < z < 0.7$. Particle acceleration in the jet causes the radio spectrum to flatten, thus the steep-spectrum ($\alpha > 0.5$) selection of Dicken et al. (2008) excludes core and jet dominated sources As for Dicken et al. (2008), we have also included the flat-spectrum, core-dominated sources 3C 273 and PKS 0521–36 for comparison. The subsample studied here has consistent, uniform multiwavelength coverage. Chapter 6 describes in detail the analysis done on the cores of these galaxies.

All the AGN in this subsample have X-ray observations save for PKS 0117–15 (3C 38), which, unfortunately, was not observed by *XMM-Newton*. The list of galaxies in the sample and the *Chandra* and *XMM-Newton* observations are listed in Table 5.1. Most of the observations were taken specifically for this project, *Chandra* observations were requested for the low-z sources to map any extended emission (jets, hotspots,

[1] http://2Jy.extragalactic.info/2Jy_home_page.html

lobes and any emission from a hot IGM for sources in dense environments). For the sources with $z > 0.2$, where extended structures cannot be resolved, we requested *XMM* observations instead, to maximise the signal to noise ratio of the AGN spectra, so as to allow spectral separation of the unresolved components.

From a radio classification point of view, the sample is dominated by powerful sources, with 6 objects being Fanaroff-Riley type I (FR I), 8 compact sources (compact steep-spectrum/gigahertz peaked-spectrum, labeled as CSS or C/J), and 32 Fanaroff-Riley type II (FR II) (Morganti et al. 1993, 1999). As for emission line classification, 10 sources are LERGs, 19 are NLRGs, 13 are BLRGs and 4 are QSOs (Tadhunter et al. 1993, 1998). Two of our BLRGs (PKS 0035-02, or 3C 17, and PKS 1151-34) have double-peaked Balmer lines, which have been a matter of debate regarding the possibility that they are generated in radiatively-inefficient scenarios (see e.g. Eracleous & Halpern 1994; Nagao et al. 2002). Recent results, however, seem to indicate that, at best, double-peaked lines are common to radiatively inefficient and efficient sources (Wu & Liu 2004), if not a sign of radiatively efficient accretion, as ordinary broad lines are (see e.g. the review by Sulentic et al. 2000).

The 2Jy sample does not overlap with the 3CRR catalogue, due to the different location of the sources (the 3CRR catalogue covers sources in the Northern hemisphere, $\delta > +10°$). Some of the brightest sources are included in the original 3C catalogue, as is the case for e.g. the quasar 3C 273 (PKS 1226+02). Although we have excluded core-dominated sources (to minimise the effects of beaming, and with the exception of PKS 0521-36 and 3C 273, which we kept for comparison), the 2Jy selection is established for a higher frequency than the 3CRR sample, which implies that, overall, more beamed sources are selected for the 2Jy sample than they are for the 3CRR. Some of the implications of this fact are discussed in Section 6.4.

Throughout this and the next Chapter I have kept the existing optical line classifications for the objects in both the 2Jy and in the 3CRR samples, for consistency, but point out when evidence suggests that this classification belies the true nature of a specific object.

Table 5.1: Objects in the 2Jy sample observed with *Chandra* (ACIS-S except for PKS 0625–53 and PKS 2135–14, which were taken with the ACIS-I) and *XMM-Newton* (MOS and PN). FRI and FRII stand for Fanaroff-Riley class I and II respectively, CSS stands for compact steep-spectrum, BL-LAC for BL-Lacertae object.

PKS	FR Class	Type	z	Instrument	Obsid	Exp (ks)
0023-26	CSS	NLRG	0.322	*XMM*	0671870601	19.55
0034-01	FRII	LERG	0.073	*Chandra*	02176	28.18
0035-02	FRII	BLRG	0.220	*Chandra*	09292	8.04
0038+09	FRII	BLRG	0.188	*Chandra*	09293	8.05
0039-44	FRII	NLRG	0.346	*XMM*	0651280901	20.57
0043-42	FRII	LERG	0.116	*Chandra*	10319	18.62
0105-16	FRII	NLRG	0.400	*XMM*	0651281001	21.27
0213-13	FRII	NLRG	0.147	*Chandra*	10320	20.15
0235-19	FRII	BLRG	0.620	*XMM*	0651281701	13.67
0252-71	CSS	NLRG	0.566	*XMM*	0651281601	19.17
0347+05	FRII	LERG	0.339	*XMM*	0651280801	16.47
0349-27	FRII	NLRG	0.066	*Chandra*	11497	20.14
0404+03	FRII	NLRG	0.089	*Chandra*	09299	8.18
0409-75	FRII	NLRG	0.693	*XMM*	0651281901	13.67
0442-28	FRII	NLRG	0.147	*Chandra*	11498	20.04
0521-36	C/J	BL-LAC/BLRG	0.055	*Chandra*	00846	9.87
0620-52	FRI	LERG	0.051	*Chandra*	11499	20.05
0625-35	FRI	LERG	0.055	*Chandra*	11500	20.05
0625-53	FRII	LERG	0.054	*Chandra*	04943	18.69
0806-10	FRII	NLRG	0.110	*Chandra*	11501	20.04
0859-25	FRII	NLRG	0.305	*XMM*	0651282201	13.85
0915-11	FRI	LERG	0.054	*Chandra*	04969	98.2
				Chandra	04970	100.13
0945+07	FRII	BLRG	0.086	*Chandra*	06842	30.17
				Chandra	07265	20.11
1136-13	FRII	Q	0.554	*Chandra*	02138	9.82
				Chandra	03973	77.37
1151-34	CSS	Q	0.258	*XMM*	0671870201	18.67
1226+02	FSRLQ	Q	0.158	*XMM*	126700601	27.19
1306-09	CSS	NLRG	0.464	*XMM*	0671871201	22.67
1355-41	FRII	Q	0.313	*XMM*	0671870501	14.97
1547-79	FRII	BLRG	0.483	*XMM*	0651281401	13.25
1559+02	FRII	NLRG	0.104	*Chandra*	06841	40.18
1602+01	FRII	BLRG	0.462	*XMM*	0651281201	13.67
1648+05	FRI	LERG	0.154	*Chandra*	05796	48.17
				Chandra	06257	50.17
1733-56	FRII	BLRG	0.098	*Chandra*	11502	20.12
1814-63	CSS	NLRG	0.063	*Chandra*	11503	20.13
1839-48	FRI	LERG	0.112	*Chandra*	10321	20.04
1932-46	FRII	BLRG	0.231	*XMM*	0651280201	13.18
1934-63	CSS	NLRG	0.183	*Chandra*	11504	20.05
1938-15	FRII	BLRG	0.452	*XMM*	0651281101	18.17
1949+02	FRII	NLRG	0.059	*Chandra*	02968	50.13
1954-55	FRI	LERG	0.060	*Chandra*	11505	20.92
2135-14	FRII	Q	0.200	*Chandra*	01626	15.13
2135-20	CSS	BLRG	0.635	*XMM*	0651281801	17.57
2211-17	FRII	LERG	0.153	*Chandra*	11506	20.04
2221-02	FRII	BLRG	0.057	*Chandra*	07869	46.20
2250-41	FRII	NLRG	0.310	*XMM*	0651280501	13.67
2314+03	FRII	NLRG	0.220	*XMM*	0651280101	21.67
				Chandra	12734	8.05
2356-61	FRII	NLRG	0.096	*Chandra*	11507	20.05

5.2 The low-z sources

As mentioned in the previous Section, we analysed *Chandra* observations for the low-*z* sources in our sample. Four low-*z* sources (PKS 0404+03, 1814–63, 2135–14, 2221–02) have *XMM* observations that we did not use, since the *Chandra* images provided all the information needed for the analysis described in Chapter 6.

The following subsections briefly describe the images and spectra of the 2Jy sources imaged by *Chandra*, with the exception of PKS 1226+02 (3C 273), which was the first object to be identified as a quasar, and as such has been thoroughly studied in the past (see e.g. Soldi et al. 2008; Jester et al. 2005, 2006; Liu & Zhang 2011, and references therein).

All the X-ray images correspond to ACIS-S observations except for PKS 0625–53 and PKS 2135–14, which were taken with the ACIS-I. The images have been filtered to show just the 0.3-7 keV energy range, and are smoothed with a Gaussian profile with $\sigma = 3$ pixels (1 pixel=0.492 arcsec), to better show the extended structures. The original radio maps can be found in Morganti et al. (1993, 1999) and references therein. No radio contours are shown in Figs. 5.18 (PKS 1814–63) and 5.20 (PKS 1934–63), since these are compact steep-spectrum sources (CSS) and have no extended radio structures.

PKS 0034–01 (3C 15)

PKS 0034–01 has a radio morphology that is intermediate between that of an FR I and an FR II. The host galaxy sits in a relatively sparse environment, and it does not appear to be disturbed or interacting (Ramos Almeida et al. 2010) but it has a dust lane (Martel et al. 1999). The *Chandra* observation shows a 6 kpc one-sided jet (for a detailed study see Dulwich et al. 2007), which is also detected in radio (Morganti et al. 1999) and the Ks band (Inskip et al. 2010). There is also some X-ray emission coincident with the edges of the radio lobes (Kataoka et al. 2003), hinting at a possible jet-driven shock, similar to the ones we studied in e.g. Cen A (Kraft et al. 2003; Croston et al. 2009) or Mrk 6 (Mingo et al. 2011). Although this object is classified as a LERG, in our plots it is near the luminosity break between LERGs and NLRGs ($L_{X,2-10keV} = 6.6 \times 10^{42}$ erg s^{-1}, see Table 6.1). Its spectrum is relatively obscured ($N_H \sim 10^{23}$ cm^{-2}), and requires two powerlaw components. We do not detect a Fe K-α line, as we did for PKS 0043–

42. It is unclear whether PKS 0034–01 is a “true” (albeit somewhat atypical) LERG, a low-luminosity NLRG, or an intermediate case. The absence of a torus (van der Wolk et al. 2010) seems to point towards the first possibility, though its poor environment makes it difficult to explain where the hot gas for a radiatively-accretion scenario might come from, given that it does not show evidence for any recent star formation either (Dicken et al. 2012).

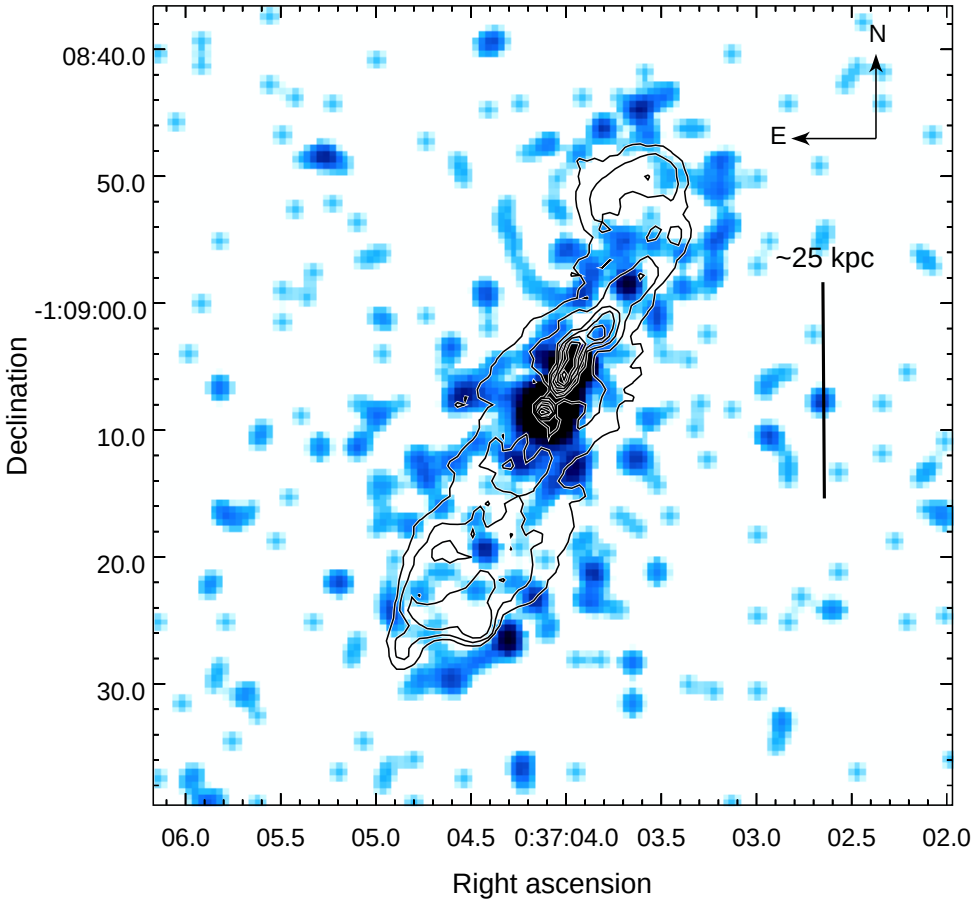

Figure 5.1: PKS 0034-01 (3C 15). The radio contours increase by factors of 2 between 0.0001 and 0.0128 Jy/beam, the beam major axis is 0.34 arcsec, and the minor axis is 0.34 arcsec.

PKS 0038+09 (3C 18)

This BLRG seems to be in a dense environment (Ramos Almeida et al. 2010). We do not detect a luminous intracluster medium, but there seems to be some extended emission around the AGN in our images. Its X-ray spectrum is bright (we had to correct it for pileup), and is well described with a single powerlaw component, with no traces of intrinsic absorption, as is expected for most broad-line objects.

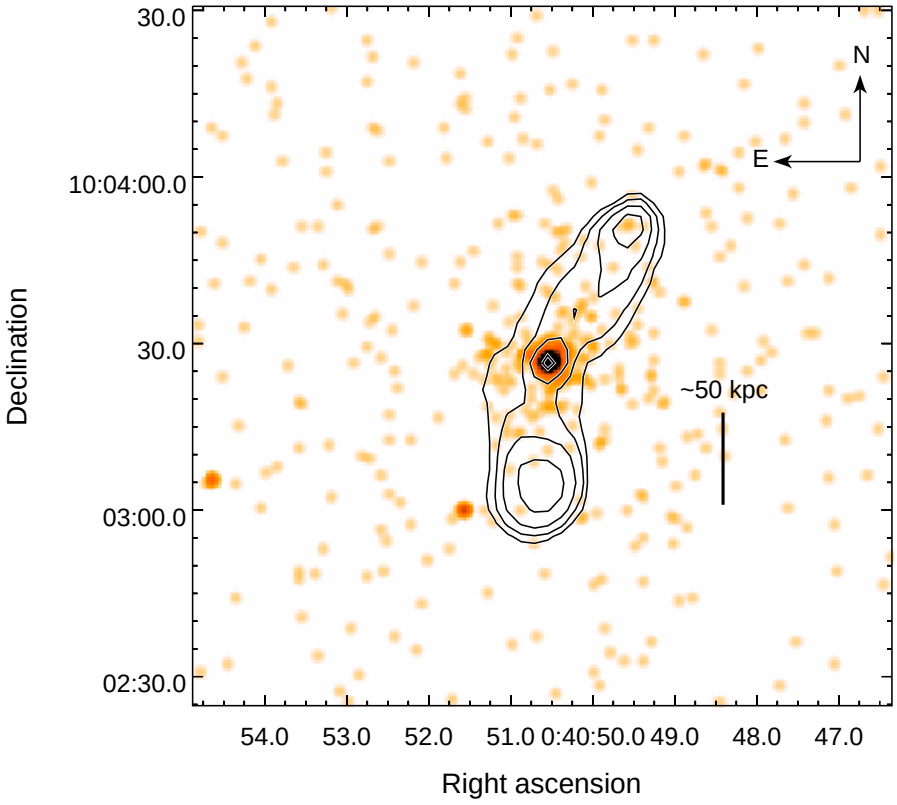

Figure 5.2: PKS 0038+09 (3C 18). The radio contours increase by factors of 2 between 0.007 and 0.112 Jy/beam, the beam major axis is 4.37 arcsec, and the minor axis is 3.39 arcsec.

PKS 0043–42

PKS 0043–42 seems to live in a dense environment (Ramos Almeida et al. 2010), from which we detect some faint extended emission in our *Chandra* image. (Inskip et al. 2010) report a possible interaction with a nearby companion. Its radio morphology is very extended, and typical of a powerful FR II, with strong hotspots and no detectable radio core (Morganti et al. 1999). Although it is classified as a LERG, PKS 0043–42 is most likely a high excitation object where the strong emission lines are simply not detected. (Ramos Almeida et al. 2010) find distinct evidence for a clumpy torus in their *Spitzer* data, and its X-ray spectrum shows clear signatures of radiatively efficient accretion, in the form of a bright hard component and a Fe K-α emission line. Its high luminosity situates this object in the parameter space occupied by the fainter NLRGs in our plots.

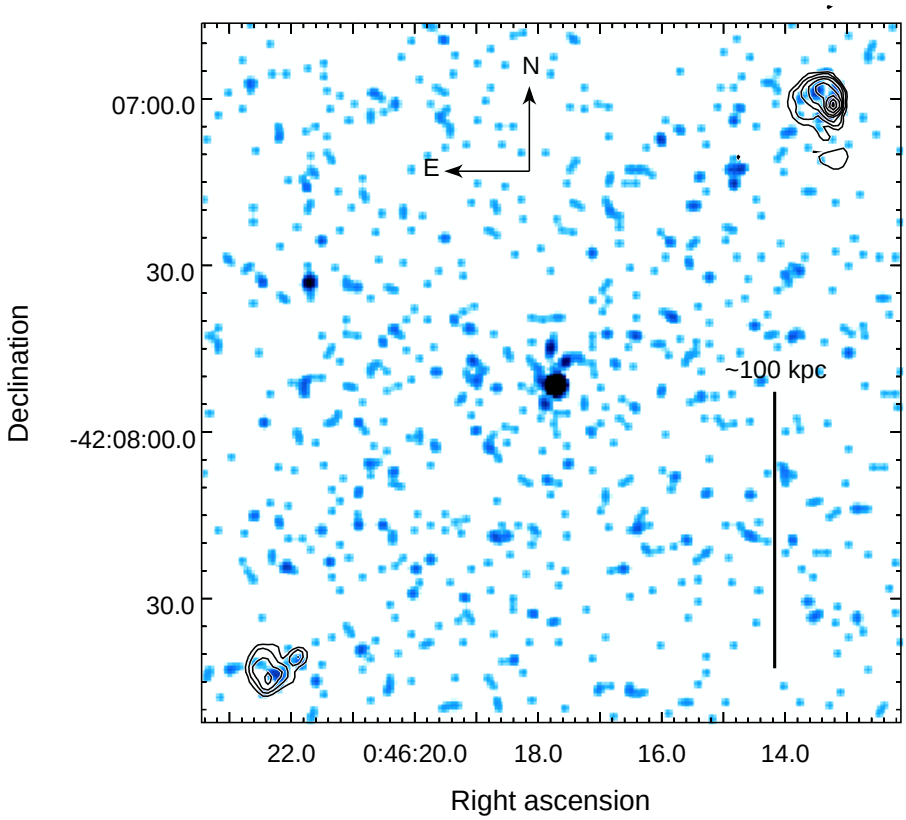

Figure 5.3: PKS 0043-42. The radio contours increase by factors of 2 between 0.0008 and 0.1024 Jy/beam, the beam major axis is 1.19 arcsec, and the minor axis is 0.88 arcsec.

PKS 0213–13 (3C 62)

This NLRG has an optical shell and a narrow tidal tail (Ramos Almeida et al. 2010). The *Chandra* image features a very bright hotspot W of the nucleus, coincident with the radio emission, and some enhanced emission inside the lobes, possibly from inverse-Compton scattering. The spectrum is dominated by the hard component, with the soft, jet-related component being very faint.

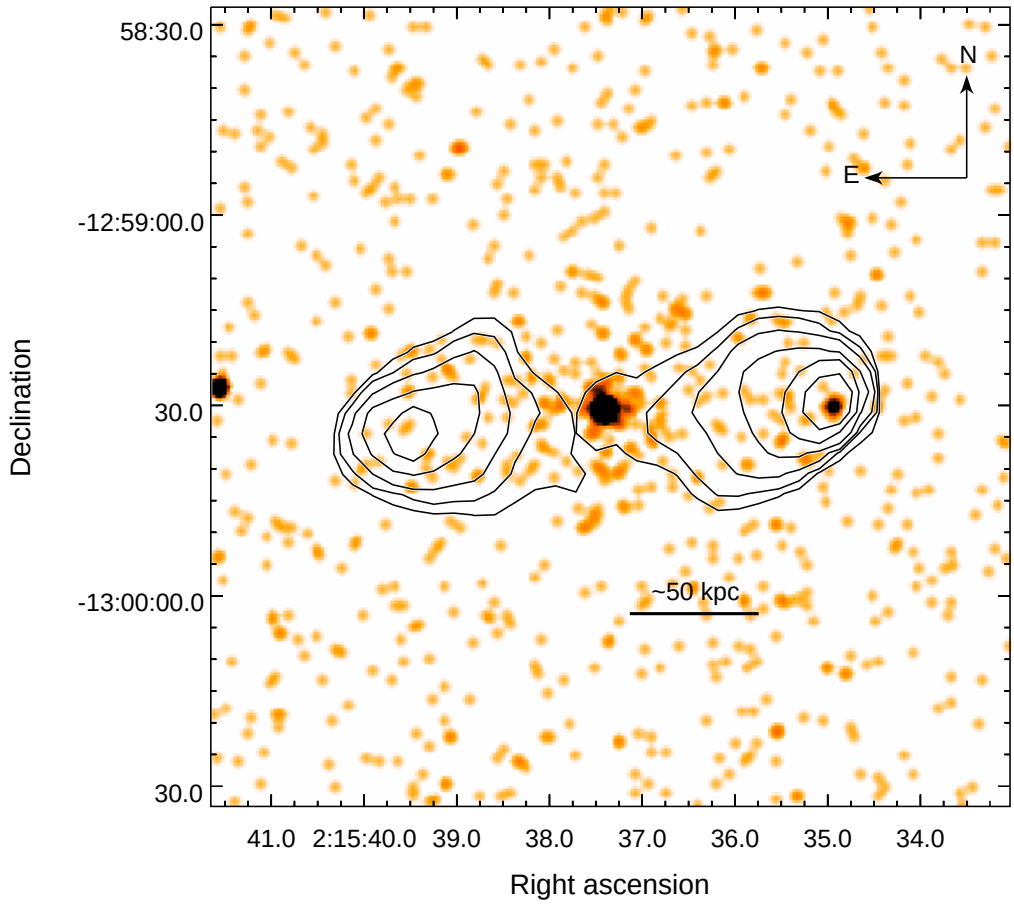

Figure 5.4: PKS 0213-13 (3C 62). The radio contours increase by factors of 2 between 0.003 and 0.192 Jy/beam, the beam major axis is 5.92 arcsec, and the minor axis is 3.44 arcsec.

PKS 0349–27

This well-known FR II galaxy has some remarkable optical features, including an extended narrow line region and bridges connecting it to two neighbouring galaxies (Ramos Almeida et al. 2010; Inskip et al. 2010). In our *Chandra* image we detect some extended emission in the E-W direction, which could be associated with the optical bridges linking the host to the other galaxies or a hot medium. We also see a faint enhancement of the emission inside the lobes, and an enhancement in emission with a slight offset with the NE radio hotspot. The X-ray spectrum shows very little absorption and is completely dominated by the hard component; we were only able to obtain an upper limit on the jet-related powerlaw (see Table 6.1).

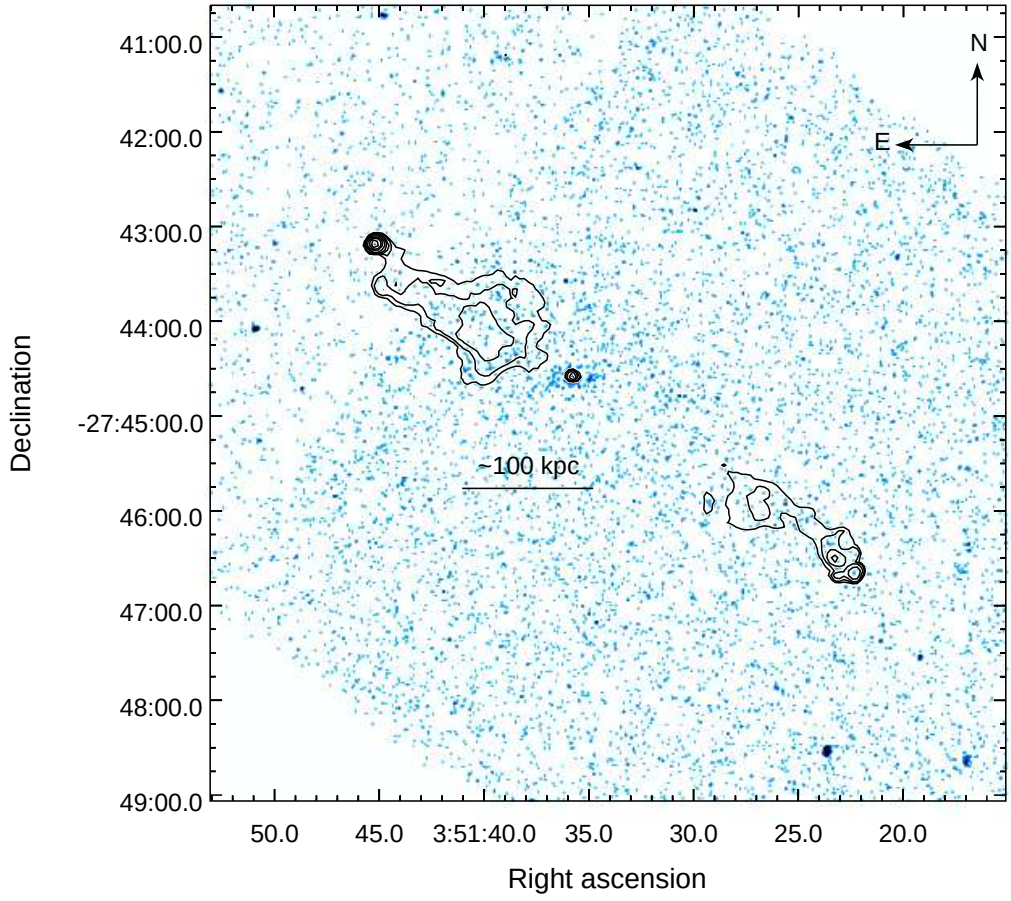

Figure 5.5: PKS 0349-27. The radio contours increase by factors of 2 between 0.0004 and 0.1024 Jy/beam, the beam major axis is 3.38 arcsec, and the minor axis is 2.52 arcsec.

PKS 0404+03 (3C 105)

The host of PKS 0404+03 has been studied in detail in the optical and IR (see Inskip et al. 2010, and references within), despite the presence of a nearby star and the high foreground N_H column. van der Wolk et al. (2010) failed to detect a dusty torus in this system. The *Chandra* image shows some emission coincident with the SE radio hotspot. The spectrum is somewhat atypical, with high intrinsic absorption, very faint soft emission ($\sim$ 20 photon counts between 0.4 and 3 keV) and a bright accretion-related component.

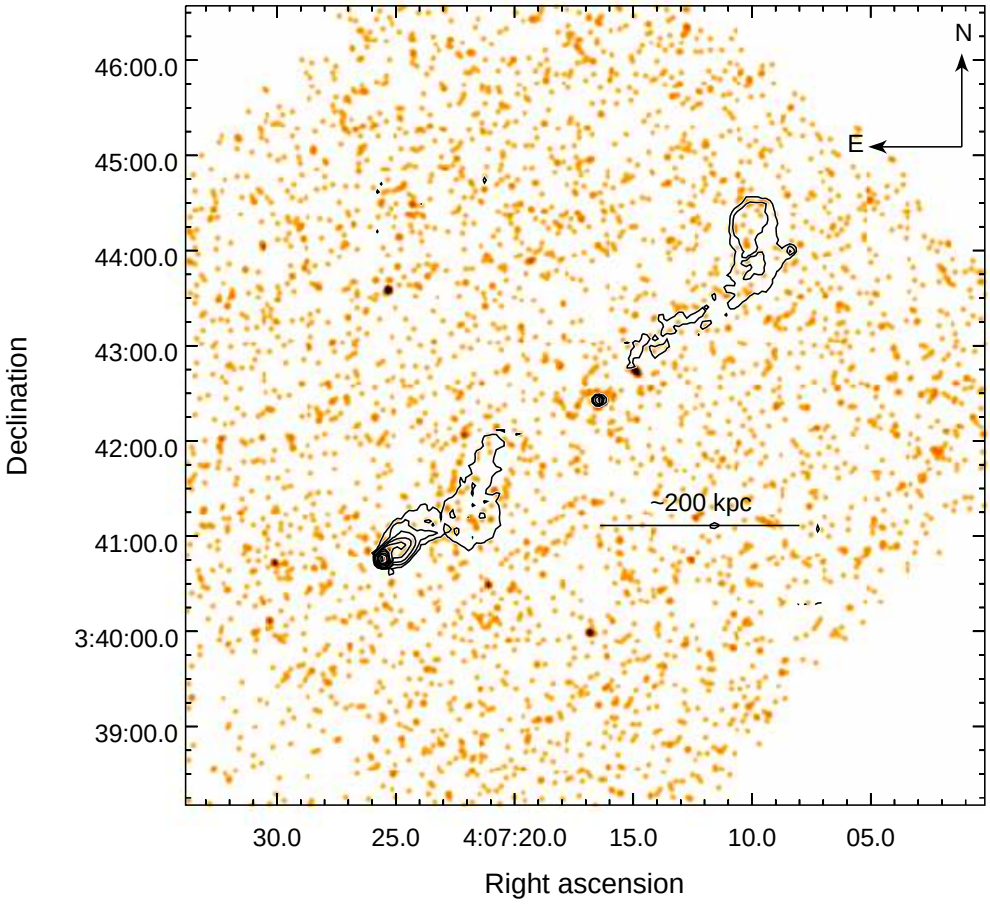

Figure 5.6: PKS 0404+03 (3C 105). The radio contours increase by factors of 2 between 0.0003 and 0.3072 Jy/beam, the beam major axis is 2.20 arcsec, and the minor axis is 2.20 arcsec.

PKS 0442–28

The *Chandra* image of this NLRG shows some extended emission, particularly surrounding the base of the N radio lobe, although there are no indications of it belonging to a cluster (Ramos Almeida et al. 2010). There is also some X-ray emission inside the lobes, presumably from inverse-Compton scattering, and a bright region coincident with the N hotspot. The spectrum is very bright, with low intrinsic absorption and a strong accretion-related component. There seems to be some excess emission around 5-6 keV, indicating the possible presence of a Fe K-α line, but adding a Gaussian component to the best fit model did not improve the statistics.

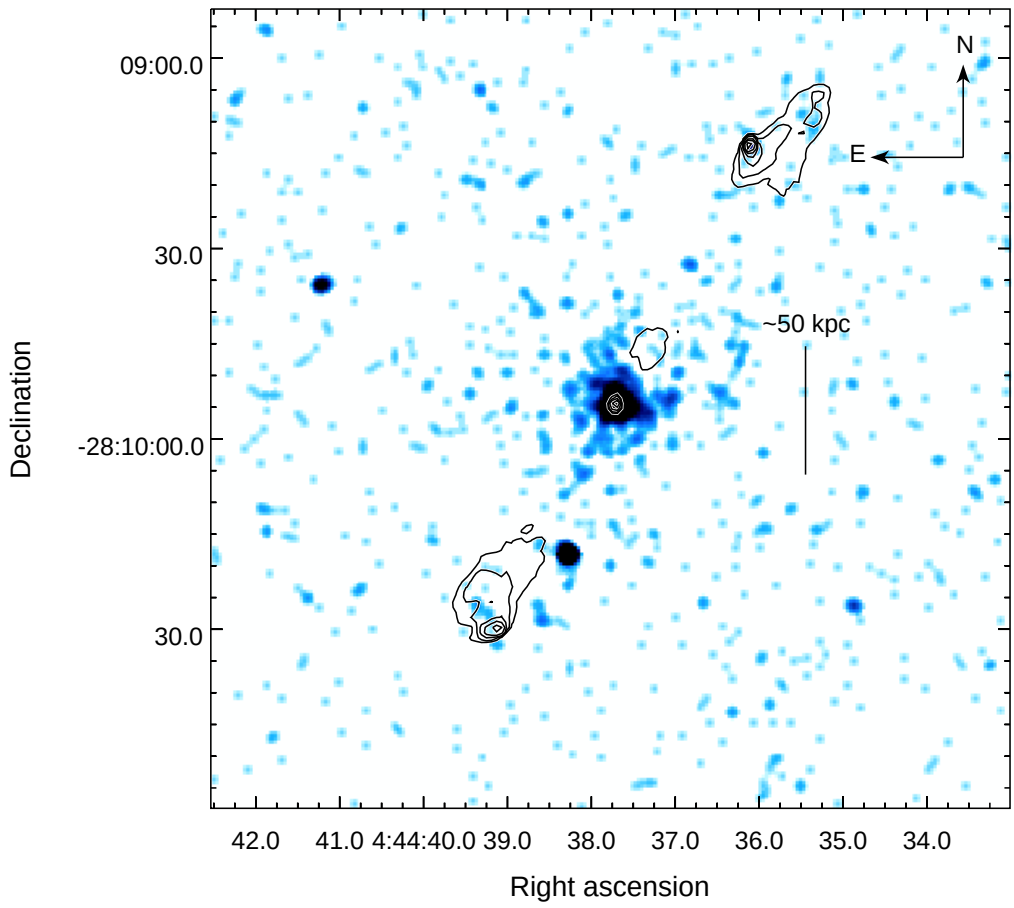

Figure 5.7: PKS 0442-28. The radio contours increase by factors of 2 between 0.001 and 0.128 Jy/beam, the beam major axis is 1.02 arcsec, and the minor axis is 0.56 arcsec.

PKS 0521–36

PKS 0521–36 is a very bright BL-Lac/BLRG (see Inskip et al. 2010, and references therein). The *Chandra* image features a large streak, and is quite piled up. The spectrum is well described with a single, unabsorbed powerlaw, as expected from this type of object.

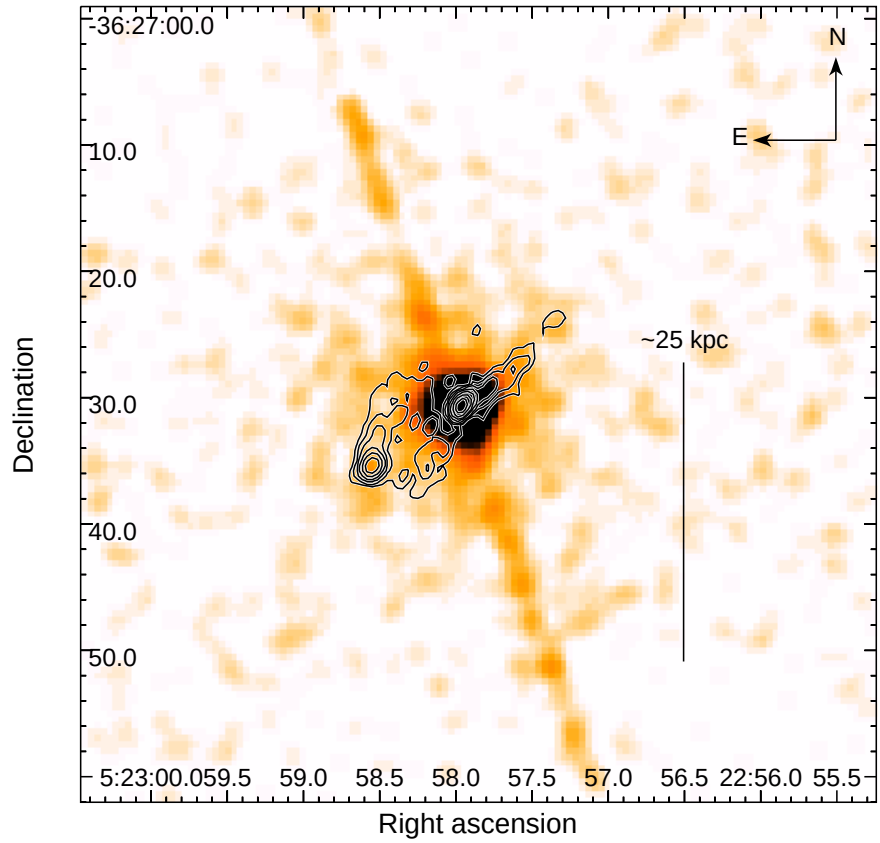

Figure 5.8: PKS 0521-36. The radio contours increase by factors of 2 between 0.02 and 2.56 Jy/beam, the beam major axis is 1.18 arcsec, and the minor axis is 0.72 arcsec. The instrumental streak is visible in the NE-SW direction.

PKS 0620–52

This LERG has the lowest redshift in our sample, and shows evidence for a young stellar population (Dicken et al. 2012). Although its optical morphology is not disturbed (Ramos Almeida et al. 2010), the presence of numerous nearby galaxies, and the fact that we detect extended emission in our *Chandra* image, make us agree with the hypothesis of Siebert et al. (1996); Trussoni et al. (1999) that this object sits in a rich cluster. The emission is slightly stronger along the Southern edge of the radio lobes. Its spectrum is quite faint; we were able to detect and fit the soft component, but obtained only an upper limit on the accretion-related emission.

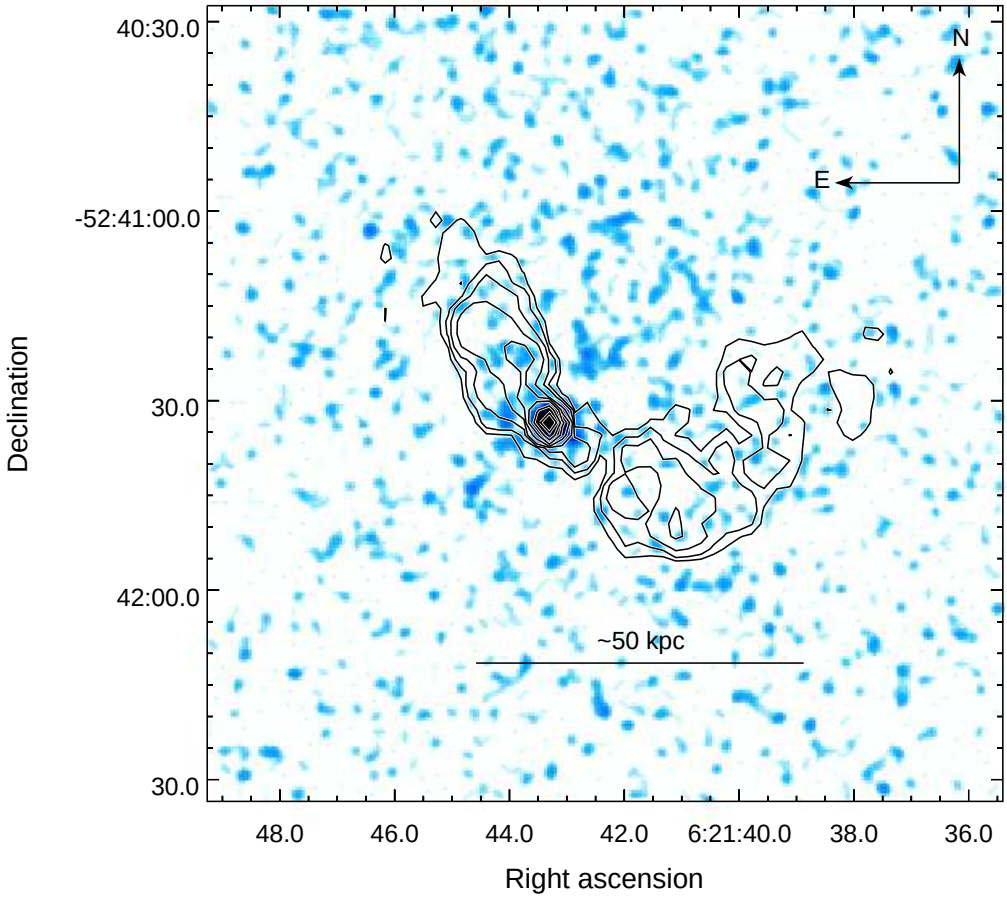

Figure 5.9: PKS 0620-52. The radio contours increase by factors of 2 between 0.0005 and 0.1280 Jy/beam, the beam major axis is 2.64 arcsec, and the minor axis is 1.53 arcsec.

PKS 0625–35

This object is suspected to be a BL-Lac (Wills et al. 2004). It has a one-sided jet (Ramos Almeida et al. 2010; Inskip et al. 2010), and it does not seem to be interacting. The presence of a cluster environment around it is also unclear (Trussoni et al. 1999). Although optically classified as a LERG, it is clear from our data that this is not a "standard" low-excitation object. The *Chandra* image shows a large streak, and is piled up. The spectrum is very bright, with some intrinsic absorption and two powerlaw components. In our plots PKS 0625–35 sits near the low-luminosity end of the NLRGs, its accretion-related luminosity being only below that of PKS 0043–42 and PKS 0034–01, which are both "dubious" LERGs. Beaming might account for the enhanced luminosity.

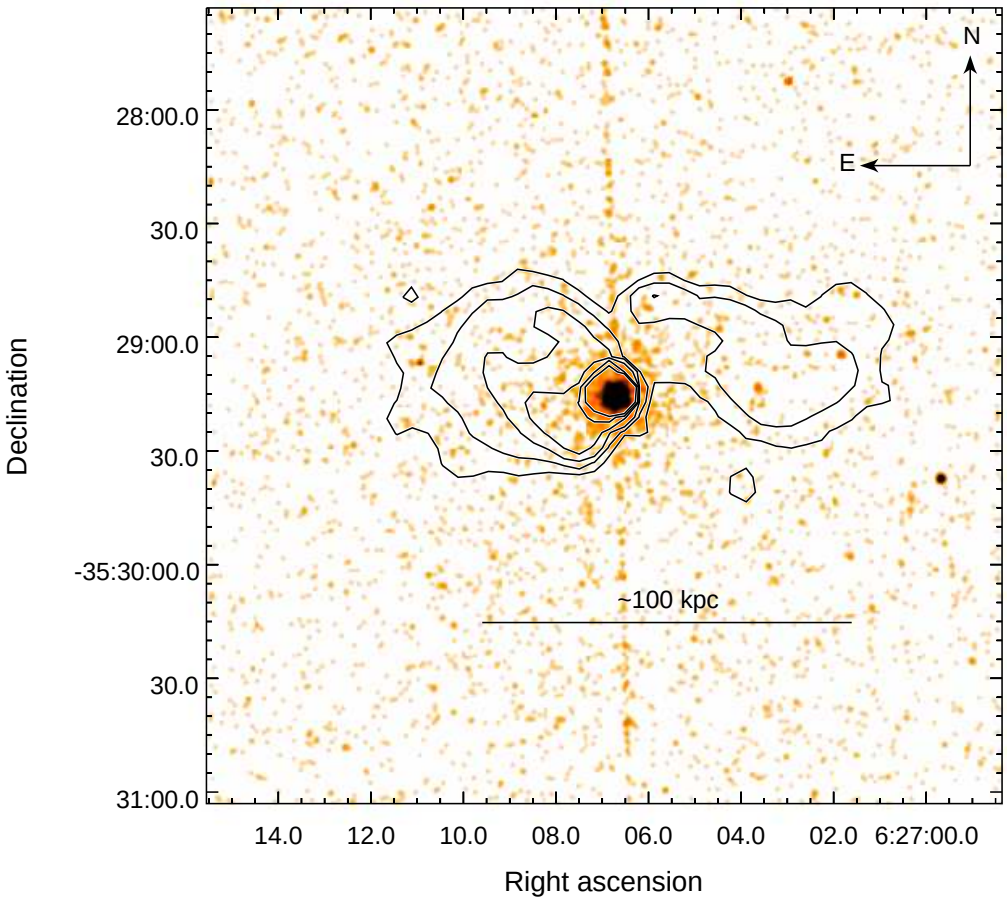

Figure 5.10: PKS 0625-35. The radio contours increase by factors of 2 between 0.001 and 0.032 Jy/beam, the beam major axis is 4.70 arcsec, and the minor axis is 3.25 arcsec. The instrumental streak is visible in the N-S direction.

PKS 0625–53

This LERG is hosted by a dumbbell galaxy, which is also the brightest member in Abell 3391. It has an FR I radio morphology with a wide-angled tail (Morganti et al. 1999) and a deflected jet. The optical images show a bridge of interaction with the W component of the dumbbell system (Ramos Almeida et al. 2010), and a strong nuclear component is not detected in the IR (Inskip et al. 2010), consistent with the classification as a low excitation object. The *Chandra* image shows emission around the galaxy from the hot ICM. The nucleus is very faint in X-rays; our spectrum only has one bin, which allows us to constrain an upper limit to the luminosity.

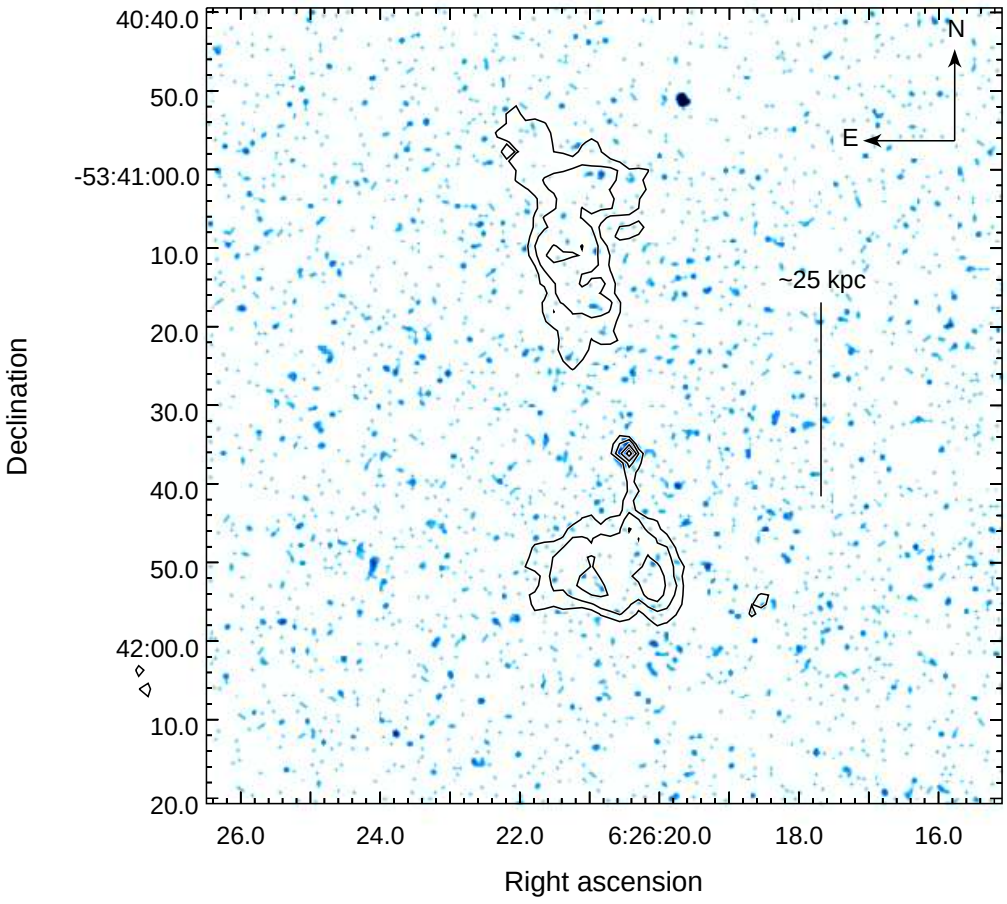

Figure 5.11: PKS 0625-53. The radio contours increase by factors of 2 between 0.0007 and 0.0112 Jy/beam, the beam major axis is 1.10 arcsec, and the minor axis is 0.92 arcsec.

PKS 0806–10 (3C 195)

The optical and IR images of this galaxy show clear signs of disturbance (Inskip et al. 2010; Ramos Almeida et al. 2010). Our *Chandra* image shows some enhancement in emission at the base of the radio lobes, and hotspots that are spatially coincident with the radio emission (Morganti et al. 1993), the Southern one being the stronger of the two. The spectrum is bright, with a strong accretion-related component and some intrinsic absorption.

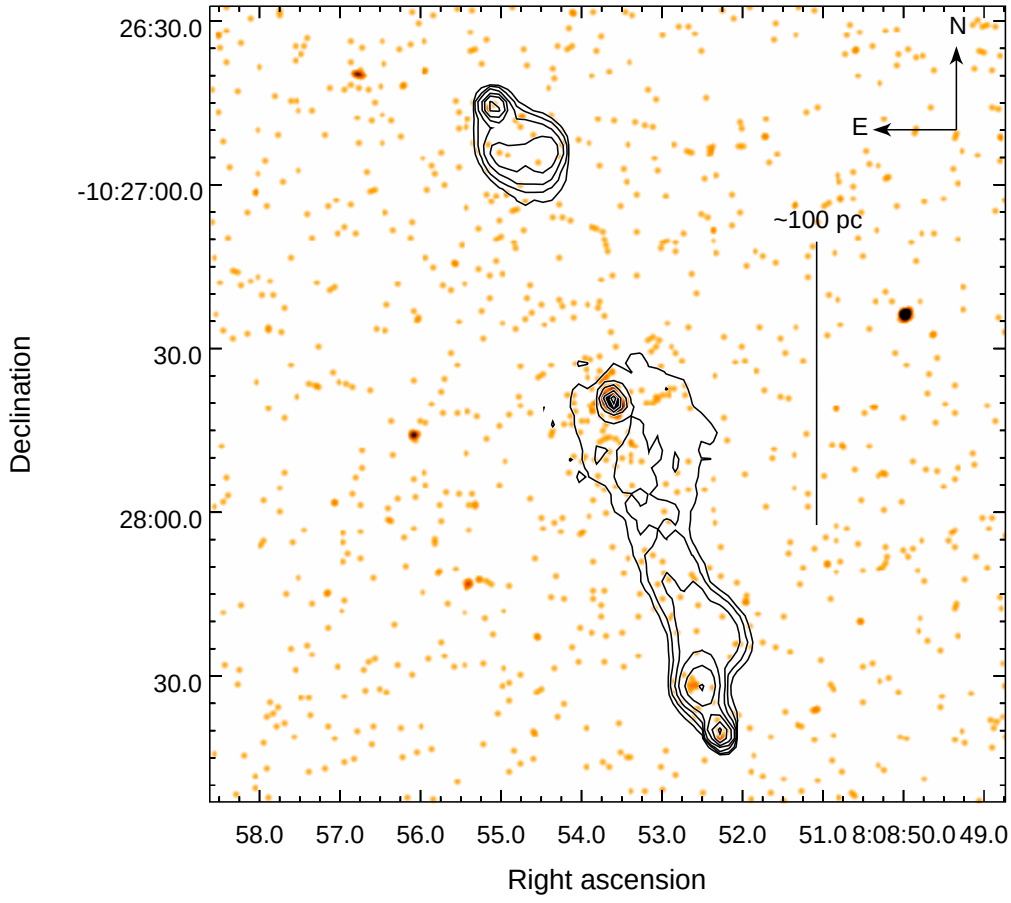

Figure 5.12: PKS 0806-10 (3C 195). The radio contours increase by factors of 2 between 0.001 and 0.064 Jy/beam, the beam major axis is 2.43 arcsec, and the minor axis is 1.60 arcsec.

PKS 0915–11 (3C 218, Hydra A)

Hydra A is a very well studied galaxy. It sits in the center of a rich cluster and is one of the most powerful local radio sources (see e.g. Lane et al. 2004, and references therein). The optical emission lines are very weak, and the K-band imaging does not show a nuclear point source (Inskip et al. 2010). It also shows evidence for recent star formation (Dicken et al. 2012), which is not common in cluster-centre galaxies, but can be attributed to a recent merger (Ramos Almeida et al. 2010, report the presence of a dust lane). The *Chandra* images show the hot gas emission from the ICM, as well as emission associated with the lobes (see e.g. Hardcastle & Croston 2010; Gitti et al. 2011; Kaastra et al. 2004, and references therein). The AGN is very faint in X-rays, and its spectrum has a rather peculiar shape, possibly because of contamination from thermal emission that our region selection cannot fully correct for. This situates Hydra A slightly apart form the bulk of the LERG population in our diagrams, relatively close to the LERG/HERG divide. The intrinsic N_H and the soft emission are rather well constrained, but the error in the normalization of the hard powerlaw component is quite large, which is reflected in the large error bars in our plots.

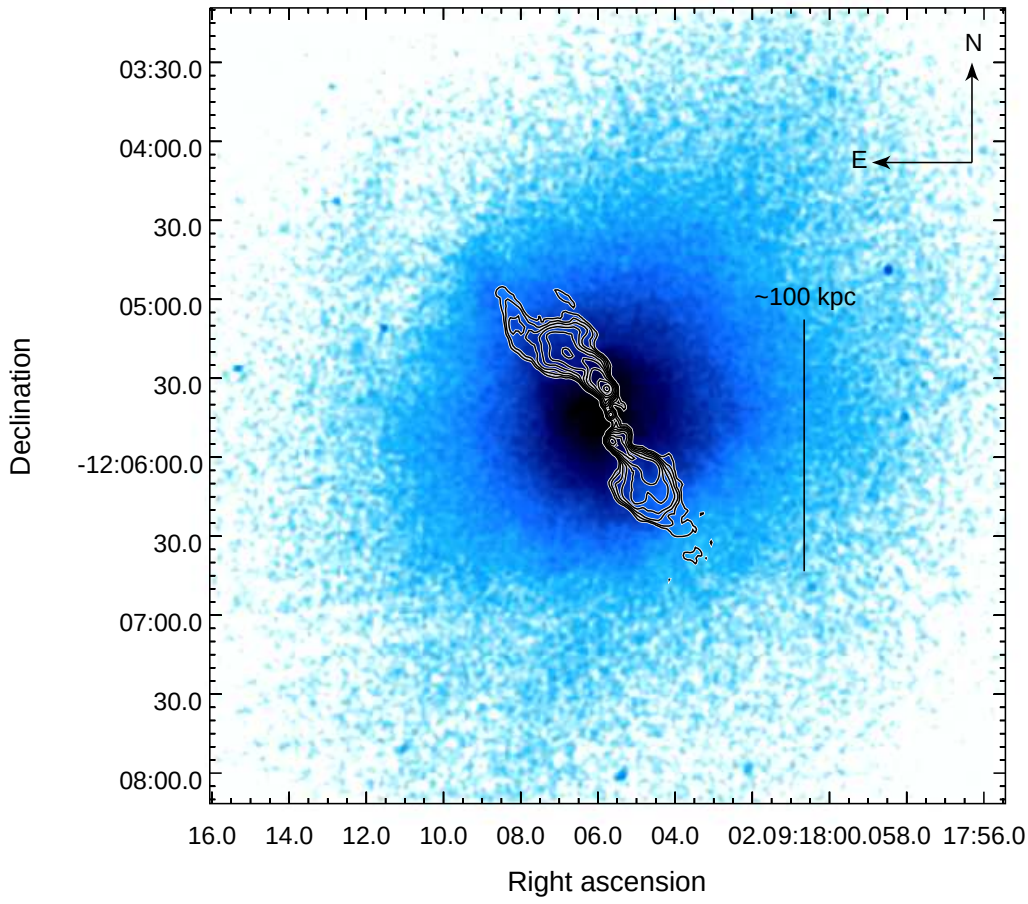

Figure 5.13: PKS 0915-11 (3C 218, Hydra A). The radio contours increase by factors of 2 between 0.004 and 1.024 Jy/beam, the beam major axis is 1.96 arcsec, and the minor axis is 1.45 arcsec.

PKS 0945+07 (3C 227)

This is a well-known BLRG (Hardcastle et al. 1998a), with a very extended optical emission line region (Prieto et al. 1993). The *Chandra* image shows some enhanced emission inside the radio lobes (Morganti et al. 1993), definitely from inverse-Compton scattering, as reported by Hardcastle et al. (2007c), and bright X-ray emission coincident with the radio hotspots, particularly for the E structures. The spectrum is very bright, and requires pileup correction and some care when selecting the extraction region (there is a faint streak in the image). It is well modelled with two powerlaws and low, but well constrained, intrinsic absorption.

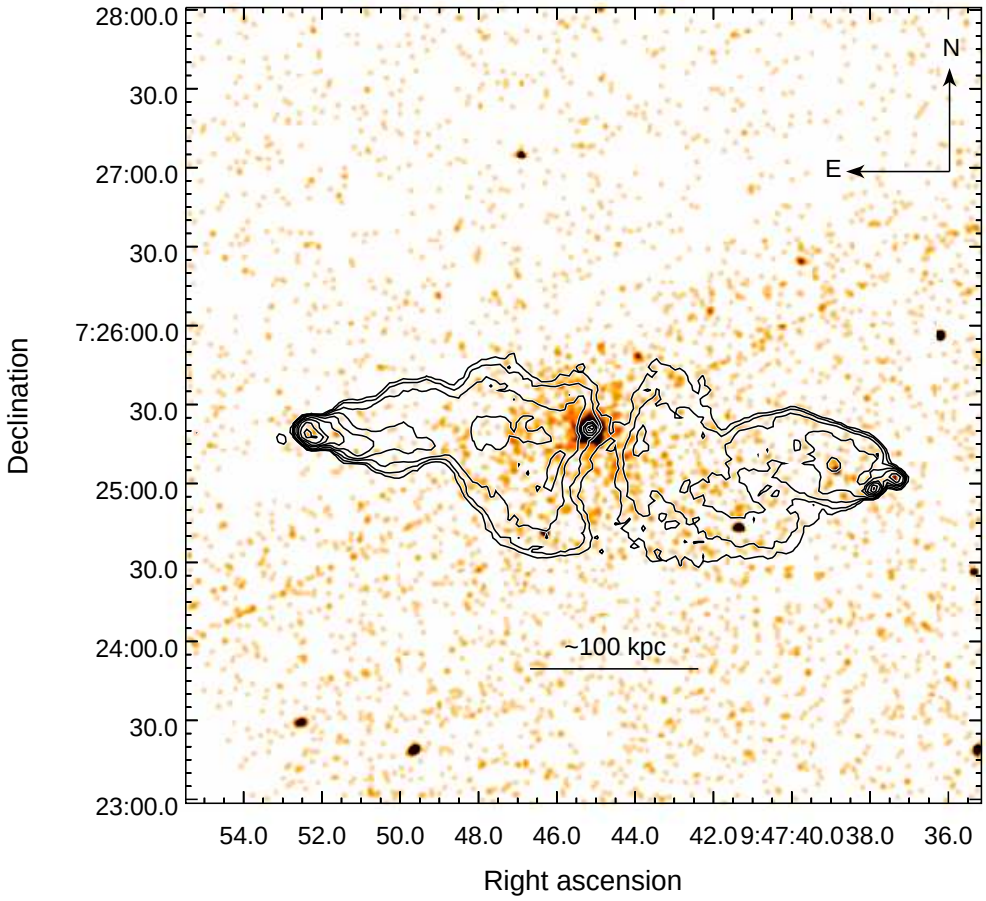

Figure 5.14: PKS 0945+07 (3C 227). The radio contours increase by factors of 2 between 0.004 and 1.024 Jy/beam, the beam major axis is 2.04 arcsec, and the minor axis is 1.49 arcsec. The instrumental streak is visible in the NW-SE direction.

PKS 1559+02 (3C 327)

The host galaxy of this NLRG is very massive, and seems to have a bifurcated dust lane (Inskip et al. 2010; Ramos Almeida et al. 2010), which crosses the nucleus. Its radio morphology is extended and well known (Morganti et al. 1993), with the E lobe being much brighter than its W counterpart. van der Wolk et al. (2010) report a large infrared excess that extends beyond what is expected for a torus. The *Chandra* image shows a very bright nucleus, which is close to the edge of the S3 chip. There is enhanced emission within the E lobe, most likely from inverse-Compton scattering (Hardcastle et al. 2007c), with two bright spots coinciding with the E radio hotspot. There seems to be some enhanced emission in the W lobe as well, but since it falls in one of the chips without retro-illumination it is hard to quantify. The spectrum is best fit with two components and low intrinsic absorption, and a Fe K-α emission line. As for PKS 0409–75 (Section 5.3), it is remarkable that the Fe line is detected despite the faintness of the accretion-related component.

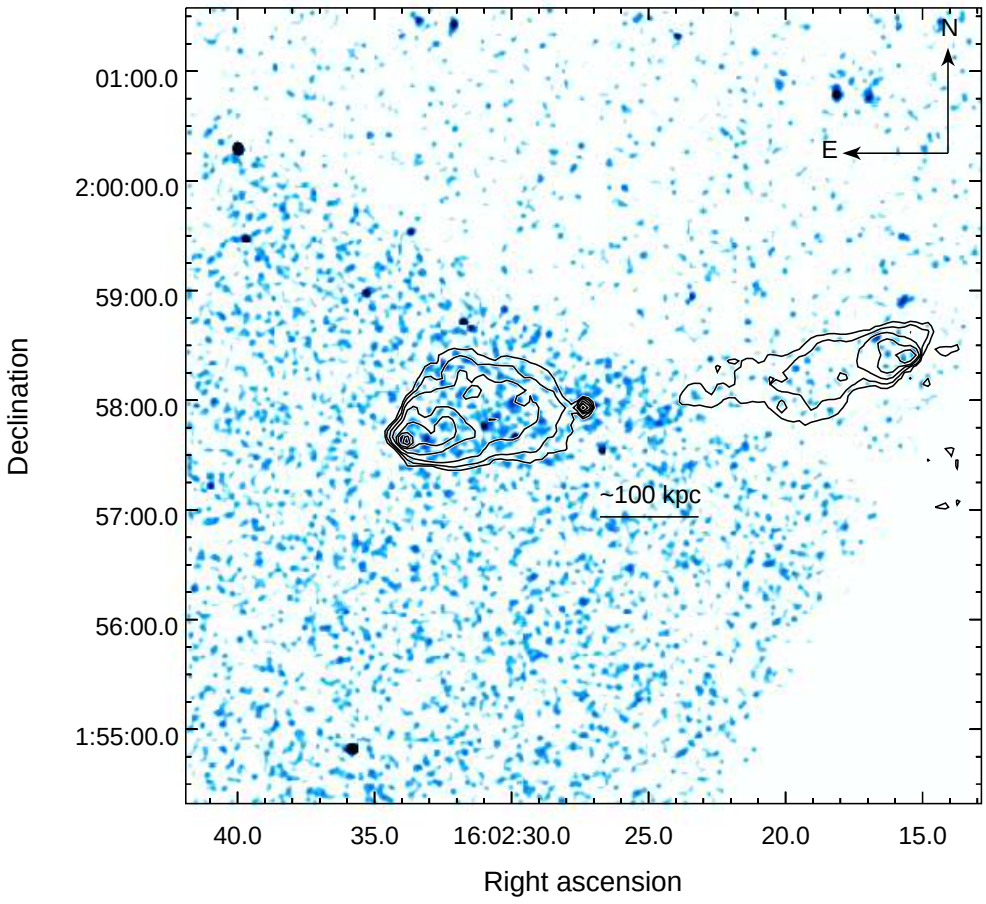

Figure 5.15: PKS 1559+02 (3C 327). The radio contours increase by factors of 2 between 0.0002 and 0.0256 Jy/beam, the beam major axis is 2.20 arcsec, and the minor axis is 2.20 arcsec.

PKS 1648+05 (3C 348, Hercules A)

Hercules A is a cluster-embedded LERG with some unusual radio properties (Morganti et al. 1993). Dust features are detected in the optical images (Ramos Almeida et al. 2010), and it seems to be at the centre of a cooling flow, and the lobes seem to be driving a shock into the ICM (Nulsen et al. 2005a,b), which is evident in the *Chandra* image, where there is clear emission from the hot ICM, with a lower density in the regions corresponding to the radio lobes. The nuclear X-ray spectrum is very faint, with soft emission being the main contributor. We were only able to constrain an upper limit for the hard component.

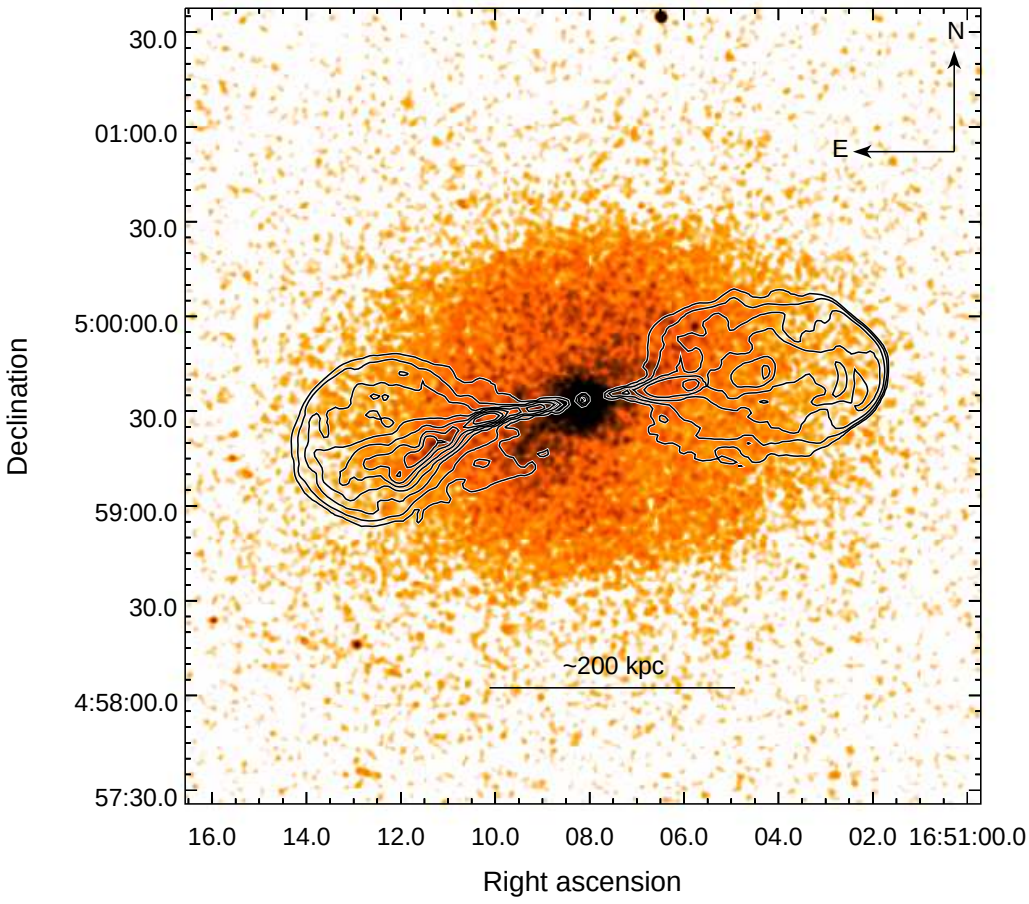

Figure 5.16: PKS 1648+05 (3C 348, Hercules A). The radio contours increase by factors of 2 between 0.002 and 0.256 Jy/beam, the beam major axis is 0.14 arcsec, and the minor axis is 0.14 arcsec.

PKS 1733–56

The host galaxy of PKS 1733–56 shows clear evidence of recent star formation (Dicken et al. 2012, 2009), and a disturbed optical morphology (Ramos Almeida et al. 2010; Inskip et al. 2010), probably caused by interactions within the dense field it inhabits. The *Chandra* image shows some diffuse emission, which could correspond to a hot ICM, and an enhancement in emission coincident with the radio hotspots. The spectrum is very bright, and had to be corrected for pileup. It is also quite typical of a BLRG, with low intrinsic absorption which does not allow us to distinguish clearly between both components. There is a faint excess $\sim$ 6 keV which could be related to a Fe K-α emission line, but adding an extra component does not improve the fit.

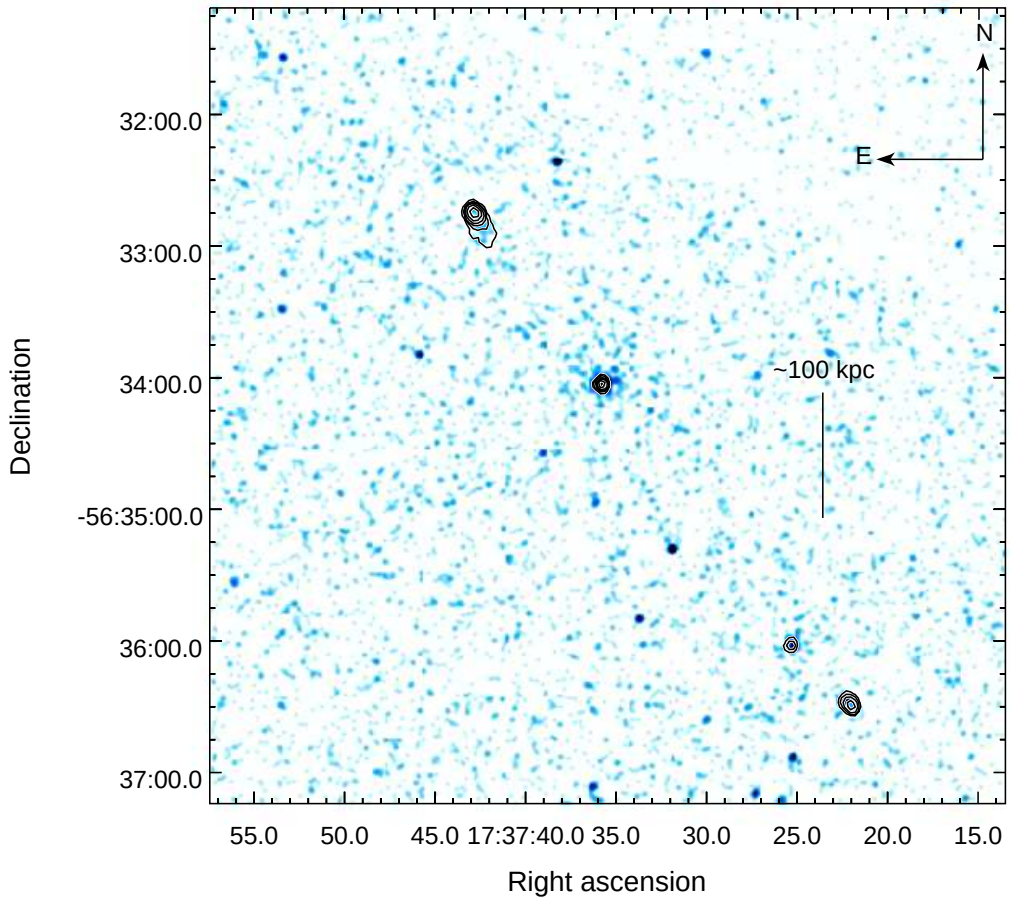

Figure 5.17: PKS 1733-56. The radio contours increase by factors of 2 between 0.004 and 0.256 Jy/beam, the beam major axis is 2.25 arcsec, and the minor axis is 1.90 arcsec.

PKS 1814–63

PKS 1814–63 shows clear traces of an optical disk and a dust lane (Ramos Almeida et al. 2010; Inskip et al. 2010), which is atypical for a system with this radio luminosity (Morganti et al. 2011). It also shows evidence for starburst activity (Dicken et al. 2012) and has an extended emission line region (Holt et al. 2008, 2009). The *Chandra* image shows no traces of an ICM. The spectrum is bright and dominated by a relatively unobscured hard component, as typical for NLRGs. It also has a Fe K-α emission line.

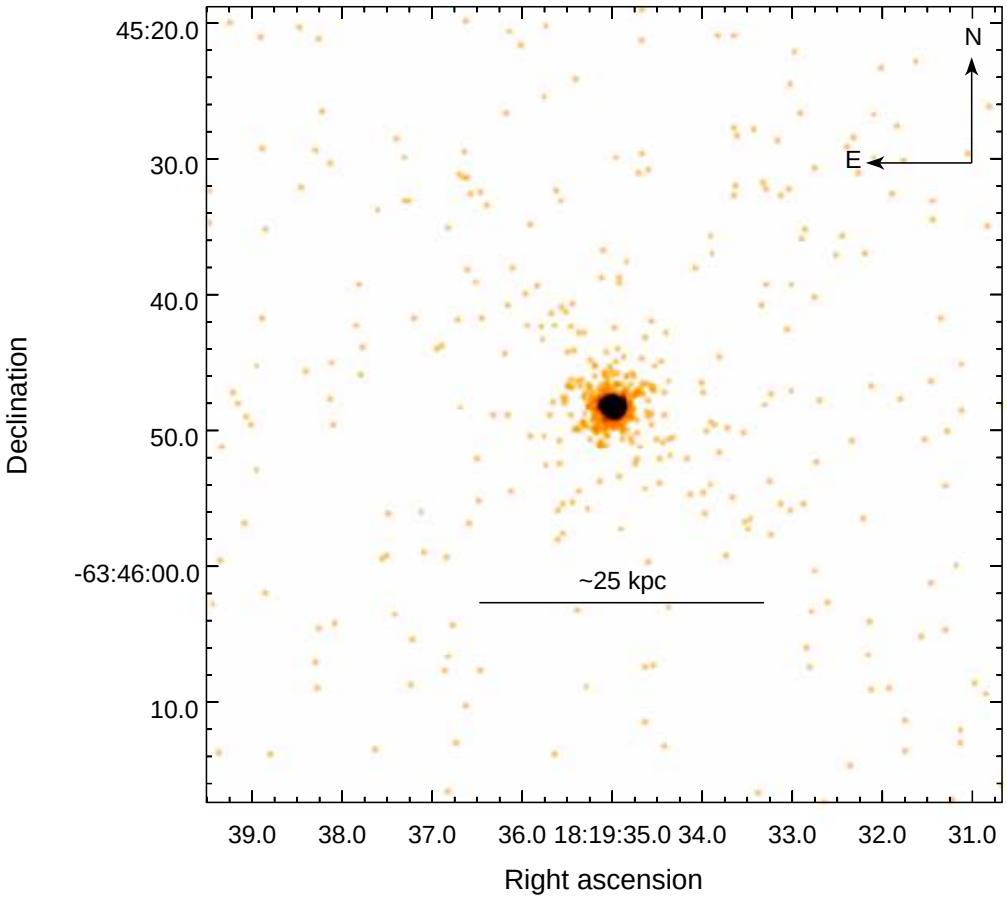

Figure 5.18: PKS 1814-63. This source has no extended radio structures.

PKS 1839–48

This FR I is another example of a cluster-embedded LERG (Ramos Almeida et al. 2010; Tadhunter et al. 1993). van der Wolk et al. (2010) report no detection of a dusty torus, which is consistent with the classification of this object as low-excitation. Although not as dense of that of Hydra A or Hercules A, there is emission from the ICM in the *Chandra* image. Its X-ray spectrum has a relatively bright soft component, but no traces of accretion-related emission, for which we were only able to constrain an upper limit.

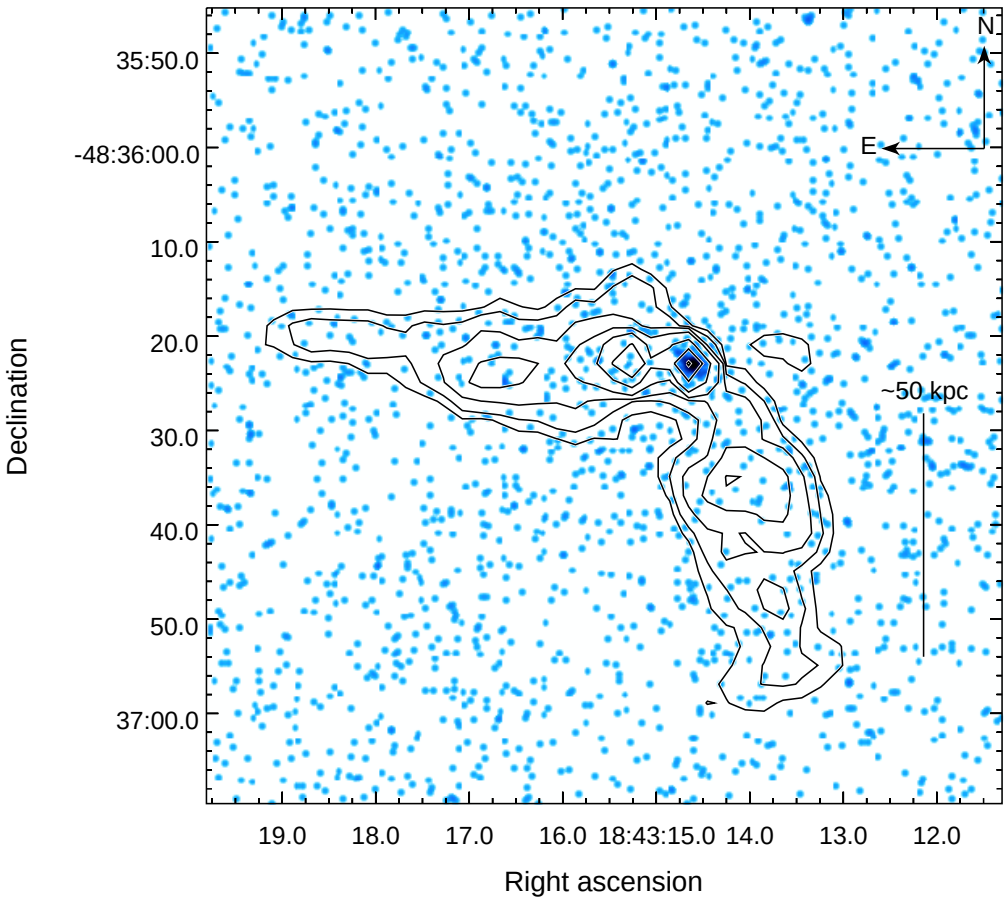

Figure 5.19: PKS 1839-48. The radio contours increase by factors of 2 between 0.001 and 0.064 Jy/beam, the beam major axis is 2.55 arcsec, and the minor axis is 1.90 arcsec.

PKS 1934–63

This source has a compact radio core (Ojha et al. 2004) and is optically very blue (Ramos Almeida et al. 2010), as well as being part of an interacting galaxy pair (Inskip et al. 2010). It also shows evidence for infalling gas (Holt et al. 2008, 2009). Its radio spectrum is self-absorbed, and thus we could only derive an upper limit to its 178 and 151 MHz fluxes. The *Chandra* image shows no signs of extended emission, only the compact source that coincides with the radio core. Its X-ray spectrum is dominated by the soft component, and we are not able to disentangle the obscuring column from the hard component, nor do we detect the Fe K-α reported by Risaliti et al. (2003) from their *Beppo-SAX* observations. It is possible that this object is heavily obscured, although we do not see an excess in IR emission to support this.

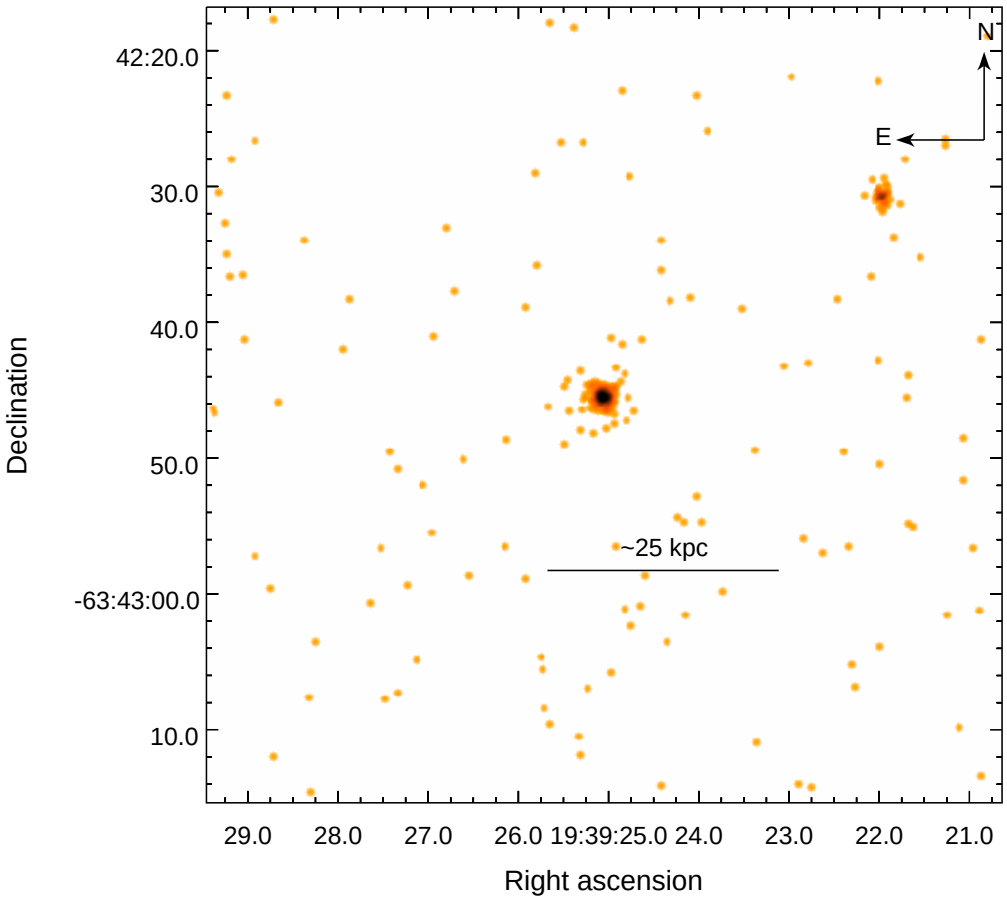

Figure 5.20: PKS 1934-63. This source has no extended radio structures.

PKS 1949+02 (3C 403)

PKS 1949+02 is a NLRG with an X-shaped radio morphology, and as such it has been studied in some detail (see Ramos Almeida et al. 2010, and references therein). The *Chandra* image shows some enhancement that could correspond to a dense medium, and two hotspot features to the E of the core spatially coincident with the radio emission. Some emission can also be observed close to the W radio hotspot. The X-ray spectrum has also been studied in detail (Kraft et al. 2005; Balmaverde et al. 2008), it is dominated by the hard component, rather obscured, and it has a very prominent Fe K-α emission line.

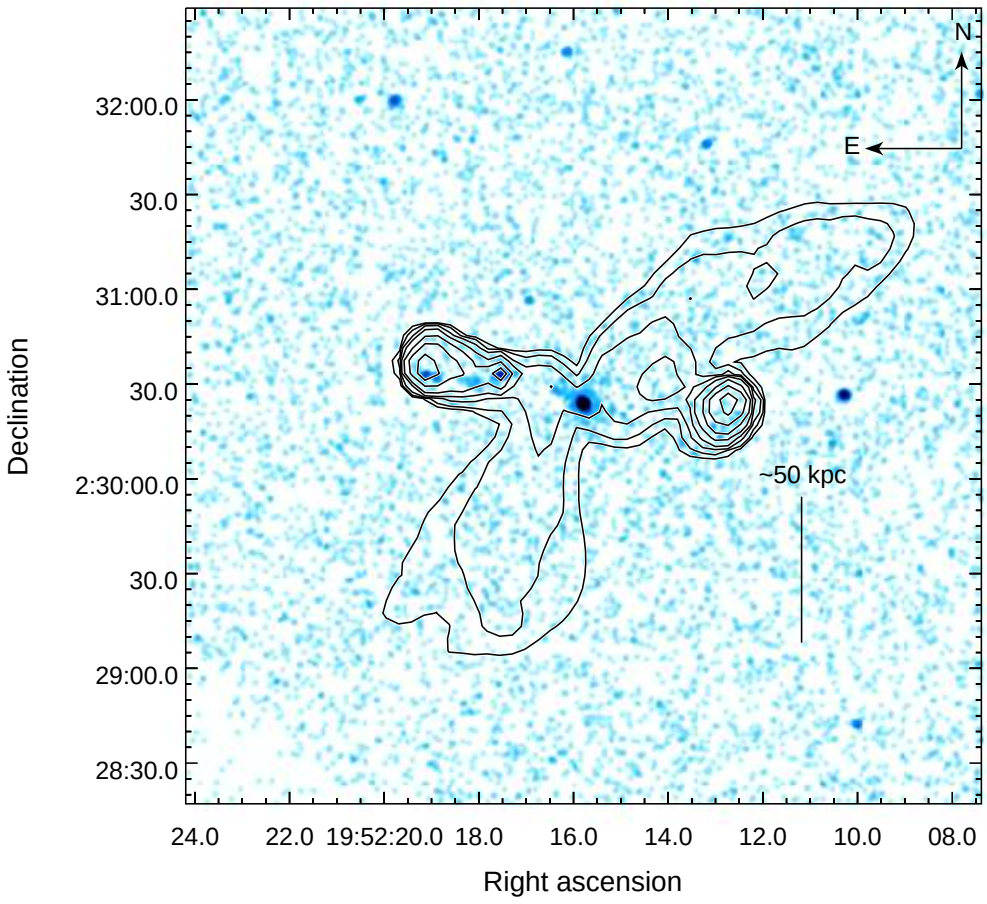

Figure 5.21: PKS 1949+02 (3C 403). The radio contours increase by factors of 2 between 0.002 and 0.256 Jy/beam, the beam major axis is 4.53 arcsec, and the minor axis is 4.13 arcsec.

PKS 1954–55

PKS 1954–55 is also located in a rich environment (Ramos Almeida et al. 2010), which is detected in X-rays, particularly at the base of the radio lobes. The X-ray spectrum of this LERG is rather faint, and only a soft component is detected.

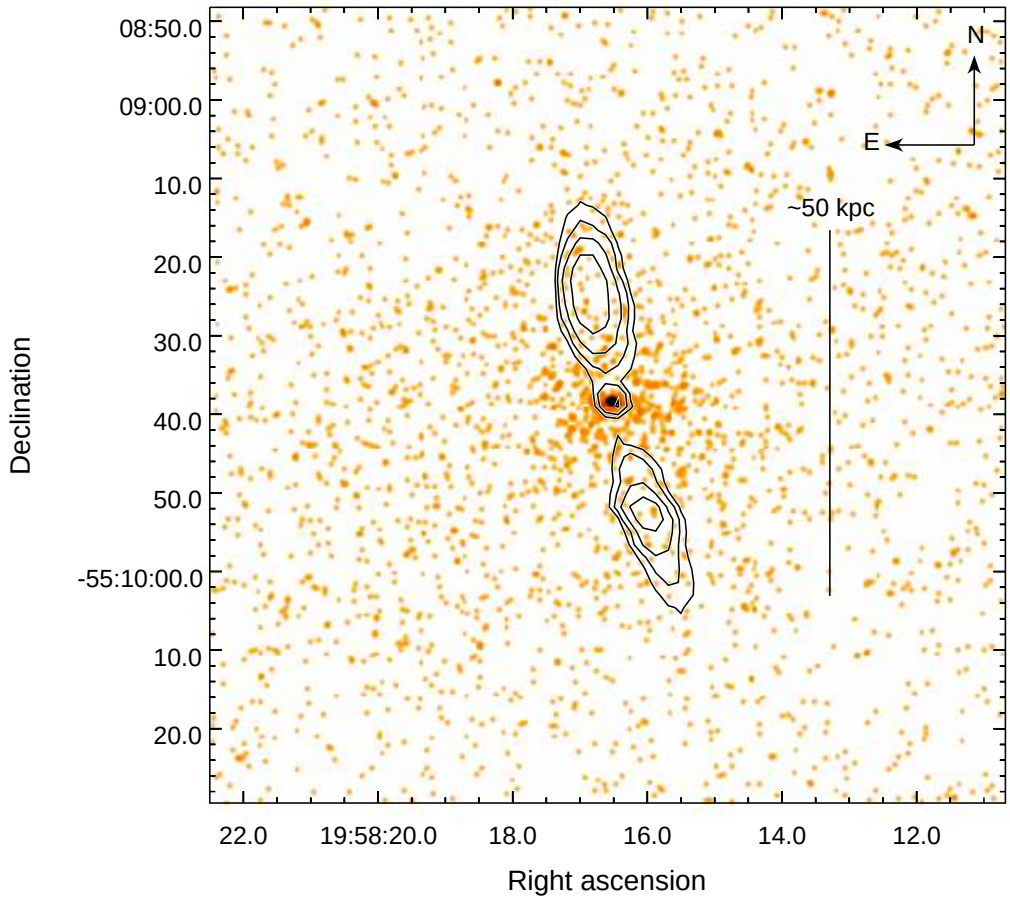

Figure 5.22: PKS 1954-55. The radio contours increase by factors of 2 between 0.004 and 0.064 Jy/beam, the beam major axis is 2.43 arcsec, and the minor axis is 1.29 arcsec.

PKS 2135–14

The host of PKS 2135–14 has a close disk galaxy companion (Ramos Almeida et al. 2010), and a disturbed morphology. The *Chandra* image shows some extended emission around the nucleus, but given the brightness of this QSO it is difficult to tell whether that emission is from the PSF or a real ICM. The spectrum of this source had to be corrected for pileup. It has two distinct components and some intrinsic obscuration. There is some excess above 5 keV which we have not been able to model.

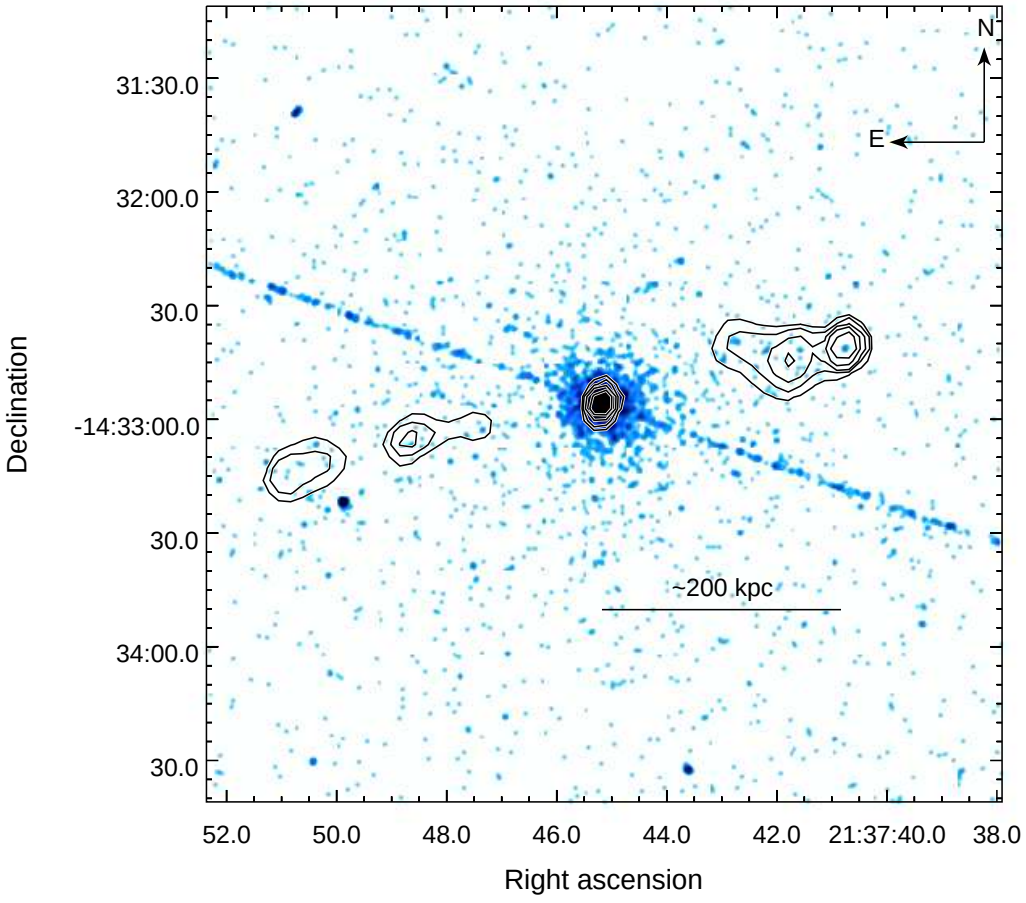

Figure 5.23: PKS 2135-14. The radio contours increase by factors of 2 between 0.004 and 0.128 Jy/beam, the beam major axis is 5.46 arcsec, and the minor axis is 3.37 arcsec. The instrumental streak is visible in the NE-SW direction.

PKS 2211–17 (3C 444)

PKS 2211–17 is another example of a cluster-embedded LERG (Ramos Almeida et al. 2010; Inskip et al. 2010). It is classified as an FR II, but its morphology is almost intermediate between both FR classes. We detect a very dense ICM with clear cavities corresponding to the radio lobes, which are driving a shock (Croston et al. 2011). Its nuclear spectrum is very faint, with only ~ 20 counts in the 0.4-7 keV energy range. We could only derive upper limits for both X-ray components.

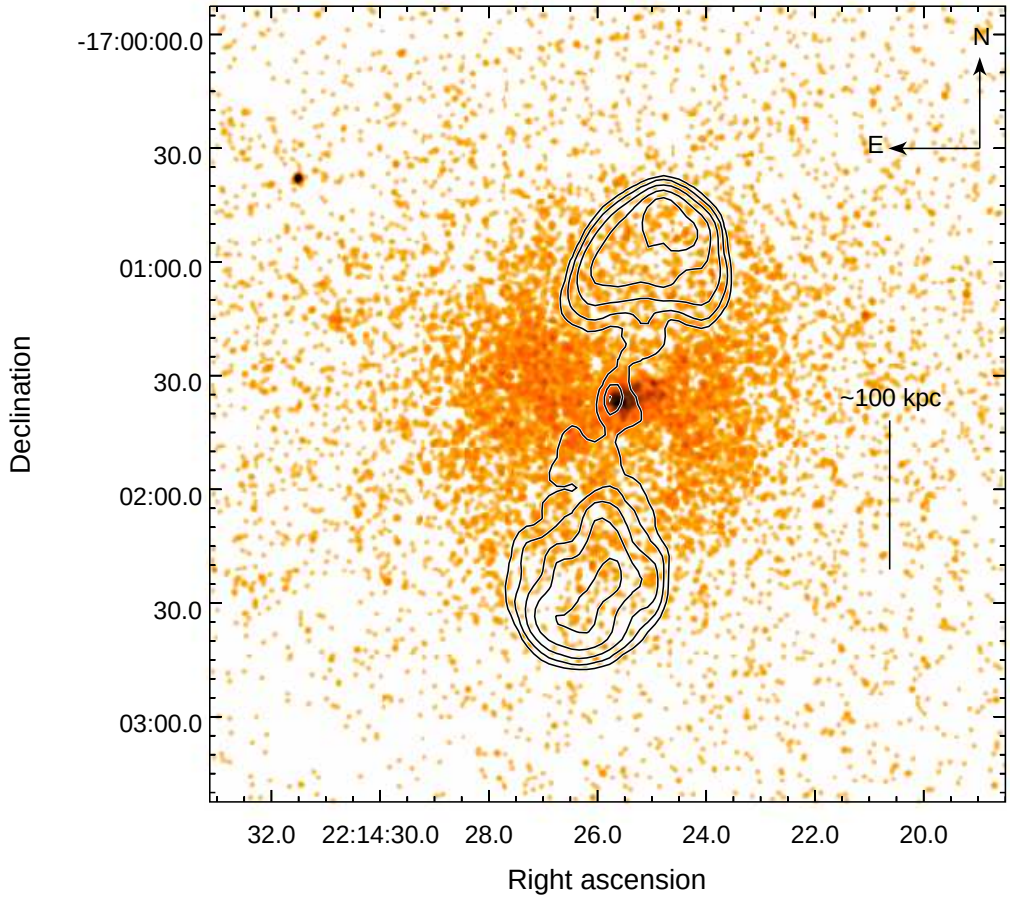

Figure 5.24: PKS 2211-11 (3C 444). The radio contours increase by factors of 2 between 0.001 and 0.016 Jy/beam, the beam major axis is 4.57 arcsec, and the minor axis is 2.03 arcsec.

PKS 2221–02 (3C 445)

This object is a relatively well-known BLRG (Leahy et al. 1997; Morganti et al. 1993). It has a very bright nucleus in the K band (Inskip et al. 2010) and an extended emission line region (Balmaverde et al. 2008). It seems to be interacting with a close companion (Ramos Almeida et al. 2010). The radio hotspots are detected by *Chandra*, though they are very far apart, and the Northern one falls outside of the S3 chip. There seems to be some enhanced emission around the nucleus as well. The X-ray spectrum is bright, but not heavily piled up. The hard component dominates, and we detect a rather prominent Fe K-α emission line.

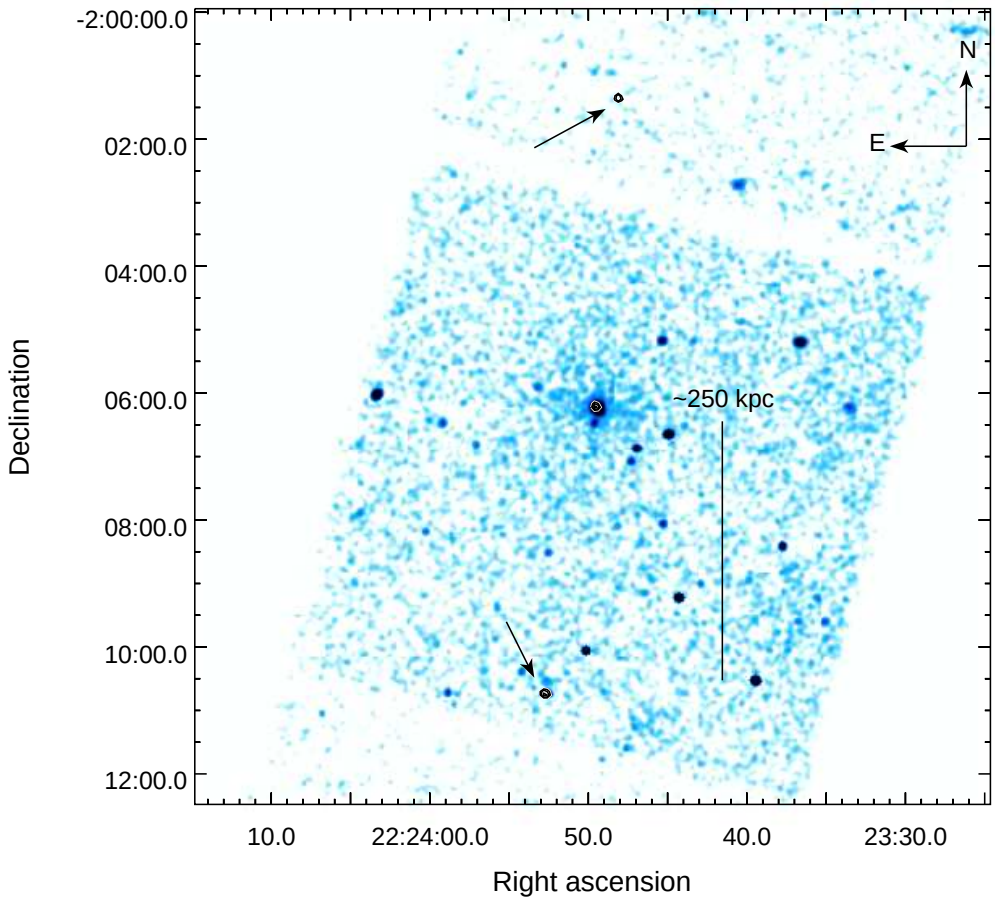

Figure 5.25: PKS 2221-02 (3C 445). The radio contours increase by factors of 2 between 0.004 and 0.032 Jy/beam, the beam major axis is 2.40 arcsec, and the minor axis is 2.40 arcsec. The arrows indicate the positions of the two hotspots.

PKS 2356–61

The host of PKS 2356–61 shows signs of a past merger (Ramos Almeida et al. 2010). It is very radio powerful and has large hotspots and shells (Subrahmanyan et al. 1996), which are also detected in our *Chandra* image. There is X-ray emission around the source and at the base of the lobes which could be related to a hot ICM. This NLRG has a spectrum clearly dominated by the accretion-related component, with a noticeable Fe K-α emission line.

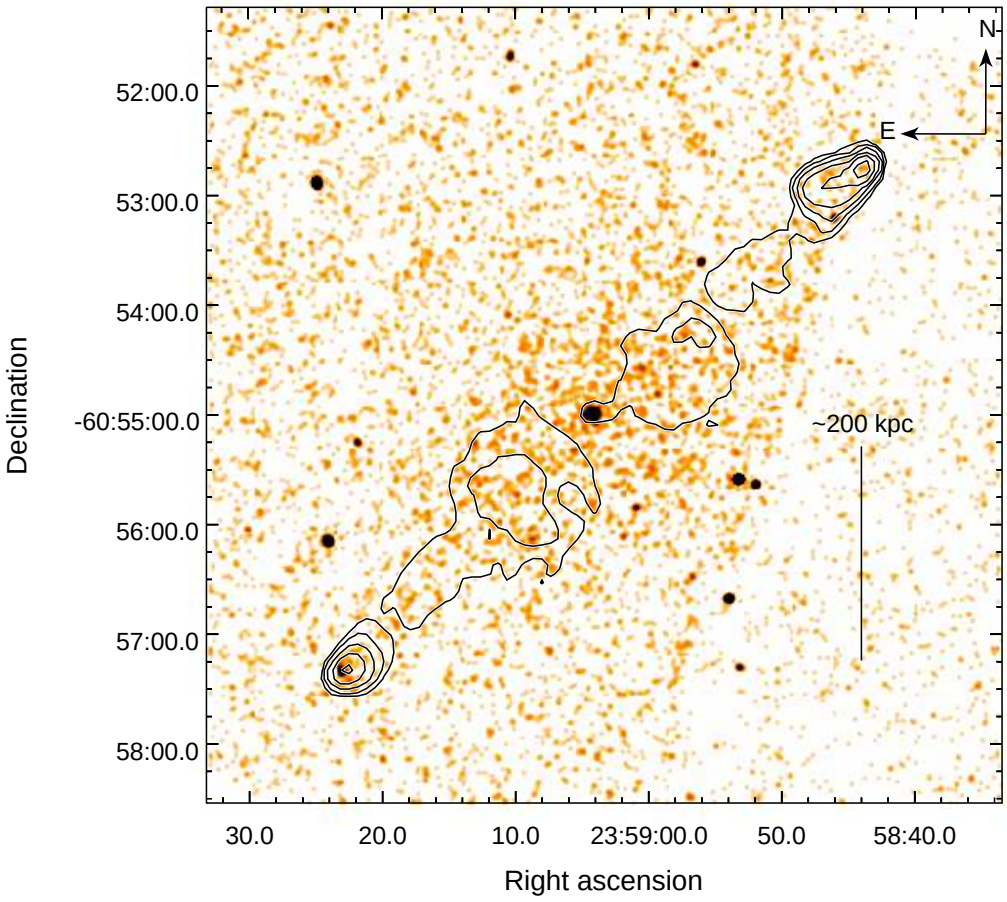

Figure 5.26: PKS 2356-61. The radio contours increase by factors of 2 between 0.02 and 0.64 Jy/beam, the beam major axis is 7.16 arcsec, and the minor axis is 6.88 arcsec.

5.3 The high-z sources

As mentioned in Section 5.1, for the sources with $0.2 < z < 0.7$ we used *XMM-Newton* observations. The following Subsections describe the spectra and environmental properties of these objects. Images are not provided, since they do not provide any additional insight on the extended structures and environments of these galaxies, given the lower spatial resolution of the *XMM* instruments as compared to *Chandra*.

PKS 0023–26

This object seems to be inhabiting a dense environment (Ramos Almeida et al. 2010). We detect with *XMM* another active galaxy (MRSS 473–052098) ~20 arcsec away from the source. PKS 0023–26 also seems to have a young stellar population (Dicken et al. 2012), and redshifted HI emission consistent with infalling gas (Holt et al. 2008). Its X-ray spectrum is quite typical for what is expected in NLRGs, with a dominating jet-related component and low intrinsic absorption.

PKS 0035–02 (3C 17)

PKS 0035–02 is a BLRG whose host galaxy is interacting (Ramos Almeida et al. 2010). It has an interesting radio morphology (Morganti et al. 1999), with a bent jet and several hotspots, also detected in the Ks band (Inskip et al. 2010). Its optical spectrum shows double-peaked Balmer lines. The *Chandra* image shows the jet (Massaro et al. 2009), and there seems to be some extended emission around the nucleus. Its spectrum shows two distinct components and some intrinsic absorption, which is not overly frequent in broad-line objects due to orientation.

PKS 0039–44

The optical nucleus of this NLRG seems to be dusty, and it is believed to have two components (Ramos Almeida et al. 2010), which are not resolved in our *XMM* images. Its X-ray spectrum is bright, with two distinct components, some intrinsic absorption and a prominent Fe K-α line.

PKS 0105–16 (3C 32)

This galaxy seems to be interacting with a nearby neighbour (Ramos Almeida et al. 2010). The spectrum we extracted from the *XMM* images is quite typical for a NLRG, with two components, intrinsic absorption and a noticeable Fe K-α line.

PKS 0235–19

The optical images of the BLRG PKS 0235–19 show a structure that might be a tidal tail or a warped disk structure (Ramos Almeida et al. 2010), which is misaligned with respect to the radio structures. The X-ray spectrum is not very bright, it features some intrinsic absorption, which allows us to isolate the soft and hard components, with the hard one being dominant.

PKS 0252–71

PKS 0252–71 has a compact radio morphology, and seems to be interacting with a neighbour (Ramos Almeida et al. 2010). Its X-ray spectrum is quite faint; it features two distinct components (the jet-related one being brighter) and some absorption.

PKS 0347+05

This object was previously classified as a BLRG, but a recent study by Tadhunter et al. (2012) suggests that this is in fact a double system with a radio-loud object and a Seyfert 1 radio-quiet AGN. It was already known that this was an interacting system (Ramos Almeida et al. 2010; Inskip et al. 2010), but given these recent results is is very possible that we are measuring data from both objects, given that the galaxies are only 5 arcsec apart, and we are thus unable to resolve them. The optical spectra analysed by Tadhunter et al. (2012) suggest that the broad lines previously attributed to the radio source belong instead to the Seyfert, and the line ratios seem to indicate that the radio galaxy is a LERG. They suggest that this latter source is just a relic, having recently switched off, since they do not detect the radio core. The *XMM* images show that the emission is centered between both sources, with more emission coming from the region associated with the radio source. The spectrum we analyse is dominated by the soft component, and heavily absorbed, though the N_H column is not very well constrained.

This is not compatible with the spectrum of a Seyfert 1 galaxy; we therefore assume that the radio-loud AGN is still active, and is indeed the main contributor to the X-ray spectrum, which is more consistent with that of a NLRG. We have decided to use the optical LERG classification for this source, although that makes it an outlier in most of our plots, due to its brightness. The X-ray excess (as compared to other LERGs) could be attributed to the contribution from the Seyfert core, and the IR excess to the presence of star formation (Dicken et al. 2012), but in any case the true nature of this source remains uncertain.

PKS 0409–75

This FR II has the highest redshift in our sample, and is one of the brightest radio sources in the Southern hemisphere (Morganti et al. 1999). It has a young stellar population (Dicken et al. 2012) and it seems to have a double optical nucleus (Ramos Almeida et al. 2010). Its X-ray spectrum is also very bright, and atypical, with the jet-related component clearly dominant, no detectable intrinsic absorption and only an upper limit on the accretion-related component, which, however, has a detectable Fe K-α line.

PKS 0859–25

This NLRG seems to be in a relatively dense environment (Ramos Almeida et al. 2010), and to have a double optical nucleus. Its *XMM* spectrum is remarkable in that it shows a very prominent Fe K-α line.

PKS 1151–34

This QSO seems to be interacting with a nearby spiral galaxy (Ramos Almeida et al. 2010). This source has double-peaked Balmer lines (Eracleous & Halpern 1994), and has thus been included in the ongoing debate over radiatively efficient versus inefficient accretion in broad-line objects (Nagao et al. 2002). Although the PAH features in the *Spitzer* observations seem to indicate a young stellar population, this is not confirmed by the far-IR observations (Dicken et al. 2012). The *XMM* spectrum is rather bright, and well modelled with two power laws (the hard component being much brighter

than the soft one), a surprisingly high absorption column (which is also not very well constrained, see Table 6.1), and a Fe K-α emission line.

PKS 1306–09

PKS 1306–09 shows clear signs of interaction with nearby neighbours, and has a double optical nucleus (Inskip et al. 2010; Ramos Almeida et al. 2010). Its *XMM* spectrum shows no signs of a jet-related component, and requires some intrinsic absorption.

PKS 1355–41

The optical images of this QSO show some features that may indicate interactions (Ramos Almeida et al. 2010). Its *XMM* spectrum requires two powerlaw components and very low intrinsic absorption.

PKS 1547–79

PKS 1547–79 shows clear signs of interaction and a double nucleus both in the optical (Ramos Almeida et al. 2010) and IR images (Inskip et al. 2010). Its *XMM* spectrum is rather peculiar, and not very bright, probably due to the high redshift. There may be signs of thermal contamination in the soft emission, and heavy intrinsic absorption is required for a good fit, but is very poorly constrained. This is very atypical for a BLRG, and possibly an effect of the poor spectral quality (the observation suffers from rather heavy flare contamination for about 70% of the exposure time), but careful flare-filtering and rebinning of the data resulted in no improvements in the fits.

PKS 1602+01 (3C 327.1)

The host galaxy seems to have a double optical nucleus (Ramos Almeida et al. 2010) and perhaps an extended emission line region (Morganti et al. 1999). The *XMM* spectrum has two bright components, with no intrinsic absorption.

PKS 1932–46

The host of this BLRG shows signs of ongoing star formation (Dicken et al. 2012), has an extended emission line region (Inskip et al. 2007) and its core seems to be relatively

faint in the K band (Inskip et al. 2010), its IR luminosity is also rather low in our plots. The X-ray spectrum is not very bright, and is best modelled with a single, unobscured component, which does not allow us to distinguish between jet and accretion-related emission.

PKS 1938–15

The host of PKS 1938–15 seems to be inhabiting a very dense environment (Ramos Almeida et al. 2010), with several close companions. The spectrum of this BLRG has two components and a low intrinsic N_H column. It has an excess compatible with a Fe K-α emission line; adding this component improves the fit slightly.

PKS 2135–20

The host of this BLRG shows evidence for star formation (Dicken et al. 2012), and traces of a past interaction (Ramos Almeida et al. 2010). Although the quality of the spectrum is rather poor, given the low luminosity of the source (for a BLRG) and the high redshift, we detect two components, heavy (although not very well constrained) intrinsic absorption, and some excess that could be compatible with a Fe K-α emission line, although it is unclear due to our low statistics.

PKS 2250–41

This source has a rather bright extended [OIII] line emission (Tadhunter et al. 2002), and it is likely to belong to a group of galaxies (Ramos Almeida et al. 2010). Its *XMM* spectrum has a very faint accretion-related component, for which we were only able to derive an upper limit, although this is clearly a high-excitation object.

PKS 2314+03 (3C 459)

The host galaxy of this NLRG is classified as an ultraluminous infrared galaxy (ULIRG) due to its intense star formation activity (Dicken et al. 2012; Tadhunter et al. 2002), it is morphologically disturbed (Ramos Almeida et al. 2010), and it also has a strong radio core (Morganti et al. 1999), which offsets it slightly from the rest of the NLRG

population in our 5 GHz plots. The X-ray spectrum has two distinct components and some intrinsic absorption, with some excess in the soft energy range.

Chapter 6

The cores of the 2Jy sample

6.1 Introduction

Our knowledge of active galactic nuclei (AGN), their observational properties and underlying mechanisms has vastly increased over the last few decades. We now know that these objects are powered through gas accretion onto some of the most supermassive black holes that sit in the centres of most galaxies (e.g. Magorrian et al. 1998). Radio-loud objects are particularly important to our understanding of AGN, since, despite the fact that they constitute only a small fraction of the overall population, it is during this phase that the impact of the AGN on their surrounding environment (through the production of jets and large-scale outflows and shocks) can be most directly be observed and measured (e.g. Kraft et al. 2003; Croston et al. 2011; Cattaneo et al. 2009).

It is now commonly accepted that the dominant fuelling mechanism for radio-quiet objects is the accretion of cold gas onto the black hole from a radiatively efficient, geometrically thin, optically thick accretion disk (Shakura & Sunyaev 1973). However, this may not be the case for radio-loud objects. Hine & Longair (1979) noticed the existence of a population of radio-loud objects which lacked the high-excitation optical emission lines traditionally associated with AGN. These so-called low-excitation radio galaxies (LERGs) cannot be unified with the rest of the AGN population, since their differences are not merely observational or caused by orientation or obscuration. They are believed to accrete hot gas (see e.g. Janssen et al. 2012) in a radiatively inefficient manner, through optically thin, geometrically thick advection-dominated flows

(ADAF, see e.g Narayan & Yi 1995). These objects thus lack the traditional accretion structures (jet and torus) commonly associated with active nuclei (see e.g. Mason et al. 2012; van der Wolk et al. 2010; Fernández-Ontiveros et al. 2012), and seem to be channeling most of the gravitational energy into the jets, rather than radiative output, which makes them very faint and hard to detect with any non-radio selected surveys.

Current models (e.g. Bower et al. 2006; Croton et al. 2006) suggest that the radiatively efficient process may be dominant at high redshifts, and to be responsible for the correlation between black hole mass and host galaxy's bulge mass (e.g. Silk & Rees 1998; Heckman et al. 2004). It may also be behind the apparent correlation (and delay) between episodes of star-formation and AGN activity in the host galaxies (e.g Hopkins 2012; Ramos Almeida et al. 2013). Radiatively inefficient accretion is believed to be more common at low redshifts (Hardcastle et al. 2007a), and to play a crucial role in the balance between gas cooling and heating, both in the host galaxy and in cluster environments (McNamara & Nulsen 2007; Antognini et al. 2012). These two types of accretion are often called 'quasar mode' and 'radio mode', which is somewhat misleading, given that there are radiatively efficient AGN with jets and radio lobes.

As pointed out by Hardcastle et al. (2009), it is important to note that the high/low-excitation division does not directly correlate with the FRI-FRII categories established by Fanaroff & Riley (1974), as is often thought. While most low-excitation objects seem to be FRI, there is a population of bona-fide FRII LERGs, as well as numerous examples of FRI HERGs (e.g Laing et al. 1994). This is most likely caused by the complex underlying relation between fuelling, jet generation and environmental interaction. There seems to be a evidence for a difference in the Eddington rate between both populations (see e.g. Hardcastle et al. 2007a; Best & Heckman 2012; Russell et al. 2012; Lin et al. 2010; Ho 2009; Mason et al. 2012; Evans et al. 2011; Plotkin et al. 2012), with LERGs typically accreting at much lower rates ($\leq$ 0.1 Eddington) than HERGs. Estimating the jet kinetic power is also complicated, given that its radio luminosity depends on the environmental density (Hardcastle & Krause 2013) and given the vastly different energy budgets and particle contents of FRI and FRII radio galaxies (see e.g. Godfrey & Shabala 2013).

From works like those of Hardcastle et al. (2006, 2009), we do know that LERGs follow the correlation of narrow-line galaxies (NLRGs) between soft X-ray and radio emission (Hardcastle & Worrall 1999), reinforcing the hypothesis that in radio-loud

objects this X-ray component originates in the jet. One of the crucial points we aim to investigate in this Chapter is the dissimilarity between the NLRG and LERG populations.

In this Chapter we analyse the X-ray emission from the 2Jy sample of radio galaxies (Wall & Peacock 1985), with an approach based on that of Hardcastle et al. (2006, 2009) used on the 3CRR galaxies. X-ray emission is less ambiguous than other wavelengths for an analysis of a sample such as the 2Jy, which contains a variety of populations, in that it is unequivocally linked to AGN activity. To fully understand the characteristics of this AGN activity, however, a multiwavelength approach is needed.

Our aim is to study the correlations between the luminosities of the sources at different wavelengths, to infer the physical processes involved. While many of the sources in the 3CRR catalogue have been observed in great detail, the multiwavelength coverage is not uniform, and the sample is not statistically complete, being more complete for redshifts <0.5. The observations of the 2Jy sample, however, were taken with the explicit purpose of providing a one on one comparison for all the objects in the sample, which provides us with the opportunity to test whether the conclusions reached by Hardcastle et al. can be extrapolated to all radio-loud AGN or are related to the biased redshift distribution of the 3CRR sources.

6.2 Data and Analysis

6.2.1 X-ray Data Analysis

As mentioned in Chapter 5, there are 47 sources in our sample, with $0.02 < z < 0.7$, listed in Table 5.1. All have X-ray observations save for PKS 0117–15 (3C 38), which, unfortunately, was not observed by *XMM-Newton*.

We analysed *Chandra* observations for the low-z sources in our sample. When using archival data we only considered ACIS-S and ACIS-I observations without gratings, and discarded calibration or very short observations that did not significantly contribute to the statistics. When more than one spectrum was extracted for a source, we carried out simultaneous fits. We reduced the data using CIAO 4.3 and the latest CALDB. We included the correction for VFAINT mode to minimise the issues with the background for all the sources with a count rate below 0.01 counts s^{-1} and observed

in VFAINT mode. For sources with rates above this threshold and below 0.1 counts s^{-1} the difference made by this correction is barely noticeable, and for the brightest sources the software is not able to properly account for the high count rate, considering some of these events as background, and resulting in dark "rings" appearing in the images, and the loss of a substantial number of counts.

We extracted spectra for all the sources, using extraction regions consistent with those of Hardcastle et al. (2009): a 2.5 pixel (1 px = 0.492 arcsec) radius circular region centered in the object as source, and an immediately external annulus, with an outer radius of 4 pixels, for the background, to minimise the contamination from any thermal components in the circumnuclear regions. For very bright sources we had to use larger regions to include most of the PSF, namely a 20 pixel radius circle for the source, and a 20 to 30 pixel circular annulus for the background. In the cases where pileup was present (PKS 0038+09, 0442–28, 0521–36, 0625–35, 0945–27, 1733–56, 1814–63, 2135–14), we corrected the ARF as described by Hardcastle et al. (2006) and Mingo et al. (2011). We generated an energy versus flux table from an initial model fit, and fed it to ChaRT, a tool that generates a PSF from a given model. We then fed the results to the tool MARX, which produces an image of the simulated PSF. We then generated a new events file from our original data and an annular extraction region, identical to the one we used to generate our spectra, but excluding the central few pixels. We used a code to fit a 5th-degree polynomial to the ratio of this events file and the whole simulated events file as a function of energy. This code reads in the ARF generated by CIAO and scales the effective area at each energy, using the polynomial fit, to effectively correct for the missing effective area due to the exclusion of the central pixels. The code then writes a new ARF which can be used to correct for the effects of excluding the central pixels.

For the sources with $0.2 < z < 0.7$ we used *XMM-Newton* observations. We extracted MOS and PN spectra for all of them, using SAS 11.0 and the latest calibration files. We used spatially coincident extraction regions for the three instruments whenever possible, using 30-arcsec source regions and off-source 90-arcsec background regions for the fainter sources, and 60-arcsec and 120-arcsec source and background regions, respectively, for the bright ones. Only a few observations were affected by flaring severe enough to require filtering. The most problematic case was PKS 1547–79, a faint source observed during a period of high flaring. We filtered the most severely

affected parts of the observation.

Four low-z sources (PKS 0404+03, 1814–63, 2135–14, 2221–02) have *XMM* observations that we did not use, since the *Chandra* spectra adequately characterised the AGN spectrum and had no contamination from any circumnuclear gas. For PKS 2314+03, however, we used both the *Chandra* and *XMM* observations, given that its spectrum is quite peculiar.

The case of 3C 273 is also peculiar, in that we only used one of the numerous observations available. We decided to use an *XMM* observation to avoid issues with the pileup. Given that the jet is not resolved in the MOS and PN cameras we took this into account when modelling the nuclear emission. We are also aware of the fact that this source is highly variable, as most bright AGN are. X-ray variability is a systematic effect that introduces scatter in our plots, but has been taken into account in our results.

We rebinned all the spectra to 20 counts per bin (after background subtraction) to make them compatible with χ^2 statistics.

6.2.2 Spectral Fitting

For spectral fitting we used XSPEC version 12.5 and followed the same approach as Hardcastle et al. (2006, 2009), as follows. We considered the energy range between 0.4 and 7 keV for the *Chandra* spectra, and 0.3 to 8 keV for the *XMM* spectra. We approached the fitting process in a systematic manner: we initially used a model a single power law and fixed Galactic absorption (wabs), adding a second power law, intrinsic absorption (zwabs) and a redshifted Gaussian profile for the Fe K-α line (zgauss) when required by the spectra. When a single power law model was sufficient to provide a good fit, we froze the parameters and added a second component with a fixed photon index and an intrinsic absorption column $N_H = 10^{23}$ cm^{-2} at the redshift of the source. If the 90 per cent uncertainty of the power law normalization was consistent with zero, we considered the upper bound as an upper limit to calculate the luminosity of this component. In most cases it was possible to discern whether and which power law would fit the soft and hard end of the spectrum: when the photon index of the 'soft' power law (which we will call 'unabsorbed' throughout this work, after Hardcastle et al. 2006, 2009) could not be properly constrained we fixed its value to Γ=2.0; for a poorly constrained 'hard' component (which we will call 'accretion-related'), we froze

Γ=1.7.

We derived the luminosity for the unabsorbed component, L_{X_u}, from the normalization of the unabsorbed power law, and used XSPEC to calculate the 2-10 keV unabsorbed luminosity (corresponding to the accretion-related component), L_{X_a}.

As mentioned in the previous Section, our *XMM* extraction regions for 3C 273 include the jet, since it is not resolved. Our spectral fit shows a soft excess that is not fit by the simple two-power law model we used for most of the other sources. Despite the slightly worse resulting χ^2, we decided not to add an additional component to model the jet. The impact on our results should be negligible.

We are also aware of the fact that the brightest sources are likely to have measurable variations in their luminosity over time. This is an intrinsic uncertainty characteristic of X-ray AGN studies, unavoidable unless follow-up observations are carried out for each source. We estimate the impact of variability and other systematics in Sections 6.4 and 6.5.

6.2.3 Other Data

To establish a direct comparison with the 3CRR sources, we used comparable measurements, which for the 2Jy sample were taken systematically.

We used the VLA and ATCA data at 5 GHz (both for overall and core luminosities) from Morganti et al. (1993, 1999). Since only some of the 2Jy sources are covered by the Parkes catalog (Wright & Otrupcek 1990), we calculated the spectral index from 408 MHz and 1.4 GHz observations (also from the Parkes catalog) and extrapolated the results to 178 MHz. We used this same spectral index to extrapolate the 151 MHz fluxes, needed to calculate the jet kinetic power (see Section 6.5.1). The low-frequency fluxes for PKS 1934-63 are upper limits, since the source is self-absorbed in radio.

For the infrared, we used 24 μm data taken by Spitzer, from Dicken et al. (2008, 2009). The 3C sources were observed at 15 μm (rest-frame), which is consistent enough for our purposes of comparison. We studied the behaviour of a number of sources at both wavelengths, and estimated that the deviation in luminosity caused by the difference between 15 and 24 μm was well below 10 per cent in all cases.

For the optical line classification we used the data from Tadhunter et al. (1993, 1998). K-band magnitudes were taken from Inskip et al. (2010) and K-corrected using

the relations given by Glazebrook et al. (1995) and Mannucci et al. (2001). The values presented in the Tables are K-corrected.

For the 3CRR sources we used the data from Hardcastle et al. (2006, 2009). In this case the 178 MHz fluxes were measured as part of the sample definition, but 1.4 GHz and 151 MHz fluxes had to be extrapolated from these measurements and the 178-750 MHz spectral indices[1] The references for the K-band magnitudes of each source are given in Table 6.6.

6.3 The X-ray 2Jy sample

The results of the spectral fits are displayed in Table 6.1. The sources where a Fe K-α line was detected are listed in Table 6.2. Details for each individual source, and references to previous work, are given in Chaper 5.

We find that our X-ray results, both on the luminosity of the cores and the detection of extended emission with *Chandra*, agree with an early *ROSAT* paper by Siebert et al. (1996). The X-ray luminosities we derive allow us to establish a direct comparison with the 3CRR sources studied by Hardcastle et al. (2006, 2009).

[1] http://3crr.extragalactic.info/

Table 6.1: Best fit parameters for all the objects in the sample. Where no errors are indicated the parameters were fixed to that value. Values followed by an asterisk represent upper limits. When the normalization of one of the powerlaws is an upper limit this component is added after the fit, to assess the contribution of a hypothetical second component. The subindices 1 and 2 refer to the unabsorbed and accretion-related components, respectively.

PKS	z	Foreground N_H $\times 10^{20}$ cm^{-2}	Intrinsic N_H $\times 10^{22}$ cm^{-2}	Γ_1	Norm 1 keV^{-1}cm^{-2}s^{-1} @1keV	Γ_2	Norm 2 keV^{-1}cm^{-2}s^{-1} @1keV	χ^2/DOF
0023-26	0.322	1.76	$0.16^{+0.11}_{-0.10}$	2.00	1.06×10^{-6}*	$1.84^{+0.51}_{-0.19}$	$1.73^{+0.55}_{-0.80} \times 10^{-5}$	20.69/23.00
0034-01	0.073	2.89	$10.07^{+4.84}_{-3.04}$	$1.24^{+0.36}_{-0.34}$	$1.17^{+0.14}_{-0.15} \times 10^{-5}$	1.70	$1.01^{+0.29}_{-0.28} \times 10^{-4}$	10.02/20.00
0035-02	0.220	2.85	$3.34^{+1.36}_{-0.97}$	2.00	$1.44^{+0.14}_{-0.13} \times 10^{-4}$	1.70	$2.59^{+0.41}_{-0.43} \times 10^{-4}$	31.12/49.00
0038+09	0.188	5.45	10.00	$0.97^{+0.07}_{-0.07}$	$1.05^{+0.07}_{-0.07} \times 10^{-3}$	1.70	4.54×10^{-4}*	84.44/82.00
0039-44	0.346	2.56	$12.40^{+1.82}_{-1.76}$	$2.87^{+0.42}_{-0.18}$	$6.60^{+1.52}_{-1.52} \times 10^{-6}$	$1.39^{+0.09}_{-0.17}$	$1.58^{+0.40}_{-0.51} \times 10^{-4}$	94.30/92.00
0043-42	0.116	2.70	$13.91^{+5.53}_{-4.08}$	2.00	$2.06^{+0.85}_{-0.86} \times 10^{-6}$	1.70	$1.51^{+0.47}_{-0.40} \times 10^{-4}$	6.32/5.00
0105-16	0.400	1.67	$16.13^{+7.34}_{-5.43}$	$1.59^{+0.18}_{-0.20}$	$2.65^{+0.21}_{-0.22} \times 10^{-5}$	$1.50^{+0.41}_{-0.39}$	$1.84^{+2.01}_{-0.40} \times 10^{-4}$	125.16/137.00
0213-13	0.147	1.89	$18.40^{+4.66}_{-3.40}$	$1.69^{+1.05}_{-1.59}$	$4.62^{+1.23}_{-1.81} \times 10^{-6}$	$1.77^{+0.18}_{-0.22}$	$1.31^{+0.64}_{-0.51} \times 10^{-3}$	45.85/50.00
0235-19	0.620	2.70	0.00	$1.43^{+0.25}_{-0.24}$	$7.30^{+1.07}_{-1.09} \times 10^{-6}$	$1.43^{+0.25}_{-0.24}$	$7.30^{+1.07}_{-1.09} \times 10^{-6}$	10.44/10.00
0252-71	0.566	3.66	$14.90^{+12.67}_{-7.09}$	$2.13^{+0.40}_{-0.33}$	$8.15^{+1.50}_{-2.14} \times 10^{-6}$	1.70	$3.87^{+1.54}_{-1.04} \times 10^{-5}$	20.40/24.00
0347+05	0.339	13.20	$74.85^{+39.25}_{-20.63}$	$1.95^{+0.25}_{-0.25}$	$1.54^{+0.17}_{-0.17} \times 10^{-5}$	1.70	$1.57^{+1.42}_{-0.79} \times 10^{-4}$	16.72/24.00
0349-27	0.066	1.00	$6.40^{+2.00}_{-1.52}$	2.00	2.67×10^{-6}*	1.70	$2.55^{+0.49}_{-0.55} \times 10^{-4}$	15.98/20.00
0404+03	0.089	12.10	$49.13^{+19.32}_{-15.61}$	2.00	1.05×10^{-5}*	1.70	$2.78^{+1.72}_{-1.14} \times 10^{-3}$	12.28/8.00
0409-75	0.693	8.71	10.00	$2.02^{+0.06}_{-0.07}$	$8.71^{+0.33}_{-0.35} \times 10^{-5}$	1.70	4.64×10^{-6}*	137.62/107.00
0442-28	0.147	2.32	$0.85^{+0.33}_{-0.31}$	2.00	$5.49^{+5.45}_{-5.30} \times 10^{-5}$	$1.13^{+0.24}_{-0.17}$	$1.18^{+0.44}_{-0.30} \times 10^{-3}$	119.53/134.00
0521-36	0.055	3.33	10.00	$1.53^{+0.03}_{-0.03}$	$6.17^{+0.12}_{-0.12} \times 10^{-3}$	1.70	2.01×10^{-4}*	417.14/366.00
0620-52	0.051	5.32	10.00	$2.40^{+0.10}_{-0.10}$	$9.51^{+0.52}_{-0.52} \times 10^{-5}$	1.70	1.27×10^{-5}*	39.24/47.00
0625-35	0.055	7.51	$5.99^{+2.56}_{-1.64}$	2.00	$1.11^{+0.09}_{-0.09} \times 10^{-3}$	1.70	$2.74^{+0.57}_{-0.45} \times 10^{-3}$	221.05/173.00
0625-53	0.054	5.51	10.00	2.00	1.15×10^{-5}*	1.70	8.51×10^{-10}*	1.00/1.00
0806-10	0.110	7.65	$21.19^{+8.22}_{-6.18}$	$3.00^{+1.04}_{-1.37}$	$1.08^{+0.34}_{-0.43} \times 10^{-5}$	1.70	$4.63^{+2.33}_{-1.52} \times 10^{-4}$	18.17/18.00
0859-25	0.305	10.80	$38.25^{+21.16}_{-23.79}$	$1.61^{+0.41}_{-0.44}$	$9.13^{+1.53}_{-0.84} \times 10^{-6}$	$1.67^{+0.39}_{-0.75}$	$1.81^{+31.00}_{-1.13\times10^{-4}} \times 10^{-4}$	24.73/24.00
0915-11	0.054	4.94	$2.39^{+1.90}_{-1.35}$	2.00	2.11×10^{-6}*	$1.35^{+0.60}_{-0.63}$	$2.49^{+4.58}_{-1.55} \times 10^{-5}$	71.33/57.00

Continued on next page

Table 6.1 – *Continued from previous page*

PKS	z	Foreground N_H $\times 10^{20}$ cm^{-2}	Intrinsic N_H $\times 10^{22}$ cm^{-2}	Γ_1	Norm 1 keV^{-1}cm^{-2}s^{-1} @1keV	Γ_2	Norm 2 keV^{-1}cm^{-2}s^{-1} @1keV	χ^2/DOF
0945+07	0.086	3.01	$1.44^{+0.20}_{-0.18}$	$3.01^{+0.62}_{-0.57}$	$8.30^{+2.62}_{-2.52} \times 10^{-5}$	$0.73^{+0.09}_{-0.09}$	$1.24^{+0.18}_{-0.14} \times 10^{-3}$	468.26/434.00
1136-13	0.554	3.59	$6.06^{+4.33}_{-2.77}$	$2.00^{+0.09}_{-0.08}$	$3.22^{+0.08}_{-0.14} \times 10^{-4}$	$1.48^{+0.44}_{-0.29}$	$1.38^{+0.22}_{-0.53} \times 10^{-4}$	705.38/619.00
1151-34	0.258	7.70	$52.76^{+52.42}_{-28.83}$	$1.86^{+0.07}_{-0.07}$	$8.02^{+0.26}_{-0.28} \times 10^{-5}$	1.70	$1.28^{+2.40}_{-0.90} \times 10^{-4}$	160.27/163.00
1226+02	0.158	1.79	$0.79^{+0.09}_{-0.06}$	$2.17^{+0.01}_{-0.02}$	$1.79^{+0.01}_{-0.02} \times 10^{-2}$	$1.16^{+0.02}_{-0.02}$	$4.93^{+0.23}_{-0.19}$	3584.67/2539.00
1306-09	0.464	3.03	$0.11^{+0.04}_{-0.04}$	2.00	$2.24 \times 10^{-6}*$	$1.77^{+0.09}_{-0.09}$	$7.25^{+0.62}_{-0.54} \times 10^{-5}$	163.12/169.00
1355-41	0.313	5.61	$0.27^{+0.24}_{+0.18}$	2.00	$1.11^{+0.39}_{-0.38} \times 10^{-5}$	1.70	$2.84^{+8.48}_{-2.45} \times 10^{-4}$	843.39/722.00
1547-79	0.483	9.69	$99.28^{+594.53}_{-46.51}$	2.00	$1.60^{+0.18}_{-0.70} \times 10^{-5}$	1.70	$2.51^{+1.86}_{-1.38} \times 10^{-4}$	17.89/18.00
1559+02	0.104	6.42	$6.02^{+3.85}_{-2.89}$	$3.37^{+0.30}_{-0.25}$	$2.12^{+0.22}_{-0.26} \times 10^{-5}$	1.70	$3.26^{+1.32}_{-0.97} \times 10^{-5}$	19.22/23.00
1602+01	0.462	6.59	0.00	$1.68^{+0.03}_{-0.03}$	$2.79^{+0.06}_{-0.06} \times 10^{-4}$	$1.68^{+0.03}_{-0.03}$	$2.79^{+0.06}_{-0.06} \times 10^{-4}$	396.19/362.00
1648+05	0.154	6.40	10.00	$0.80^{+1.34}_{-1.61}$	$5.01^{+1.85}_{-1.91} \times 10^{-6}$	1.70	$1.45 \times 10^{-3}*$	6.53/4.00
1733-56	0.098	8.89	10.00	$1.54^{+0.05}_{-0.05}$	$1.06^{+0.04}_{-0.04} \times 10^{-3}$	1.70	$1.67 \times 10^{-4}*$	142.22/133.00
1814-63	0.063	7.76	$2.00^{+0.28}_{-0.28}$	2.00	$2.03^{+1.35}_{-1.40} \times 10^{-5}$	$1.26^{+0.18}_{-0.17}$	$1.90^{+0.23}_{-0.25} \times 10^{-3}$	119.13/126.00
1839-48	0.112	5.70	10.00	$1.35^{+0.23}_{-0.22}$	$1.17^{+0.21}_{-0.21} \times 10^{-5}$	1.70	$8.82 \times 10^{-6}*$	6.98/8.00
1932-46	0.231	5.01	0.00	$1.82^{+0.08}_{-0.07}$	$6.20^{+0.29}_{-0.27} \times 10^{-5}$	$1.82^{+0.08}_{-0.07}$	$6.20^{+0.29}_{-0.27} \times 10^{-5}$	52.79/74.00
1934-63	0.183	6.15	10.00	$1.36^{+0.18}_{-0.18}$	$2.44^{+0.28}_{-0.28} \times 10^{-5}$	1.70	$1.88 \times 10^{-5}*$	14.91/15.00
1938-15	0.452	9.66	$0.37^{+0.15}_{-0.12}$	2.00	$4.28^{+0.77}_{-1.89} \times 10^{-5}$	$1.51^{+0.06}_{-0.08}$	$8.92^{+1.00}_{-0.63} \times 10^{-5}$	189.19/194.00
1949+02	0.059	14.80	$42.69^{+8.26}_{-3.06}$	$2.05^{+0.30}_{-0.29}$	$1.50^{+0.17}_{-0.17} \times 10^{-5}$	$1.41^{+0.10}_{-0.14}$	$1.24^{+0.39}_{-0.49} \times 10^{-3}$	78.24/81.00
1954-55	0.060	4.61	10.00	$0.97^{+0.37}_{-0.38}$	$4.00^{+1.43}_{-1.38} \times 10^{-6}$	1.70	$7.34 \times 10^{-6}*$	1.78/2.00
2135-14	0.200	4.73	$18.38^{+11.73}_{-7.97}$	$1.90^{+0.17}_{-0.12}$	$8.26^{+0.39}_{-0.39} \times 10^{-4}$	1.70	$1.79^{+0.68}_{-0.41} \times 10^{-3}$	120.06/96.00
2135-20	0.635	3.38	$64.52^{+44.68}_{-24.56}$	2.00	$4.75^{+0.97}_{-1.01} \times 10^{-6}$	1.70	$4.63^{+4.04}_{-2.60} \times 10^{-5}$	12.24/14.00
2211-17	0.153	2.51	10.00	2.00	$4.74 \times 10^{-6}*$	1.70	$4.87 \times 10^{-9}*$	1.00/1.00
2221-02	0.057	5.01	$19.69^{+3.12}_{-1.97}$	$0.82^{+0.26}_{-0.29}$	$5.17^{+0.47}_{-0.50} \times 10^{-5}$	1.70	$2.21^{+0.27}_{-0.17} \times 10^{-3}$	169.28/144.00
2250-41	0.310	1.48	10.00	$1.93^{+1.69}_{-1.16}$	$4.62^{+2.55}_{-2.77} \times 10^{-6}$	1.70	$4.08^{+1640.00}_{-4.08} \times 10^{-8}$	13.49/8.00
2314+03	0.220	5.22	$9.58^{+7.88}_{-4.17}$	$2.16^{+0.21}_{-0.19}$	$1.55^{+0.13}_{-0.17} \times 10^{-5}$	1.70	$3.23^{+1.47}_{-0.79} \times 10^{-5}$	67.19/46.00
2356-61	0.096	2.34	$14.68^{+1.50}_{-1.29}$	$3.08^{+0.57}_{-0.88}$	$8.43^{+2.02}_{-2.15} \times 10^{-6}$	1.70	$9.82^{+0.98}_{-0.92} \times 10^{-4}$	47.84/47.00

Table 6.2: Objects for which a Fe Kα emission line was detected. Where no errors are quoted the parameter had to be fixed for the overall model fit.

PKS	peak keV	eq. width keV
0039-44	$6.32^{+0.68}_{-0.18}$	0.06
0043-42	$6.48^{+0.32}_{-0.05}$	0.88
0105-16	$6.22^{+0.78}_{-0.22}$	0.09
0409-75	$6.68^{+0.09}_{-0.15}$	0.44
0859-25	$6.51^{+0.47}_{-0.10}$	0.28
1151-34	6.34	0.10
1559+02	$6.44^{+0.05}_{-0.05}$	4.00
1814-63	$6.40^{+0.09}_{-0.07}$	0.15
1938-15	$6.51^{+0.07}_{-0.06}$	0.16
2221-02	$6.37^{+0.05}_{-0.05}$	0.17
2356-61	$6.30^{+0.08}_{-0.07}$	0.14

In our analysis of the X-ray emission of the 2Jy objects we observe trends similar to those observed by Hardcastle et al. (2006, 2009) for the 3CRR sources. The luminosity distribution of the sources versus redshift is as expected, with a greater abundance of low-luminosity sources at low z, and only the brighter objects detected at high z (see Figures 6.1 and 6.2). This effect is, at least in part, caused by the detection limits and sample selection criteria (see Section 5.1).

It is important to keep in mind that the luminosities we derive for the X-ray components may suffer from contamination from each other. This is particularly evident in the broad-line and quasar-like objects. In these objects there is little or no intrinsic absorption to allow us to distinguish both components, thus we adopt the same value for L_{X_u} and L_{X_a}. This effect can be seen in Figures 6.1, 6.2 and 6.3, where a few BLRGs and QSOs seem to have systematically higher luminosities than the rest of their populations.

These plots show a distinct separation between the different populations. Low-excitation objects have much lower accretion-related X-ray emission than any of the other groups. This is consistent with the hypothesis in which LERGs lack the traditional accretion features characteristic of the high-excitation population (see e.g. Hardcastle et al. 2007a). The separation between narrow-line (NLRG) and broad-line (BLRG) objects is more striking in Figure 6.2 due both to the possible contamination by jet emission in broad-line objects, and to the influence of relativistic beaming, which 'boosts' the soft X-ray emission in objects whose jets are viewed at small inclination

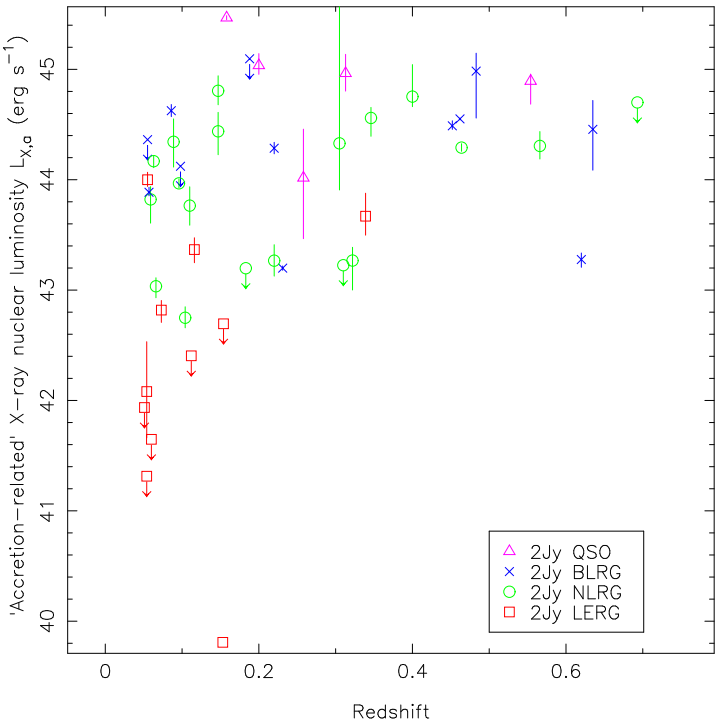

Figure 6.1: X-ray luminosity for the accretion-related component L_{X_a} of the 2Jy sources against redshift. Open and filled symbols refer to the 2Jy and 3CRR objects, respectively. Red squares represent LERGs, green circles NLRGs, blue crosses BLRGs, and purple triangles QSOs.

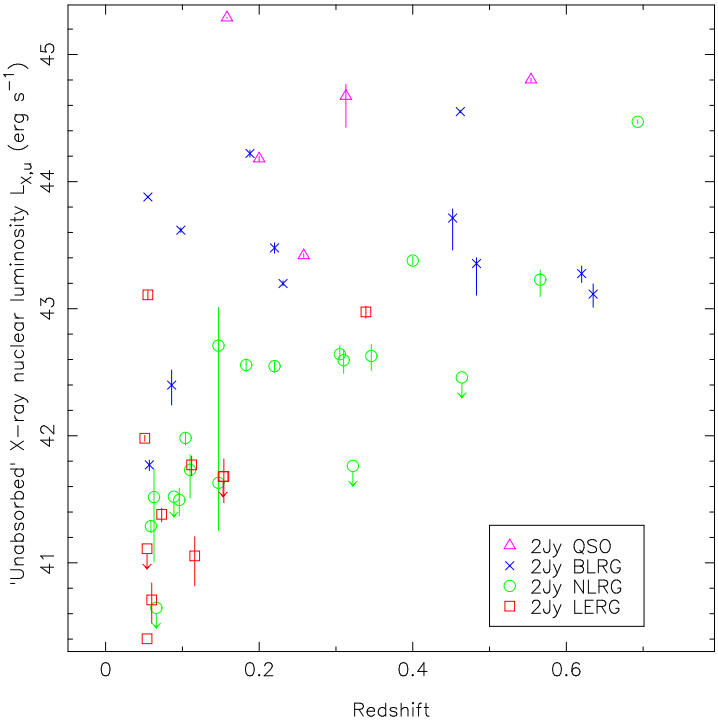

Figure 6.2: X-ray luminosity for the unabsorbed component L_{X_u} of the 2Jy sources against redshift. Only the 2Jy sources are plotted. Arrows indicate upper limits. Colours and symbols as in Fig. 6.1.

angles.

The four LERGs that fall in the NLRG parameter space in Figure 6.1 may, in fact,be high-excitation objects. 3C 15 (PKS 0034-01) is very luminous and has a relatively well constrained, obscured, hard component (see Section 5.2). Although we do not detect unequivocal signs of accretion in the form of an emission Fe Kα line, this could be due to the low statistics, rather than the absence of the line itself. PKS 0043-42 does have a Fe Kα line, and Ramos Almeida et al. (2011a) find IR evidence for a torus (see also Section 5.2). PKS 0625-35 (Section 5.2) is extremely bright and is suspected to be a BL-Lac (Wills et al. 2004). In this case it is hard to tell whether this object is a LERG with a low inclination angle or has been classified as such because the optical emission lines cannot be detected at such low inclinations.

A special mention should be made of PKS 0347+05. This object is classified as a BLRG in our sample, but recent evidence suggests that this is, in fact, a double system, with a LERG and a radio-quiet Seyfert 1 in close interaction (see Section 5.3). We have decided to keep this object in our plots and classify it as a LERG based on its optical spectrum (Tadhunter et al. 2012), for consistency with the rest of our analysis, though it is a clear outlier in most of our plots.

Figure 6.3 shows the distribution of 2Jy sources according to the relation between their unabsorbed and accretion-related X-ray luminosities. Each population occupies a different area in the parameter space, with a certain degree of overlap between the brighter NLRGs and fainter BLRGs, as can be expected from unification models. For the same reason, there is some overlap between the fainter NLRGs and the brighter LERGs. However, it is evident from Figure 6.3 that LERGs have a much lower L_{X_a}/L_{X_u} ratio than any of the other populations. This reinforces the conclusions from the previous paragraph about the nature of accretion in LERGs. Adding the 3CRR objects makes this even more evident, as can be seen in the equivalent plot by Hardcastle et al. (2009). As in Figure 6.1, the four 'dubious' LERGs seem to fall in the parameter space occupied by NLRGs.

6.4 Correlations

As described in Section 6.2.2, from the analysis of the X-ray cores we derived the luminosity of the unabsorbed (L_{X_u}) and accretion-related components (L_{X_a}). For our

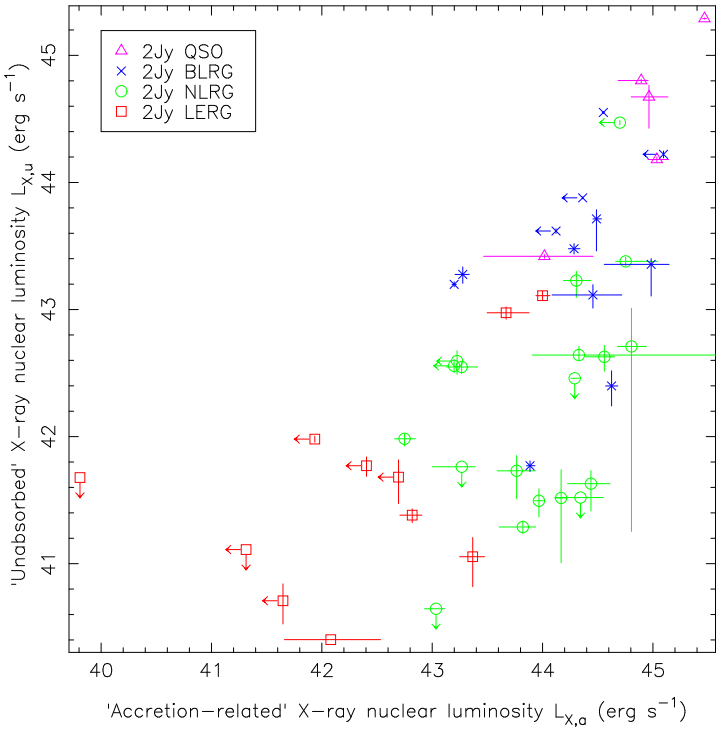

Figure 6.3: X-ray luminosity of the 2Jy sources, showing the unabsorbed component L_{X_u} against X-ray luminosity for the 'accretion-related' component L_{X_a}. Arrows indicate upper limits. Colours and symbols as in Fig. 6.1.

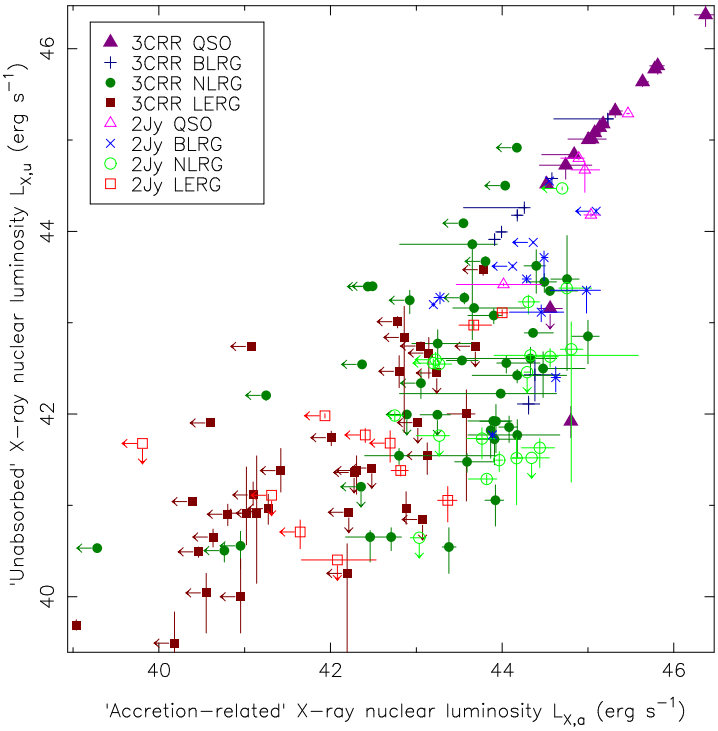

Figure 6.4: X-ray luminosity for the unabsorbed component L_{X_u} against X-ray luminosity for the 'accretion-related' component L_{X_a}. The 2Jy sources are represented with brighter colours, the 3C sources are faded. Arrows indicate upper limits. Colours and symbols as in Fig. 6.1.

analysis we compared these luminosities with those derived from the 178 MHz, 5 GHz (core), 24 μm and [OIII] fluxes, all of which are displayed in Table 6.3. As in the case of the 3CRR objects (Hardcastle et al. 2009), the 2Jy sample is a flux-limited sample, thus correlations are expected in luminosity-luminosity plots. We test for partial correlation in the presence of redshift to account for this, following the method and code described by Akritas & Siebert (1996), which takes into account upper limits in the data. The results of the partial correlation analysis are given in Table 6.4.

While the relations between these luminosities can provide some insight into the physical processes going on in each source, it is important to keep in mind that there are several intrinsic effects that limit this insight, orientation, beaming and environmental interference being perhaps the most relevant. These effects are also the most likely cause of scatter in the plots that we present in the following Sections. In this

Table 6.3: Luminosities for the sources in the 2Jy sample, following the format of Hardcastle et al. (2009). The values are given as the logarithm of the luminosity in erg s^{-1}, upper limits are indicated with a negative sign before the value. We have converted the radio and IR luminosity densities into νL_ν to allow for direct comparison between the magnitudes in different bands. Where measurements could not be obtained their absence is indicated with a dash. E stands for LERG, N for NLRG, B for BLRG, Q for Quasar.

PKS	Type	z	L_{178}	L_5	L_{X_u}			L_{X_a}			L_{IR}	$L_{[OIII]}$
0023-26	N	0.3220	43.1995	-	-41.7630	-	-	43.2675	43.0002	43.3871	44.0083	42.1761
0034-01	E	0.0730	41.5867	41.2511	41.3818	41.3219	41.4316	42.8183	42.7068	42.9062	43.0790	40.4914
0035-02	B	0.2200	42.7985	42.5488	43.4787	43.4369	43.5184	44.2855	44.2345	44.3386	44.2986	42.0792
0038+09	B	0.1880	42.6169	41.5383	44.2211	44.1928	44.2478	-45.0957	-	-	44.5053	42.1761
0039-44	N	0.3460	43.1535	40.6509	42.6282	42.5145	42.7184	44.5595	44.3935	44.6551	45.2193	43.0414
0043-42	E	0.1160	42.1566	40.9657	41.0552	40.8193	41.2055	43.3669	43.2479	43.4739	43.6785	40.6990
0105-16	N	0.4000	43.4682	40.6056	43.3793	43.3423	43.4118	44.7524	44.6612	45.0429	44.8354	42.3979
0213-13	N	0.1470	42.3706	-	41.6300	41.4145	41.7323	44.4381	44.2259	44.6096	43.9029	42.1139
0235-19	B	0.6200	43.8768	-	43.2763	43.2061	43.3359	43.2763	43.2061	43.3359	45.3503	43.2788
0252-71	N	0.5660	43.8008	-	43.2278	43.0951	43.3013	44.3057	44.1877	44.4365	44.6714	42.1461
0347+05	E	0.3390	43.0134	40.3314	42.9743	42.9242	43.0204	43.6696	43.4976	43.8776	44.2241	40.9590
0349-27	N	0.0660	41.4014	39.7998	-40.6457	-	-	43.0344	42.9299	43.1111	43.0560	41.0792
0404+03	N	0.0890	41.7898	40.1009	-41.5201	-	-	44.3437	44.1142	44.5513	43.8783	41.4624
0409-75	N	0.6930	44.4056	41.2734	44.4708	44.4532	44.4871	-44.6998	-	-	44.5990	42.1139
0442-28	N	0.1470	42.5893	40.9848	42.7098	41.2542	43.0095	44.8055	44.6787	44.9417	44.2050	41.8388
0521-36	B	0.0550	41.8739	41.7060	43.8792	43.8707	43.8875	-44.3627	-	-	44.2909	41.1600
0620-52	E	0.0510	41.1170	40.8899	41.9805	41.9561	42.0035	-41.9354	-	-	42.5477	-39.4150
0625-35	E	0.0550	41.1784	41.3137	43.1093	43.0720	43.1431	44.0000	43.9391	44.0670	43.3494	-40.4771
0625-53	E	0.0540	41.7439	40.1449	-41.1107	-	-	-41.3137	-	-	42.1729	-40.0414
0806-10	N	0.1100	42.1093	40.8854	41.7310	41.5105	41.8504	43.7651	43.5873	43.9357	45.0004	42.7709
0859-25	N	0.3050	43.2810	42.0771	42.6419	42.5997	42.7092	44.3297	43.9065	45.5883	44.5421	41.9777
0915-11	E	0.0540	42.5674	40.8864	-40.4020	-	-	42.0803	41.6608	42.5321	42.9201	40.4624
0945+07	B	0.0860	42.0389	40.4438	42.3991	42.2416	42.5182	44.6248	44.5719	44.6818	44.0509	41.9031
1136-13	Q	0.5540	43.5461	-	44.8021	44.7831	44.8131	44.8932	44.6843	44.9564	45.3264	43.7324
1151-34	Q	0.2580	42.7489	-	43.4187	43.4033	43.4325	44.0164	43.4650	44.4575	44.6217	42.4472
1226+02	Q	0.1580	42.8550	43.8874	45.2902	45.2857	45.2949	45.4669	45.4495	45.4860	45.6289	43.4800
1306-09	N	0.4640	43.1813	-	-42.4592	-	-	44.2909	44.2573	44.3264	44.6644	42.1461
1355-41	Q	0.3130	42.9741	41.6516	44.6732	44.4271	44.7655	44.9641	44.8024	45.1361	45.3247	42.8865
1547-79	B	0.4830	43.4741	40.9513	43.3551	43.1056	43.4010	44.9838	44.5588	45.1465	44.9409	43.4314
1559+02	N	0.1040	42.3780	40.5543	41.9832	41.9263	42.0263	42.7488	42.6579	42.8484	44.9319	42.2553
1602+01	B	0.4620	43.6639	42.2472	44.5507	44.5419	44.5592	44.5507	44.5419	44.5592	44.8836	42.8129
1648+05	E	0.1540	43.6328	40.4129	41.6811	41.4731	41.8172	-42.6949	-	-	43.1741	40.6532
1733-56	B	0.0980	42.0457	41.8810	43.6182	43.5998	43.6359	-44.1220	-	-	43.9524	41.8129
1814-63	N	0.0630	42.1275	-	41.5170	41.0075	41.7390	44.1678	44.1085	44.2161	43.8851	40.6335
1839-48	E	0.1120	41.9730	41.3632	41.7705	41.6868	41.8408	-42.4046	-	-	43.0864	-39.3617
1932-46	B	0.2310	43.3967	41.5878	43.1983	43.1791	43.2184	43.1983	43.1791	43.2184	43.6958	42.3802
1934-63	N	0.1830	-43.3798	-	42.5568	42.5027	42.6044	-43.1977	-	-	44.3024	42.0792
1938-15	B	0.4520	43.5708	41.3177	43.7138	43.4614	43.7853	44.4878	44.4560	44.5339	44.8070	42.8808
1949+02	N	0.0590	41.6303	39.5819	41.2886	41.2371	41.3360	43.8210	43.6067	43.9377	44.2903	41.8573
1954-55	E	0.0600	41.5454	40.2738	40.7084	40.5256	40.8410	-41.6471	-	-	42.4294	-39.0000
2135-14	Q	0.2000	42.4922	41.7612	44.1805	44.1596	44.2006	45.0350	44.9548	45.1425	45.1763	43.1139
2135-20	B	0.6350	43.6840	-	43.1152	43.0110	43.1955	44.4560	44.0865	44.7177	45.0205	43.1461
2211-17	E	0.1530	42.8790	39.7356	-41.6781	-	-	-39.8085	-	-	42.5933	40.3802
2221-02	B	0.0570	41.4983	40.4621	41.7707	41.7262	41.8084	43.8865	43.8540	43.9311	44.3153	42.2304
2250-41	N	0.3100	43.2265	40.5518	42.5944	42.4901	42.6764	-43.2248	-	-	44.6544	42.6990
2314+03	N	0.2200	42.9494	42.8189	42.5477	42.4961	42.5830	43.2661	43.1263	43.4112	44.9483	42.2041
2356-61	N	0.0960	42.3572	40.5681	41.4955	41.3678	41.5890	43.9668	43.9249	44.0075	44.0745	41.9542

Table 6.4: Results of partial correlation analysis described in Section 6.4. The number of objects for each correlation is given in column 4, and it includes all the objects in the corresponding subsample given in column 3. The last column indicates the strength of the partial correlation between the quantities in columns 1 and 2 in the presence of redshift. We consider the correlation significant if $\tau/\sigma > 3$.

x	y	subsample	n	τ	σ	τ/σ
L_{178}	L_{Xu}	2Jy+3CRR NLRG	109	0.210	0.044	4.744
		2Jy NLRG	19	0.243	0.141	1.727
L_{178}	L_{Xa}	all	149	0.118	0.029	4.116
		2Jy+3CRR HERG	104	0.130	0.037	3.477
		2Jy+3CRR LERG	44	0.014	0.031	0.460
L_5	L_{Xu}	all	139	0.458	0.046	10.029
L_5	L_{Xa}	all	139	0.264	0.047	5.651
		2Jy+3CRR, QSOs excluded	121	0.141	0.045	3.109
		2Jy+3CRR LERG	44	0.150	0.057	2.625
L_{IR}	L_{Xu}	all	119	0.359	0.055	6.537
		2Jy+3CRR HERG	85	0.277	0.070	3.940
L_{IR}	L_{Xa}	all	119	0.480	0.046	10.358
		2Jy+3CRR HERG	85	0.410	0.062	6.637
$L_{[OIII]}$	L_{Xa}	all	124	0.420	0.046	9.141
		2Jy+3CRR HERG	90	0.353	0.060	5.908
L_{178}	L_{IR}	all	141	0.190	0.035	5.408
		2Jy+3CRR HERG	107	0.207	0.044	4.715
		2Jy+3CRR NLRG	62	0.182	0.059	3.073
		2Jy+3CRR LERG	34	0.107	0.076	1.399
L_{178}	$L_{[OIII]}$	all	135	0.191	0.035	5.467
		2Jy+3CRR HERG	101	0.205	0.043	4.801
		2Jy+3CRR NLRG	56	0.152	0.054	2.844
		2Jy+3CRR LERG	34	0.121	0.066	1.835
L_{IR}	$L_{[OIII]}$	all	113	0.592	0.063	9.320
		2Jy HERG+LERG	47	0.676	0.095	7.154
		2Jy+3CRR HERG	84	0.533	0.068	7.806
		2Jy HERG	37	0.600	0.104	5.769

Chapter we therefore describe the correlations between these luminosities without reference to any particular model, merely attempting to establish the physical scenarios and measurement systematics that may cause these correlations to arise.

To allow direct comparison with the results of Hardcastle et al. (2009), we have plotted both the 2Jy and the 3CRR objects in our Figures. Fig. 6.4 summarises the X-ray characteristics of both populations. In terms of sample size, we have multiwavelength luminosities for 47 2Jy objects and 135 3CRR sources (although in the latter the data are less complete, see the tables in Section 6.7), more than doubling the number of objects studied by Hardcastle et al. (2009).

The differences between the LERGs and HERGs observed in Fig. 6.3 are highlighted by the addition of the 3CRR objects. It is also clearer that there is an overlap in the parameter space between BLRGs and NLRGs. Two 3CRR NLRGs with very low values of L_{X_a} are M 87 and 3C 338, both of which are believed to be radiatively inefficient accretors that would normally be classified as LERGs (see discussion in Evans et al. 2008). 3C 123 is probably more appropriately classified as a reddened NLRG, and the X-ray spectrum of 3C 200 is more compatible with that of a NLRG (see Appendix A of Hardcastle et al. 2006).

There are also some differences between the 2Jy and 3CRR populations, which can be partly attributed to the slightly different selection criteria used in both samples, and which may cause the 2Jy sample to have more beamed objects (as discussed in Section 5.1), as well as issues with sample completeness in the latter sample (the 3CRR sample is nearly complete in X-rays for low-z objects, but not so for $z > 0.5$). While we consider that these effects do not invalidate our results, it is essential to keep in mind that any selection criteria for an AGN sample introduce a certain bias. We will discuss other possible sources of bias in Section 6.5.

6.4.1 X-ray/Radio correlations

The 178 MHz luminosity is not only an indicator of the time-averaged jet power, but also of the age of the source, and is related to the properties of the external environment (Hardcastle & Krause 2013). By adding the 2Jy sources to the L_{178}/L_{X_u} plot (Fig. 6.5), a correlation between these quantities for the NLRGs is more readily apparent than it was for Hardcastle et al. (2009), despite the scatter (see Table 6.4 and Table 5 in

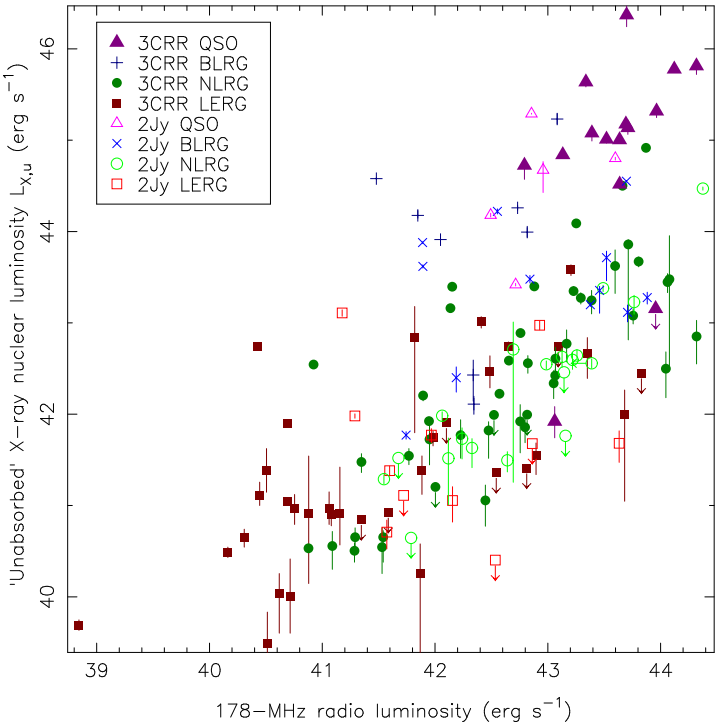

Figure 6.5: X-ray luminosity for the unabsorbed component L_{X_u} as a function of 178 MHz total radio luminosity. The 2Jy sources are represented with brighter colours, the 3C sources are faded. Arrows indicate upper limits. Colours and symbols as in Fig. 6.1.

Hardcastle et al. (2009)). The situation is not so clear for the BLRGs and QSOs, most likely due to the contamination from the accretion-related component. In the case of the LERGs the scatter is expected due to the fact that there are no selection effects on orientation. All of this suggests that there may be a weak physical link between the unabsorbed X-ray power (prior to beaming correction) and the overall radio power (related to the overall AGN power).

There is no apparent correlation between L_{178}/L_{X_u} if only the 2Jy sources are considered (see Table 6.4). This is most likely due to the large scatter in the jet-related quantities, and L_{X_u} in particular, caused by the presence of beamed objects in the 2Jy sample, a consequence of the selection criteria, as well as the low number of sources. In fact, the values of τ in the L_{178}/L_{X_u} correlation when only the 2Jy sources are considered is larger than it is for the combined 2Jy and 3CRR samples, but the scatter (indicated by σ) is much larger in the former case, resulting in $\tau/\sigma < 3$.

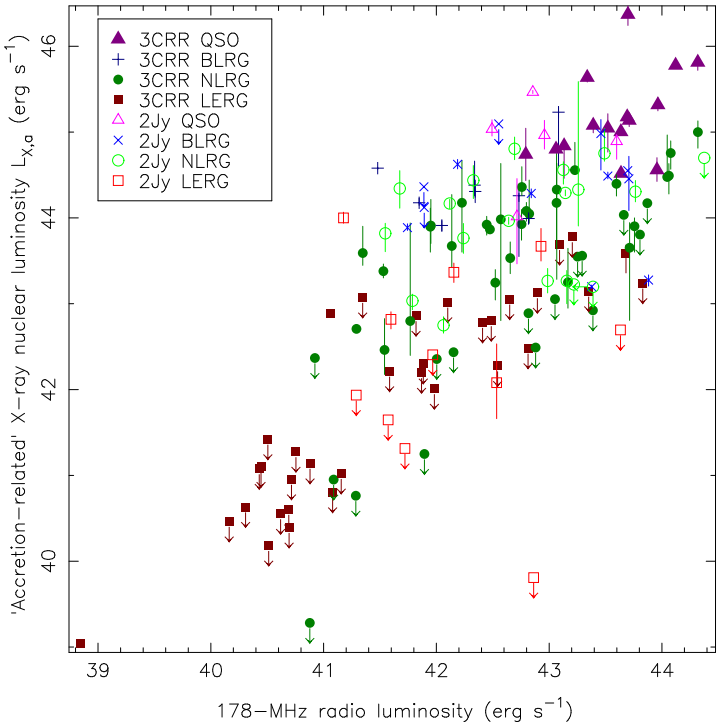

Figure 6.6: X-ray luminosity for the 'accretion-related' component L_{X_a} as a function of 178 MHz total radio luminosity. The 2Jy sources are represented with brighter colours, the 3C sources are faded. Arrows indicate upper limits. Colours and symbols as in Fig. 6.1.

By contrast, and as already pointed out by Hardcastle et al. (2009), there seems to be a strong correlation between L_{178}/L_{X_a} for all the populations excluding the LERGs, which seem to lie mostly below this correlation (see Fig. 6.6 and Table 6.4). The BLRGs and QSOs are not clearly outlying in this plot, despite the contamination from the jet-related X-ray component.

Fig. 6.7 shows the relation between the 5 GHz core luminosity and the unabsorbed X-ray component. The correlation between these quantities is strong (Table 6.4), despite the scatter, due to the fact that both quantities are subject to beaming. The fact that the LERGs lie in the same correlation as the NLRGs is evidence for the jet-related nature of the soft X-ray component in radio-loud sources (see e.g. Hardcastle et al. 2009; Worrall et al. 1987, and references within). For consistency with the rest of the AGN classes, however, there must be a contribution from the same mechanism that causes the soft emission in radio-quiet objects, at least in radiatively-efficient sources.

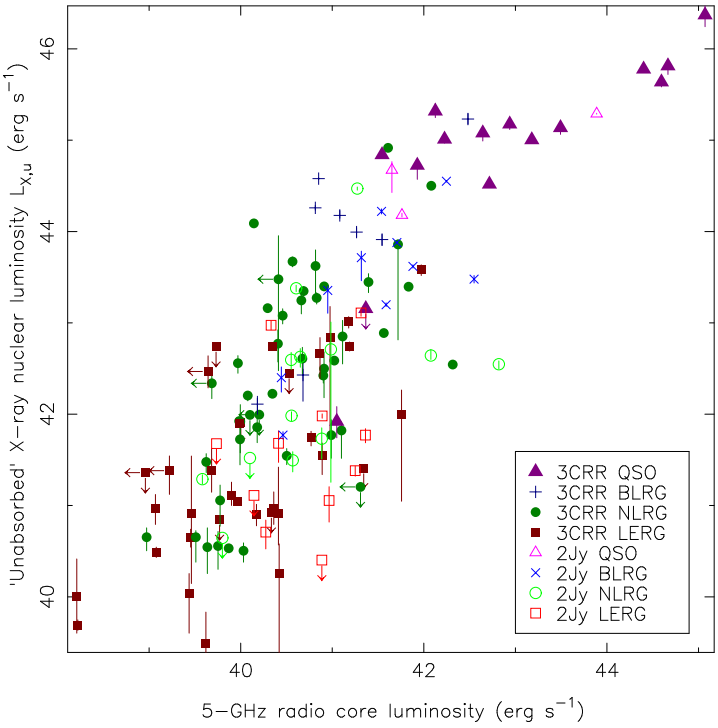

Figure 6.7: X-ray luminosity for the unabsorbed component L_{X_u} as a function of 5 GHz radio core luminosity. Arrows indicate upper limits. Colours and symbols as in Fig. 6.1.

Figure 6.8 shows the relation between the 5 GHz core luminosity and the accretion-related X-ray component. In this plot it becomes apparent that the LERGs show a distinct behaviour, completely apart from the high-excitation population. The correlation between these two quantities is less strong than between $L_{5GHz,core}$ and L_{X_u} (Table 6.4), and almost disappears if the QSOs are removed.

Correlations between both X-ray luminosities and the 5 GHz radio core luminosity are expected due to their mutual dependence on redshift. If the X-ray luminosity were simply related to the AGN power, and independent from orientation and beaming, it would not be strongly correlated to the 5 GHz core luminosity. As argued by e.g. Hardcastle & Worrall (1999), Doppler beaming can introduce up to three orders of magnitude of scatter in these correlations, given its strong influence on $L_{5GHz,core}$. The correlation we observe between $L_{5GHz,core}$ and L_{X_u}, in particular, reinforces the hypothesis that the soft X-ray flux is related to jet emission in radio-loud sources.

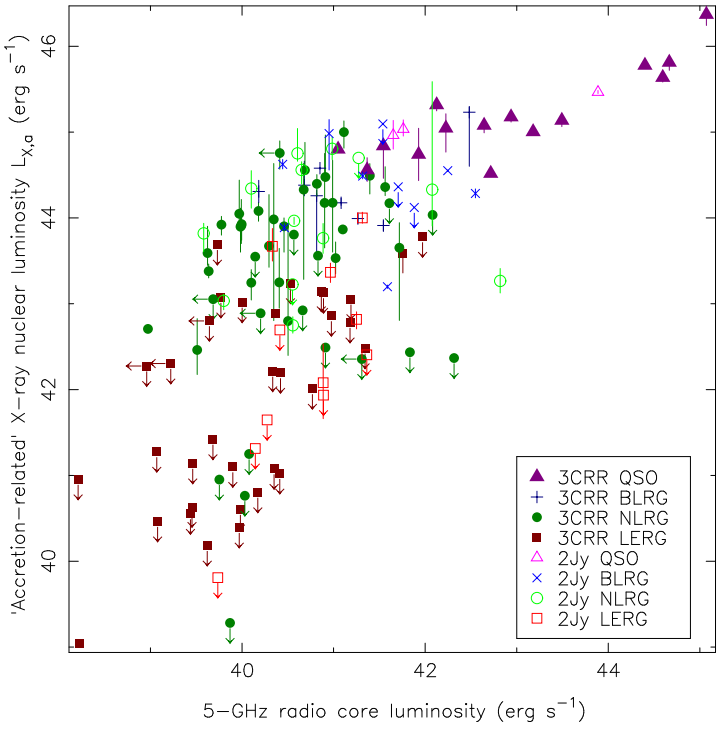

Figure 6.8: X-ray luminosity for the 'accretion-related' component L_{X_a} as a function of 5 GHz radio core luminosity. Arrows indicate upper limits. Colours and symbols as in Fig. 6.1.

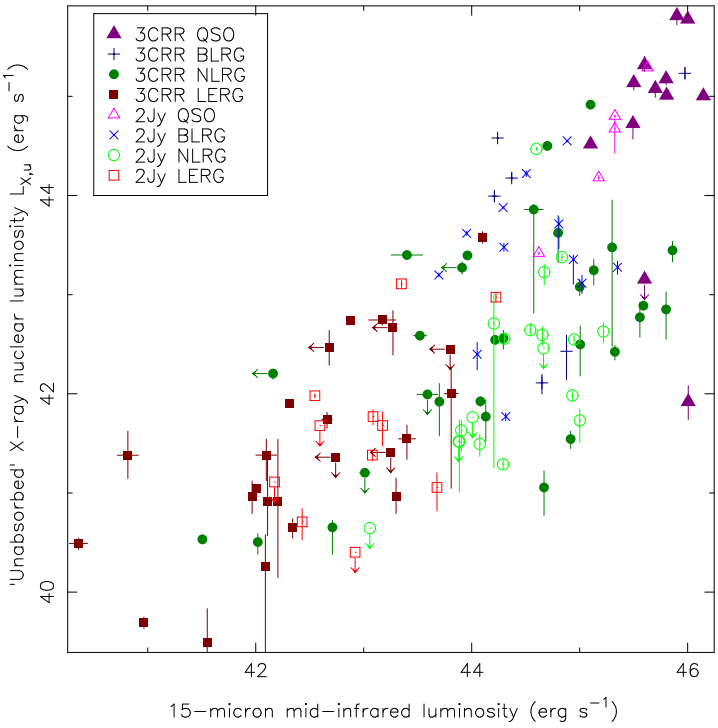

Figure 6.9: X-ray luminosity for the unabsorbed component L_{X_u}, as a function of total infrared (24 μm for the 2Jy sources, 15 μm for the 3C sources) luminosity. Arrows indicate upper limits. Colours and symbols as in Fig. 6.1.

6.4.2 X-ray/IR correlations

The main source of uncertainty in L_{IR} comes from its dependence with orientation, which is believed to introduce a large uncertainty (see e.g. Runnoe et al. 2012; Hardcastle et al. 2009, and references therein).

Despite the large scatter, there is an evident overall correlation between L_{IR} and L_{X_u} (Fig. 6.9 and Table 6.4), which was already visible in the plots of Hardcastle et al. (2009). The 2Jy sources fill some of the gaps left by the 3CRR sources in the parameter space. The correlation disappears for individual populations, however.

The correlation between L_{IR} and L_{X_a} is very strong (Fig. 6.10 and Table 6.4). This is expected, since both luminosities are indicators of the overall power of the accretion disk. Some of the scatter in this correlation is likely to come from the fact that L_{IR} is more dependent on orientation than L_{X_a}, and the way in which the latter is affected by obscuration (objects with a much larger L_{IR} than L_{X_a} are likely to be

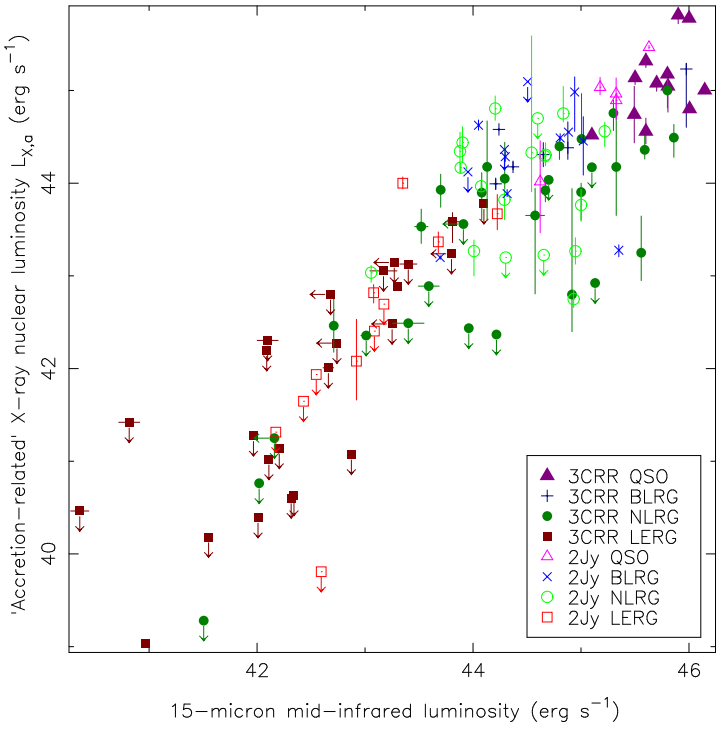

Figure 6.10: X-ray luminosity for the 'accretion-related' component L_{X_a}, as a function of total infrared (24 μm for the 2Jy sources, 15 μm for the 3C sources) luminosity. Arrows indicate upper limits. Colours and symbols as in Fig. 6.1.

Compton-thick). It is also very likely that L_{X_a} is more affected by beaming than L_{IR}, as suggested by Hardcastle et al. (2009). It may seem surprising that broad-line objects follow the correlation despite the scatter introduced by beaming, and despite the fact that in some of them L_{X_a} is contaminated from L_{X_u}. However, the infrared luminosity in these sources is likely to include some non-thermal contamination from synchrotron emission associated with the jet, and due to their orientation, the contribution from the torus is also larger. These effects effectively boost their IR emission and brings them closer to the correlation.

Some of the NLRGs in our sample are quite heavily obscured, and we could only constrain an upper limit to their absorption column and accretion-related X-ray luminosity. These objects are probably Compton-thick, and lie to the lower right of the correlation in this plot.

The behaviour of the LERGs in this Figure is most significant, reinforcing the idea that LERGs cannot be explained as heavily obscured, 'traditional' HERGs. LERGs are underluminous in X-rays, and lie below the correlation for HERGs. Adding an intrinsic absorption column $N_H = 10^{24}$ cm^{-2} is still insufficient to boost the X-ray luminosity of most of these objects enough to situate them on the correlation. The overlap between the populations happens mostly for objects whose classifications are not clear, and the scatter caused by systematics is probably the main cause behind this overlap.

The origin of the IR emission in LERGs should be questioned. We know from cases like M 87 that no accretion-related component is detected on small scales (see Section 4.1 in Hardcastle et al. 2009), although IR emission is measured with *Spitzer*. It is very likely that in LERGs the IR emission is associated with the jet and the old stellar population, and is therefore not reliable as an estimator of accretion.

6.4.3 X-ray/[OIII] correlations

As pointed out by Hardcastle et al. (2009), there is a strong correlation between $L_{[OIII]}$ and L_{X_a} (Fig. 6.11 and Table 6.4), given that both quantities directly trace accretion. As in the case of the correlation between L_{IR} and L_{X_a}, the LERGs fall below the correlation expected for high-excitation objects. The scatter in this plot is much higher than that seen in Figure 6.10. Infrared emission is a better indicator of accretion than [OIII], since it is less contaminated by the jet and stellar processes, as well as easier to

measure.

The relation between the [OIII] and jet-related X-ray luminosity is shown in Fig. 6.12. This plot is surprising in that it separates the populations quite clearly. This is not expected a priori, since [OIII] traces the photoionizing power of the AGN, which is directly related to accretion, and not directly dependent on jet power, which is traced by L_{X_u}.

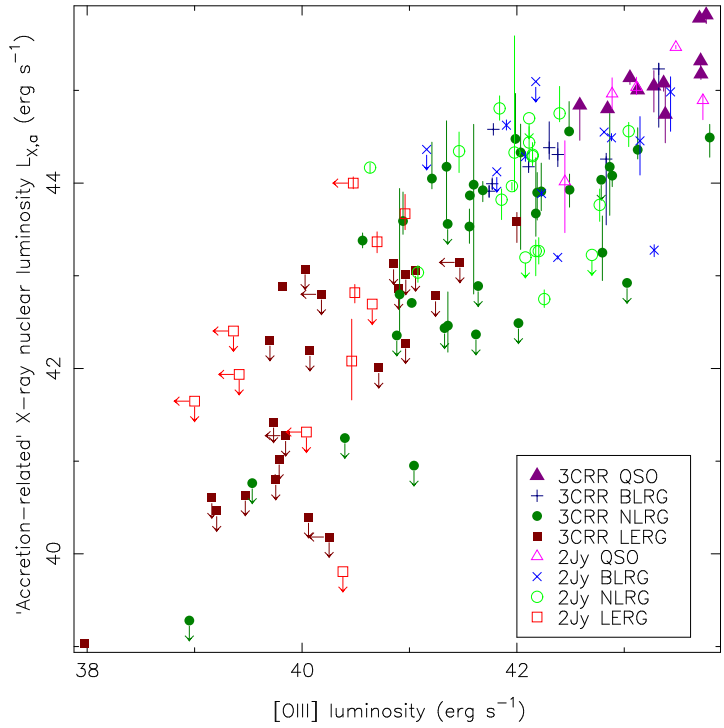

Figure 6.11: X-ray luminosity for the 'accretion-related' component L_{X_a} against the [OIII] emission line luminosity. Arrows indicate upper limits. Colours and symbols as in Fig. 6.1.

The LERGs are underluminous in [OIII], as expected, and show a great deal of scatter due to the effect of the random orientation on their X-ray emission. Broad-line objects have boosted X-ray luminosities both due to beaming and to contamination from the accretion-related component, and lie towards the top right corner of the plot. Their relative faintness in [OIII] can be explained by obscuration, as suggested by Jackson & Browne (1990). This causes some BLRGs and most NLRGs to appear as overluminous in [OIII] with respect to the other populations.

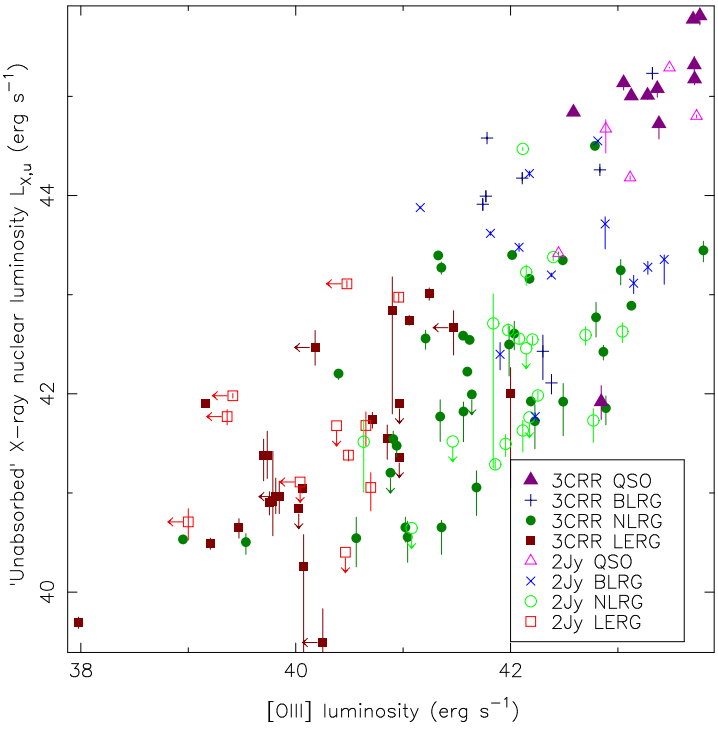

Figure 6.12: X-ray luminosity for the unabsorbed component L_{X_u} against the [OIII] emission line luminosity. Arrows indicate upper limits. Colours and symbols as in Fig. 6.1.

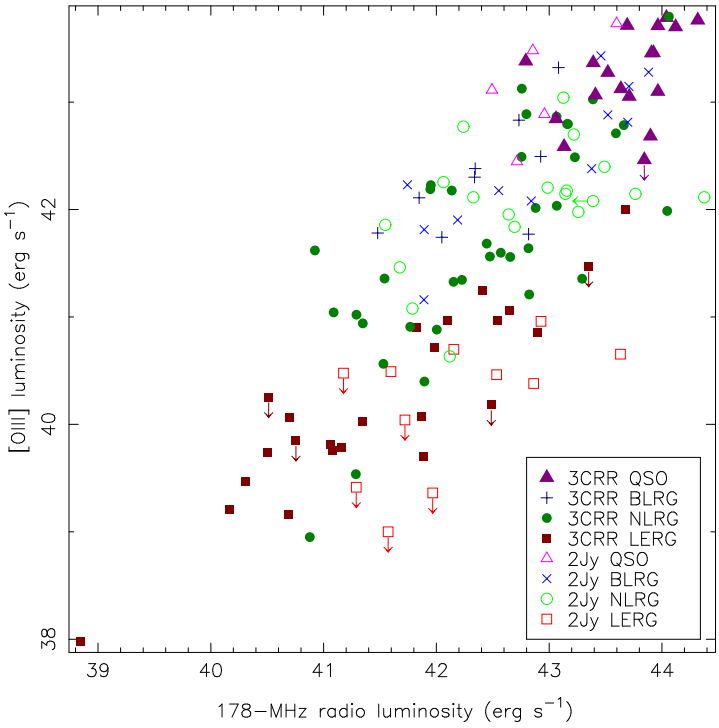

Figure 6.13: [OIII] emission line luminosity against the 178 MHz total radio luminosity. Arrows indicate upper limits. Colours and symbols as in Fig. 6.1.

6.4.4 Radio/IR/[OIII] correlations

Hardcastle et al. (2009) found correlations between the overall radio luminosity and the infrared and [OIII] luminosities. We observe the same in our plots and correlation analysis (Table 6.4), with the 2Jy sources filling some of the gaps in the parameter space (Figs. 6.13, 6.14). The LERGs have higher (relative) radio luminosities than the other populations, as expected. Beaming is likely to introduce scatter in the radio luminosity in both plots, while orientation is likely to influence the scatter in IR luminosities. For the 3CRR objects it can be seen that the broad-line objects have systematically higher [OIII] luminositites than narrow-line objects for the same luminosity, but this is not so clear for the 2Jy sources alone, due to their redshift distribution.

By contrast, and as observed by Hardcastle et al. (2009), the radio core luminosity is not well correlated with either L_{IR} nor $L_{[OIII]}$ (Figs. 6.15, 6.16). The QSOs have radio cores that are far more luminous than those of the other classes. All the populations, in fact, seem to be in different regions of the parameter space, with the broad-line

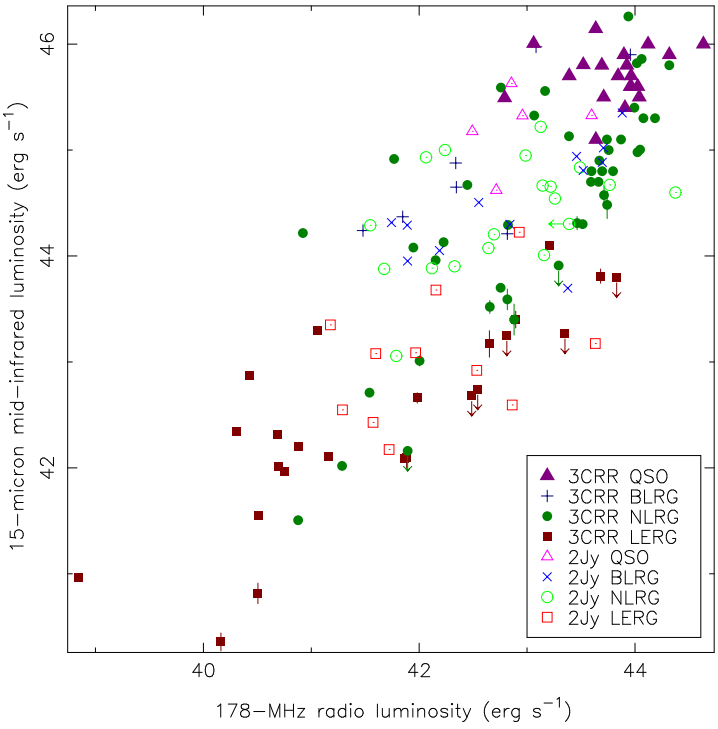

Figure 6.14: 178 MHz total radio luminosity against the total infrared (24 μm for the 2Jy sources, 15 μm for the 3C sources) luminosity. Arrows indicate upper limits. Colours and symbols as in Fig. 6.1.

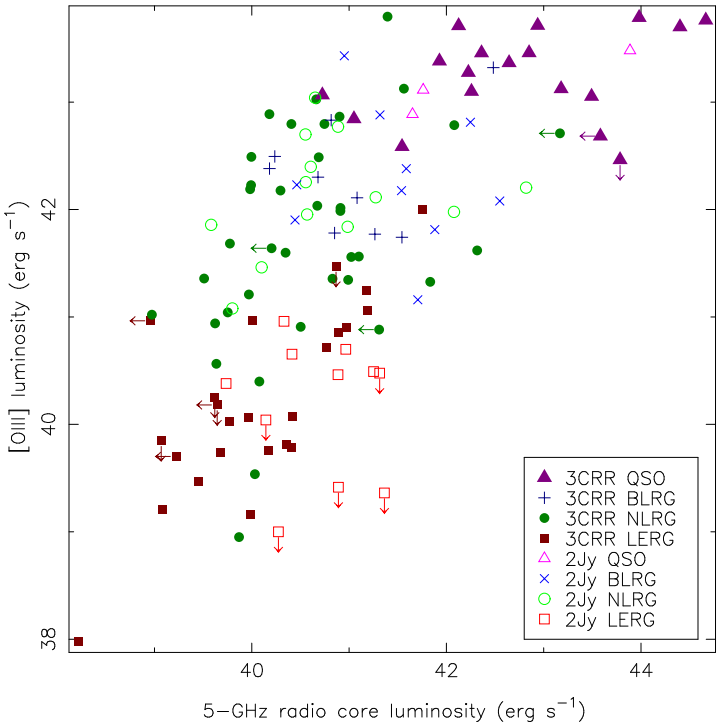

Figure 6.15: [OIII] emission line luminosity against the 5 GHz radio core luminosity. Arrows indicate upper limits. Colours and symbols as in Fig. 6.1.

objects having more luminous radio cores than the narrow-line objects for the same L_{IR} and $L_{[OIII]}$ due to beaming, and LERGs being fainter in both plots, but also more radio-luminous, in proportion, than NLRGs.

The correlation between L_{IR} and $L_{[OIII]}$ is very strong (Figure 6.17 and Table 6.4), and made much clearer by the addition of the 2Jy objects. Orientation effects are likely to affect both quantities in the same way (except for [OIII] absorption in some objects), and neither magnitude is affected by beaming, which greatly reduces the scatter. Contamination from the jet is also likely to favour both quantities equally, by adding to the IR emission and introducing an additional source of photoionization.

6.5 Jet power and Eddington rates

One of the hypotheses that has gained more strength in recent years over the mechanisms underlying accretion in LERGs postulates that there is an accretion rate switch

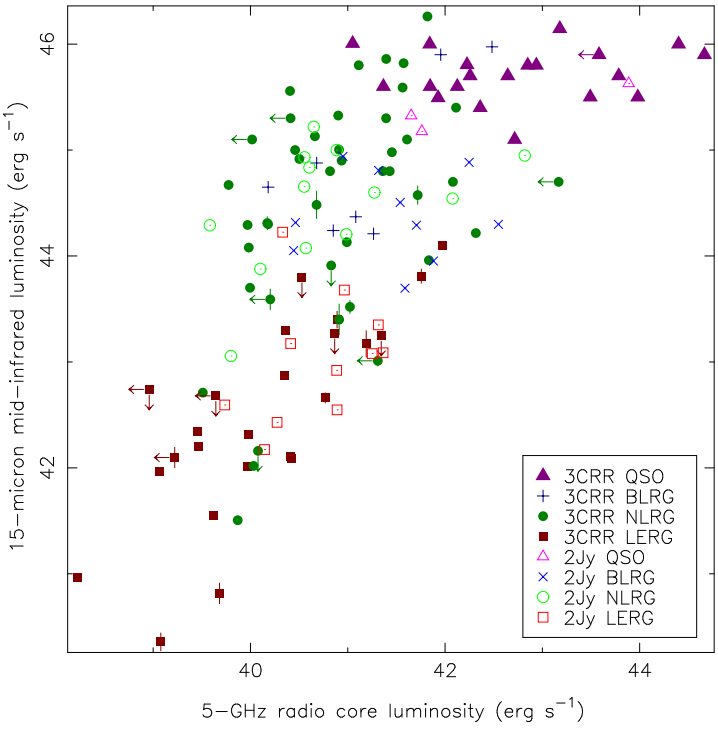

Figure 6.16: 5 GHz radio core luminosity against the total infrared (24 μm for the 2Jy sources, 15 μm for the 3C sources) luminosity. Arrows indicate upper limits. Colours and symbols as in Fig. 6.1.

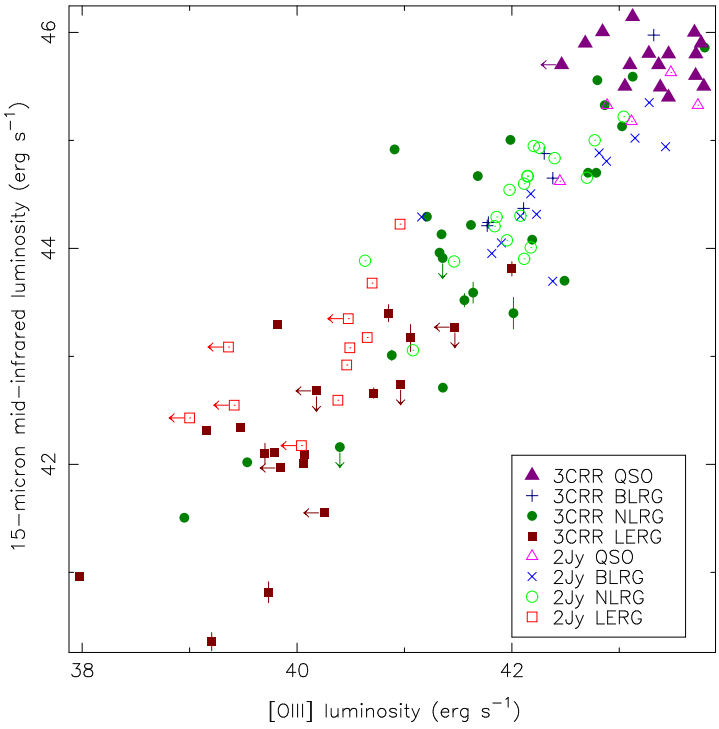

Figure 6.17: Total infrared (24 μm for the 2Jy sources, 15 μm for the 3C sources) luminosity against the [OIII] emission line luminosity. Arrows indicate upper limits. Colours and symbols as in Fig. 6.1.

between these objects and the high-excitation population at about 1 – 10 per cent of the Eddington rate (see e.g. Best & Heckman 2012; Russell et al. 2012, and references therein). In this Section we aim to test this hypothesis, taking into account not just the radiative power from the AGN, but also the kinetic power of the jet, denoted Q in this thesis.

6.5.1 Jet power estimations

To estimate the jet kinetic power we used both the correlations of Cavagnolo et al. (2010), which relies on 1.4-GHz measurements, and of Willott et al. (1999), which is derived from 151-MHz fluxes, with a correction factor $f = 15$ (see discussion in Hardcastle et al. 2009). Cavagnolo et al. (2010) derived their correlation from X-ray cavity measurements; this method, as pointed out by Russell et al. (2012), is subject to uncertainties in the volume estimations and on how much of the AGN power is actually transferred to the interstellar/intergalactic medium. Given that the objects in our samples are far more powerful than the ones considered by Cavagnolo et al. (2010), it is possible that their correlation underestimates the jet powers in our case, but it is the best estimate based on actual data. Willott et al. (1999) derived their correlation from minimum energy synchrotron estimates and [OII] emission line measurements, which make the slope of the correlation somewhat uncertain, as well as introducing an additional uncertainty (in form of the factor f) in the normalization.

Godfrey & Shabala (2013) discuss these issues in detail, arguing that, given the vastly different particle contents and energy budgets of FRI and FRII sources, as well as the dependence of the jet luminosity with the environment (jets are more luminous in denser environments, see e.g. Hardcastle & Krause 2013), it is very likely that, a priori, a single correlation cannot be used across the entire population of radio-loud objects. However, they find that such a correlation does work, and conclude that environmental factors and spectral ageing 'conspire' to reduce the radiative efficiency of FRII sources, effectively situating them on the same $Q_{jet} - L_{151}$ correlation as the low-power FRI galaxies. This makes the use of these correlations qualitatively inaccurate, but quantitatively correct, within the assumptions, as lower limits to the jet kinetic power.

We have repeated the luminosity versus jet power plots of Godfrey & Shabala

(2013) for our sources, using both the Cavagnolo et al. (2010) and Willott et al. (1999) correlations, and we find them to agree very well, with slight divergences at the high and low ends of the distribution due to the different shapes of both correlations. For our analysis we have used the relation of Willott et al. (1999), both for consistency with the analysis of Hardcastle et al. (2006, 2009), and because of the relatively higher reliability of low-frequency measurements. As a further check, we have compared the jet power we obtained for PKS 2211-17 with that obtained independently by Croston et al. (e.g. 2011), and have found them to agree within the uncertainties.

6.5.2 Black hole masses and bolometric corrections

We calculated the black hole masses for the objects in our sample from the K_s-band magnitudes of Inskip et al. (2010) and a slight variation of the well-known correlation between these quantities and the black hole mass (Graham 2007). We cross-tested the results with the black hole masses obtained from the B-band magnitudes of Ramos Almeida et al. (2010) (using the corrections of Fukugita et al. 1995) and the relations from Graham (2007), and found them to be mostly consistent, save for an overall effect that might be related to the different apertures used (the B-band derived masses tend to be smaller).

15 of our objects are missing from the work of Inskip et al. (2010). We obtained *2MASS* magnitudes for some of them, so 11 sources do not have K-band measurements and are thus missing from the following tables and plots. Of these, 3 are QSOs, 4 BLRGs, 3 NLRGs and 1 LERG. Given that the black hole masses derived from K-band magnitudes for broad-line objects and QSOs are not reliable, we can assume that our sample is adequately covered. A further source of uncertainty for the $M_{BH} - L_K$ correlation originates from the fact that black hole masses in clusters are expected to be systematically higher (see e.g. Volonteri & Ciotti 2012). This is particularly important for LERGs inhabiting rich environments, a point we return to in the next Section.

When cross-checking *UKIRT* and *2MASS* observations for the 3CRR sources we found five objects where differences greater than 0.4 mag (after aperture and K corrections) were present between both instruments. After checking carefully these discrepancies, we have relied on *2MASS* measurements whenever possible. It is important to keep in mind not only the limitations of the available data, but also the large degree of

scatter present in the correlation of Graham (2007).

We derived the bolometric luminosity from the different bands, and studied their consistency. We used the correlations of Marconi & Hunt (2003) for the X-ray 2-10 keV luminosity, the simple relation of Best & Heckman (2012) for the [OIII] luminosity and the relation of Runnoe et al. (2012) for the IR luminosity. These values are shown in Table 6.5.

It is worth noting that all these relations are a subject of debate. The $L_{X,2-10keV}/L_{bol}$ relation was initially postulated for bright quasars (Elvis et al. 1994), and although more complex relations like that of Marconi & Hunt (2003) agree with the initial results, they cannot be be fully applied to low-luminosity and low-excitation sources (see e.g. Ho 2009). The mid-IR luminosity seems to be a very reliable estimator of the bolometric luminosity of an AGN, despite issues with non-thermal contamination where a jet is present (see e.g. Fernández-Ontiveros et al. 2012), and a minor contribution from star formation. The main issue with this correlation lies in the dependence on orientation, which can introduce a bias of up to 40% (see e.g. Runnoe et al. 2012). [OIII] has been widely used to assess the bolometric luminosity, given that the conversion factor between the two is just a constant, but it is not reliable when there are other sources of photoionization, and it is known to underestimate the bolometric luminosity in low-excitation sources (see e.g. Netzer 2009) and is also orientation-dependent (Dicken et al. 2009; Jackson & Browne 1990).

Table 6.5: K-band magnitudes, K-corrections (calculated using the relations of Glazebrook et al. 1995; Mannucci et al. 2001), absolute magnitudes, black hole masses, Eddington luminosities, X-ray, [OIII] and infrared-derived Eddington ratios and jet Eddington ratios for the sources in the 2Jy sample. The K-band magnitudes from Inskip et al. (2010) are marked as I10 in the reference column, the magnitudes taken directly from the 2MASS catalogue are marked as 2M. The errors quoted for $L_{X,rad}/L_{X,Edd}$ are derived from both the errors in the X-ray powerlaw normalization and the errors in the intrinsic N_H, to show the maximum possible uncertainty. Where N_H was fixed to 10^{23} cm^{-2}, the upper and lower values of the X-ray luminosity were calculated for $N_H = 0$ and $N_H = 10^{24}$ cm^{-2} respectively. For PKS 0521–36 the intrinsic absorption is unconstrained, thus an upper limit is given for $L_{X,rad}/L_{X,Edd}$, indicated with an asterisk. E stands for LERG, N for NLRG, B for BLRG, Q for Quasar.

PKS	Type	Ref	z	mag K_s	K-corr	Mag K_s	M_{BH}	L_{Edd}	$L_{X,rad}/L_{X,Edd}$	$L_{[OIII],rad}/L_{[OIII],Edd}$	$L_{IR,rad}/L_{IR,Edd}$	Q/L_{Edd}
							$\times 10^9$ M$_\odot$	$\times 10^{40}$ W				
0023-26	N	I10	0.322	15.036	-0.604	-26.70	1.67	2.17	$1.76^{+0.10}_{-0.11} \times 10^{-3}$	2.42×10^{-2}	1.15×10^{-2}	9.10×10^{-2}
0034-01	E	I10	0.073	12.569	-0.183	-25.21	0.53	0.69	$1.50^{+0.28}_{-0.28} \times 10^{-3}$	1.56×10^{-3}	8.28×10^{-3}	1.23×10^{-2}
0035-02	B	I10	0.220	14.107	-0.482	-26.47	1.40	1.81	$4.41^{+0.54}_{-0.47} \times 10^{-2}$	2.32×10^{-2}	2.17×10^{-2}	5.25×10^{-2}
0038+09	B	I10	0.188	14.299	-0.428	-25.94	0.93	1.21	$8.14^{+0.08}_{-0.56} \times 10^{-1}$	4.34×10^{-2}	4.57×10^{-2}	4.82×10^{-2}
0039-44	N	I10	0.346	15.411	-0.622	-26.53	1.46	1.89	$9.81^{+1.97}_{-1.84} \times 10^{-2}$	2.03×10^{-1}	8.99×10^{-2}	9.79×10^{-2}
0043-42	E	I10	0.116	12.999	-0.283	-25.94	0.94	1.22	$4.18^{+0.82}_{-0.65} \times 10^{-3}$	1.44×10^{-3}	1.22×10^{-2}	2.29×10^{-2}
0105-16	N	I10	0.400	15.419	-0.649	-26.91	1.96	2.55	$1.33^{+0.64}_{-0.39} \times 10^{-1}$	3.44×10^{-2}	3.64×10^{-2}	1.38×10^{-1}
0213-13	N	I10	0.147	13.502	-0.349	-26.07	1.03	1.33	$9.57^{+3.05}_{-2.85} \times 10^{-2}$	3.41×10^{-2}	1.59×10^{-2}	2.98×10^{-2}
0347+05	B	I10	0.339	14.286	-0.617	-27.59	3.28	4.27	$2.31^{+1.66}_{-0.66} \times 10^{-2}$	7.46×10^{-4}	8.21×10^{-3}	2.72×10^{-2}
0349-27	E	I10	0.066	12.853	-0.166	-24.68	0.36	0.46	$4.16^{+0.56}_{-0.55} \times 10^{-3}$	9.04×10^{-3}	1.20×10^{-2}	1.23×10^{-2}
0404+03	N	I10	0.089	13.417	-0.221	-24.85	0.41	0.53	$1.80^{+0.83}_{-0.62} \times 10^{-1}$	1.91×10^{-2}	3.84×10^{-2}	1.88×10^{-2}
0442-28	N	I10	0.147	13.160	-0.349	-26.41	1.33	1.73	$2.30^{+0.10}_{-0.09} \times 10^{-1}$	1.40×10^{-2}	1.96×10^{-2}	3.52×10^{-2}

Continued on next page

Table 6.5 – *Continued from previous page*

PKS	Type	Ref	z	mag K_s	K-corr	Mag K_s	M_{BH}	L_{Edd}	$L_{X,rad}/L_{X,Edd}$	$L_{[OIII],rad}/L_{[OIII],Edd}$	$L_{IR,rad}/L_{IR,Edd}$	Q/L_{Edd}
							$\times 10^9$ $M_\odot$	$\times 10^{40}$ W				
0521-36	B	I10	0.055	10.913	-0.139	-26.18	1.12	1.45	6.98×10^{-2}*	3.48×10^{-3}	2.57×10^{-2}	9.28×10^{-3}
0620-52	E	2M	0.051	9.801	-0.129	-27.11	2.27	2.95	$3.06^{+9.80}_{-3.06} \times 10^{-5}$	3.09×10^{-5}	8.18×10^{-4}	1.09×10^{-3}
0625-35	E	I10	0.055	10.724	-0.139	-26.36	1.29	1.68	$2.00^{+0.23}_{-0.18} \times 10^{-2}$	6.27×10^{-4}	5.19×10^{-3}	2.13×10^{-3}
0625-53	E	I10	0.054	10.042	-0.137	-27.00	2.09	2.72	$6.41^{+0.02}_{-6.41} \times 10^{-6}$	1.41×10^{-4}	4.91×10^{-4}	4.24×10^{-3}
0806-10	N	I10	0.110	12.137	-0.269	-26.67	1.62	2.11	$7.84^{+2.01}_{-1.69} \times 10^{-3}$	9.78×10^{-2}	5.71×10^{-2}	8.91×10^{-3}
0859-25	N	I10	0.305	14.758	-0.589	-26.83	1.83	2.38	$3.84^{+3.72}_{-2.05} \times 10^{-2}$	1.39×10^{-2}	2.44×10^{-2}	1.01×10^{-1}
0915-11	E	I10	0.054	10.868	-0.137	-26.18	1.12	1.45	$9.17^{+1.23}_{-0.62} \times 10^{-5}$	6.98×10^{-4}	2.88×10^{-3}	3.79×10^{-2}
0945+07	B	I10	0.086	12.376	-0.214	-25.81	0.84	1.10	$2.08^{+0.10}_{-0.07} \times 10^{-1}$	2.56×10^{-2}	2.39×10^{-2}	1.54×10^{-2}
1151-34	Q	2M	0.258	14.040	-0.537	-27.08	2.22	2.88	$1.23^{+1.53}_{-0.15} \times 10^{-2}$	3.40×10^{-2}	2.29×10^{-2}	2.77×10^{-2}
1226+02	Q	2M	0.158	9.937	-0.371	-29.82	1.18	1.54	$2.06^{+0.92}_{-0.05}$	6.87×10^{-1}	2.12×10^{-1}	5.58×10^{-2}
1306-09	N	I10	0.464	15.120	-0.666	-27.61	3.33	4.33	$1.88^{+0.02}_{-0.04} \times 10^{-2}$	1.13×10^{-2}	1.63×10^{-2}	4.35×10^{-2}
1355-41	Q	I10	0.313	12.744	-0.597	-28.91	8.95	11.63	$5.60^{+1.69}_{-0.12} \times 10^{-2}$	2.32×10^{-2}	1.73×10^{-2}	1.10×10^{-2}
1547-79	B	I10	0.483	15.185	-0.669	-27.66	3.44	4.47	$1.51^{+44.55}_{-0.91} \times 10^{-1}$	2.11×10^{-1}	2.45×10^{-2}	7.76×10^{-2}
1559+02	N	I10	0.104	12.205	-0.256	-26.46	1.38	1.80	$4.75^{+0.14}_{-1.67} \times 10^{-4}$	3.50×10^{-2}	5.90×10^{-2}	1.34×10^{-2}
1648+05	E	2M	0.154	12.550	-0.363	-27.14	2.33	3.03	$2.42^{+554.08}_{-2.42} \times 10^{-4}$	5.21×10^{-4}	2.18×10^{-3}	1.61×10^{-1}
1733-56	B	I10	0.098	12.485	-0.242	-26.03	1.00	1.30	$3.75^{+1.53}_{-0.03} \times 10^{-2}$	1.76×10^{-2}	1.74×10^{-2}	1.54×10^{-2}
1814-63	N	I10	0.063	11.896	-0.159	-25.52	0.68	0.88	$6.34^{+0.22}_{-0.46} \times 10^{-2}$	1.71×10^{-3}	2.23×10^{-2}	2.64×10^{-2}
1839-48	E	2M	0.112	11.841	-0.274	-27.01	2.11	2.74	$1.19^{+1.35}_{-1.19} \times 10^{-4}$	2.94×10^{-5}	2.14×10^{-3}	6.66×10^{-3}
1932-46	B	I10	0.231	14.971	-0.499	-25.84	0.86	1.12	$6.90^{+0.09}_{-0.18} \times 10^{-3}$	7.49×10^{-2}	1.35×10^{-2}	2.72×10^{-1}
1934-63	N	I10	0.183	14.023	-0.419	-26.14	1.09	1.41	$2.20^{+12.07}_{-2.20} \times 10^{-3}$	2.98×10^{-2}	2.86×10^{-2}	2.73×10^{-2}
1949+02	N	I10	0.059	11.333	-0.149	-25.92	0.92	1.20	$1.63^{+0.81}_{-0.43} \times 10^{-2}$	2.10×10^{-2}	3.32×10^{-2}	6.30×10^{-3}
2135-14	Q	2M	0.200	12.404	-0.449	-28.00	4.47	5.81	$1.40^{+0.38}_{-1.40} \times 10^{-1}$	7.82×10^{-2}	2.74×10^{-2}	8.54×10^{-3}
2211-17	E	I10	0.153	13.422	-0.361	-26.25	1.18	1.54	$2.81^{+0.16}_{-2.81} \times 10^{-7}$	5.46×10^{-4}	1.72×10^{-3}	7.27×10^{-2}
2221-02	B	I10	0.057	11.448	-0.144	-25.73	0.79	1.03	$2.31^{+0.25}_{-0.22} \times 10^{-2}$	5.77×10^{-2}	4.17×10^{-2}	3.20×10^{-3}
2250-41	N	I10	0.310	15.508	-0.594	-26.12	1.07	1.40	$4.35^{+28.50}_{-4.35} \times 10^{-4}$	1.25×10^{-1}	4.97×10^{-2}	1.56×10^{-1}
2356-61	N	I10	0.096	12.559	-0.237	-25.90	0.91	1.18	$2.58^{+0.19}_{-0.22} \times 10^{-2}$	2.68×10^{-2}	2.35×10^{-2}	3.24×10^{-2}

6.5.3 AGN power and accretion rate

We plotted the radiative Eddington rates (L_{rad}/L_{Edd}) derived from the different bands against each other first, to establish their relative reliabilities. We find that the [OIII] and IR-derived luminosities are well correlated, but the plot shows a scatter of over an order of magnitude. Moreover, there seem to be some systematic differences between the 2Jy and 3CRR populations, which we attribute to the relative better quality of the data for the 2Jy objects.

Jet power versus radiative luminosity plots can also be enlightening in discerning the relative contributions of both components for each population. Fig. 6.18 shows $L_{bol,[X]}/L_{Edd}$ versus Q/L_{Edd} for the 2Jy and the 3CRR sources, where Q is the jet power as defined by Willott et al. (1999). Figs. 6.19 and 6.20 show the same plot for [OIII] and IR derived bolometric luminosities, respectively. Figure 6.20 is the one with the smallest degree of scatter. Reassuringly, and as verified in the histograms, in all the plots adding both components still results in sub-Eddington accretion, even in the brightest sources.

The X-ray derived Eddington rates show the greatest degree of uncertainty on individual measurements, two orders of magnitude for some sources, and even higher for the LERGs. This is most likely intrinsic to the nature of X-ray measurements of AGNs, where source variability, intrinsic absorption and beaming contribute to the scatter. We redid the plot purposefully overestimating the errors by including the uncertainty in the intrinsic N_H (when the N_H was assumed to be 10^{23} cm^{-2} we assumed upper and lower values of 10^{24} and 0 cm^{-2}, respectively). We found that this was still not enough to bring some of the NLRGs and most of the LERGs to the correlation. LERGs seem to have systematically lower (by over three orders of magnitude in some cases) radiative Eddington rates in X-rays than they do when these rates are derived from IR or [OIII] measurements.

While IR measurements are most reliable to determine accretion in high-excitation sources, they appear to overestimate this component in LERGs. Most IR points in Figure 6.20 are detections, not upper limits. As pointed out in Section 6.4.3, it is likely that in these objects the IR emission is associated with the jet and the old stellar population, rather than accretion. For the same reason, [OIII] measurements are also likely to be an overestimation, since the jet and stellar photoionization can boost this

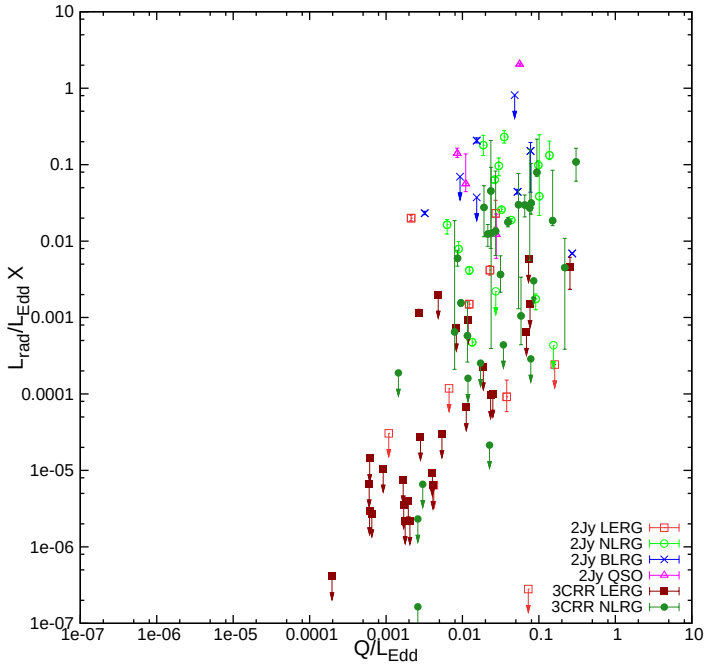

Figure 6.18: $L_{bol,[X]}/L_{Edd}$ versus Q/L_{Edd} for the 2Jy and the 3CRR sources. Error bars reflect the uncertainties in the accretion-related luminosity, but not systematics such as the uncertainty in absorption or intrinsic variability. Arrows indicate upper limits.

emission. We conclude that for LERGs the Eddington rate is best derived from X-ray measurements.

In all these plots a division between high and low-excitation sources is clearly visible. A trend between jet power and radiative luminosity can be observed for the LERGs. We can assume that a certain degree of contamination from jet emission is present in the radiative component in the three plots, and is probably causing this apparent trend.

Several conclusions can be drawn from the behaviour of the HERGs in these plots. The fact that we do not see a decrease in jet power at high radiative luminosities indicates that, even if there is a switch between radiatively inefficient and efficient accretion, jet generation is not switched off when radiatively efficient accretion takes over. There are several NLRGs, in fact, where the contribution from the jet kinetic luminosity is higher than that of the radiative luminosity (see also Punsly & Zhang 2011). The amount of scatter in the plots may suggest that these processes are independent.

This hypothesis must be treated carefully, however, due to the sources of bias

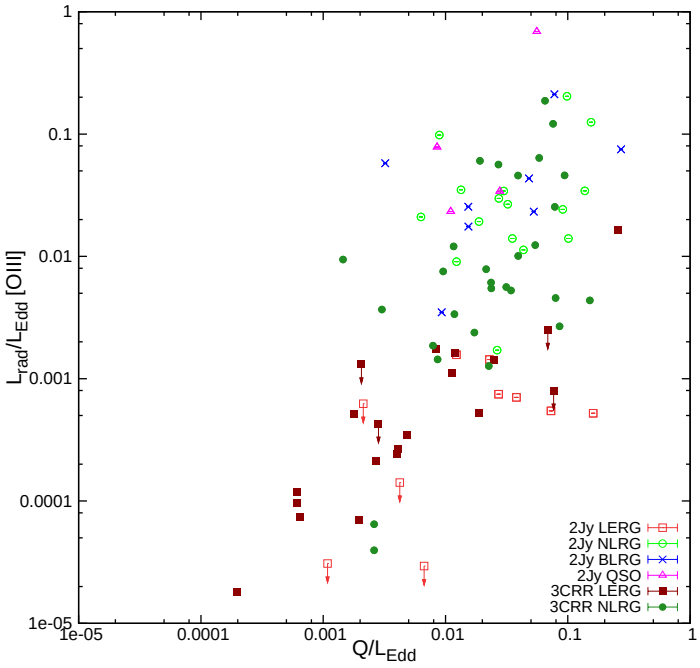

Figure 6.19: $L_{bol,[OIII]}/L_{Edd}$ versus Q/L_{Edd} for the 2Jy and the 3CRR sources. Arrows indicate upper limits.

present in this kind of analysis. The timescales involved are much shorter for the radiative luminosity than they are for the jet power estimations. This is likely to introduce a great amount of scatter in these plots. It is possible that the sources we are selecting had more luminous cores in the past, which would belie their true Q/L_{rad} ratio. Moreover, our study does not include radio-quiet objects, which are far more numerous than the radio-loud population, and which would presumably occupy the upper left corner in the parameter space, given that their radiative output exceeds by far any contribution from a jet.

To assess the extent of bias we plotted the HERGs in our 2Jy and 3CRR samples next to the SDSS selected quasars of Punsly & Zhang (2011). Fig. 6.21 shows $L_{bol,[OIII]}$ versus Q for these objects. Given that we are effectively selecting the most radio-powerful objects for our samples, this plot shows that there is a correlation for the maximum possible jet power and the radiative power, despite the scatter. The SDSS QSOs fill the gap between our sources and the more radio-quiet population, and overlap with our sample, showing that there is a continuity in the overall distribution. This

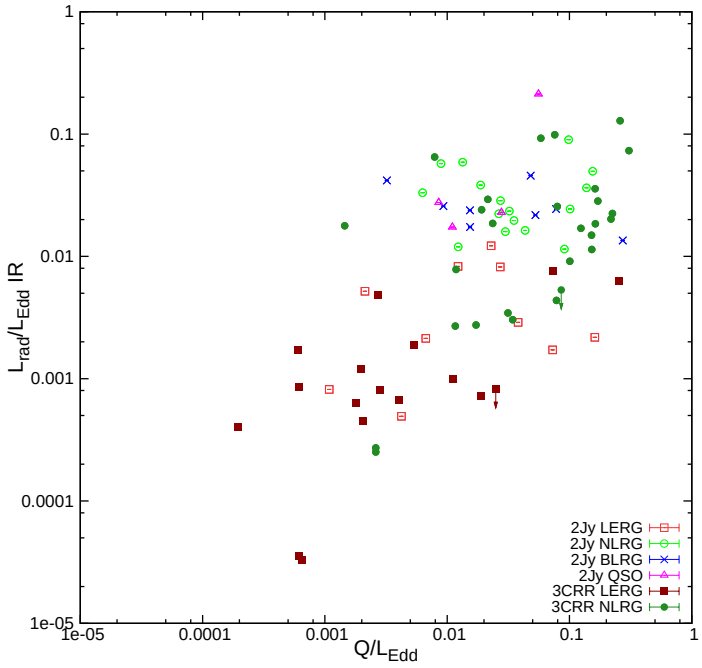

Figure 6.20: $L_{bol,IR}/L_{Edd}$ versus Q/L_{Edd} for the 2Jy and the 3CRR sources. Arrows indicate upper limits.

reinforces the conclusions of Punsly & Zhang (2011), who pointed out that there is no reason to expect $L_{bol,[OIII]}$ and Q to be correlated beyond the scaling with the central black hole and the contribution to $L_{bol,[OIII]}$ from jet photoionization for the overall AGN population.

6.5.4 An Eddington switch?

We plotted histograms of the total Eddington luminosity ($(L_{rad} + Q_{jet})/L_{Edd}$) for the three bands and the high/low-excitation populations. In all cases we found the distribution to be clearly bimodal, with HERGs having systematically higher Eddington rates (peaking at $\sim$ 20 per cent Eddington) than LERGs (peaking at $\sim$ 1 per cent Eddington). The narrowest distribution is that obtained from the IR data (Figure 6.22), but those derived from X-ray and [OIII] measurements have coincident peaks and outliers.

Despite the fact that they have no influence on the result, we decided to remove the broad-line objects from the histograms to allow direct comparison between the 2Jy and 3CRR samples (we have no K-band measurements for 3CRR BLRGs and QSOs),

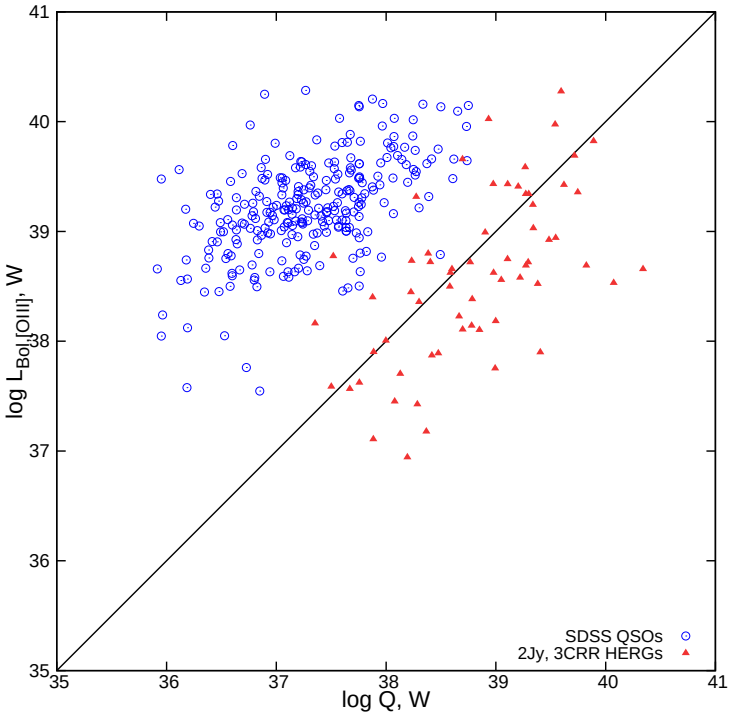

Figure 6.21: $L_{bol,[OIII]}$ versus Q for the 2Jy and the 3CRR high-excitation objects and the SDSS quasars from Punsly & Zhang (2011). The line represents a 1:1 relation between both quantities.

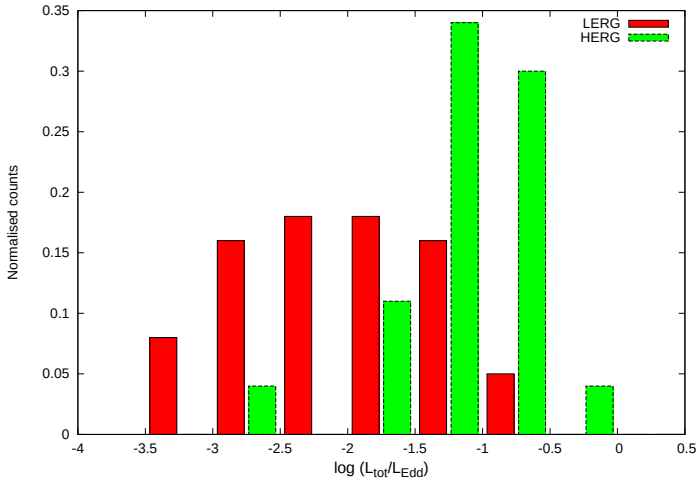

Figure 6.22: Histogram of total Eddington rate ($(L_{bol,IR} + Q)/L_{Edd}$) distribution for the 2Jy and the 3CRR sources. Broad-line objects are excluded from the HERGs to allow direct comparison between both samples.

and to remove the bias derived from black hole masses that are, at best, uncertain for these objects (e.g. 3C 273 in the X-ray histogram appears as super-Eddington, due to its luminosity, high jet power, and, probably, underestimated BH mass).

Before any conclusions can be drawn on the existence of an Eddington switch between LERGs and HERGs, it is important to consider the nature of outliers (i.e. high Eddington LERGs and low Eddington HERGs). In the case of the HERGs, the two objects with very low Eddington rates are M 87 and 3C 338, which are outliers in all our plots and, as pointed out at the beginning of Section 6.4, are most likely LERGs (Evans et al. 2008). The LERGs with high Eddington rates fall into two categories: 'dubious' LERGs and cluster-embedded objects. To the former category belong PKS 0034-01 (3C 15), PKS 0043-42, PKS 0347+05, PKS 0625-35, 3C 123 and 3C 200 (see Hardcastle et al. 2006). To the latter category belong PKS 2211-17, PKS 1648+05 (Hercules A), PKS 0915-11 (Hydra A), 3C 319 and 3C 438. All these objects (save perhaps for Hydra A, which has a peculiar spectrum) are bona-fide LERGs embedded in very dense clusters. It is possible that a boost of the jet luminosity due to the dense environment and an underestimation of the black hole mass (Volonteri & Ciotti 2012) are combining to produce this effect.

To test this effect we have redone the histogram assuming that the LERGs have

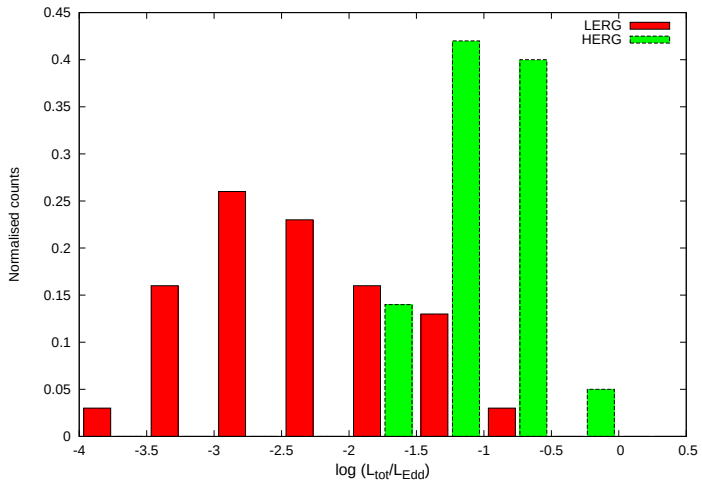

Figure 6.23: Histogram of total Eddington rate distribution $(L_{bol,IR} + Q)/L_{Edd}$ for the HERGs, Q/L_{Edd} for the LERGs) for the 2Jy and the 3CRR sources. Broad-line objects are excluded from the HERGs to allow direct comparison between both samples.

no measurable radiative contribution from radiatively efficient accretion (that is, taking into account only Q for these objects), and excluding all the sources for which the optical classification might not be reliable. This histogram is shown in Figure 6.23. Although the separation between both populations is now clearer, there is still some overlap. The remaining LERGs with $log(Q/L_{Edd}) > -1.5$ are the cluster-embedded objects mentioned above. While it is difficult to assess by how much the black hole mass is underestimated in these galaxies, some of the plots of Volonteri & Ciotti (2012) show that they could be off by over half an order of magnitude. Hardcastle & Krause (2013) show that there is almost an order of magnitude scatter on the radio luminosity in their simulations for objects with the same jet powers, caused by the range of environmental densities they tested. Therefore, the combination of these two effects could be enough to account for the high values of Q in cluster-embedded objects, and the reason behind the overlap between both populations. If this were the case, our results would be compatible with a simple Eddington switch between radiatively inefficient, low-excitation objects, and radiatively efficient, high-excitation ones.

6.6 Summary and Conclusions

It is now clear that a classification that is based purely on morphological features, as that of Fanaroff & Riley (1974), emission line properties, or orientation, as predicted by models such as that of Antonucci (1993), cannot account for the underlying variety within the AGN population. As suggested by e.g. Lin et al. (2010), we need a classification that encompasses both the physical properties and the observational properties of AGNs. This is particularly important for the LERG/HERG case, since the difference between both classes lies in their underlying physical scenarios.

Although recent studies take into account this intrinsic difference between both populations, and progress is being made towards understanding the properties of LERGs, most samples are still use restrictive selection criteria, employ only one or two energy bands to characterise the populations, contain objects which are misclassified, and bolometric corrections that do not accurately describe the less powerful sources. In this work we present consistent results that question the accuracy of some of these assumptions, and prove that further, more careful analysis is needed to understand the relationship between radiative output and jet production in the overall AGN population.

Throughout this work we have shown that the best way to reliably classify AGN populations is through a multiwavelength approach, which we use on our sample of 47 2Jy and 135 3CRR sources (more than double the size of that studied by Hardcastle et al. 2009). We show that several objects classified as LERGs based on their optical spectra (PKS 0034-01, PKS 0043-42, PKS 0625-35, 3C 123, 3C 200 and more recently PKS 0347+05) are most likely high-excitation sources, and vice-versa, some objects classified as NLRGs (M 87 and 3C 338 being the clearest cases) are LERGs where the high-excitation lines are produced through other processes.

We find the same strong correlations between hard (2-10 keV) X-ray, mid-IR and [OIII] emission as Hardcastle et al. (2006, 2009), confirming that these quantities are all related to radiatively efficient accretion. We confirm the jet-related nature of the soft X-ray emission, as suggested by Hardcastle & Worrall (1999). We also show that selection criteria must be taken into account when studying correlations between these quantities: relativistic beaming can introduce a large scatter in the plots, resulting in poorer partial correlations. We find that all the correlations of Hardcastle et al. (2009)

become stronger by the addition of the 2Jy objects.

By comparing the accretion-related correlations, we show that mid-IR measurements are best to constrain the accretion properties of high-excitation objects, while for the low-excitation population X-rays are the best band to set an upper limit on radiatively efficient accretion, given that they are less subject to contamination from stellar processes and the presence of a jet (this is taken into account by the soft X-ray component, whose jet-related nature we confirm). Radio measurements are essential to establish the extent of radiatively inefficient accretion, and the amount of AGN power invested in the jet.

We emphasise the fact that bolometric corrections, M_{BH}/L correlations and jet power estimations only give an overall indication of AGN behaviour, and may be inaccurate for individual sources, given the vast range of environments and nuclear powers involved. Further studies of individual SEDs and jet-environment interaction simulations are needed to establish how reliable these correlations are, in particular for the case of LERGs.

Despite these intrinsic limitations, we find unequivocal proof for the radiatively inefficient nature of the LERGs, as well as confirmation for the fact that these objects accrete at very low Eddington rates ($\leq$ 10 per cent in all cases, with the distribution peaking $\sim$ 1 per cent). We find that the HERGs in our sample are narrowly distributed around 10-30 per cent Eddington rates. However, we find an overlap between both populations, that is not consistent with a simple switch. Even after discarding the 'dubious' objects, we find that LERGs embedded in very rich clusters have higher Eddington rates. For these sources the central back hole masses must be underestimated and the jet luminosity is higher (Hardcastle & Krause 2013). These two factors can account for the order of magnitude in Eddington rate that makes these objects overlap with the HERGs, in which case a simple switch between both populations would be feasible.

We do not see signs in our plots for radiatively efficient accretion completely taking over from jet production. In fact, we find several NLRGs in which the dominant energetic contribution from the AGN stems from the jet, rather than radiative luminosity. Selection on radio flux selects for the objects with the largest values of Q at any given epoch. We find that jet kinetic power and radiative luminosity seem to be independent in high-excitation objects, confirming the conclusions of Punsly & Zhang

(2011). While a better understanding of the timescales and the addition of radio-quiet objects to the plots are necessary to fully understand whether these quantities are truly independent, our plots seem to indicate that they are.

6.7 Appendix: 3CRR tables

Table 6.6: K-band magnitudes, K-corrections (calculated using the relations of Glazebrook et al. 1995; Mannucci et al. 2001), absolute magnitudes, black hole masses, Eddington luminosities, X-ray, [OIII] and infrared-derived Eddington ratios and jet Eddington ratios for the sources in the 3CRR sample. The errors quoted for $L_{X,rad}/L_{X,Edd}$ are derived from the errors in the X-ray powerlaw normalization. Upper limits are indicated with an asterisk. E stands for LERG, N for NLRG, B for BLRG, Q for Quasar. The K magnitudes given correspond to the following references: L Lilly & Longair (1984), S Simpson et al. (2000), V de Vries et al. (1998), B Best et al. (1998). 2M stands for sources where the measurements were taken directly from 2MASS.

PKS	Type	Ref	z	mag K_s	K-corr	Mag K_s	M_{BH}	L_{Edd}	$L_{X,rad}/L_{X,Edd}$	$L_{[OIII],rad}/L_{[OIII],Edd}$	$L_{IR,rad}/L_{IR,Edd}$	Q/L_{Edd}
							$\times 10^9$ M$_\odot$	$\times 10^{40}$ W				
4C12.03	0	L	0.156	13.130	-0.367	-26.60	1.54	2.00	9.20×10^{-4}*	1.62×10^{-3}	-	1.18×10^{-2}
3C20	1	L	0.174	14.060	-0.403	-25.96	0.95	1.24	$3.16^{+7.29}_{-0.90} \times 10^{-2}$	4.58×10^{-3}	2.57×10^{-2}	7.98×10^{-2}
3C28	0	L	0.195	13.570	-0.441	-26.77	1.75	2.27	9.97×10^{-5}*	1.42×10^{-3}	8.27×10^{-4}	2.49×10^{-2}
3C31	0	2M	0.017	8.481	-0.043	-25.77	0.82	1.07	2.92×10^{-6}*	9.72×10^{-5}	8.55×10^{-4}	6.12×10^{-4}
3C33	1	S	0.060	11.720	-0.150	-25.54	0.69	0.90	$2.75^{+2.54}_{-1.62} \times 10^{-2}$	6.04×10^{-2}	2.41×10^{-2}	1.91×10^{-2}
3C35	0	L	0.068	11.770	-0.170	-25.80	0.84	1.09	1.98×10^{-3}*	3.43×10^{-4}	-	4.82×10^{-3}
3C42	1	S	0.395	15.140	-0.648	-27.16	2.36	3.07	$2.99^{+4.67}_{-2.86} \times 10^{-2}$	1.24×10^{-2}	-	5.42×10^{-2}
3C46	1	V	0.437	14.830	-0.660	-27.74	3.67	4.78	-	4.59×10^{-2}	-	3.92×10^{-2}
3C55	1	L	0.735	16.540	-0.763	-27.50	3.05	3.97	-	-	1.29×10^{-1}	2.59×10^{-1}
3C66B	0	2M	0.022	9.500	-0.055	-25.36	0.60	0.78	2.22×10^{-6}*	5.14×10^{-4}	6.37×10^{-4}	1.78×10^{-3}
3C76.1	0	2M	0.032	10.870	-0.083	-24.95	0.44	0.57	2.76×10^{-5}*	4.30×10^{-4}	8.04×10^{-4}	2.83×10^{-3}
3C79	1	S	0.256	14.420	-0.534	-26.67	1.62	2.11	$2.71^{+13.20}_{-2.15} \times 10^{-2}$	1.22×10^{-1}	9.85×10^{-2}	7.58×10^{-2}
3C83.1B	0	2M	0.026	10.850	-0.065	-24.41	0.29	0.38	2.95×10^{-5}*	-	1.88×10^{-3}	5.38×10^{-3}
3C84	1	2M	0.018	8.126	-0.045	-26.26	1.19	1.55	1.90×10^{-4}*	9.41×10^{-3}	1.79×10^{-2}	1.46×10^{-3}
3C98	1	2M	0.031	10.930	-0.078	-24.74	0.38	0.49	$1.56^{+0.15}_{-0.15} \times 10^{-3}$	7.52×10^{-3}	-	9.57×10^{-3}
3C123	0	L	0.218	13.960	-0.479	-26.67	1.63	2.12	$4.54^{+1.58}_{-2.20} \times 10^{-3}$	1.65×10^{-2}	6.21×10^{-3}	2.55×10^{-1}
3C153	1	S	0.277	14.220	-0.560	-27.09	2.24	2.91	4.39×10^{-4}*	5.25×10^{-3}	3.04×10^{-3}	3.43×10^{-2}
3C171	1	S	0.238	14.720	-0.510	-26.17	1.11	1.45	$2.96^{+1.05}_{-0.89} \times 10^{-2}$	1.87×10^{-1}	-	6.53×10^{-2}
DA240	0	2M	0.036	10.724	-0.091	-25.30	0.58	0.75	1.17×10^{-5}*	2.66×10^{-4}	-	4.81×10^{-1}
3C172	1	L	0.519	15.670	-0.675	-27.36	2.75	3.58	-	-	9.14×10^{-3}	8.61×10^{-4}
3C192	1	S	0.060	12.120	-0.151	-25.14	0.51	0.66	$5.78^{+10.30}_{-3.16} \times 10^{-4}$	1.21×10^{-2}	2.69×10^{-3}	1.16×10^{-2}
3C200	0	V	0.458	15.590	-0.665	-27.11	2.27	2.95	5.85×10^{-3}*	-	7.58×10^{-3}	7.32×10^{-2}

Continued on next page

Table 6.6 – *Continued from previous page*

PKS	Type	Ref	z	mag K_s	K-corr	Mag K_s	M_{BH}	L_{Edd}	$L_{X,rad}/L_{X,Edd}$	$L_{[OIII],rad}/L_{[OIII],Edd}$	$L_{IR,rad}/L_{IR,Edd}$	Q/L_{Edd}
							$\times 10^9$ $M_\odot$	$\times 10^{40}$ W				
3C223	1	S	0.137	13.770	-0.328	-25.59	0.72	0.93	$1.35^{+6.90}_{-0.70} \times 10^{-2}$	5.64×10^{-2}	-	2.71×10^{-2}
3C228	1	L	0.552	16.250	-0.682	-26.95	2.02	2.62	$4.51^{+6.33}_{-4.13} \times 10^{-3}$	-	2.02×10^{-2}	2.18×10^{-1}
3C236	0	L	0.099	12.220	-0.244	-26.29	1.22	1.59	7.36×10^{-4}*	1.75×10^{-3}	-	8.32×10^{-3}
3C263.1	1	L	0.824	16.610	-0.818	-27.79	3.81	4.95	-	-	2.24×10^{-2}	2.24×10^{-1}
3C264	0	2M	0.021	9.489	-0.053	-25.26	0.56	0.73	4.01×10^{-6}*	6.97×10^{-5}	1.20×10^{-3}	1.96×10^{-3}
3C272.1	0	2M	0.003	6.222	-0.007	-23.46	0.14	0.18	4.09×10^{-7}*	1.80×10^{-5}	4.04×10^{-4}	1.96×10^{-4}
3C274	1	2M	0.004	5.812	-0.011	-25.38	0.61	0.79	1.64×10^{-7}*	3.95×10^{-5}	2.52×10^{-4}	2.61×10^{-3}
3C274.1	1	L	0.422	15.360	-0.657	-27.12	2.29	2.97	3.02×10^{-3}*	2.67×10^{-3}	5.32×10^{-3}	8.56×10^{-2}
3C280	1	B	0.996	16.800	-0.902	-28.19	5.17	6.72	$1.09^{+0.55}_{-0.48} \times 10^{-1}$	-	7.33×10^{-2}	3.06×10^{-1}
3C284	1	L	0.239	13.990	-0.512	-26.91	1.96	2.54	$1.26^{+7.94}_{-1.22} \times 10^{-2}$	5.45×10^{-3}	-	2.37×10^{-2}
3C285	1	L	0.079	12.440	-0.198	-25.53	0.68	0.89	$5.94^{+1.63}_{-1.23} \times 10^{-3}$	1.44×10^{-3}	-	8.61×10^{-3}
3C288	0	L	0.246	13.420	-0.521	-27.56	3.21	4.17	9.65×10^{-5}*	-	1.14×10^{-3}	2.34×10^{-2}
3C289	1	B	0.967	16.720	-0.891	-28.18	5.13	6.67	-	-	3.57×10^{-2}	1.62×10^{-1}
3C293	0	2M	0.045	10.841	-0.115	-25.77	0.82	1.07	$1.16^{+0.12}_{-0.11} \times 10^{-3}$	2.14×10^{-4}	4.87×10^{-3}	2.69×10^{-3}
3C295	1	L	0.461	14.330	-0.665	-28.39	5.99	7.79	$1.85^{+6.61}_{-0.26} \times 10^{-2}$	4.36×10^{-3}	1.49×10^{-2}	1.52×10^{-1}
3C296	0	2M	0.024	8.764	-0.061	-26.30	1.23	1.60	1.44×10^{-5}*	1.19×10^{-4}	3.55×10^{-5}	6.12×10^{-4}
3C300	1	L	0.272	15.110	-0.554	-26.16	1.10	1.43	2.88×10^{-4}*	2.54×10^{-2}	4.37×10^{-3}	7.83×10^{-2}
3C305	1	2M	0.042	10.643	-0.106	-25.75	0.81	1.05	6.56×10^{-6}*	3.67×10^{-3}	-	3.01×10^{-3}
3C310	0	L	0.054	11.660	-0.137	-25.39	0.61	0.80	-	2.29×10^{-4}	7.24×10^{-4}	1.87×10^{-2}
3C315	1	L	0.108	12.920	-0.266	-25.84	0.87	1.12	2.53×10^{-4}*	2.37×10^{-3}	2.73×10^{-3}	1.71×10^{-2}
3C319	0	L	0.192	14.910	-0.436	-25.15	0.51	0.66	1.49×10^{-3}*	7.99×10^{-4}	2.54×10^{-3}	7.65×10^{-2}
3C321	1	L	0.096	12.220	-0.237	-26.24	1.17	1.52	$6.48^{+172.00}_{-4.38} \times 10^{-4}$	1.86×10^{-3}	6.48×10^{-2}	7.88×10^{-3}
3C326	1	L	0.090	13.070	-0.222	-25.20	0.53	0.69	-	2.14×10^{-5}	9.48×10^{-4}	2.26×10^{-2}
NGC6109	0	2M	0.030	10.325	-0.076	-25.27	0.56	0.73	3.51×10^{-6}*	-	-	1.70×10^{-3}
3C337	1	B	0.635	16.550	-0.709	-27.05	2.17	2.82	-	-	1.14×10^{-2}	1.52×10^{-1}
3C338	1	2M	0.030	9.170	-0.077	-26.50	1.43	1.86	2.32×10^{-6}*	6.47×10^{-5}	2.72×10^{-4}	2.61×10^{-3}
3C340	1	B	0.775	16.920	-0.788	-27.29	2.60	3.38	-	-	2.84×10^{-2}	1.71×10^{-1}
3C341	1	L	0.448	15.330	-0.663	-27.31	2.64	3.43	$1.05^{+2.32}_{-0.61} \times 10^{-3}$	6.38×10^{-2}	9.22×10^{-2}	5.81×10^{-2}
NGC6251	0	2M	0.024	9.026	-0.062	-26.14	1.08	1.41	6.72×10^{-6}*	-	1.70×10^{-3}	6.01×10^{-4}
3C346	1	L	0.162	13.100	-0.379	-26.73	1.70	2.21	1.60×10^{-4}*	3.36×10^{-3}	7.84×10^{-3}	1.18×10^{-2}
3C349	1	L	0.205	14.470	-0.458	-26.00	0.98	1.27	$1.76^{+0.26}_{-0.24} \times 10^{-2}$	1.00×10^{-2}	-	3.91×10^{-2}

Continued on next page

Table 6.6 – *Continued from previous page*

PKS	Type	Ref	z	mag K_s	K-corr	Mag K_s	M_{BH}	L_{Edd}	$L_{X,rad}/L_{X,Edd}$	$L_{[OIII],rad}/L_{[OIII],Edd}$	$L_{IR,rad}/L_{IR,Edd}$	Q/L_{Edd}
							$\times 10^9$ $M_\odot$	$\times 10^{40}$ W				
3C352	1	B	0.806	16.720	-0.807	-27.61	3.32	4.32	-	-	1.85×10^{-2}	1.63×10^{-1}
3C386	0	2M	0.018	9.673	-0.045	-24.71	0.37	0.48	2.19×10^{-6}*	1.31×10^{-3}	4.53×10^{-4}	2.05×10^{-3}
3C388	0	L	0.091	11.960	-0.225	-26.34	1.26	1.64	6.68×10^{-5}*	1.10×10^{-3}	9.90×10^{-4}	1.12×10^{-2}
3C433	1	L	0.102	11.900	-0.250	-26.69	1.65	2.15	$1.24^{+0.42}_{-0.38} \times 10^{-2}$	7.86×10^{-3}	2.94×10^{-2}	2.15×10^{-2}
3C436	1	L	0.215	13.840	-0.474	-26.76	1.73	2.26	$3.67^{+2.75}_{-1.52} \times 10^{-3}$	5.62×10^{-3}	3.45×10^{-3}	3.15×10^{-2}
3C438	0	L	0.290	13.900	-0.574	-27.54	3.16	4.11	6.48×10^{-4}*	2.51×10^{-3}	1.20×10^{-3}	6.87×10^{-2}
3C441	1	B	0.708	16.200	-0.747	-27.72	3.62	4.71	-	-	1.70×10^{-2}	1.24×10^{-1}
3C442A	0	2M	0.027	9.860	-0.069	-25.57	0.70	0.92	7.58×10^{-6}*	-	-	1.67×10^{-3}
3C449	0	2M	0.017	9.070	-0.044	-25.31	0.58	0.75	2.73×10^{-6}*	7.45×10^{-5}	3.27×10^{-5}	6.51×10^{-4}
3C452	1	L	0.081	12.030	-0.202	-26.00	0.98	1.27	$4.50^{+16.20}_{-3.70} \times 10^{-2}$	6.09×10^{-3}	1.85×10^{-2}	2.35×10^{-2}
NGC7385	0	2M	0.024	9.540	-0.062	-25.62	0.73	0.95	1.05×10^{-5}*	-	-	9.18×10^{-4}
3C457	1	L	0.428	15.720	-0.658	-26.80	1.79	2.33	$7.93^{+13.70}_{-0.89} \times 10^{-2}$	4.61×10^{-2}	-	9.42×10^{-2}
3C465	0	2M	0.029	10.070	-0.075	-25.52	0.68	0.88	9.31×10^{-6}*	2.42×10^{-4}	6.75×10^{-4}	4.04×10^{-3}

Table 6.7: Luminosities for the sources in the 3CRR sample, following the format of Hardcastle et al. (2006, 2009). The values are given as the logarithm of the luminosity in erg s^{-1}, upper limits are indicated with a negative sign before the value. We have converted the radio and IR luminosity densities into νL_ν to allow for direct comparison between the magnitudes in different bands. Where measurements could not be obtained their absence is indicated with a dash. E stands for LERG, N for NLRG, B for BLRG, Q for Quasar.

PKS	Type	z	L_{178}	L_5	L_{X_u}			L_{X_a}			L_{IR}		$L_{[OIII]}$	$L_{[OII]}$
4C12.03	E	0.1560	42.1013	40.0017	-41.9060	-	0.0000	-43.0170	-	0.0000	-	0.0000	40.9665	0.0000
3C6.1	N	0.8404	43.8704	41.6091	44.9162	44.8949	44.9360	-44.1719	-	0.0000	45.1002	0.0100	-	42.1543
3C16	E	0.4050	43.0924	39.7307	-42.7423	-	0.0000	-43.6879	-	0.0000	-	0.0000	-	41.8057
3C19	N	0.4820	43.2520	40.1444	44.0894	44.0579	44.1188	-43.5489	-	0.0000	-	0.0000	-	0.0000
3C20	N	0.1740	42.8230	39.9703	42.5581	42.4484	42.6413	44.0492	43.9381	44.4412	44.2932	0.0035	41.2089	40.7289
3C22	B	0.9380	43.9571	41.9547	-	0.0000	-	0.0000	-	0.0000	45.9002	0.0100	-	43.1572
3C28	E	0.1952	42.5424	-38.9594	-41.3604	-	0.0000	-42.2744	-	0.0000	-42.7400	-	40.9640	41.8114
3C31	E	0.0167	40.3077	39.4535	40.6532	40.5441	40.7404	-40.6319	-	0.0000	42.3414	0.0015	39.4714	0.0000
3C33	N	0.0595	41.9462	39.9828	41.9243	41.8751	41.9685	43.8976	43.6021	44.1139	44.0800	0.0117	42.1890	41.4406
3C33.1	B	0.1810	42.3392	40.6806	42.4288	42.1425	42.5929	44.3821	44.2571	44.6617	44.8776	0.0020	42.3011	0.0000
3C34	N	0.6890	43.6979	40.8040	-	0.0000	-	0.0000	-	0.0000	-	0.0000	-	43.6127
3C35	E	0.0677	41.3467	39.7695	-40.8451	-	0.0000	-43.0729	-	0.0000	-	0.0000	40.0283	0.0000
3C41	N	0.7950	43.6626	40.7233	-	0.0000	-	0.0000	-	0.0000	-	0.0000	-	42.6972
3C42	N	0.3950	43.0675	40.6734	42.6079	42.4437	42.7325	44.3302	43.2845	44.6355	-	0.0000	42.0354	41.8854
3C46	N	0.4373	43.1596	40.7466	-	0.0000	-	0.0000	-	0.0000	-	0.0000	42.7965	42.2165
3C47	Q	0.4250	43.5207	42.2260	45.0103	44.9687	45.0425	45.0459	44.7669	45.2142	45.8053	0.0044	43.2762	42.6262
3C48	Q	0.3670	43.6366	43.1792	45.0042	44.9950	45.0133	45.0042	44.9950	45.0133	46.1455	0.0018	43.1244	42.2544
3C49	N	0.6207	43.4355	41.5437	-	0.0000	-	0.0000	-	0.0000	-	0.0000	-	0.0000
3C55	N	0.7350	44.0178	41.5741	-	0.0000	-	0.0000	-	0.0000	45.8200	0.0132	-	42.3405
3C61.1	N	0.1860	42.7551	39.9953	41.9213	41.5769	42.1044	43.9280	43.7402	44.0973	43.7000	0.0300	42.4902	41.4403
3C66B	E	0.0215	40.6944	39.9703	41.0414	41.0000	41.0792	-40.3922	-	0.0000	42.0084	0.0037	40.0600	39.8727
3C67	B	0.3102	42.7322	40.8156	44.2593	44.2336	44.2853	44.2593	43.5494	44.2853	-	0.0000	42.8315	42.2615
3C76.1	E	0.0324	40.7548	39.0689	40.9638	40.7924	41.1206	-41.2751	-	0.0000	41.9658	0.0168	-39.8475	0.0000
3C79	N	0.2559	43.0655	40.9018	42.4234	42.3410	42.4898	44.1755	43.6517	44.7510	45.3259	0.0035	42.8646	42.2075
3C83.1B	E	0.0255	40.8799	39.4614	40.9138	40.1461	41.5416	-41.1397	-	0.0000	42.2051	0.0041	-	0.0000
3C84	N	0.0177	40.9226	42.3157	42.5441	42.5185	42.5682	-42.3676	-	0.0000	44.2169	0.0002	41.6192	41.0919

Continued on next page

Table 6.7 – *Continued from previous page*

PKS	Type	z	L_{178}	L_5	L_{X_u}			L_{X_a}			L_{IR}		$L_{[OIII]}$	$L_{[OII]}$
3C98	N	0.0306	41.2914	38.9731	40.6532	40.5051	40.7559	42.7076	42.6721	42.7404	-	0.0000	41.0215	40.2447
3C109	B	0.3056	43.0828	42.4818	45.2322	45.1760	45.2907	45.2322	44.6019	45.2907	45.9747	0.0013	43.3212	42.0912
4C14.11	E	0.2060	42.4093	41.1794	43.0107	42.9433	43.0684	-42.7817	-	0.0000	-	0.0000	41.2426	0.0000
3C123	E	0.2177	43.6816	41.7564	42.0013	41.0468	42.2651	43.5834	43.3586	43.6839	43.8100	0.0669	42.0004	0.0000
3C132	N	0.2140	42.5229	40.1008	-41.9919	-	0.0000	43.2455	43.0436	43.3983	-	0.0000	-	0.0000
3C138	Q	0.7590	43.9246	42.8496	-	0.0000	-	0.0000	-	0.0000	45.8002	0.0100	43.4593	42.5693
3C147	Q	0.5450	44.0397	43.9804	-	0.0000	-	0.0000	-	0.0000	45.5002	0.0100	43.7867	43.4467
3C153	N	0.2769	42.8171	-40.2033	-41.9946	-	0.0000	-42.8895	-	0.0000	43.5900	0.0969	41.6395	42.4892
3C171	N	0.2384	42.7987	40.1805	41.8567	41.6881	41.9789	44.0807	43.9622	44.1807	-	0.0000	42.8881	42.4459
3C172	N	0.5191	43.4640	40.1724	-	0.0000	-	0.0000	-	0.0000	44.3100	0.0621	-	42.7670
3C173.1	E	0.2920	42.8954	40.8900	41.5453	41.3385	41.6853	-43.1274	-	0.0000	43.4000	0.0792	40.8524	0.0000
3C175	Q	0.7680	43.9641	42.2579	-	0.0000	-	0.0000	-	0.0000	45.7002	0.0100	43.0988	42.7688
3C175.1	N	0.9200	43.9469	42.0856	-	0.0000	-	0.0000	-	0.0000	-	0.0000	-	42.6686
3C184	N	0.9940	44.0784	-40.4118	43.4771	42.4771	43.9542	44.7559	44.5682	44.8976	45.3002	0.0100	-	42.8927
3C184.1	N	0.1187	41.9508	39.9921	41.7250	41.4456	41.8908	43.9106	43.7026	44.2154	-	0.0000	42.2266	41.4811
DA240	E	0.0356	41.0800	40.1726	40.9031	40.7782	41.0128	-40.8029	-	0.0000	-	0.0000	39.7558	40.0358
3C192	N	0.0598	41.5401	39.5101	40.6532	40.3802	40.7243	42.4624	42.1761	42.8261	42.7100	0.0280	41.3577	41.3107
3C196	Q	0.8710	44.6342	41.8419	-	0.0000	-	0.0000	-	0.0000	46.0002	0.0100	-	0.0000
3C200	E	0.4580	43.2054	41.9718	43.5812	43.5185	43.6359	-43.7785	-	0.0000	44.1002	0.0100	-	0.0000
4C14.27	N	0.3920	43.0522	-39.6843	42.3387	42.1701	42.4769	-43.0542	-	0.0000	-	0.0000	-	0.0000
3C207	Q	0.6840	43.7102	43.4923	45.1367	45.0645	45.1875	45.1367	45.0645	45.1875	45.5002	0.0100	43.0529	-42.1529
3C215	Q	0.4110	43.1324	41.5438	44.8401	44.8062	44.8714	44.8401	44.4616	44.8714	-	0.0000	42.5859	42.2159
3C217	N	0.8975	43.8783	-40.8009	-	0.0000	-	0.0000	-	0.0000	-	0.0000	-	43.2903
3C216	Q	0.6680	43.8443	43.7850	-	0.0000	-	0.0000	-	0.0000	45.7002	0.0100	-42.4635	42.4335
3C219	B	0.1744	42.8176	41.2650	43.9934	43.9373	44.0425	43.9934	43.9373	44.0425	44.2100	0.0158	41.7710	41.2689
3C220.1	N	0.6100	43.6624	42.0810	44.5009	44.4758	44.5245	-44.0358	-	0.0000	44.7002	0.0100	42.7854	42.4554
3C220.3	N	0.6850	43.7404	-40.0165	-	0.0000	-	0.0000	-	0.0000	45.1002	0.0100	-	0.0000
3C223	N	0.1368	42.1371	40.2946	43.1605	43.1163	43.1943	43.6727	43.4259	44.2725	-	0.0000	42.1770	41.7138
3C225B	N	0.5800	43.7418	40.6795	-	0.0000	-	0.0000	-	0.0000	44.4826	0.1291	-	42.6162
3C226	N	0.8200	43.9394	41.8193	-	0.0000	-	0.0000	-	0.0000	46.2609	0.0061	-	42.7356
4C73.08	N	0.0581	41.3471	39.6230	41.4771	41.3617	41.5682	43.5911	43.4472	43.9031	-	0.0000	40.9404	40.5704
3C228	N	0.5524	43.7136	41.7184	43.8588	42.8141	43.9115	43.6521	42.8062	43.9446	44.5743	0.0872	-	42.1466

Continued on next page

Table 6.7 – *Continued from previous page*

PKS	Type	z	L_{178}	L_5	L_{X_u}			L_{X_a}			L_{IR}		$L_{[OIII]}$	$L_{[OII]}$
3C234	N	0.1848	42.7581	41.5635	42.8891	42.8673	42.9124	44.3601	44.2601	44.5967	45.5900	0.0055	43.1253	42.1202
3C236	E	0.0989	41.8200	40.9760	42.8388	41.7975	43.1790	-42.8591	-	0.0000	-	0.0000	40.8996	41.1678
4C74.16	?	0.8100	43.8163	41.1096	-	0.0000	-	0.0000	-	0.0000	-	0.0000	-	0.0000
3C244.1	N	0.4280	43.3882	40.6622	43.2465	43.0988	43.3550	-42.9230	-	0.0000	45.1300	0.0091	43.0263	0.0000
3C247	N	0.7489	43.6287	41.4088	-	0.0000	-	0.0000	-	0.0000	-	0.0000	-	43.0098
3C249.1	Q	0.3110	42.7925	41.9289	44.7247	44.5712	44.7725	44.7406	44.4349	45.0448	45.4930	0.0014	43.3816	0.0000
3C254	Q	0.7340	43.9644	42.1258	45.3181	45.2480	45.4014	45.3181	45.2480	45.4014	45.6002	0.0100	43.7106	43.1306
3C263	Q	0.6520	43.6926	42.9382	45.1761	45.1173	45.2430	45.1761	45.1173	45.2430	45.8002	0.0100	43.7141	42.9041
3C263.1	N	0.8240	44.0237	41.4536	-	0.0000	-	0.0000	-	0.0000	44.9800	0.0164	-	42.9654
3C264	E	0.0208	40.6912	39.9823	41.9031	41.8921	41.9085	-40.6035	-	0.0000	42.3149	0.0030	39.1598	40.1025
3C265	N	0.8108	44.0618	41.3953	43.4472	43.3307	43.5389	44.4914	44.2788	44.6335	45.8600	0.0104	43.7962	43.8462
3C268.1	N	0.9731	44.1855	41.3936	-	0.0000	-	0.0000	-	0.0000	45.3002	0.0100	-	42.2744
3C268.3	B	0.3710	42.9248	40.2367	-	0.0000	-	0.0000	-	0.0000	-	0.0000	42.4946	0.0000
3C272.1	E	0.0029	38.8423	38.2211	39.6902	39.6335	39.7482	-39.0370	-	0.0000	40.9638	0.0009	37.9769	0.0000
A1552	E	0.0837	41.5851	40.3353	-40.9243	-	0.0000	-42.2132	-	0.0000	-	0.0000	-	0.0000
3C274	N	0.0041	40.8783	39.8689	40.5315	40.5051	40.5563	-39.2809	-	0.0000	41.5055	0.0025	38.9510	0.0000
3C274.1	N	0.4220	43.2925	40.8299	43.2730	43.2068	43.3296	-43.5595	-	0.0000	-43.9100	-	41.3562	0.0000
3C275.1	Q	0.5570	43.6369	42.7159	44.5185	44.5051	44.5441	44.5185	44.5051	44.5441	45.1002	0.0100	-	42.6666
3C277.2	N	0.7660	43.8052	40.5658	43.6715	43.6138	43.7217	-43.8054	-	0.0000	-	0.0000	-	43.2089
3C280	N	0.9960	44.3187	41.1125	42.8513	42.5502	43.0274	45.0000	44.8129	45.1303	45.8002	0.0100	-	43.6825
3C284	N	0.2394	42.5717	40.3470	42.2238	42.1881	42.2566	43.9832	42.8034	44.6340	-	0.0000	41.5979	0.0000
3C285	N	0.0794	41.5301	39.6354	40.5441	40.2553	40.7559	43.3802	43.3010	43.4624	-	0.0000	40.5636	40.4644
3C286	Q	0.8490	44.0262	41.8467	-	0.0000	-	0.0000	-	0.0000	45.6002	0.0100	-	42.6937
3C288	E	0.2460	42.8128	41.3434	-41.4093	-	0.0000	-42.4809	-	0.0000	-43.2500	-	0.0000	0.0000
3C289	N	0.9674	43.9943	42.1128	-	0.0000	-	0.0000	-	0.0000	45.4002	0.0100	-	42.5749
3C292	N	0.7100	43.5970	40.8177	43.6232	43.3222	43.7993	44.3979	44.2553	44.5051	44.8002	0.0100	-	0.0000
3C293	E	0.0452	41.0608	40.3608	40.9685	40.7924	41.1492	42.8808	42.8451	42.9138	43.2995	0.0011	39.8143	41.5578
3C295	N	0.4614	44.0474	40.9102	42.4982	42.1803	42.6820	44.4768	44.4281	44.9668	45.0042	0.0050	41.9868	42.3268
3C296	E	0.0237	40.5059	39.6818	41.3802	41.1461	41.6232	-41.4205	-	0.0000	40.8157	0.0969	39.7350	0.0000
3C299	N	0.3670	42.9772	40.2269	-	0.0000	-	0.0000	-	0.0000	-	0.0000	-	42.6644
3C300	N	0.2720	42.8798	40.9110	43.3998	43.3834	43.4156	-42.4893	-	0.0000	43.4000	0.1461	42.0153	42.4788
3C303	B	0.1410	42.0487	41.5434	43.9125	43.8470	43.9686	43.9125	43.8470	43.9686	-	0.0000	41.7422	41.9044

Continued on next page

Table 6.7 – *Continued from previous page*

PKS	Type	z	L_{178}	L_5	L_{X_u}			L_{X_a}			L_{IR}		$L_{[OIII]}$	$L_{[OII]}$
3C305	N	0.0417	41.0896	39.7525	40.5563	40.3010	40.7160	-40.9515	-	0.0000	-	0.0000	41.0428	40.1270
3C309.1	Q	0.9040	44.1214	44.4001	45.7782	45.7634	45.7924	45.7782	45.7634	45.7924	46.0002	0.0100	43.6998	42.9398
3C310	E	0.0540	41.8686	40.4203	40.2553	39.0000	40.5798	-42.1942	-	0.0000	42.0892	0.0322	40.0735	0.0000
3C314.1	E	0.1197	41.8839	-39.2214	41.3817	41.1221	41.5430	-42.3038	-	0.0000	42.0977	0.0969	39.7017	0.0000
3C315	N	0.1083	42.0038	-41.3085	-41.2041	-	0.0000	-42.3562	-	0.0000	43.0100	0.0483	40.8823	0.0000
3C319	E	0.1920	42.4864	-39.6436	42.4679	42.2884	42.6389	-42.8004	-	0.0000	-42.6800	-	-40.1809	39.9811
3C321	N	0.0960	41.7680	40.5025	41.5441	41.4472	41.6232	42.7993	42.3979	43.9415	44.9163	0.0007	40.9078	41.3173
3C326	N	0.0895	41.8938	40.0772	42.2041	42.1461	42.2304	-41.2498	-	0.0000	-42.1600	-	40.3988	41.2462
3C325	Q	0.8600	43.9563	41.3659	-43.1556	-	0.0000	44.5590	44.4250	44.7022	45.6002	0.0100	-	42.7930
3C330	N	0.5490	43.7569	40.4583	43.0792	42.9890	43.1538	43.9031	43.6021	44.0000	45.0002	0.0100	-	43.1867
NGC6109	E	0.0296	40.6190	39.4369	40.0414	39.6021	40.2553	-40.5515	-	0.0000	-	0.0000	-	0.0000
3C334	Q	0.5550	43.3906	42.6441	45.0792	44.9912	45.1523	45.0792	44.9912	45.1523	45.7002	0.0100	43.3666	42.5366
3C336	Q	0.9270	43.9071	42.3604	-	0.0000	-	0.0000	-	0.0000	45.4002	0.0100	43.4581	0.0000
3C341	N	0.4480	43.1666	40.4066	42.7720	42.5725	42.9224	43.2492	42.9487	43.6449	45.5576	0.0018	42.7967	41.7667
3C338	N	0.0303	41.2855	40.0314	40.5051	40.3802	40.5911	-40.7631	-	0.0000	42.0184	0.0073	39.5364	40.7946
3C340	N	0.7754	43.6701	40.9367	-	0.0000	-	0.0000	-	0.0000	44.9002	0.0100	-	42.6683
3C337	N	0.6350	43.5154	40.1812	-	0.0000	-	0.0000	-	0.0000	44.3002	0.0100	-	41.6347
3C343	Q	0.9880	43.8978	-43.5827	-	0.0000	-	0.0000	-	0.0000	45.9002	0.0100	42.6832	41.9932
3C343.1	N	0.7500	43.5921	-43.1670	-	0.0000	-	0.0000	-	0.0000	44.7002	0.0100	42.7097	42.4397
NGC6251	E	0.0240	40.4296	40.3504	42.7404	42.7243	42.7559	-41.0752	-	0.0000	42.8730	0.0005	-	0.0000
3C346	N	0.1620	42.1523	41.8338	43.3957	43.3805	43.4102	-42.4354	-	0.0000	43.9602	0.0040	41.3273	0.0000
3C345	Q	0.5940	43.3374	44.5944	45.6365	45.5832	45.7076	45.6365	45.5832	45.7076	-	0.0000	-	0.0000
3C349	N	0.2050	42.4751	41.1003	41.8217	41.5166	41.9175	43.8669	43.8188	43.9127	-	0.0000	41.5625	0.0000
3C351	Q	0.3710	43.0614	41.0496	41.9204	41.7417	42.0828	44.8010	44.7691	44.8191	46.0053	0.0011	42.8446	0.0000
3C352	N	0.8060	43.7964	41.4316	-	0.0000	-	0.0000	-	0.0000	44.8002	0.0100	-	43.0465
3C380	Q	0.6910	44.3181	44.6657	45.8129	45.7202	45.8893	45.8129	45.7202	45.8893	45.9002	0.0100	43.7626	42.9926
3C381	B	0.1605	42.3445	40.1820	42.1106	41.9987	42.1969	44.3086	44.1773	44.4385	44.6500	0.0097	42.3819	40.9171
3C382	B	0.0578	41.4794	40.8512	44.5798	44.5682	44.5911	44.5798	44.5682	44.5911	44.2400	0.0077	41.7817	40.7303
3C386	E	0.0177	40.5130	39.6196	39.4914	38.4500	39.8325	-40.1818	-	0.0000	41.5504	0.0071	-40.2525	0.0000
3C388	E	0.0908	41.9820	40.7684	41.7411	41.6530	41.8131	-42.0086	-	0.0000	42.6600	0.0492	40.7140	40.5164
3C390.3	B	0.0569	41.8471	41.0818	44.1761	44.1461	44.2304	44.1761	44.1461	44.2304	44.3700	0.0107	42.1089	40.9501
3C401	E	0.2010	42.6506	41.1898	42.7447	42.6916	42.7911	-43.0535	-	0.0000	43.1700	0.1249	41.0567	0.0000

Continued on next page

Table 6.7 – *Continued from previous page*

PKS	Type	z	L_{178}	L_5	L_{X_u}			L_{X_a}			L_{IR}		$L_{[OIII]}$	$L_{[OII]}$
3C427.1	E	0.5720	43.8301	40.5288	-42.4501	-	0.0000	-43.2388	-	0.0000	-43.8002	-	0.0000	0.0000
3C433	N	0.1016	42.4461	39.7746	41.0558	40.7736	41.2240	43.9222	43.8001	44.0180	44.6700	0.0045	41.6829	0.0000
3C436	N	0.2145	42.6549	41.0218	42.5873	42.5488	42.6213	43.5316	43.3502	43.7197	43.5200	0.0621	41.5585	0.0000
3C438	E	0.2900	43.3509	40.8658	42.6669	42.3912	42.8390	-43.1449	-	0.0000	-43.2700	-	-41.4700	0.0000
3C441	N	0.7080	43.6964	41.3593	-	0.0000	-	0.0000	-	0.0000	44.8002	0.0100	-	42.4218
3C442A	E	0.0270	40.7149	38.2103	40.0000	39.6021	40.4150	-40.9529	-	0.0000	-	0.0000	-	40.5639
3C449	E	0.0171	40.1630	39.0785	40.4914	40.4314	40.5441	-40.4628	-	0.0000	40.3576	0.0843	39.2058	0.0000
3C452	N	0.0811	42.2269	40.9899	41.7709	41.5185	41.9395	44.1761	43.6021	44.6721	44.1300	0.0098	41.3456	41.4447
NGC7385	E	0.0243	40.4446	39.9000	41.1139	41.0000	41.2553	-41.0982	-	0.0000	-	0.0000	-	0.0000
3C454.3	Q	0.8590	43.6992	45.0711	46.3711	46.2430	46.4698	46.3711	46.2430	46.4698	-	0.0000	-	0.0000
3C455	Q	0.5427	43.4100	40.7248	-	0.0000	-	0.0000	-	0.0000	-	0.0000	43.0668	42.8068
3C457	N	0.4280	43.2285	40.6877	43.3481	43.2998	43.3965	44.5574	44.5188	44.8801	-	0.0000	42.4863	0.0000
3C465	E	0.0293	41.1566	40.4122	40.9138	40.5682	41.4200	-41.0205	-	0.0000	42.1090	0.0069	39.7872	0.0000

Chapter 7

Conclusions and Future Work

In this thesis I study the properties of radio-loud AGN, aiming to better characterise the population and its impact on the host galaxies. In Section 1.5 I gave a list of aims that are addressed throughout this thesis. They can be divided into three categories.

7.1 Characterisation of the radio-loud AGN population

In Chapters 5 and 6 I presented results on the 2Jy sample of radio-loud AGN. This sample is statistically complete and contains examples of every radio-powerful AGN class, which makes it perfectly suited to study the overall properties of the population.

I analysed the X-ray properties of the sample, and correlated the soft and hard X-ray luminosities with the radio, mid-IR and optical luminosities, to study the relations between jet- and accretion-related quantities in the different bands.

I found the same strong correlations between hard (2-10 keV) X-ray, mid-IR and [OIII] emission as Hardcastle et al. (2006, 2009), confirming that these quantities are all related to radiatively efficient accretion. I confirmed the jet-related nature of the soft X-ray emission, as suggested by Hardcastle & Worrall (1999).

I found unequivocal proof for the radiatively inefficient nature of the LERGs, as well as confirmation for the fact that these objects accrete at very low Eddington rates ($\leq$ 10 per cent in all cases, with the distribution peaking at $\sim$ 1 per cent). I found that the HERGs in our sample are narrowly distributed around 10-30 per cent Eddington rates. However, there is an overlap between both populations, which is not consis-

tent with a simple switch. Even after discarding the 'dubious' objects, I found that LERGs embedded in very rich clusters have higher Eddington rates. For these sources the central back hole masses must be underestimated and the jet luminosity is higher (Hardcastle & Krause 2013). These two factors can account for the order of magnitude in Eddington rate that makes these objects overlap with the HERGs, in which case a simple switch between both populations would be feasible.

There are no signs in our plots for radiatively efficient accretion completely taking over from jet production. In fact, I found several NLRGs in which the dominant energetic contribution from the AGN comes from the jet, within the uncertainties, rather than radiative luminosity. Jet kinetic power and radiative luminosity seem to be independent in high-excitation objects, confirming the conclusions of Punsly & Zhang (2011). While a better understanding of the timescales and the addition of radio-quiet objects to the plots are necessary to fully understand whether these quantities are truly independent, our plots seem to indicate that they are.

In Chapter 3 I also studied the obscuration variability of Mrk 6, finding that the hypothesis of a variable absorption gas column, with timescales of 2-6 years, caused by clumpiness of the accreting gas close to the black hole, is a likely explanation for the variations we see between the *Chandra* and *XMM* spectra. If this is indeed the case, and as already pointed out by Risaliti et al. (2002), this scenario could be more common than previously thought, and applicable also to intermediate Seyfert systems, such as Mrk 6. This could have interesting consequences on the structure of the 'traditional' accretion structures attributed to radiatively-efficient AGN.

The results on the energetics of the source showed that Bondi accretion might not be enough to power it, so that it is possible that cold gas accretion is the dominant mechanism in this system, unlike what is seen in many more powerful radio sources (see e.g. Hardcastle et al. 2007a; Balmaverde et al. 2008, and Chapter 6). Cold gas has also been suggested as the primary source of fuel for Cen A and NGC 3801 (Croston et al. 2007). It is also possible that the active nucleus of Mrk 6 is accreting both the hot phase of the ISM and cold gas from a past merger. This is consistent with recent results on early-type galaxies by Pellegrini (2010).

7.1.1 Future work

While the cores of the 2Jy sample have been studied in detail, the extended emission has not been characterised. This is particularly interesting for the low-z objects imaged by *Chandra* (see Chapter 5), where the extended structures are resolved. My next research project involves studying the non-thermal emission in these sources.

Several of the 2Jy sources show X-ray jets. While those of 3C 15 and Hercules A have been studied in detail, some have not been observed in X-rays before, as is the case for PKS 1733-56. Jets are also possibly observed in PKS 1814-63, PKS 1949+02 (3C 403), and PKS 2221-02 (3C 445). I will extract spectra for these jets whenever possible, or constrain their luminosity in the fainter cases, to study their radio/X-ray luminosity ratio, assess the degree of particle acceleration involved and study the extent of beaming expected.

X-ray hotspots are present in 12 sources. For the most part they are coincident with the radio hotspots, with small offsets in a couple of objects. For most cases we expect the X-ray emission to be too faint to extract a proper spectrum, but luminosity constraints and comparison with the radio emission will allow us to determine the degree of particle acceleration involved. I will also study the reasons behind mismatches between radio and X-ray hotspots.

In at least three sources with FR II (Fanaroff & Riley 1974) radio morphology, we observe enhancements in X-ray emission inside the radio lobes, probably associated with inverse-Compton processes, which I aim to characterise. This will also allow me to study the magnetic field strength and particle population inside the lobes, and how close they are to equipartition, in a similar manner as the work by Croston et al. (2005).

My future work at the University of Leicester will involve a characterisation of the AGN in the 3XMM catalogue, which will be released shortly. This work will be an extension and a progression from that done on the 2Jy and 3CRR sources, and will involve radio-quiet AGN as well. I will use multiwavelength data to test the luminosity correlations found for the 2Jy sample, and investigate how accretion works in AGN overall. I will also study the low-luminosity end of the radio-quiet population, and try to determine diagnostics to disentangle the AGN and star formation contributions.

I will also submit a *Suzaku* proposal to monitor the absorption variability of Mrk 6 on shorter timescales than those observed, aiming to characterise the structure and

location of the obscuring material, and determine whether radio activity may have any influence on the different timescales observed in this source and those found in radio-quiet systems (e.g. Risaliti et al. 2002).

7.2 The impact of low-power sources

In Chapters 3 and 4 I presented results on the shocks being driven by the radio bubbles of Markarian 6 and the Circinus galaxy, respectively.

For Markarian 6 I found shells of strongly shocked gas around both radio bubbles, with Mach numbers 3.2-5.5 consistent with the Rankine-Hugoniot conditions for a strong shock. This is the third clear detection of such a process in a low-power radio source, and therefore reinforces the hypothesis that this mechanism may be very common and may play an important role in the process by which these young radio sources form their stellar populations.

It is very likely that much of the gas in the shells will escape the gravitational potential of the host galaxy. Our results show that shock heating is the dominant process, the thermal energy in the shock being an order of magnitude larger than the work required to inflate the radio cavities, which implies that the impact of the outburst on the host galaxy's ISM is likely to be dramatic. Moreover, the inner set of bubbles is expanding perpendicularly to the external ones, and into denser regions of the host galaxy. Although the shock will probably be weaker, due to the increased density, the expansion of the inner bubbles is likely to cause a more direct disruption on the ISM and so is likely to have a bigger impact on star formation. Unfortunately the resolution of the current generation of X-ray telescopes does not allow us to determine the details of this ejection of gas.

For the Circinus galaxy I also found shells of shocked gas around the radio lobes, expanding into the halo regions of the galaxy with Mach numbers $\mathcal{M} \sim 2.7$–3.6 for the W shell and $\mathcal{M} \sim 2.8$–5.3 for the E shell, consistent with the Rankine-Hugoniot conditions for a strong shock.

I ruled out the possibility that this emission is caused by AGN photoionization, and discarded the scenario in which the radio structures are the result of star formation or a supernova-driven wind; instead we argue that they are caused by the interaction of a radio jet with the surrounding gas. The total energy (thermal and kinetic) involved in

the creation of these shells is $\sim 2 \times 10^{55}$ erg. Their age is estimated to be $\sim 10^6$ years. From these parameters I inferred the kinetic luminosity of the jet, which is $\sim 10^{41}$ erg s^{-1}. This has potential consequences for other Seyfert systems, as well as our own galaxy: there is a possibility that the Fermi bubbles observed in the Milky way have been caused by a similar process to that observed in Circinus.

The presence in Circinus of two symmetrical structures resembling jet termination points or hotspots, together with the slightly different X-ray spectra and flattening of radio spectral index in these regions, suggests that the radio jet may still be active, even if it is not visible. This suggests that "invisible" jets may be a more common occurrence among Seyfert and late type galaxies than previously thought, given that it is difficult to separate the different radio structures in galaxies with active star formation, when the radio bubbles are faint or their orientation is similar to that of the disk. This opens new questions about the role of low radio luminosity, star-forming, active galaxies, which are often ignored in survey studies.

In Circinus the X-ray and radio emission from the shocked shells are spatially coincident. This, added to the fact that the radio emission is edge-brightened, allowed us to draw a parallel between these structures and what is observed in supernova remnants: the radio emission from the shells comes from shock-compressed or (re)accelerated cosmic ray electrons in the environment, but particle acceleration, if present at all, is not efficient enough to produce TeV electrons, so that only thermal emission is observed in X-rays. This correspondence has been long expected for AGN, given the similarity between the physical processes involved in SN and jet-driven shocks, but has not been unequivocally observed before. We believe this scenario may be common in other low-power radio galaxies, and potentially very relevant to those with late-type hosts, but can only be observed where we are able to spatially resolve the different structures, something that has been achieved for Circinus due to its proximity to us.

7.2.1 Future work

While finding sources where the type of work described in this Section can be carried out is rather difficult, there are some good candidates. One of them is 3C 15, part of the 2Jy sample, for which I have submitted a *Chandra* observation proposal.

3C 15 is a powerful radio galaxy ($L_{1.4GHz} = 5.2 \times 10^{25}$ W Hz^{-1}), whose radio

Source	$L_{1.4GHz}$ W Hz^{-1} sr^{-1}	$L_{jet,kin}$ erg s^{-1}	$E_{tot,lobes}$ erg
Circinus	2.2×10^{20}	10^{41}	2×10^{55}
Mrk 6	1.7×10^{23}	10^{42}	$2.6 - 4.6 \times 10^{56}$
NGC 3801	1.2×10^{23}	3×10^{42}	1.7×10^{56}
3C 444	3.3×10^{26}	2.9×10^{45}	8.2×10^{60}

Table 7.1: Radio core luminosity, jet kinetic luminosity, and total energy (thermal+kinetic) inferred from the radio lobes for different galaxies, illustrating power scaling.

lobe morphology is intermediate between that of an FRI and an FRII. It also has a knotty 6 kpc one-sided jet, visible in radio through to X-ray energies. This object is representative of the intermediate-power population of radio galaxies, and as such it bridges the gap between low-power sources, such as Circinus, and high-power ones, such as 3C 444. (see Table 7.1), making it an ideal candidate to study the universality of this correlation.

This elliptical galaxy sits in a relatively sparse environment, which could account in part for its atypical morphology: its shells are narrower, and more akin to those of Cen A or NGC 3801, rather than the spherical bow-shock seen in 3C 444. A deep *Chandra* observation, added to the multiwavelength data from the 2Jy sample, will allow us to characterise the external medium into which the lobes of 3C 15 are expanding, and thus help us determine the role of the environment in the behaviour of moderately powerful radio galaxies.

Given that there are examples of shocks in low radio-power, radiatively efficient, and high-radio power, radiatively inefficient sources, understanding the fuelling mechanisms of 3C 15 will allow us to determine how efficiently the energy derived from accretion is transferred to the environment as a function of the accretion rate and mode of the AGN. Since we also expect there to be a dependence with the medium through which the shock propagates, the environment of 3C 15 might prove essential to break the degeneracy between these parameters.

7.3 Classifications and diagnostics

In Chapter 6 I studied the reliability of some of the classifications and diagnostic tools that are commonly used to study samples of AGN.

It is now clear that a classification that is based purely on morphological features, as that of Fanaroff & Riley (1974), emission line properties, or orientation, as predicted by models such as that of Antonucci (1993), cannot account for the underlying variety within the AGN population. As suggested by e.g. Lin et al. (2010), we need a classification that encompasses both the physical properties and the observational properties of AGNs. This is particularly important for the LERG/HERG case, since the difference between both classes lies in their underlying physical scenarios.

Throughout this work I have shown that the best way to reliably classify AGN populations is through a multiwavelength approach. I showed that several objects classified as LERGs based on their optical spectra (PKS 0034-01, PKS 0043-42, PKS 0625-35, 3C 123, 3C 200 and more recently PKS 0347+05) are most likely high-excitation sources, and vice-versa, some objects classified as NLRGs (M 87 and 3C 338 being the clearest cases) are LERGs where the high-excitation lines are produced through other processes. Multiwavelength data could also help in the case of nearby, low-power sources, as was the case for Mrk 6, to establish whether they should be treated as radio-loud or radio-quiet sources in term of their spectral characteristics.

I found that bolometric corrections, M_{BH}/L correlations and jet power estimations only give an overall indication of AGN behaviour, and may be inaccurate for individual sources, given the vast range of environments and nuclear powers involved. Further studies of individual SEDs and jet-environment interaction simulations are needed to establish how reliable these correlations are, in particular for the case of LERGs and low-power sources. For example, the X-ray bolometric corrections derived by Elvis et al. (1994) are applicable to most quasars, but are likely to be very inaccurate for less powerful sources, and completely wrong in the case of LERGs.

Mid-IR measurements have proved, throughout this work, to be the best to constrain the accretion properties of high-excitation objects, while for the low-excitation population X-rays are the best band to set an upper limit on radiatively efficient accretion, given that they are less subject to contamination from stellar processes and the presence of a jet (this is taken into account by the soft X-ray component, whose

jet-related nature I confirm). Radio measurements are essential to establish the extent of radiatively inefficient accretion, and the amount of AGN power invested in the jet.

7.3.1 Future work

The future steps to take in this case are obvious: systematic studies of AGN SED across all classes are needed to properly establish the validity of bolometric corrections, and to derive class-specific corrections that can be used in samples. I will attempt to do this for part of the 3XMM catalogue as part of my future work, for the low-luminosity end of the population.

I will also try to develop a series of diagnostics that establish the accretion mode and rate across the entire AGN population.

Bibliography

Abramowicz, M. A., Igumenshchev, I. V., Quataert, E., & Narayan, R. 2002, ApJ, 565, 1101 13

Akritas, M. G. & Siebert, J. 1996, MNRAS, 278, 919 177

Alexander, D. M. & Hickox, R. C. 2012, New A Rev., 56, 93 24

Alexander, P. 2002, MNRAS, 335, 610 22

Allen, S. W., Dunn, R. J. H., Fabian, A. C., Taylor, G. B., & Reynolds, C. S. 2006, MNRAS, 372, 21 12

Antognini, J., Bird, J., & Martini, P. 2012, ApJ, 756, 116 164

Antonucci, R. 1993, ARA&A, 31, 473 2, 207, 225

Attridge, J. M., Roberts, D. H., & Wardle, J. F. C. 1999, ApJ, 518, L87 20

Balbus, S. A. & Hawley, J. F. 1991, ApJ, 376, 214 6

Balmaverde, B., Baldi, R. D., & Capetti, A. 2008, A&A, 486, 119 12, 75, 149, 154, 220

Beck, R., Brandenburg, A., Moss, D., Shukurov, A., & Sokoloff, D. 1996, ARA&A, 34, 155 107, 108

Beck, R., Carilli, C. L., Holdaway, M. A., & Klein, U. 1994, A&A, 292, 409 98, 107

Begelman, M. C. & Cioffi, D. F. 1989, ApJ, 345, L21 22

Belsole, E., Worrall, D. M., Hardcastle, M. J., & Croston, J. H. 2007, MNRAS, 381, 1109 24

Bennett, A. S. 1962, MmRAS, 68, 163 1

Benson, A. J. 2010, Phys. Rep., 495, 33 29

Best, P. N. 2004, MNRAS, 351, 70 24

Best, P. N. & Heckman, T. M. 2012, MNRAS, 421, 1569 13, 26, 164, 195, 197

Best, P. N., Kauffmann, G., Heckman, T. M., et al. 2005, MNRAS, 362, 25 4

Best, P. N., Longair, M. S., & Roettgering, H. J. A. 1998, MNRAS, 295, 549 210

Bicknell, G. V. 1984, ApJ, 286, 68 20

Blandford, R. D. & Begelman, M. C. 1999, MNRAS, 303, L1 13

Bondi, H. 1952, MNRAS, 112, 195 12

Bower, R. G., Benson, A. J., Malbon, R., et al. 2006, MNRAS, 370, 645 29, 42, 78, 164

Bowyer, C. S., Lampton, M., Mack, J., & de Mendonca, F. 1970, ApJ, 161, L1 2

Brenneman, L. W. & Reynolds, C. S. 2009, ApJ, 702, 1367 16

Brüggen, M. & Kaiser, C. R. 2001, MNRAS, 325, 676 107

Burbidge, E. M., Burbidge, G. R., & Prendergast, K. H. 1959, ApJ, 130, 26 16

Burbidge, G. R. 1956, ApJ, 124, 416 23

Capetti, A., Axon, D. J., Kukula, M., et al. 1995, ApJ, 454, L85+ 58

Capetti, A., Axon, D. J., Macchetto, F. D., Marconi, A., & Winge, C. 1999, ApJ, 516, 187 79

Capetti, A., Kharb, P., Axon, D. J., Merritt, D., & Baldi, R. D. 2009, AJ, 138, 1990 5

Carter, C., Karovska, M., Jerius, D., Glotfelty, K., & Beikman, S. 2003, in Astronomical Society of the Pacific Conference Series, Vol. 295, Astronomical Data Analysis Software and Systems XII, ed. H. E. Payne, R. I. Jedrzejewski, & R. N. Hook, 477 47

Cattaneo, A., Faber, S. M., Binney, J., et al. 2009, Nature, 460, 213 2, 5, 163

Cavagnolo, K. W., McNamara, B. R., Nulsen, P. E. J., et al. 2010, ApJ, 720, 1066 195, 196

Condon, J. J. 1992, ARA&A, 30, 575 100

Croston, J. H., Hardcastle, M. J., Birkinshaw, M., Worrall, D. M., & Laing, R. A. 2008a, MNRAS, 386, 1709 22, 60, 70, 105

Croston, J. H., Hardcastle, M. J., Harris, D. E., et al. 2005, ApJ, 626, 733 22, 23, 221

Croston, J. H., Hardcastle, M. J., Kharb, P., Kraft, R. P., & Hota, A. 2008b, ApJ, 688, 190 18, 24, 26, 42, 60, 79

Croston, J. H., Hardcastle, M. J., Mingo, B., et al. 2011, ApJ, 734, L28 2, 5, 19, 23, 26, 153, 163, 196

Croston, J. H., Kraft, R. P., & Hardcastle, M. J. 2007, ApJ, 660, 191 18, 26, 42, 49, 60, 69, 70, 72, 75, 79, 99, 105, 220

Croston, J. H., Kraft, R. P., Hardcastle, M. J., et al. 2009, MNRAS, 395, 1999 24, 42, 67, 78, 79, 105, 114

Croton, D. J., Springel, V., White, S. D. M., et al. 2006, MNRAS, 365, 11 29, 42, 78, 164

Curran, S. J., Koribalski, B. S., & Bains, I. 2008, MNRAS, 389, 63 81, 97

Danforth, C. W., Shull, J. M., Rosenberg, J. L., & Stocke, J. T. 2006, ApJ, 640, 716 89

De Lucia, G. & Blaizot, J. 2007, MNRAS, 375, 2 29

de Rosa, A., Panessa, F., Bassani, L., et al. 2012, MNRAS, 420, 2087 92, 93

de Vaucouleurs, G., de Vaucouleurs, A., Corwin, H. G., et al. 1995, VizieR Online Data Catalog, 7155, 0 62

de Vries, W. H., O'Dea, C. P., Perlman, E., et al. 1998, ApJ, 503, 138 210

Dewangan, G. C., Griffiths, R. E., Dasgupta, S., & Rao, A. R. 2007, ApJ, 671, 1284 10

Di Matteo, T., Allen, S. W., Fabian, A. C., Wilson, A. S., & Young, A. J. 2003, ApJ, 582, 133 13

Dicken, D., Tadhunter, C., Axon, D., et al. 2009, ApJ, 694, 268 142, 168, 197

Dicken, D., Tadhunter, C., Axon, D., et al. 2012, ApJ, 745, 172 115, 127, 134, 142, 144, 157, 159, 160, 161

Dicken, D., Tadhunter, C., Morganti, R., et al. 2008, ApJ, 678, 712 111, 168

Dickey, J. M. & Lockman, F. J. 1990a, ARA&A, 28, 215 46, 59

Dickey, J. M. & Lockman, F. J. 1990b, ARA&A, 28, 215 79

Dulwich, F., Worrall, D. M., Birkinshaw, M., Padgett, C. A., & Perlman, E. S. 2007, MNRAS, 374, 1216 114

Dunn, R. J. H., Fabian, A. C., & Celotti, A. 2006, MNRAS, 372, 1741 20

Duric, N. & Seaquist, E. R. 1988, ApJ, 326, 574 106

Edge, D. O., Shakeshaft, J. R., McAdam, W. B., Baldwin, J. E., & Archer, S. 1959, MmRAS, 68, 37 1

Elmouttie, M., Haynes, R. F., Jones, K. L., Sadler, E. M., & Ehle, M. 1998a, MNRAS, 297, 1202 79, 80, 81, 83, 97, 99, 100, 103, 104, 106

Elmouttie, M., Koribalski, B., Gordon, S., et al. 1998b, MNRAS, 297, 49 81, 83, 84, 87, 92, 97, 101

Elvis, M., Maccacaro, T., Wilson, A. S., et al. 1978, MNRAS, 183, 129 2

Elvis, M., Wilkes, B. J., McDowell, J. C., et al. 1994, ApJS, 95, 1 197, 225

Eracleous, M. & Halpern, J. P. 1994, ApJS, 90, 1 16, 112, 159

Evans, D. A., Hardcastle, M. J., Croston, J. H., Worrall, D. M., & Birkinshaw, M.

2005, MNRAS, 359, 363 46
Evans, D. A., Hardcastle, M. J., Lee, J. C., et al. 2008, ApJ, 688, 844 180, 205
Evans, D. A., Kraft, R. P., Worrall, D. M., et al. 2004, ApJ, 612, 786 50
Evans, D. A., Reeves, J. N., Hardcastle, M. J., et al. 2010, ApJ, 710, 859 56
Evans, D. A., Summers, A. C., Hardcastle, M. J., et al. 2011, ApJ, 741, L4 13, 164
Fabbiano, G., Elvis, M., Markoff, S., et al. 2003, ApJ, 588, 175 13
Fabian, A. C. & Canizares, C. R. 1988, Nature, 333, 829 12
Fanaroff, B. L. & Riley, J. M. 1974, MNRAS, 167, 31P 18, 42, 164, 207, 221, 225
Fath, E. A. 1909, Lick Observatory Bulletin, 5, 71 1
Feldmeier, J. J., Brandt, W. N., Elvis, M., et al. 1999, ApJ, 510, 167 48, 49, 53, 54
Fernández-Ontiveros, J. A., Prieto, M. A., Acosta-Pulido, J. A., & Montes, M. 2012, Journal of Physics Conference Series, 372, 012006 12, 164, 197
Ferrarese, L. & Merritt, D. 2000, ApJ, 539, L9 5
For, B.-Q., Koribalski, B., & Jarrett, T. 2012, ArXiv e-prints 97
Frank, J., King, A., & Raine, D. J. 2002, Accretion Power in Astrophysics: Third Edition 6
Freeman, K. C., Karlsson, B., Lynga, G., et al. 1977, A&A, 55, 445 79
Friedman, H. & Byram, E. T. 1967, Science, 158, 257 1
Fukugita, M., Shimasaku, K., & Ichikawa, T. 1995, PASP, 107, 945 196
Gallimore, J. F., Axon, D. J., O'Dea, C. P., Baum, S. A., & Pedlar, A. 2006, AJ, 132, 546 18, 42, 78
Gandhi, P., Horst, H., Smette, A., et al. 2009, A&A, 502, 457 11
Gebhardt, K., Rich, R. M., & Ho, L. C. 2005, ApJ, 634, 1093 5
Genzel, R., Lutz, D., Sturm, E., et al. 1998, ApJ, 498, 579 100
Getman, K. V., Flaccomio, E., Broos, P. S., et al. 2005, ApJS, 160, 319 46
Gitti, M., Nulsen, P. E. J., David, L. P., McNamara, B. R., & Wise, M. W. 2011, ApJ, 732, 13 134
Glazebrook, K., Peacock, J. A., Miller, L., & Collins, C. A. 1995, MNRAS, 275, 169 169, 198, 210
Godfrey, L. E. H. & Shabala, S. S. 2013, ArXiv e-prints 22, 164, 195
Govoni, F., Falomo, R., Fasano, G., & Scarpa, R. 2000, A&A, 353, 507 24
Graham, A. W. 2007, MNRAS, 379, 711 5, 196, 197
Guidetti, D., Laing, R. A., Bridle, A. H., Parma, P., & Gregorini, L. 2011, MNRAS,

413, 2525 106, 108

Guidetti, D., Laing, R. A., Croston, J. H., Bridle, A. H., & Parma, P. 2012, ArXiv e-prints 106

Guo, F., Li, S., Li, H., et al. 2012, ApJ, 747, 98 107

Haardt, F. & Maraschi, L. 1991, ApJ, 380, L51 8, 10

Hardcastle, M. J. 2004, A&A, 414, 927 24

Hardcastle, M. J. 2009, in Astronomical Society of the Pacific Conference Series, Vol. 407, The Low-Frequency Radio Universe, ed. D. J. Saikia, D. A. Green, Y. Gupta, & T. Venturi, 121 20

Hardcastle, M. J., Alexander, P., Pooley, G. G., & Riley, J. M. 1998a, MNRAS, 296, 445 136

Hardcastle, M. J., Birkinshaw, M., & Worrall, D. M. 1998b, MNRAS, 294, 615 23

Hardcastle, M. J. & Croston, J. H. 2010, MNRAS, 404, 2018 134

Hardcastle, M. J., Evans, D. A., & Croston, J. H. 2006, MNRAS, 370, 1893 46, 47, 164, 165, 166, 167, 169, 172, 180, 196, 205, 207, 213, 219

Hardcastle, M. J., Evans, D. A., & Croston, J. H. 2007a, MNRAS, 376, 1849 6, 14, 25, 75, 164, 172, 220

Hardcastle, M. J., Evans, D. A., & Croston, J. H. 2009, MNRAS, 396, 1929 11, 16, 19, 43, 49, 55, 164, 165, 166, 167, 169, 172, 175, 177, 178, 180, 181, 182, 185, 187, 190, 195, 196, 207, 213, 219

Hardcastle, M. J., Kraft, R. P., Sivakoff, G. R., et al. 2007b, ApJ, 670, L81 20

Hardcastle, M. J., Kraft, R. P., Worrall, D. M., et al. 2007c, ApJ, 662, 166 22, 70, 105, 136, 138

Hardcastle, M. J. & Krause, M. G. H. 2013, MNRAS, 601 22, 164, 180, 195, 206, 208, 220

Hardcastle, M. J., Massaro, F., & Harris, D. E. 2010a, MNRAS, 401, 2697 17

Hardcastle, M. J., Virdee, J. S., Jarvis, M. J., et al. 2010b, MNRAS, 409, 122 26

Hardcastle, M. J. & Worrall, D. M. 1999, MNRAS, 309, 969 10, 164, 183, 207, 219

Harper, Jr., D. A. & Low, F. J. 1973, ApJ, 182, L89 11

Harris, G. L. H. & Harris, W. E. 2011, MNRAS, 410, 2347 5

Harwood, J. J. & Hardcastle, M. J. 2012, Monthly Notices of the Royal Astronomical Society, 423, 1368 104

Heckman, T. M. 1980, A&A, 87, 152 16

Heckman, T. M., Kauffmann, G., Brinchmann, J., et al. 2004, ApJ, 613, 109 164
Heckman, T. M., Smith, E. P., Baum, S. A., et al. 1986, ApJ, 311, 526 24
Heinz, S., Reynolds, C. S., & Begelman, M. C. 1998, ApJ, 501, 126 78
Hill, G. J. & Lilly, S. J. 1991, ApJ, 367, 1 24
Hine, R. G. & Longair, M. S. 1979, MNRAS, 188, 111 4, 12, 163
Ho, L. C. 2008, ARA&A, 46, 475 12, 13, 14
Ho, L. C. 2009, ApJ, 699, 626 164, 197
Holt, J., Tadhunter, C. N., & Morganti, R. 2008, MNRAS, 387, 639 144, 147, 157
Holt, J., Tadhunter, C. N., & Morganti, R. 2009, MNRAS, 400, 589 144, 147
Hopkins, P. F. 2012, MNRAS, 420, L8 164
Hota, A. & Saikia, D. J. 2006, MNRAS, 371, 945 18, 24, 42
Hummel, E., Beck, R., & Dahlem, M. 1991, A&A, 248, 23 98, 107
Immler, S., Brandt, W. N., Vignali, C., et al. 2003, AJ, 126, 153 43, 48, 49, 53, 54, 55
Ineson, J., Croston, J., Hardcastle, M., et al. 2012, in Galaxy Clusters as Giant Cosmic Laboratories, ed. J.-U. Ness, 25 24
Inskip, K. J., Tadhunter, C. N., Dicken, D., et al. 2007, MNRAS, 382, 95 160
Inskip, K. J., Tadhunter, C. N., Morganti, R., et al. 2010, MNRAS, 407, 1739 114, 117, 120, 122, 126, 129, 131, 133, 134, 138, 142, 144, 147, 153, 154, 157, 158, 160, 161, 168, 196, 198
Jackson, N. & Browne, I. W. A. 1990, Nature, 343, 43 188, 197
Jaffe, W., Meisenheimer, K., Röttgering, H. J. A., et al. 2004, Nature, 429, 47 11
Janssen, R. M. J., Röttgering, H. J. A., Best, P. N., & Brinchmann, J. 2012, A&A, 541, A62 25, 163
Jester, S., Harris, D. E., Marshall, H. L., & Meisenheimer, K. 2006, ApJ, 648, 900 114
Jester, S., Röser, H.-J., Meisenheimer, K., & Perley, R. 2005, A&A, 431, 477 114
Jones, C., Forman, W., Vikhlinin, A., et al. 2002, ApJ, 567, L115 78
Jones, K. L., Koribalski, B. S., Elmouttie, M., & Haynes, R. F. 1999, MNRAS, 302, 649 81, 97
Jorstad, S. G., Marscher, A. P., Lister, M. L., et al. 2005, AJ, 130, 1418 20
Kaastra, J. S., Tamura, T., Peterson, J. R., et al. 2004, A&A, 413, 415 134
Kadler, M., Kerp, J., Ros, E., et al. 2004, A&A, 420, 467 18
Kaiser, C. R. & Alexander, P. 1997, MNRAS, 286, 215 22, 103
Kallman, T. R. & McCray, R. 1982, ApJS, 50, 263 58, 92

Kaspi, S., Smith, P. S., Netzer, H., et al. 2000, ApJ, 533, 631 6

Kataoka, J., Leahy, J. P., Edwards, P. G., et al. 2003, A&A, 410, 833 114

Keel, W. C., White, III, R. E., Owen, F. N., & Ledlow, M. J. 2006, AJ, 132, 2233 24

Kellermann, K. I., Sramek, R., Schmidt, M., Shaffer, D. B., & Green, R. 1989, AJ, 98, 1195 3, 4

Kharb, P., Hota, A., Croston, J. H., et al. 2010, ApJ, 723, 580 60

Kharb, P., O'Dea, C. P., Baum, S. A., Colbert, E. J. M., & Xu, C. 2006, ApJ, 652, 177 42, 43, 45, 56, 58, 59, 60, 69, 70, 72, 78, 109

Kharb, P., O'Dea, C. P., Baum, S. A., et al. 2008, ApJS, 174, 74 104

King, A. 2008, Disk Accretion in Galactic Nuclei 6

Komossa, S., Burwitz, V., Hasinger, G., et al. 2003, ApJ, 582, L15 5

Kormendy, J. & Bender, R. 2011, Nature, 469, 377 5

Kovács, Z., Gergely, L., & Biermann, P. L. 2011, MNRAS, 416, 991 7

Kraft, R. P., Hardcastle, M. J., Worrall, D. M., & Murray, S. S. 2005, ApJ, 622, 149 149

Kraft, R. P., Vázquez, S. E., Forman, W. R., et al. 2003, ApJ, 592, 129 2, 5, 24, 26, 42, 59, 70, 72, 78, 105, 114, 163

Krolik, J. H. & Begelman, M. C. 1988, ApJ, 329, 702 11

Kukula, M. J., Ghosh, T., Pedlar, A., & Schilizzi, R. T. 1999, ApJ, 518, 117 104

Kukula, M. J., Holloway, A. J., Pedlar, A., et al. 1996, MNRAS, 280, 1283 42, 45, 58, 60

Labiano, A. 2008, A&A, 488, L59 17

Laing, R. A. & Bridle, A. H. 2002, MNRAS, 336, 1161 20

Laing, R. A., Jenkins, C. R., Wall, J. V., & Unger, S. W. 1994, in Astronomical Society of the Pacific Conference Series, Vol. 54, The Physics of Active Galaxies, ed. G. V. Bicknell, M. A. Dopita, & P. J. Quinn, 201 19, 164

Landau, L. D. & Lifshitz, E. M. 1987, Fluid Mechanics, Second Edition: Volume 6 (Course of Theoretical Physics), 2nd edn. (Butterworth-Heinemann) 25, 61, 70, 71, 98

Lane, W. M., Clarke, T. E., Taylor, G. B., Perley, R. A., & Kassim, N. E. 2004, AJ, 127, 48 134

Leahy, J. P., Black, A. R. S., Dennett-Thorpe, J., et al. 1997, MNRAS, 291, 20 154

Ledlow, M. J. & Owen, F. N. 1996, AJ, 112, 9 18

Ledlow, M. J., Owen, F. N., & Keel, W. C. 1998, ApJ, 495, 227 24

Ledlow, M. J., Owen, F. N., Yun, M. S., & Hill, J. M. 2001, ApJ, 552, 120 24

Lilly, S. J. & Longair, M. S. 1984, MNRAS, 211, 833 210

Lin, Y.-T., Shen, Y., Strauss, M. A., Richards, G. T., & Lunnan, R. 2010, ApJ, 723, 1119 13, 164, 207, 225

Liu, L. & Zhang, Y. 2011, Journal of Astrophysics and Astronomy, 32, 173 114

Longair, S. 1992, High Energy Astrophysics, High Energy Astrophysics No. v. 1 (Cambridge University Press) 21

Longinotti, A. L., Bianchi, S., Ballo, L., de La Calle, I., & Guainazzi, M. 2009, MNRAS, 394, L1 56

Magorrian, J., Tremaine, S., Richstone, D., et al. 1998, AJ, 115, 2285 2, 5, 163

Maiolino, R., Krabbe, A., Thatte, N., & Genzel, R. 1998, ApJ, 493, 650 11

Maitra, D., Markoff, S., & Falcke, H. 2009, A&A, 508, L13 13

Malizia, A., Bassani, L., Capalbi, M., et al. 2003, A&A, 406, 105 54

Mannucci, F., Basile, F., Poggianti, B. M., et al. 2001, MNRAS, 326, 745 169, 198, 210

Marconi, A. & Hunt, L. K. 2003, ApJ, 589, L21 73, 197

Marconi, A., Moorwood, A. F. M., Origlia, L., & Oliva, E. 1994, The Messenger, 78, 20 83, 84, 91, 92

Markevitch, M., Govoni, F., Brunetti, G., & Jerius, D. 2005, ApJ, 627, 733 106

Marshall, N., Warwick, R. S., & Pounds, K. A. 1981, MNRAS, 194, 987 2

Martel, A. R., Baum, S. A., Sparks, W. B., et al. 1999, ApJS, 122, 81 114

Mason, R. E., Lopez-Rodriguez, E., Packham, C., et al. 2012, AJ, 144, 11 12, 13, 14, 164

Massaro, F., Harris, D. E., Chiaberge, M., et al. 2009, ApJ, 696, 980 157

Matsushita, S., Kawabe, R., Kohno, K., et al. 2005, ApJ, 618, 712 100

McHardy, I. M., Uttley, P., Taylor, R. D., & Seymour, N. 2004, in American Institute of Physics Conference Series, Vol. 714, X-ray Timing 2003: Rossi and Beyond, ed. P. Kaaret, F. K. Lamb, & J. H. Swank, 174–181 10

McKinney, J. C. & Gammie, C. F. 2004, ApJ, 611, 977 14

McLure, R. J. & Jarvis, M. J. 2002, MNRAS, 337, 109 6

McNamara, B. R. & Nulsen, P. E. J. 2007, ARA&A, 45, 117 2, 27, 29, 42, 60, 78, 164

McNamara, B. R., Wise, M., Nulsen, P. E. J., et al. 2000, ApJ, 534, L135 42, 78

Merloni, A. & Heinz, S. 2008, MNRAS, 388, 1011 29

Milne, D. K. 1987, Australian Journal of Physics, 40, 771 106

Mingo, B., Hardcastle, M. J., Croston, J. H., et al. 2011, ApJ, 731, 21 xv, 79, 99, 105, 109, 114, 166

Mingo, B., Hardcastle, M. J., Croston, J. H., et al. 2012, ApJ, 758, 95 xv

Morganti, R., Fanti, R., Gioia, I. M., et al. 1988, A&A, 189, 11 23, 69, 104

Morganti, R., Holt, J., Tadhunter, C., et al. 2011, A&A, 535, A97 144

Morganti, R., Killeen, N. E. B., & Tadhunter, C. N. 1993, MNRAS, 263, 1023 19, 111, 112, 114, 133, 136, 138, 140, 154, 168

Morganti, R., Oosterloo, T., Tadhunter, C. N., et al. 1999, A&AS, 140, 355 19, 112, 114, 117, 131, 157, 159, 160, 161, 168

Mulchaey, J. S. & Jeltema, T. E. 2010, ApJ, 715, L1 62

Naab, T., Johansson, P. H., Ostriker, J. P., & Efstathiou, G. 2007, ApJ, 658, 710 63

Nagao, T., Murayama, T., Shioya, Y., & Taniguchi, Y. 2002, ApJ, 567, 73 112, 159

Narayan, R. & Yi, I. 1995, ApJ, 452, 710 13, 14, 164

Nenkova, M., Sirocky, M. M., Ivezić, Ž., & Elitzur, M. 2008a, ApJ, 685, 147 11

Nenkova, M., Sirocky, M. M., Nikutta, R., Ivezić, Ž., & Elitzur, M. 2008b, ApJ, 685, 160 11

Nesvadba, N. P. H., Boulanger, F., Salome, P., et al. 2010, ArXiv e-prints 60

Netzer, H. 2009, MNRAS, 399, 1907 197

Nulsen, P. E. J., Hambrick, D. C., McNamara, B. R., et al. 2005a, ApJ, 625, L9 42, 140

Nulsen, P. E. J., McNamara, B. R., Wise, M. W., & David, L. P. 2005b, ApJ, 628, 629 140

Ogle, P. M., Brookings, T., Canizares, C. R., Lee, J. C., & Marshall, H. L. 2003, A&A, 402, 849 92

Ojha, R., Fey, A. L., Johnston, K. J., et al. 2004, AJ, 127, 1977 147

Osterbrock, D. E. 1989, Astrophysics of gaseous nebulae and active galactic nuclei 16

Osterbrock, D. E. & Koski, A. T. 1976, MNRAS, 176, 61P 42

Ostriker, J. P., Choi, E., Ciotti, L., Novak, G. S., & Proga, D. 2010, ApJ, 722, 642 6

O'Sullivan, E., Forbes, D. A., & Ponman, T. J. 2001, MNRAS, 328, 461 62, 66, 71

O'Sullivan, E., Ponman, T. J., & Collins, R. S. 2003, MNRAS, 340, 1375 71

Pearson, T. J. 1996, in Astronomical Society of the Pacific Conference Series, Vol. 100,

Energy Transport in Radio Galaxies and Quasars, ed. P. E. Hardee, A. H. Bridle, & J. A. Zensus, 97 20

Pellegrini, S. 2010, ApJ, 717, 640 75, 220

Pellegrini, S., Venturi, T., Comastri, A., et al. 2003, ApJ, 585, 677 13

Peterson, B. 1997, An Introduction to Active Galactic Nuclei (Cambridge University Press) 1, 16

Peterson, J. R. & Fabian, A. C. 2006, Phys. Rep., 427, 1 26

Plotkin, R. M., Anderson, S. F., Brandt, W. N., et al. 2012, ApJ, 745, L27 13, 16, 164

Prieto, M. A., Walsh, J. R., Fosbury, R. A. E., & di Serego Alighieri, S. 1993, MNRAS, 263, 10 136

Proga, D. & Begelman, M. C. 2003, ApJ, 592, 767 12

Pudritz, R. E., Hardcastle, M. J., & Gabuzda, D. C. 2012, Space Sci. Rev., 169, 27 20

Punsly, B. & Zhang, S. 2011, ApJ, 735, L3 xii, 201, 202, 203, 204, 208, 220

Ramos Almeida, C., Dicken, D., Tadhunter, C., et al. 2011a, MNRAS, 413, 2358 17, 175

Ramos Almeida, C., Levenson, N. A., Alonso-Herrero, A., et al. 2011b, ApJ, 731, 92 11

Ramos Almeida, C., Rodríguez Espinosa, J. M., Acosta-Pulido, J. A., et al. 2013, MNRAS, 542 164

Ramos Almeida, C., Tadhunter, C. N., Inskip, K. J., et al. 2010, MNRAS, 1609 25, 114, 116, 117, 119, 120, 124, 127, 129, 131, 133, 134, 138, 140, 142, 144, 145, 147, 149, 151, 152, 153, 154, 156, 157, 158, 159, 160, 161, 196

Rawlings, S. & Saunders, R. 1991, Nature, 349, 138 18

Rees, M. J., Netzer, H., & Ferland, G. J. 1989, ApJ, 347, 640 16

Reichstein, A. & Gabuzda, D. 2012, Journal of Physics Conference Series, 355, 012021 20

Reynolds, C., Punsly, B., Kharb, P., O'Dea, C. P., & Wrobel, J. 2009, ApJ, 706, 851 60

Reynolds, C. S., Fabian, A. C., Celotti, A., & Rees, M. J. 1996, MNRAS, 283, 873 20

Risaliti, G., Elvis, M., Fabbiano, G., et al. 2007, ApJ, 659, L111 16

Risaliti, G., Elvis, M., & Nicastro, F. 2002, ApJ, 571, 234 11, 16, 49, 74, 220, 222

Risaliti, G., Woltjer, L., & Salvati, M. 2003, A&A, 401, 895 147

Rosenblatt, E. I., Malkan, M. A., Sargent, W. L. W., & Readhead, A. C. S. 1992, ApJS,

81, 59 49
Runnoe, J. C., Brotherton, M. S., & Shang, Z. 2012, MNRAS, 422, 478 185, 197
Russell, H. R., McNamara, B. R., Edge, A. C., et al. 2012, ArXiv e-prints 13, 14, 164, 195
Rybicki, G. B. & Lightman, A. P. 1986, Radiative Processes in Astrophysics, ed. Rybicki, G. B. & Lightman, A. P. (Wiley-VCH) 7, 8, 9, 15, 20, 23
Sabater, J., Best, P. N., & Argudo-Fernández, M. 2013, MNRAS, 430, 638 24
Saikia, D. J. & Jamrozy, M. 2009, Bulletin of the Astronomical Society of India, 37, 63 4, 42, 78
Sambruna, R. M., Brandt, W. N., Chartas, G., et al. 2001a, ApJ, 546, L9 79
Sambruna, R. M., Netzer, H., Kaspi, S., et al. 2000, in Bulletin of the American Astronomical Society, Vol. 32, Bulletin of the American Astronomical Society, 1187–+ 79
Sambruna, R. M., Netzer, H., Kaspi, S., et al. 2001b, ApJ, 546, L13 79
Sault, R. J., Teuben, P. J., & Wright, M. C. H. 1995, in Astronomical Society of the Pacific Conference Series, Vol. 77, Astronomical Data Analysis Software and Systems IV, ed. R. A. Shaw, H. E. Payne, & J. J. E. Hayes, 433 81
Sazonov, S., Willner, S. P., Goulding, A. D., et al. 2012, ApJ, 757, 181 10
Schawinski, K. 2010, ArXiv e-prints 60
Schawinski, K., Lintott, C. J., Thomas, D., et al. 2009, ApJ, 690, 1672 60
Scheuer, P. A. G. 1974, MNRAS, 166, 513 22, 103
Schmidt, M. 1969, ARA&A, 7, 527 1
Schulz, H. 1988, A&A, 203, 233 101
Schurch, N. J., Griffiths, R. E., & Warwick, R. S. 2006, MNRAS, 371, 211 43, 48, 49, 54, 55
Seyfert, C. K. 1943, ApJ, 97, 28 1
Shabala, S. & Alexander, P. 2009, ApJ, 699, 525 78
Shakura, N. I. & Sunyaev, R. A. 1973, A&A, 24, 337 6, 163
Shepherd, M. C., Pearson, T. J., & Taylor, G. B. 1994, in Bulletin of the American Astronomical Society, Vol. 26, Bulletin of the American Astronomical Society, 987–989 81
Siebert, J., Brinkmann, W., Morganti, R., et al. 1996, MNRAS, 279, 1331 127, 169
Silk, J. & Rees, M. J. 1998, A&A, 331, L1 5, 164

Simpson, C., Ward, M., & Wall, J. V. 2000, MNRAS, 319, 963 210
Simpson, J. P., Colgan, S. W. J., Erickson, E. F., et al. 2002, ApJ, 574, 95 106
Smith, D. A. & Wilson, A. S. 2001, ApJ, 557, 180 79, 80, 83, 84
Smith, D. A., Wilson, A. S., Young, A. J., & Terashima, Y. 2000, in Bulletin of the American Astronomical Society, Vol. 32, Bulletin of the American Astronomical Society, 1563–+ 79
Soldi, S., Türler, M., Paltani, S., et al. 2008, A&A, 486, 411 114
Sramek, R. A. & Weedman, D. W. 1980, ApJ, 238, 435 4
Subrahmanyan, R., Saripalli, L., & Hunstead, R. W. 1996, MNRAS, 279, 257 156
Sulentic, J. W., Marziani, P., & Dultzin-Hacyan, D. 2000, ARA&A, 38, 521 16, 112
Sunyaev, R. A. & Titarchuk, L. G. 1980, A&A, 86, 121 10
Sutherland, R. S. & Bicknell, G. V. 2007, ApJS, 173, 37 104
Swartz, D. A., Ghosh, K. K., Tennant, A. F., & Wu, K. 2004, ApJS, 154, 519 57
Tadhunter, C., Dickson, R., Morganti, R., et al. 2002, MNRAS, 330, 977 161
Tadhunter, C. N., Morganti, R., di Serego-Alighieri, S., Fosbury, R. A. E., & Danziger, I. J. 1993, MNRAS, 263, 999 111, 112, 145, 168
Tadhunter, C. N., Morganti, R., Robinson, A., et al. 1998, MNRAS, 298, 1035 112, 168
Tadhunter, C. N., Ramos Almeida, C., Morganti, R., et al. 2012, MNRAS, 427, 1603 158, 175
Tajer, M., Polletta, M., Chiappetti, L., et al. 2007, A&A, 467, 73 3
Trussoni, E., Vagnetti, F., Massaglia, S., et al. 1999, A&A, 348, 437 127, 129
Tüllmann, R., Breitschwerdt, D., Rossa, J., Pietsch, W., & Dettmar, R.-J. 2006a, A&A, 457, 779 97
Tüllmann, R., Pietsch, W., Rossa, J., Breitschwerdt, D., & Dettmar, R.-J. 2006b, A&A, 448, 43 97
Vallée, J. P. 2011, New A Rev., 55, 91 107
van der Wolk, G., Barthel, P. D., Peletier, R. F., & Pel, J. W. 2010, A&A, 511, A64 12, 115, 122, 138, 145, 164
van Weeren, R. J., Röttgering, H. J. A., Brüggen, M., & Hoeft, M. 2010, Science, 330, 347 106
Venturi, T., Bardelli, S., Morganti, R., & Hunstead, R. W. 2000, MNRAS, 314, 594 24
Vink, J. & Laming, J. M. 2003, ApJ, 584, 758 107

Völk, H. J., Berezhko, E. G., & Ksenofontov, L. T. 2005, A&A, 433, 229 107
Volonteri, M. & Ciotti, L. 2012, ArXiv e-prints 196, 205, 206
Wall, J. V. & Peacock, J. A. 1985, MNRAS, 216, 173 111, 165
Wandel, A., Peterson, B. M., & Malkan, M. A. 1999, ApJ, 526, 579 6
Wang, J., Fabbiano, G., Elvis, M., et al. 2009, ApJ, 694, 718 58, 91, 92
Wild, V., Heckman, T., & Charlot, S. 2010, MNRAS, 405, 933 26
Willott, C. J., Rawlings, S., Blundell, K. M., & Lacy, M. 1999, MNRAS, 309, 1017 195, 196, 200
Wills, K. A., Morganti, R., Tadhunter, C. N., Robinson, T. G., & Villar-Martin, M. 2004, MNRAS, 347, 771 129, 175
Wilson, A. S., Shopbell, P. L., Simpson, C., et al. 2000, AJ, 120, 1325 81, 83, 84, 87, 92
Wilson, A. S. & Ulvestad, J. S. 1987, ApJ, 319, 105 106
Wilson, W. E., Ferris, R. H., Axtens, P., et al. 2011, MNRAS, 416, 832 80
Wing, J. D. & Blanton, E. L. 2011, AJ, 141, 88 24
Woltjer, L. 1959, ApJ, 130, 38 1, 16
Worrall, D. M. 2009, A&A Rev., 17, 1 22
Worrall, D. M., Tananbaum, H., Giommi, P., & Zamorani, G. 1987, ApJ, 313, 596 182
Wright, A. & Otrupcek, R. 1990, in PKS Catalog (1990), 0 168
Wu, X.-B. & Liu, F. K. 2004, ApJ, 614, 91 112
Yamasaki, N. Y., Sato, K., Mitsuishi, I., & Ohashi, T. 2009, PASJ, 61, 291 97
Yang, Y., Wilson, A. S., Matt, G., Terashima, Y., & Greenhill, L. J. 2009, ApJ, 691, 131 92
Young, A. J., Wilson, A. S., & Mundell, C. G. 2002, ApJ, 579, 560 42
Yuan, F. 2007, in Astronomical Society of the Pacific Conference Series, Vol. 373, The Central Engine of Active Galactic Nuclei, ed. L. C. Ho & J.-W. Wang, 95 13
Yuan, F., Markoff, S., & Falcke, H. 2002, A&A, 383, 854 13
Zensus, J. A. 1997, ARA&A, 35, 607 20
Zhou, Y. Y., Yu, K. N., Young, E. C. M., Wang, J. M., & Ma, E. 1997, ApJ, 475, L9 15